Interfaces in crystalline materials

Aurélien Vattré

HABILITATION À DIRIGER DES RECHERCHES

AURÉLIEN VATTRÉ

Maître de Recherche à l'ONERA

Interfaces in crystalline materials

Université Sorbonne Paris Nord
Habilitation soutenue le 10 mai 2023 devant le jury composé de :

Ioan Ionescu	Président
Brigitte Bacroix	Rapporteure
Stéphane Berbenni	Rapporteur
Marc Fivel	Rapporteur
Renald Brenner	Examinateur

ONERA
THE FRENCH AEROSPACE LAB

HABILITATION À DIRIGER DES RECHERCHES

Interfaces in crystalline materials

Interfaces such as grain boundaries in polycrystalline as well as and heterointerfaces in multiphase are ubiquitous in materials science and engineering with wide-ranging properties and applications. Therefore, understanding the basics of interfaces is key in optimization of ceramics for a wide range of applications including electrochemical energy conversion and storage, optical, magnetic, and mechanical applications, thermal applications including thermal and environmental barrier coatings in automobile and aeronautical industries.

Far from being featureless dividing surfaces between neighboring crystals, elucidating features of solid-solid interfaces is challenging and requires theoretical and numerical strategies to describe the physical and mechanical characteristics of these internal interfaces. The first part of this manuscript is concerned with interface-dominated microstructures emerging from polymorphic structural (diffusionless) phase transformations. Under high hydrostatic compression and shock-wave conditions, the pressure-driven phase transitions and the formation of internal diffuse interfaces in iron are captured by a thermodynamically consistent framework for combining nonlinear elastoplasticity and multivariant phase-field approach at large strains. The calculations investigate the crucial role played by the plastic deformation in the morphological and microstructure evolution processes under high hydrostatic compression and shock-wave conditions. The second section is intended to describe such imperfect interfaces at a finer scale, for which the semicoherent interfaces are described by misfit dislocation networks that produce a lattice-invariant deformation which disrupts the uniformity of the lattice correspondence across the interfaces and thereby reduces coherency. For the past ten years, the constant effort has been devoted to combining the closely related Frank-Bilby and O-lattice techniques with the Stroh sextic formalism for the anisotropic elasticity theory of interfacial dislocation patterns. The structures and energetics are quantified and used for rapid computational design of interfaces with tailored misfit dislocation patterns, including the interface sink strength for radiation-induced point defects and semicoherent interfaces.

Contents

Remerciements

Je tiens à remercier les membres du jury, qui ont accepté d'évaluer ce mémoire : Brigitte Bacroix, Stéphane Berbenni, Renald Brenner, Marc Fivel et Ioan Ionescu. Je remercie plus particulièrement les rapporteurs d'avoir pris le temps si précieux de rapporter ce travail dans les moindres détails. Merci pour vos retours positifs si encourageants !

Bien entendu, le contenu de ce travail aurait été réduit à une peau de chagrin sans les échanges constants avec mes anciens collègues de la Direction des Applications Militaires du Commissariat à l'Énergie Atomique, Christophe Denoual, Jean-Lin Dequiedt, Yves-Patrick Pellegrini et Ronan Madec. Outre-Atlantique, je mesure la chance d'avoir fait des rencontres inspirantes, en particulier avec Robert Balluffi, David Barnett, Michael Demkowicz, John Hirth, Ernian Pan, et j'en oublie, Niaz Abdorrahim, Tom Arsenlis, Sylvie Aubry, Nicolas Bertin, Wei Cai, Christian Brandl, Kedar Kolluri, Enrique Martinez, Ryan Sills, et j'en oublierai encore ! Je tiens aussi à remercier mes collègues les plus proches de l'Office, Christophe Bovet, Jean-Didier Garaud, Serge Kruch, Johann Rannou, sans désir d'exhaustivité. Je remercie Anne Tanguy d'avoir régulièrement soutenu cette habilitation, et ce depuis le début de l'aventure. Une attention particulière et amicale se tourne vers Vincent Chiaruttini, la seule personne disponible à 3h au mat' pour discuter, en partie, des correspondances théoriques et numériques entre une fissure et une dislocation... bienvenue dans le monde de cette dernière, mais arrêtons d'échanger si tard (quoique, continuons, mais n'en parlons ni à Aurélie, ni à Aurélie...). Je souhaite chaleureusement remercier toute l'équipe du secrétariat du Département Matériaux et Structures : votre aide à résoudre quotidiennement des problèmes administratifs est précieuse.

Merci enfin à un groupe spécial $\mathrm{A}^3 = \{$ Achille (4 mois), Anton (2 ans), Aurélie $\}^\star$ pour le bonheur non borné qu'il m'apporte au quotidien. Cette habilitation, qui contient les « mille-feuilles » et autres « Rubik's cubes » déjà contemplés, est aussi la votre !

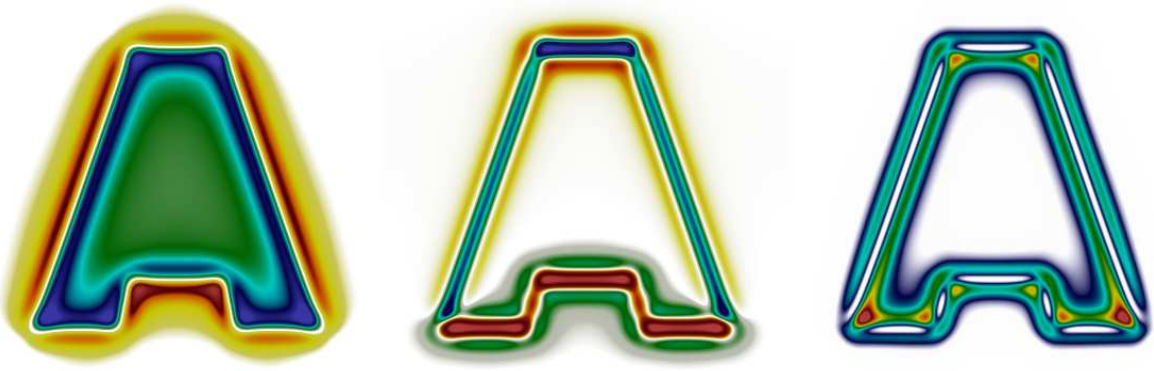

* Solutions régularisées et anisotropes de la contrainte normale, de cisaillement et de la densité d'énergie d'une boucle prismatique de dislocation simplement connexe, plongée dans un « mille-feuille »

Chapter 1

Introduction

Interfaces in polycrystalline as well as multiphase solids of natural and synthetic origin have found their places in various applications, ranging from semiconductor devices to advanced multifunctional coatings in automobile and aeronautical industries. Remarkably, the behavior of polycrystalline materials is often reduced to the analysis of their inherent grain boundaries, while the most recent roadmaps on photonics and phononics propose to design on-demand bandgaps by tailoring the topological interface states in metamaterials. As claimed by Wolfgang Pauli, however, because "God made the bulk; the surface was invented by the devil!", the interface engineering of solid-state materials inevitably requires specific experimental and numerical contributions to describe the physical and mechanical characteristics of these internal interfaces. Far from being featureless dividing surfaces between neighboring crystals, the study of the structure and properties of homo- and hetero-phase interfaces has thus become as a central area in a broder field of the materials science and engineering.

The manuscript is divided into two chapters, considering first the thermodynamics of diffuse interfaces in chapter 2, which was developed more than a hundred years ago by Gibbs. The description of the structures and energetics of imperfect interfaces, namely semicoherent interfaces, is then treated in chapter 3. These semicoherent interfaces are also described by misfit dislocation networks that produce a lattice-invariant deformation which disrupts the uniformity of the lattice correspondence across the interfaces and thereby reduces coherency. This topic has more recently received considerable attention due to the development of high-resolution techniques and increased computational resources in recent decades.

The first introductive chapter 2 is thus concerned with the internal interfaces emerging from polymorphic structural (diffusionless) phase transformations. The formation of these solid-solid interfaces during the pressure-driven phase transitions in iron is captured by a thermodynamically consistent framework for combining nonlinear elastoplasticity and multivariant phase-field approach at large strains. Treatments of thermodynamics and kinetic relations of the phase transitions are formulated by the free energy landscape that involves the concept of reaction pathways with respect to the point group symmetry properties of both low- (cubic) and high- (hexagonal) pressure crystal lattices of iron. The phase-field formalism coupled with finite elastoplastic deformations is implemented into a three-dimensional finite element scheme and is applied to the body-centered cubic into hexagonal close-packed phase transitions under high hydrostatic compression and shock-wave conditions. The calculations exhibit the crucial role played by the plastic deformation in the morphological and microstructure evolution processes. However, the coexistence over a wide range of pressure of both cubic and hexagonal lattice structures in the interface-dominated microstructure leads, in general, to the loss of lattice coherence at the interfaces, for which the lattice correspondence across the grain boundaries and heterophase interfaces require a fine dislocation-based description of internal interfaces. It is this last objective that is covered by the main chapter 3.

Chapter 3 is therefore dedicated to the structures and energetics of heterophase interfaces. Although the simplest interface is a single isolated planar interface separating two adjacent crystals, also viewed as a planar interface in bimaterials, such an idealized interface between two dissimilar

crystals provides the essential basis for understanding the properties of interface-dominated materials. For the past ten years, the constant effort has been devoted to combining the closely related Frank-Bilby and O-lattice techniques with the Stroh sextic formalism for the anisotropic elasticity theory of interfacial dislocation patterns. The key formalism is used by means of a Fourier series-based analysis to determine the reference states of semicoherent interfaces that gives rise to dislocation arrays whose far-field elastic fields meet the condition of vanishing far-field strains and prescribed misorientations. In accordance with the quantized Frank-Bilby equation, these interface dislocation structures, which are also viewed as Volterra dislocations that have been inserted into the reference state, generate persistent short-range elastic stresses near the interfaces. The corresponding energetics have been quantified and used for rapid computational design of interfaces with tailored misfit dislocation patterns. In particular, a coupled approach with an object kinetic Monte Carlo code has revealed that elastic interactions between radiation-induced point defects and semicoherent interfaces lead to significant increases in interface sink strength, compared to the case with no defect-interface interactions. The original work has also been extended to bilayers of finite thickness terminated with free surfaces, layered superlattices with differing layer thicknesses as well as multilayered magneto-electro-elastic plates for semicoherent interfaces with relaxed dislocation patterns at semicoherent interfaces including core-spreading effects. Overall, the elastic full-field solutions have been compared with atomistic calculations for many specific lattice structures, which provide an opportunity for rigorous validation of the anisotropic elasticity theory of interfacial dislocations as well as for collaborations with individuals outside the home laboratory.

Although the reader may be disappointed (I understand it...) not to find the content of the two chapters combined together in a unified formalism, chapter 4 provides concluding remarks and further directions for near future developments.

Chapter 2

Crystalline interfaces during solid-solid phase transitions in iron

Selected peer-reviewed articles

[P26] N. Bruzy, C. Denoual, **A. Vattré**. *Polyphase crystal plasticity for high strain rate: application to twinning and retwinning in tantalum*. Journal of the Mechanics and Physics of Solids, 104921, 2022.

[P22] **A. Vattré**, C. Denoual. *Continuum nonlinear dynamics of unstable shock waves induced by structural phase transformations in iron*. Journal of the Mechanics and Physics of Solids, 131, 387-403, 2019.

[P12] C. Denoual, **A. Vattré**. *A phase field approach with a reaction pathways-based potential to model reconstructive martensitic transformations with a large number of variants*. Journal of the Mechanics and Physics of Solids, 90, 91-107, 2016.

[P11] **A. Vattré**, C. Denoual. *Polymorphism of iron at high pressure: a 3D phase-field model for displacive transitions with finite elastoplastic deformations*. Journal of the Mechanics and Physics of Solids, 92, 1-27, 2016.

2.1 Motivation

The high-pressure and high-deformation states of iron (Fe) are of vital importance in many technological and sociological applications [33] as well as in geophysics due to the role of Fe properties in the Earth and telluric exoplanet internal structure [233]. Fundamental understanding of the physical and mechanical properties of Fe under extreme conditions, where the deformation state is caused by various irreversible processes (e.g. plasticity and polymorphic structural (diffusionless) solid-solid phase transformations), is therefore crucial in both materials science and condensed matter physics.

The first indirect evidence of polymorphic phase transitions in iron has been discovered by [17] under shock compression. The authors reported a series of three discontinuous jumps in the velocity of the free surface and postulated that the three shock-wave structure is produced by a compressive elastic precursor (Ep wave) followed by a plastic wave (P wave), and, a third wave attributed to a phase transformation (PT wave). Wave profile measurements indicate that the onset of the phase transition occurred at a pressure of $\sim$ 13 GPa and room temperature on the Hugoniot. Since the pioneering experiments, efforts succeeded in acquiring static high pressure X-ray diffraction analysis, where the stable ferromagnetic body-centered cubic ground state (bcc α-Fe) has shown a magnetic and structural transition to the nonmagnetic hexagonal close-packed phase (hcp ϵ-Fe) at about 13 GPa, revealing the same transition as in shock experiments. Therefore, both bcc and hcp phases have been observed to coexist over a wide range of pressure, which captures

the signature of a diffusionless solid-to-solid martensitic transition in iron. While the phase diagram of iron under hydrostatic pressure is well established [217], detailed in situ observations via dynamic X-ray diffraction techniques during shock-loading have supported unambiguously that the high pressure phase has hcp crystal structure [139, 287]. However, due to the considerable experimental difficulties of quantifying plasticity with respect to the polymorphic phase transformations during shock wave propagation in solids, the complete irreversible deformation mechanism still remains poorly investigated.

The high pressure-induced transition in iron has been intensively described using ab-initio electronic structure calculations, where some simulation results remain debated. Although the broad outline of the transition has been settled by crystallographic considerations [49, 179, 23], a major problem deals with the accuracy in determining the energy landscape for the bcc-to-hcp transition [84, 170]. Furthermore, ab-initio computational resources are limited to small system sizes, for which plasticity-induced effects in iron cannot be captured by first-principles calculations. Alternative approaches are based on large-scale molecular dynamics simulations that give insight into the motion of multi-million-atoms. Shock waves have also been simulated by employing embedded atom method potentials and varying initial shock strength [137, 138, 136]. For low particle velocities, an elastic shock wave of uniaxially compressed bcc was observed. With increasing shock strength, a two-wave shock structure was identified with an elastic precursor followed by a slower phase-transition wave. No direct evidence of plastic wave profile was observed, certainly due to the small time scale compared to experiments that exhibit a three-wave structure at the nanosecond scale [17, 19]. While further work is needed to understand the detailed mechanisms of plasticity under shock conditions, phase-field models provide a companion approach to shock response of crystalline materials at higher time and length scales.

Various continuum mechanics approaches to simulate martensitic phase transitions in the context of plasticity theory have been developed and can be categorized by the nature of the scale description of the constitutive relations. A first micromechanical class of models aims to deliver predictions of macroscopic observables, e.g. stress-strain curves, by including microstructural aspects via homogenization and averaging techniques. In a multiscale strategy, relevant approaches track the volume fraction of martensite phase in the small [129, 215] and large [148, 177] strain formulations. However, these models are generally unable to predict detailed microstructural changes and spatial arrangements of parent−product interfaces during phase transformations at the nanometer scale. A second class of models for displacive transformations has pushed toward smaller scales in an effort to capture transformational processes by tracking the kinetics of interface orientations and variants with respect to the associated configurational forces. Thus, structural phase-field approaches have been successfully applied to model microstructure evolution by formulating thermodynamic driving forces for martensitic transitions between stable states [157, 10, 142, 77, 291]. Treatments of thermodynamics and kinetic relations in phase-field approaches are related to the pioneering works by [50] and [3], within which a material system tends to evolve towards a minimum state of free energy.

Chapter 2 introduces a thermodynamically consistent framework for combining nonlinear elastoplasticity and multivariant phase-field approach at large strains [252]. In accordance with the Clausius-Duhem inequality in section 2.2, the Helmholtz free energy and time-dependent constitutive relations give rise to displacive driving forces for pressure-induced martensitic phase transitions in materials. Inelastic forces are obtained by using a representation of the energy landscape that involves the concept of reaction pathways with respect to the point group symmetry operations of crystal lattices [76]. Using the element-free Galerkin method with high-performance computing resources, the finite deformation framework is used to analyze the polymorphic α- into ϵ-Fe iron phase transitions under high hydrostatic compression [252] and shock-wave [253] loadings, as detailed in sections 2.3 and 2.4, respectively, while a recent application to twinning and retwinning in tantalum can be found in Ref. [44]. The three-dimensional nonlinear simulations accurately reproduce observable characteristics reported by the experimental literature, for which

the crucial role played by the plastic deformation is analyzed with respect to the peculiar formation of interface-dominated microstructure with a specific selection of high-pressure variants.

2.2 A phase-field model coupled with finite elastoplasticity

This section is concerned with a thermodynamically consistent phase-field formalism for solid-state transitions. The model is formulated in a Lagrangian framework for finite strains, motivated by obtaining isothermal driving forces and constitutive relations at a material point.

2.2.1 Kinematics

An arbitrary material point X is defined in a homogeneous reference configuration $\Omega_0 \subset \mathbb{R}^3$, for which the motion of Ω_0 is given by the mapping $x = \chi(X,t) : \Omega_0 \to \Omega \subset \mathbb{R}^3$ with respect to time t. The total deformation gradient $\mathbf{F}$ is related to the following multiplicative decomposition [158, 159, 148, 161], i.e.,

$$\mathbf{F} = \left.\frac{\partial \chi}{\partial X}\right|_t = \boldsymbol{\nabla}\chi = \mathbf{Fe}\cdot\mathbf{Ft}\cdot\mathbf{Fp}\,, \tag{2.1}$$

with $\boldsymbol{\nabla}$ the material gradient with respect to X. Here, the reference configuration is associated with the initial single-crystal bcc iron, and, the total deformation gradient is decomposed into elastic $\mathbf{Fe}$, plastic $\mathbf{Fp}$, and, transformational $\mathbf{Ft}$ distortions, leading to the pressure-induced phase transformation from the bcc to hcp phases.

Similarly to classical crystal elastoplasticity theories [151, 156], the decomposition eq. (2.1) is not uniquely defined and different ordering relations have been taken into account in the literature [241]. Because the local irreversible plastic deformation $\mathbf{Fp}$ of the neighborhood of X, e.g. caused by dislocation glides, does not alter the crystal orientation and structure of the lattice vectors, the transformational component $\mathbf{Ft}$ occurs between $\mathbf{Fp}$ and $\mathbf{Fe}$, where the elastic contribution accounts for the lattice stretching $\mathbf{Ue}$ and rotation $\mathbf{Re}$. The polar decomposition to $\mathbf{Fe}$ reads: $\mathbf{Fe} = \mathbf{Re}\cdot\mathbf{Ue}$, with $\mathbf{Ue}^2 = \mathbf{Fe}^{\mathrm{t}}\cdot\mathbf{Fe}$, and, $\det\mathbf{Fe} = \det\mathbf{Ue} = j_{\mathrm{e}}$. The superscript $^{\mathrm{t}}$ denotes the transpose operation. Although the controversy regarding the decomposition is beyond the scope of this paper, both tensors $\mathbf{Fp}$ and $\mathbf{Ft}$ describe here two intermediate configurations, $\Omega\mathrm{p}$ and $\Omega\mathrm{t}$, as shown in Fig. (2.1). For more justifications regarding the three-term multiplication decomposition eq. (2.1) for nonlinear elasticity coupled to martensitic phase transformations and plasticity, the reader is referred to the recent analysis on combined kinematics in Ref. [161]. It follows from eq. (2.1) that the total spatial velocity gradient tensor $\mathbf{L}$ is given by

$$\mathbf{L} = \dot{\mathbf{F}}\cdot\mathbf{F}^{-1} = \mathbf{Le} + \mathbf{Fe}\cdot\mathbf{Lt}\cdot\mathbf{Fe}^{-1} + \mathbf{Fet}\cdot\mathbf{Lp}\cdot\mathbf{Fet}^{-1}\,, \tag{2.2}$$

with $\mathbf{Fet} = \mathbf{Fe}\cdot\mathbf{Ft}$. The superposed dot in eq. (2.2) denotes the time derivative. The elastic $\mathbf{Le}$, transformational $\mathbf{Lt}$, and, plastic $\mathbf{Lp}$ velocity strain tensors are similarly defined by

$$\mathbf{Le} = \dot{\mathbf{Fe}}\cdot\mathbf{Fe}^{-1},\ \mathbf{Lt} = \dot{\mathbf{Ft}}\cdot\mathbf{Ft}^{-1},\ \text{and}\ \ \mathbf{Lp} = \dot{\mathbf{Fp}}\cdot\mathbf{Fp}^{-1}\,, \tag{2.3}$$

which are related to the current and the intermediate configurations, i.e., Ω, $\Omega\mathrm{t}$ and $\Omega\mathrm{p}$, respectively. Furthermore, two basic kinematic assumptions are considered in the present theory:

1. The measures of volume changes after each deformation processes satisfy:

$$j_{\mathrm{e}} = \det\mathbf{Fe} > 0,\ j_{\mathrm{t}} = \det\mathbf{Ft} > 0,\ \text{and}\ \ \det\mathbf{Fp} = 1\,, \tag{2.4}$$

so that, $\mathbf{Fe}$, $\mathbf{Ft}$ and $\mathbf{Fp}$ are invertible, and, the plastic flow preserves the volume.

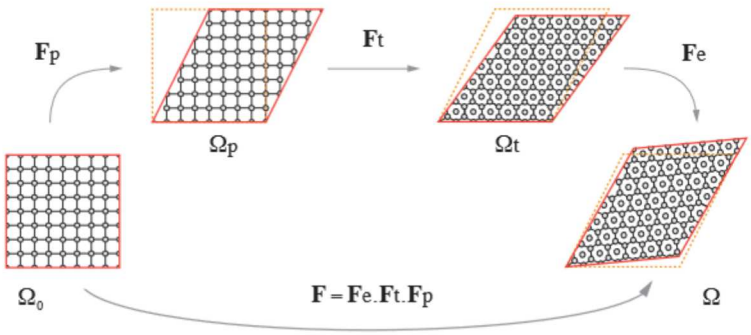

FIGURE 2.1: Schematics of the reference Ω_0, intermediate, Ωp and Ωt, and, current Ω configurations, for which the total deformation gradient tensor $\mathbf{F}$ is decomposed multiplicatively into plastic $\mathbf{F}$p, transformational $\mathbf{F}$t and elastic $\mathbf{F}$e distortions.

2. The model is restricted to isotropic plastic theories with irrotational plastic flows. Therefore,

$$\dot{\mathbf{F}}\mathrm{p} = \mathbf{D}\mathrm{p}\cdot\mathbf{F}\mathrm{p}, \text{ with } \mathbf{D}\mathrm{p} = \mathrm{sym}\,\mathbf{L}\mathrm{p} = \mathbf{L}\mathrm{p}\,, \tag{2.5}$$

where sym $\mathbf{L}$p denotes the symmetric part of $\mathbf{L}$p.

Figure (2.1) illustrates the multiplicative split of the total deformation gradient tensor $\mathbf{F}$. In agreement with the conservation law of mass, the determinant of $\mathbf{F}$ gives the volume change between the current (with a volume V) and the reference (V_0) configurations, i.e., $j = \det\mathbf{F} = \rho_0/\rho = V/V_0$, where ρ (ρ_0 with $\dot{\rho}_0 = 0$) is the current (reference) mass density.

2.2.2 Balance laws

During the different deformation processes, the equilibrium equations of force must be fulfilled. In the Lagrangian description, the local form of the linear momentum balance is given by

$$\boldsymbol{\nabla}\cdot\mathbf{P} + \rho_0\,\boldsymbol{b} = \rho_0\,\ddot{\boldsymbol{u}} \text{ in } \Omega_0\,, \tag{2.6}$$

where $\mathbf{P}$ is the first (non-symmetric) Piola-Kirchhoff stress tensor, $\boldsymbol{b}$ are external body forces per unit mass, and, $\ddot{\boldsymbol{u}} = \ddot{\boldsymbol{x}}(\boldsymbol{X}, t)$ is the acceleration of the material point $\boldsymbol{X}$, with $\boldsymbol{u}$ the corresponding displacement field, defined by $\boldsymbol{u} = \boldsymbol{x}(\boldsymbol{X}, t) - \boldsymbol{X}$.

An appropriate formulation of the constitutive relations for isothermal and irreversible processes of deformation requires a thermodynamically consistent formalism, within which the balance law in eq. (2.6) holds at all points $\boldsymbol{X}$ in the domain of Ω_0.

2.2.3 The Clausius-Duhem inequality

The martensitic phase-field approach coupled with large elastoplastic deformations is derived within a thermodynamic framework in which the second law of thermodynamics plays a crucial role. When the thermal effects are ignored, the fundamental Clausius-Duhem inequality is expressed in terms of stress power per unit reference volume [67] as

$$\int_{\Omega_0} \left(\mathbf{P}:\dot{\mathbf{F}} - \rho_0\,\dot{\psi}\right)\,\mathrm{d}\Omega_0 \geq 0\,, \tag{2.7}$$

where : denotes the double inner tensor product, and, ψ the specific Helmholtz free energy. Equation (2.7) shows that the first Piola-Kirchhoff stress tensor $\mathbf{P}$ and the deformation gradient $\mathbf{F}$ are work-conjugate variables, while $\mathbf{P}:\dot{\mathbf{F}}$ defines the mechanical stress power per unit volume in the Lagrangian formulation.

Within the model of the multiplicative decomposition in finite strains, it is conveniently postulated that the Helmholtz free energy can be written in the following form:

$$\psi \doteq \psi\left(\mathbf{Fe}, \mathbf{Ft}, \boldsymbol{\nabla}\mathbf{Ft}\right) , \tag{2.8}$$

where $\boldsymbol{\nabla}\mathbf{Ft}$ is a phenomenological third-order gradient term that acts as a penalty for spatial nonuniformity to produce diffuse interfaces. Because the elastic response is not affected by the plastic activities, the elastic part of the Helmholtz free energy is supposed to depend on the elastic and transformational distortions only. Moreover, it is assumed that both transformational and plastic works are not dependent on each other, so that the free energy may be additively decomposed into elastic ψ_{e}, transformational ψ_{t}, and, purely empirical gradient penalty ψ_{∇} contributions. With the aforementioned considerations, the Helmholtz free energy can thus be written as

$$\psi \doteq \psi_{\mathrm{e}}\left(\mathbf{Fe}, \mathbf{Ft}\right) + \psi_{\mathrm{t}}\left(\mathbf{Ft}\right) + \psi_{\nabla}\left(\boldsymbol{\nabla}\mathbf{Ft}\right) , \tag{2.9}$$

which, in contrast with ab-initio electronic structure calculations, is not uniquely defined. However, such elastic/inelastic splitting, comparable to the classical phase-field models with elastic and chemical potentials [278, 10], is fundamental for applications that exhibit a strong coupling between acoustic waves and phase transformations, e.g. wave propagation influencing the early stages of the phase transitions induced by shock loadings. Thus, eqs. (2.1) and (2.9) yield to the rates of the total deformation and free energy, i.e.,

$$\begin{aligned} \dot{\mathbf{F}} &= \dot{\mathbf{Fe}}\cdot\mathbf{Ft}\cdot\mathbf{Fp} + \mathbf{Fe}\cdot\dot{\mathbf{Ft}}\cdot\mathbf{Fp} + \mathbf{Fe}\cdot\mathbf{Ft}\cdot\dot{\mathbf{Fp}} \\ \dot{\psi} &= \left.\frac{\partial\psi_{\mathrm{e}}}{\partial\mathbf{Fe}}\right|_{\mathbf{Ft}} : \dot{\mathbf{Fe}} + \left.\frac{\partial\psi_{\mathrm{e}}}{\partial\mathbf{Ft}}\right|_{\mathbf{Fe}} : \dot{\mathbf{Ft}} + \frac{\partial\psi_{\mathrm{t}}}{\partial\mathbf{Ft}} : \dot{\mathbf{Ft}} + \frac{\partial\psi_{\nabla}}{\partial\boldsymbol{\nabla}\mathbf{Ft}} \therefore \boldsymbol{\nabla}\dot{\mathbf{Ft}} , \end{aligned} \tag{2.10}$$

where $\therefore$ denotes the triple inner tensor product. Inserting eqs. (2.10) into the global form of the Clausius-Duhem inequality (2.7) and applying the chain rule, the non-negative requirement leads therefore to

$$\begin{aligned} \int_{\Omega_0} \Bigg\{ \left(\mathbf{P}\cdot\mathbf{Fp}^{\mathrm{t}}\cdot\mathbf{Ft}^{\mathrm{t}} - \rho_0 \left.\frac{\partial\psi_{\mathrm{e}}}{\partial\mathbf{Fe}}\right|_{\mathbf{Ft}}\right) : \dot{\mathbf{Fe}} + \left(\mathbf{Fe}^{\mathrm{t}}\cdot\mathbf{P}\cdot\mathbf{Fp}^{\mathrm{t}} - \rho_0 \left.\frac{\partial\psi_{\mathrm{e}}}{\partial\mathbf{Ft}}\right|_{\mathbf{Fe}} - \rho_0 \frac{\partial\psi_{\mathrm{t}}}{\partial\mathbf{Ft}}\right) : \dot{\mathbf{Ft}} + \boldsymbol{\Sigma}_* : \mathbf{Dp} \\ - \rho_0 \frac{\partial\psi_{\nabla}}{\partial\boldsymbol{\nabla}\mathbf{Ft}} \therefore \boldsymbol{\nabla}\dot{\mathbf{Ft}} \Bigg\} \mathrm{d}\Omega_0 \geq 0 , \end{aligned} \tag{2.11}$$

where $\boldsymbol{\Sigma}_*$ is a work-conjugate stress measure related to the first Piola-Kirchhoff $\mathbf{P}$, as follows

$$\boldsymbol{\Sigma}_* = \mathbf{Fe}^{\mathrm{t}}\cdot\mathbf{P}\cdot\mathbf{Fp}^{\mathrm{t}} . \tag{2.12}$$

Using the permutability of time and space differentiation in the reference configuration and the Gauss theorem, the last right-hand side term in eq. (2.11) can be rewritten, i.e.,

$$\int_{\Omega_0} \left(\frac{\partial\psi_{\nabla}}{\partial\boldsymbol{\nabla}\mathbf{Ft}} \therefore \boldsymbol{\nabla}\dot{\mathbf{Ft}}\right) \mathrm{d}\Omega_0 = -\int_{\Omega_0} \left(\boldsymbol{\nabla}\cdot\frac{\partial\psi_{\nabla}}{\partial\boldsymbol{\nabla}\mathbf{Ft}} : \dot{\mathbf{Ft}}\right) \mathrm{d}\Omega_0 + \int_{\Sigma_0} \underbrace{\left(\dot{\mathbf{Ft}} : \frac{\partial\psi_{\nabla}}{\partial\boldsymbol{\nabla}\mathbf{Ft}}\cdot\boldsymbol{n}\right)}_{\text{surface dissipation}} \mathrm{d}\Sigma_0 , \tag{2.13}$$

where Σ_0 is a boundary of Ω_0 with unit outward normal $\boldsymbol{n}$. Assuming that the surface dissipation is absent during the transformational process, additional boundary conditions as set of nine equations for phase transitions may also be derived by

$$\frac{\partial\psi_{\nabla}}{\partial\boldsymbol{\nabla}\mathbf{Ft}}\cdot\boldsymbol{n} = \mathbf{0}, \text{ with } \dot{\mathbf{Ft}} \neq \mathbf{0} \text{ at } \Sigma_0 , \tag{2.14}$$

corresponding to the orthogonality relations between $\boldsymbol{\nabla}\mathbf{F}\mathrm{t}$ and the external surfaces Σ_0. Thus, eqs. (2.11−2.14) yield to a local formulation of the free energy imbalance in terms of dissipation per unit reference volume of mechanical energy $\mathcal{D}$, as follows

$$\mathcal{D} = \left(\mathbf{P}\cdot\mathbf{F}\mathrm{p}^{\mathrm{t}}\cdot\mathbf{F}\mathrm{t}^{\mathrm{t}} - \rho_0 \left.\frac{\partial\psi_{\mathrm{e}}}{\partial\mathbf{F}\mathrm{e}}\right|_{\mathbf{F}\mathrm{t}} \right) : \dot{\mathbf{F}}\mathrm{e} + \mathbf{X}\mathrm{t} : \dot{\mathbf{F}}\mathrm{t} + \boldsymbol{\Sigma}_* : \mathbf{D}\mathrm{p} \geq 0\,, \tag{2.15}$$

where the dissipative forces $\mathbf{X}\mathrm{t}$, conjugated to dissipative rate $\dot{\mathbf{F}}\mathrm{t}$, are given by

$$\mathbf{X}\mathrm{t} = \mathbf{F}\mathrm{e}^{\mathrm{t}}\cdot\mathbf{P}\cdot\mathbf{F}\mathrm{p}^{\mathrm{t}} - \rho_0 \left.\frac{\partial\psi_{\mathrm{e}}}{\partial\mathbf{F}\mathrm{t}}\right|_{\mathbf{F}\mathrm{e}} - \rho_0\frac{\partial\psi_{\mathrm{t}}}{\partial\mathbf{F}\mathrm{t}} + \rho_0\,\boldsymbol{\nabla}\cdot\frac{\partial\psi_{\nabla}}{\partial\boldsymbol{\nabla}\mathbf{F}\mathrm{t}}\,. \tag{2.16}$$

The relation (2.16) defines the thermodynamic displacive driving forces for change in $\mathbf{F}\mathrm{t}$, acting on a material point $\boldsymbol{X}$ under isothermal conditions. Although the plastic deformation is not integrated as an internal state variable, e.g. via a defect-energy term as in Refs. [107, 2], but rather as a kinematic variable, the plastic contribution may significantly alter the state of residual stress and also play an important role in dictating the morphology of the microstructural changes and in modeling the irreversibility of phase transitions.

2.2.4 Constitutive equations

Constitutive equations for reversible elastic deformations and irreversible processes of deformable material bodies undergoing phase and plastic deformations are required to be consistent with the Clausius-Duhem inequality.

Hyperelasticity

The standard assumption that the rate of dissipation is independent of $\dot{\mathbf{F}}\mathrm{e}$ in eq. (2.15), i.e., elasticity is a non-dissipative process, results in the hyperelasticity constitutive relation in terms of the first Piola-Kirchhoff stress field, as follows

$$\mathbf{P} = \rho_0 \left.\frac{\partial\psi_{\mathrm{e}}}{\partial\mathbf{F}\mathrm{e}}\right|_{\mathbf{F}\mathrm{t}} \cdot \mathbf{F}\mathrm{t}^{-\mathrm{t}}\cdot\mathbf{F}\mathrm{p}^{-\mathrm{t}}\,. \tag{2.17}$$

A quadratic form for the strain energy density per unit reference volume is assumed, for which a dependence of ψ_{e} on $\mathbf{F}\mathrm{e}$ and $\mathbf{F}\mathrm{t}$ manifests explicitly via the anisotropic elastic components:

$$\rho_0\psi_{\mathrm{e}} = \tfrac{1}{2}\mathbf{E}\mathrm{e} : \mathbb{D}\left(\mathbf{C}\mathrm{et}\right) : \mathbf{E}\mathrm{e}\,, \tag{2.18}$$

where $\mathbf{E}\mathrm{e}$ is the elastic Green-Lagrange strain tensor, defined by

$$\mathbf{E}\mathrm{e} = \tfrac{1}{2}\left(\mathbf{C}\mathrm{e} - \mathbf{I}\right)\,, \tag{2.19}$$

with $\mathbf{C}\mathrm{e} = \mathbf{F}\mathrm{e}^{\mathrm{t}}\cdot\mathbf{F}\mathrm{e}$ the right elastic Cauchy-Green deformation tensor, so that $\mathbf{C}\mathrm{et} = \mathbf{F}\mathrm{t}^{\mathrm{t}}\cdot\mathbf{C}\mathrm{e}\cdot\mathbf{F}\mathrm{t}$. Inserting eq. (2.18) into the hyperelasticity condition (2.17), the nonlinear stress-elastic strain constitutive relation is rewritten as follows

$$\mathbf{P} = \mathbf{F}\mathrm{e}\cdot\mathbf{S}\mathrm{e}\cdot\mathbf{F}\mathrm{t}^{-\mathrm{t}}\cdot\mathbf{F}\mathrm{p}^{-\mathrm{t}} + \mathbf{F}\mathrm{et}\cdot\left(\mathbf{E}\mathrm{e} : \frac{\partial\mathbb{D}\left(\mathbf{C}\mathrm{et}\right)}{\partial\mathbf{C}\mathrm{et}} : \mathbf{E}\mathrm{e}\right)\cdot\mathbf{F}\mathrm{p}^{-\mathrm{t}}\,, \tag{2.20}$$

where $\mathbf{S}\mathrm{e} = \mathbb{D}\left(\mathbf{C}\mathrm{et}\right) : \mathbf{E}\mathrm{e}$ is an elastic stress measure associated with $\mathbf{E}\mathrm{e}$, and, $\partial_{\mathbf{C}\mathrm{et}}\mathbb{D}$ is a sixth-order tensor, i.e., the derivative of $\mathbb{D}$ with respect of $\mathbf{C}\mathrm{et}$. It is worth pointing out that the anisotropic pressure-dependent elastic stiffness tensors of both bcc and hcp phases are explicitly taken into account in the present formalism.

With use of the non-dissipative properties of hyperelasticity, the local dissipation considered in the Clausius-Duhem inequality (2.15) can also be conceptually divided into transformational $\mathcal{D}_t$ and plastic $\mathcal{D}_p$ dissipative rates per unit reference volume, i.e.,

$$\mathcal{D} \doteq \mathcal{D}_t + \mathcal{D}_p \geq 0\,, \tag{2.21}$$

due to the onset of the phase transitions or the movements of interface during phase transitions, and, to the plastic deformation in materials, respectively. For simplicity, it is assumed that both transformational and plastic dissipative processes are thermodynamically uncoupled such that the inequality (2.21) splits into two stronger non-negative inequalities, as follows

$$\mathcal{D}_t = \mathbf{X}t : \dot{\mathbf{F}}t \geq 0 \;\text{ and, }\; \mathcal{D}_p = \boldsymbol{\Sigma}_* : \mathbf{D}p \geq 0\,. \tag{2.22}$$

Kinetic constitutive relations that relate the rates $\dot{\mathbf{F}}t$ and $\mathbf{D}p$ to the associated driving forces for both dissipative processes in hyperelastic materials must also be defined such that the inequalities in eqs. (2.22) are satisfied. These steps are carried out in the two subsequent sections.

Kinetics of phase transitions

For solid-state structural transformations, a linear kinetic equation that relates the rate of the transformational distortion $\dot{\mathbf{F}}t$ to the displacive driving forces $\mathbf{X}t$ is suggested, i.e.,

$$\upsilon\, \dot{\mathbf{F}}t = \mathbf{X}t\,, \tag{2.23}$$

where $\upsilon > 0$ is a viscosity-like parameter. For example, the case with $\upsilon \to 0$ represents an instantaneous relaxation. The evaluation of the kinetic equations for martensitic phase transitions is still a subject of intense debates, within which the average transformational kinetics may be influenced by the nucleation processes, interface mobilities, collective dislocation behaviors, as well as inertial effects. In the context of the time-dependent Ginzburg-Landau formalism, a detailed modeling of the kinetics of phase transitions in iron is not the purpose of the present analysis. However, the linear form of the driving forces $\mathbf{X}t$ gives rise to thermodynamic consistency conditions for phase transformations, so that the dissipation inequality in eq. (2.22) is unequivocally satisfied, as follows

$$\mathcal{D}_t = \upsilon\, |\mathbf{X}t|^2 \geq 0\,, \tag{2.24}$$

with $|\mathbf{X}t|$ the Frobenius norm of $\mathbf{X}t$. A nonequilibrium thermodynamic system is also characterized when $\mathcal{D}_t > 0$, e.g. corresponding to mobile solid-solid interfaces when $\mathbf{X}t > \mathbf{0}$. Using eqs. (2.16) and (2.20), eq. (2.23) yields

$$\upsilon\, \dot{\mathbf{F}}t = \mathbf{X}t = \underbrace{\mathbf{C}e \cdot (\mathbb{D}\,(\mathbf{C}et) : \mathbf{E}e) \cdot \mathbf{F}t^{-t}}_{\text{forces due to elastic energy}} - \underbrace{\rho_0 \frac{\partial \psi_t}{\partial \mathbf{F}t} + \rho_0\, \boldsymbol{\nabla} \cdot \frac{\partial \psi_\nabla}{\partial \boldsymbol{\nabla}\mathbf{F}t}}_{\text{transformational forces}}\,, \tag{2.25}$$

including mechanical elastically and transformational inelastically induced driving forces, with a gradient-related term for interface energy. Equation (2.25) shows competition between driving forces due to elastic energy and the inelastic transformational forces related to microstructure evolution processes in materials. In particular, the (meta)stable equilibrium configurations are achieved when $\mathbf{X}t = \mathbf{0}$, exhibiting a force balance between the elastic and inelastic contributions.

A general quadratic form for the gradient energy penalty that is localized at the diffuse interfaces between two phases may be defined by

$$\rho_0\, \psi_\nabla = \tfrac{1}{2} \boldsymbol{\nabla}\mathbf{F}t \;\therefore\; {}^6\boldsymbol{\Lambda} \;\therefore\; \boldsymbol{\nabla}\mathbf{F}t\,, \tag{2.26}$$

where ${}^6\mathbf{\Lambda}$ is a positive definite symmetric (major symmetry) sixth-order tensor that takes into account the gradient-energy interaction between different phases. Assuming an isotropic description of the interface energy and neglecting the interactions between all phases [160] such that ${}^6\mathbf{\Lambda} = \lambda\ {}^6\mathbf{I}$, with ${}^6\mathbf{I}$ the sixth-rank identity tensor, eq. (2.26) reduces to

$$\rho_0\,\psi_\nabla = \tfrac{1}{2}\lambda\,\boldsymbol{\nabla}\mathbf{F}\mathrm{t} \,\therefore\, {}^6\mathbf{I} \,\therefore\, \boldsymbol{\nabla}\mathbf{F}\mathrm{t} = \tfrac{1}{2}\lambda\,\boldsymbol{\nabla}\mathbf{F}\mathrm{t} \,\therefore\, \boldsymbol{\nabla}\mathbf{F}\mathrm{t}\,, \tag{2.27}$$

where the positive scalar λ controls phenomenologically the finite width of interfaces. The latter distance may be correlated to the short-range elastic fields produced by discrete intrinsic dislocation arrays between bcc/hcp semicoherent heterophase interfaces and also computed by using a recent formalism linking the Frank-Bilby equation and anisotropic elasticity theory, as investigated in chapter 3. Finally, the driving forces expressed in the Ginzburg-Landau formalism are given by

$$v\,\dot{\mathbf{F}}\mathrm{t} = \mathbf{X}\mathrm{t} = \mathbf{C}\mathrm{e}\cdot(\mathbb{D}\,(\mathbf{C}\mathrm{et}) : \mathbf{E}\mathrm{e})\cdot\mathbf{F}\mathrm{t}^{-\mathrm{t}} - \rho_0\frac{\partial\psi_\mathrm{t}}{\partial\mathbf{F}\mathrm{t}} + \lambda\,\boldsymbol{\nabla}^2\mathbf{F}\mathrm{t}\,, \tag{2.28}$$

with $\boldsymbol{\nabla}^2$ the Laplacian operator.

Plastic flow rule

Macroscopic quasi-perfectly plastic regimes have been observed in polycrystalline bcc iron samples under high-strain rate compressions [132]. To go beyond the elastic limit, the large strain perfectly plastic J_2 flow theory has also been incorporated in the present model. Accordingly, the evolution of the plastic distortion $\mathbf{F}\mathrm{p}$, given in terms of the plastic deformation rate $\mathbf{D}\mathrm{p}$, is determined by considering the postulate of maximum dissipation [118]. The space of admissible stresses $\mathcal{E}_\sigma$ is written as

$$\mathcal{E}_\sigma = \{\sigma \mid \phi\,(\sigma) < 0\}\,, \tag{2.29}$$

where the yield function ϕ is expressed in terms of the Cauchy stress σ, defined by

$$\sigma = j^{-1}\,\mathbf{P}\cdot\mathbf{F}^\mathrm{t} = j^{-1}\,\mathbf{F}\mathrm{e}\cdot\mathbf{S}\mathrm{e}\cdot\mathbf{F}\mathrm{e}^\mathrm{t} + j^{-1}\,\mathbf{F}\mathrm{et}\cdot\left(\mathbf{E}\mathrm{e} : \frac{\partial\mathbb{D}\,(\mathbf{C}\mathrm{et})}{\partial\mathbf{C}\mathrm{et}} : \mathbf{E}\mathrm{e}\right)\cdot\mathbf{F}\mathrm{et}^\mathrm{t}\,, \tag{2.30}$$

according to eq. (2.20). The work-conjugate stress $\mathbf{\Sigma}_*$ in eq. (2.12) may also be related to the Cauchy stress tensor σ by

$$\mathbf{\Sigma}_* = j\,\mathbf{F}\mathrm{et}^\mathrm{t}\cdot\sigma\cdot\mathbf{F}\mathrm{et}^{-\mathrm{t}} = \mathbf{F}\mathrm{t}^\mathrm{t}\cdot\mathbf{\Sigma}\cdot\mathbf{F}\mathrm{t}^{-\mathrm{t}}\,, \tag{2.31}$$

where $\mathbf{\Sigma} = j\,\mathbf{F}\mathrm{e}^\mathrm{t}\cdot\sigma\cdot\mathbf{F}\mathrm{e}^{-\mathrm{t}}$. Thus, the rate of plastic deformation $\mathbf{D}\mathrm{p}$ is given by the associated flow rule, as follows

$$\mathbf{D}\mathrm{p} = \dot{\eta}\ \mathbf{F}\mathrm{et}^{-1}\cdot\frac{\partial\phi}{\partial\sigma}\cdot\mathbf{F}\mathrm{et} = \dot{\eta}\ \mathbf{H}\,, \tag{2.32}$$

with $\dot{\eta} \geq 0$ a non-negative scalar-valued factor, so-called the plastic multiplier, that is required to satisfy the consistency relation: $\dot{\eta}\,\phi = 0$. The outward normal to the yield surface is given by $\mathbf{H}$ in the stress space, for which the yield function ϕ in eqs. (2.29) and (2.32) is described with the von Mises yield criterion, i.e.,

$$\phi\,(\sigma) = \sqrt{3\,J_2\,(\sigma)} - \sigma_0 \ \text{ with, } \ J_2 = \tfrac{1}{2}\,\mathrm{dev}\,\sigma : \mathrm{dev}\,\sigma\,, \tag{2.33}$$

where $\sigma_0 > 0$ is the yield stress measure, and, $\mathrm{dev}\,\sigma$ denotes the deviatoric part of σ. Finally, including the direction of the plastic flow into the rate $\mathbf{D}\mathrm{p}$, eq. (2.32) yields

$$\mathbf{D}\mathrm{p} = \tfrac{3}{2}\,\dot{\eta}\ \mathbf{F}\mathrm{et}^{-1}\cdot\frac{\mathrm{dev}\,\sigma}{\sigma_0}\cdot\mathbf{F}\mathrm{et}\,, \tag{2.34}$$

for which the dissipation inequality for plastic flow in eq. (2.22) with (2.31) is satisfied, i.e.,

$$\mathcal{D}_{\mathrm{p}} = \tfrac{3}{2}\, j\, \dot{\eta}\, \frac{|\mathrm{dev}\boldsymbol{\sigma}|^2}{\sigma_0} \geq 0\,. \tag{2.35}$$

According to eqs. (2.24) and (2.35), the present formalism is also thermodynamically consistent since the Clausius-Duhem inequality (2.21) is fulfilled.

2.2.5 Multiple reaction pathways and energy landscape

In what follows in section 2.2.5, focus is on the $\alpha \leftrightarrow \epsilon$ phase transitions in iron, where the energy landscape is defined by reaction pathways for multivariants with respect to the point group symmetry properties of the bcc and hcp lattices.

The bcc-to-hcp transition mechanism

As illustrated in Fig. (2.2a), the considered crystallographic relations in the bcc-to-hcp martensitic phase transition are given by the Mao-Bassett-Takahashi mechanism [179], as follows

$$[001]_{\mathrm{bcc}} \parallel [2\bar{1}\bar{1}0]_{\mathrm{hcp}} \;\text{ and, }\; (110)_{\mathrm{bcc}} \parallel (0001)_{\mathrm{hcp}}\,, \tag{2.36}$$

which differs from the transformation path proposed in Ref. [49] by a rotation of $\sim \pm 5.2^{\circ}$ around the $[0001]_{\mathrm{hcp}}$ axis [271]. The structural relations in eq. (2.36) are achieved by considering two transformation operations, as shown in Fig. (2.2b). The hcp phase may be obtained by applying a shear to a $(110)_{\mathrm{bcc}}$ plane, which consists of an elongation and a compression along the $[1\bar{1}0]_{\mathrm{bcc}}$ and the $[001]_{\mathrm{bcc}}$ directions, respectively. This transformation is required to form a regular hexagon (in red in Fig. 2.2b) and may be related to a homogeneous linear mapping $\mathbf{U}$, i.e.,

$$\mathbf{U} = \begin{bmatrix} \frac{3}{4\sqrt{2}} + \frac{1}{4}\sqrt{\frac{3}{2}}\, c_{/a} & -\frac{3}{4\sqrt{2}} + \frac{1}{4}\sqrt{\frac{3}{2}}\, c_{/a} & 0 \\ -\frac{3}{4\sqrt{2}} + \frac{1}{4}\sqrt{\frac{3}{2}}\, c_{/a} & \frac{3}{4\sqrt{2}} + \frac{1}{4}\sqrt{\frac{3}{2}}\, c_{/a} & 0 \\ 0 & 0 & \frac{\sqrt{3}}{2} \end{bmatrix}, \tag{2.37}$$

where $c_{/a} = c\,/a$ is the lattice ratio for the pure ϵ-Fe phase [55], while the volume change accompanying the phase transition is determined by $\det \mathbf{U} = 9c_{/a}\,/16$. Then, the mechanism involves a shuffle $\boldsymbol{t}$, which corresponds to atomic displacements of every other deformed $(110)_{\mathrm{bcc}}$ plane in one of the two possible opposite $[1\bar{1}0]_{\mathrm{bcc}}$ directions. The close-packed structure of hcp is also obtained, where a ratio $c_{/a}$ of 1.603 ± 0.001 has been experimentally determined along this bcc-to-hcp path in iron [179, 78], reflecting a $\sim 10\%$ volume reduction.

In the described case, the transformations $\mathbf{U}$ and $\boldsymbol{t}$ are illustrated separately but can occur simultaneously, as discussed by using first-principles simulations [81]. For both scenarios, the shuffle does not induce any lattice-distortion transformations and has therefore no direct coupling with the overall stress in the deforming materials. Although not visible for a given deformation state at the macroscopic scale, the shuffling modes, however, may have important implications on the free energy along the reaction pathways as well as the kinetics of phase transitions, which are not taken into account in the present formalism. Assuming to take place at a smaller time scale compared to the lattice-distortion transformations, additional variables of state (also, additional associated kinetic equations) should therefore be introduced to characterize such atomistic displacements. With the aforementioned considerations, and because of the required number of finite element meshes for three-dimensional calculations, the example applications to high-pressure compression in sections 2.3 and 2.4 focus on the first cycle of forward and reverse martensitic transitions only, for which the shuffle does not modify the point group symmetries. For higher-order

cycles, this mechanism may be responsible for the generation of an unbounded set of variants. The notion of transformation cycles has been addressed in Ref. [76], where a two-dimensional simulation has shown that variants could hierarchically nucleate into previously created ones over up to five levels of transformations for the square to hexagonal martensitic phase transitions.

When $c_{/a}$ is experimentally chosen to determine eq. (2.37), the corresponding homogeneous mapping $\mathbf{U}$ contains obviously and inseparably both elastic and irreversible part of the deformation in samples. A homogeneous distortion $\mathbf{U}\mathrm{t}$ is therefore introduced to identify the pure transformational component of the total deformation provided by experimental data under high hydrostatic pressure, i.e.,

$$\mathbf{U}\mathrm{t} = \kappa \mathbf{U}\,, \tag{2.38}$$

where κ is a elastic correction factor, as discussed in Ref. [252].

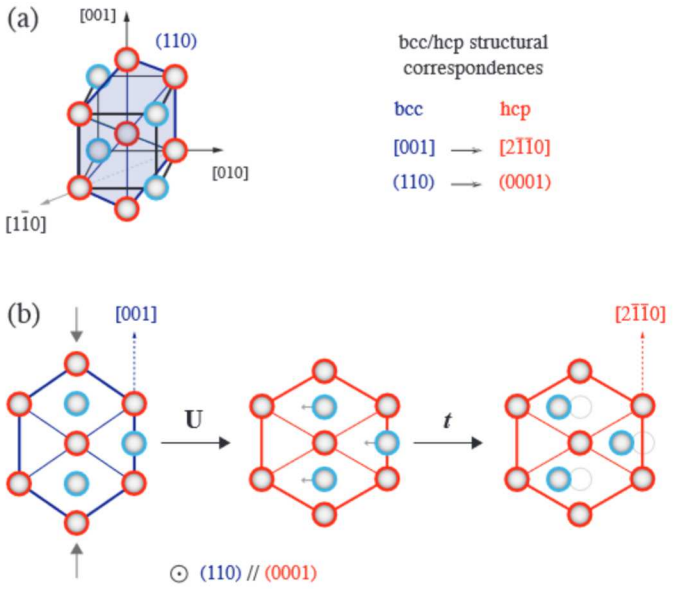

FIGURE 2.2: Crystallographic relations in the bcc-to-hcp martensitic phase transition established in Refs. [179, 23]. (a) Red atoms in a bcc atomic-side unit cell are located at a $(110)_{\mathrm{bcc}}$ layer and the blue atoms at the adjacent layers. (b) The transition path consists of two transformations. First, a shear deformation $\mathbf{U}$ leads to an elongation and a compression along the $[1\bar{1}0]_{\mathrm{bcc}}$ and the $[001]_{\mathrm{bcc}}$ directions, respectively. The deformation transforms a polygon in blue into a regular hexagon in red, corresponding to the $(0001)_{\mathrm{hcp}}$ hcp basal plane. Then, a shuffle $\boldsymbol{t}$ is applied to the entire plane that contains the blue atoms, e.g. by shifting all these atoms in the $[1\bar{1}0]_{\mathrm{bcc}}$ direction.

Multiple symmetry-related variants

During the forward $\alpha \rightarrow \epsilon$ and the reverse $\epsilon \rightarrow \alpha'$ martensitic transformations, significant differences in orientation from the initial α-Fe phase may exist. To make the clear distinction in phase orientation between variant formation and selection, α' denotes here the reversed α phase, as depicted by the two-dimensional schematic network in Fig. (2.3a).

A rigorous link between the standard crystallographic concepts of holohedry with group-subgroup relationships, crystal system and Bravais lattice type (cubic and hexagonal), is explicitly included into the phase-field formalism. For the forward $\alpha \rightarrow \epsilon$ transition, the generation of all hcp variants ${}^{\epsilon n}_{\alpha}\mathbf{U}\mathrm{t}$ from the linear mapping $\mathbf{U}\mathrm{t}$ is described by

$${}^{\epsilon n}_{\alpha}\mathbf{U}\mathrm{t} = \mathbf{R}^{\mathrm{t}}_{\mathrm{bcc}} \cdot \mathbf{U}\mathrm{t} \cdot \mathbf{R}_{\mathrm{bcc}}\,, \tag{2.39}$$

where $\mathbf{R}_{\text{bcc}}$ is a rotation matrix in the point group of cubic lattice ${}^{n}\mathcal{H}_{\text{bcc}}$ and n the number of hcp variants [206]. Because of the high symmetry of the considered phase, a total number of 6 hcp variants are generated, i.e., $n = 1, \ldots, 6$, within which 18 operations in the basic group of 24 rotations for cubic lattices are redundant. To complete the phase transformations with the reverse $\epsilon \rightarrow \alpha'$ transitions, the bcc variants ${}^{\alpha' m}_{\epsilon n}\mathbf{U}\text{t}$ are deduced by performing the following operation:

$$ {}^{\alpha' m}_{\epsilon n}\mathbf{U}\text{t} = \mathbf{R}^{\text{t}}_{\text{bcc}} \cdot \mathbf{R}^{\text{t}}_{\text{hcp}} \cdot \mathbf{U}\text{t}^{-1} \cdot \mathbf{R}_{\text{hcp}} \cdot \mathbf{U}\text{t} \cdot \mathbf{R}_{\text{bcc}} \,, \tag{2.40} $$

where $\mathbf{R}_{\text{hcp}}$ is a rotation matrix in the point group of hexagonal lattice ${}^{m}\mathcal{H}_{\text{hcp}}$ and m the number of bcc variants [206]. Equation (2.40) consists in generating 12 bcc variants, i.e., $m = 1, \ldots, 12$, so that a total of 19 variants (including the identity as the 19$^{\text{th}}$ variant) are identified to describe the complete bcc-hcp-bcc transition in terms of multiple symmetry-related variant structures. Figure (2.3a) depicts the forward transition of the initial bcc phase, leading to six equivalent hcp phases, and, the reverse transition from each hcp phase that leads to three bcc phases.

All tabulated hcp and bcc variants with the corresponding holohedral subgroups ${}^{m}\mathcal{H}_{\text{bcc}}$ and ${}^{n}\mathcal{H}_{\text{hcp}}$ are given in Tab. 1 from Ref. [252], where the rotation axes are expressed in the hcp and bcc lattice basis, respectively. For clarity, the matrices defined by eqs. (2.39) and (2.40) are written in the following as ${}^{k}\mathbf{U}\text{t}$ with $k = 1, \ldots, 18$, i.e.,

$$ {}^{k}\mathbf{U}\text{t} = \begin{cases} {}^{\epsilon n}_{\alpha}\mathbf{U}\text{t} & 1 \leq k \leq 6 \\ {}^{\alpha' m}_{\epsilon n}\mathbf{U}\text{t} & 7 \leq k \leq 18 \,, \end{cases} \tag{2.41} $$

which are associated with the variant of interest V_k for the forward $(1 \leq k \leq 6)$ and the reverse $(7 \leq k \leq 18)$ transformations.

Reaction pathways in strain spaces

Instead of introducing the Landau thermodynamic potential [162], where the classical Landau-type approach with polynomials is not convenient to apply for reconstructive transitions due to the large numbers of potential energy wells [28], the concept of reaction pathways [77, 76] is used to describe the phase transitions in iron. In particular, the minimum inelastic energy density profile between two different pure phases is represented by a single reaction pathway, along which the associated function $\hat{\psi}_{\text{t}_k}$ is assumed to possess the same symmetries as all symmetry-related variants V_k, and, to satisfy the principle of material objectivity [27], e.g.,

$$ \hat{\psi}_{\text{t}_k} \doteq \hat{\psi}_{\text{t}_k}\left({}^{k}\hat{\mathbf{C}}\text{t}\right) , \tag{2.42} $$

where ${}^{k}\hat{\mathbf{C}}\text{t}$ are the transformational Cauchy-Green strain measures for all pure phases, given by

$$ {}^{k}\hat{\mathbf{C}}\text{t} = {}^{k}\mathbf{U}\text{t}^{\text{t}} \cdot {}^{k}\mathbf{U}\text{t} \,, \tag{2.43} $$

as listed in Appendix A from Ref. [252], with the aid of eqs. (2.39−2.41). Here and in the following, the superimposed caret will be used to indicate quantities strictly defined along the pathways. To model continuous forward and the reverse transformations, each transition pathway k is represented by linear interpolation between starting ${}^{k}\hat{\mathbf{C}}\text{t}_{\text{start}}$ and ending ${}^{k}\mathbf{C}\text{t}_{\text{end}}$ strain states, as follows

$$ {}^{k}\hat{\mathbf{C}}\text{t}\,(s_k) = (1 - s_k)\,{}^{k}\hat{\mathbf{C}}\text{t}_{\text{start}} + s_k\,{}^{k}\hat{\mathbf{C}}\text{t}_{\text{end}} \,, \tag{2.44} $$

with $s_k \in [0, 1]$ the curvilinear coordinates along k. For instance, hcp variants V_k are parameterized by: ${}^{k}\hat{\mathbf{C}}\text{t}_{\text{start}} = \mathbf{I}$ and ${}^{k}\hat{\mathbf{C}}\text{t}_{\text{end}} = {}^{k}\mathbf{U}\text{t}^2$, with $1 \leq k \leq 6$. Generating the reaction pathways with eqs. (2.37−2.44) and using projection matrices $\mathbf{C}_1$, $\mathbf{C}_2$ and $\mathbf{C}_3$, an example of three-dimensional

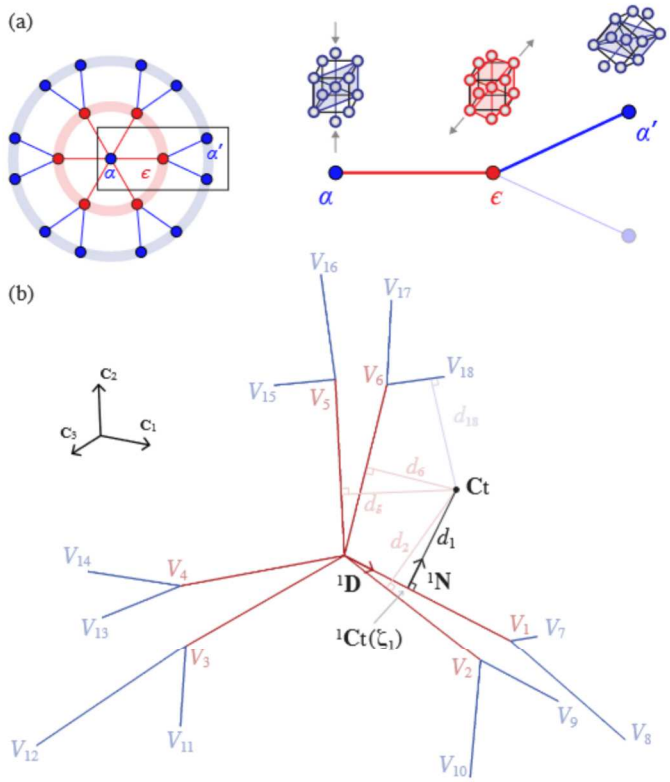

FIGURE 2.3: (a) Schematic illustration of the multiple symmetry-related variants for the forward $\alpha \rightarrow \epsilon$ (in red) and the reverse $\epsilon \rightarrow \alpha'$ (blue) phase transitions in iron. (b) The corresponding reaction pathway network in a specific $\{\mathbf{C}_1, \mathbf{C}_2, \mathbf{C}_3\}$ strain space, within which the transformational Cauchy-Green tensor $\mathbf{Ct} = \mathbf{Ft}^{\mathrm{t}} \cdot \mathbf{Ft}$ as well as some quantities described in the text, are defined.

representation of the network is shown in Fig. (2.3b), within which each pathway connects continuously and linearly with two pure bcc/hcp variants V_k in the $\{\mathbf{C}_1, \mathbf{C}_2, \mathbf{C}_3\}$ strain space. The projection is not unique and the specific strain space in Fig. (2.3b) is characterized by using the following matrices:

$$\mathbf{C}_1 = \begin{bmatrix} 1 & 1 & 0 \\ 1 & -3 & 0 \\ 0 & 0 & 0 \end{bmatrix}, \quad \mathbf{C}_2 = \begin{bmatrix} 0 & 0 & 0 \\ 0 & 1 & 1 \\ 0 & 1 & -3 \end{bmatrix}, \quad \mathbf{C}_3 = \begin{bmatrix} -3 & 0 & 1 \\ 0 & 0 & 0 \\ 1 & 0 & 1 \end{bmatrix}. \tag{2.45}$$

The reaction pathway network describes also a six-dimensional energy landscape, for which each straight segment represents a minimum-energy reaction pathway that connects two stable/(meta)stable states with possible (if any) saddle points [28].

Inelastic energy landscape

In order to define the total inelastic energy landscape ψ_{t} in a whole strain space, e.g. not only restricted along the pathways as $\hat{\psi}_{\mathrm{t}_k}$, the partition of unity approach is used as a weighted sum of the contribution ψ_{t_k} of each individual pathway k. Thus, the overall inelastic energy density ψ_{t} is formally defined by introducing the weighting functions $\omega_k(\mathbf{Ct})$, i.e.,

$$\psi_{\mathrm{t}}(\mathbf{Ct}) = \sum_{k=1}^{18} \omega_k(\mathbf{Ct})\ \psi_{\mathrm{t}_k}(\mathbf{Ct}), \tag{2.46}$$

for any transformational Cauchy-Green tensor $\mathbf{Ct} = \mathbf{Ft}^{\mathrm{t}} \cdot \mathbf{Ft}$. Without loss of generality, for any given tensor $\mathbf{A}$, e.g. $\mathbf{Ct}$ and $\mathbf{Cet}$, these functions $\omega_k(\mathbf{A})$ satisfy the partition of unity condition,

namely:

$$\sum_{k=1}^{18} \omega_k(\mathbf{A}) = 1 \text{ with, } \omega_k(\mathbf{A}) = \frac{d_k^{-h}(\mathbf{A})}{\sum_{i=1}^{18} d_i^{-h}(\mathbf{A})}, \tag{2.47}$$

where h is a positive parameter that controls the weighted average of all pathways. The quantities $d_k(\mathbf{A})$ correspond to the minimum Euclidean distances in the strain space between $\mathbf{A}$ and the pathways k, defined by

$$d_k(\mathbf{A}) = |{}^k\boldsymbol{\Pi}(\mathbf{A})| = \min_{\zeta_k \in [0,1]} |\mathbf{A} - {}^k\hat{\mathbf{A}}(\zeta_k)|, \tag{2.48}$$

where ${}^k\hat{\mathbf{A}}(\zeta_k)$ are also mapped onto the reaction pathways with $\zeta_k(\mathbf{A})$ the corresponding reaction coordinates. For example, when $\mathbf{A} = \mathbf{C}$t: Fig. (2.3b) shows the projected tensor ${}^1\hat{\mathbf{C}}\mathrm{t}(\zeta_1)$ onto the forward pathway 1, between the initial single-crystal bcc phase and the hcp variant V_1. Introducing the convenient curvilinear coordinates $\zeta_k^\infty(\mathbf{A})$ for fictitious unbounded pathways, as follows

$$\zeta_k^\infty(\mathbf{A}) = {}^k\hat{\mathbf{D}} : (\mathbf{A} - {}^k\hat{\mathbf{C}}\mathrm{t}_{\text{start}}) = \frac{{}^k\hat{\mathbf{C}}\mathrm{t}_{\text{end}} - {}^k\hat{\mathbf{C}}\mathrm{t}_{\text{start}}}{|{}^k\hat{\mathbf{C}}\mathrm{t}_{\text{end}} - {}^k\hat{\mathbf{C}}\mathrm{t}_{\text{start}}|} : (\mathbf{A} - {}^k\hat{\mathbf{C}}\mathrm{t}_{\text{start}}), \tag{2.49}$$

where ${}^k\hat{\mathbf{D}}$ defines the normalized direction of the pathway k, the argmin ζ_k in eq. (2.48) is also determined by solving $\partial_{\zeta_k} d_k(\mathbf{A}) = 0$ for a given $\mathbf{C}$t, leading to

$$\zeta_k(\mathbf{A}) = \begin{cases} \zeta_k^\infty(\mathbf{A}) & \text{if : } \quad \zeta_k^\infty(\mathbf{A}) \in [0,1] \\ 0 & \text{if : } \quad \zeta_k^\infty < 0 \\ 1 & \text{if : } \quad \zeta_k^\infty > 1, \end{cases} \tag{2.50}$$

so that the distance measure $d_k(\mathbf{A})$ in eq. (2.48) with (2.50) represents the minimum distance from $\mathbf{A}$ to a given segment in $\mathbb{R}^6$.

On the other hand, it is assumed that each potential ψ_{t_k} in eq. (2.46) is related to the minimum energy density $\hat{\psi}_{\mathrm{t}_k}$ combining with an additional out-of-path component, i.e.,

$$\psi_{\mathrm{t}_k}(\mathbf{C}\mathrm{t}) = \hat{\psi}_{\mathrm{t}_k}(\zeta_k(\mathbf{C}\mathrm{t})) + \underbrace{\sigma\, d_k(\mathbf{C}\mathrm{t}) + \pi\, |\operatorname{tr} {}^k\boldsymbol{\Pi}(\mathbf{C}\mathrm{t})|}_{\text{out-of-path component}}, \tag{2.51}$$

such that $\partial_{\mathbf{C}\mathrm{t}} \operatorname{tr} {}^k\boldsymbol{\Pi}(\mathbf{C}\mathrm{t})$ and ${}^k\hat{\mathbf{D}}$ are orthogonal to each other, i.e., $\partial_{\mathbf{C}\mathrm{t}} \operatorname{tr} {}^k\boldsymbol{\Pi}(\mathbf{C}\mathrm{t}) : {}^k\hat{\mathbf{D}} = 0$. Here, $\operatorname{tr}\mathbf{A}$ denotes the trace of $\mathbf{A}$. The parameters σ and π in eq. (2.51) scale two different out-of-path energy barriers: one component is linearly proportional to the Euclidean distance from the pathways with σ, while the second coefficient π is used to distinguish different force magnitudes for isochoric and volumetric transformational deformations, when $\pi \neq 0$.

Figure (2.4) illustrates the construction of the overall inelastic energy landscape ψ_{t} defined by eq. (2.46) with eq. (2.51), for all $\mathbf{C}$t of the neighborhood of the associated reaction pathway network in Fig. (2.3b). In accordance with the model parameters discussed in section 2.3.1, Fig. (2.4a) shows the given (invariant) minimum energy density $\hat{\psi}_{\mathrm{t}_k}$ along all reaction coordinates $\zeta_k(\mathbf{C}\mathrm{t})$ of the individual pathways k. Then, the weighting functions $\omega_k(\mathbf{C}\mathrm{t})$ are used to extrapolate each contribution into the whole space: Fig. (2.4b) depicts a 5×10^8 J.m^{-3}-iso-surface of the extended inelastic energy part $\omega_k(\mathbf{C}\mathrm{t})\,\hat{\psi}_{\mathrm{t}_k}$ in the $\{\mathbf{C}_1, \mathbf{C}_2, \mathbf{C}_3\}$ strain space. As illustrated by arrows, the iso-surface is perpendicular to the reaction pathways and the energy profile is "sombrero-shaped" along the axis $\mathbf{C}_1 + \mathbf{C}_2 + \mathbf{C}_3$. Figure (2.4c) shows a 10^9 J.m^{-3}-iso-volume related to the out-of-path contribution $\sigma d_k(\mathbf{C}\mathrm{t})$ only, i.e., with $\pi = 0$ in eq. (2.51). For sake of clarity, this additional energy potential is depicted in Fig. (2.4d) onto two planes passing by variants V_1 and V_3 (upper plane) and variants V_5 and V_6 (lower plane). It is also shown that the energy profile is exclusively controlled by the iso-distances around the paths, as illustrated by the cylinders around the paths and by the half-spheres at their ends. Finally, Fig. (2.4e) gives the same 10^9 J.m^{-3}-iso-volume of

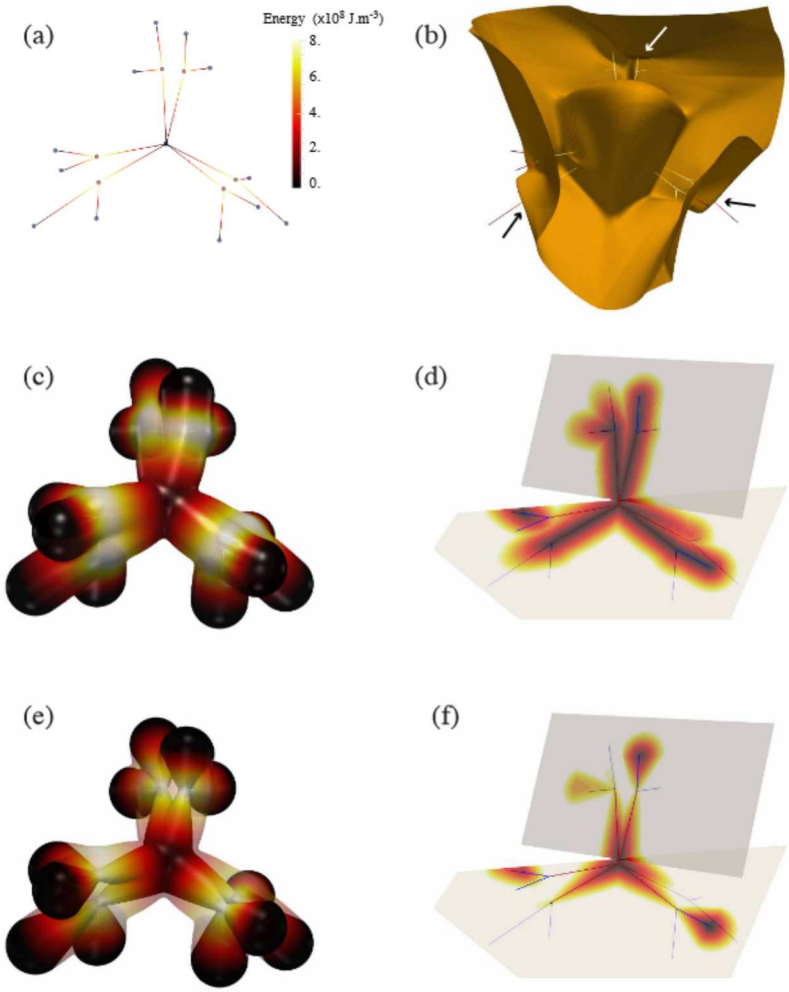

FIGURE 2.4: Construction of the total inelastic energy landscape ψ_t associated with the multiple reaction pathways V_k in iron. (a) Invariant and minimum energy profile along the individual reaction pathways k from 0 (in dark red, for the pure bcc phases) to $\sim 8 \times 10^8$ J.m^{-3} (in white, for hcp phases). (b) Extrapolation of the minimum energy potential in the whole $\{\mathbf{C}_1, \mathbf{C}_2, \mathbf{C}_3\}$ strain space, e.g. 5×10^8 J.m^{-3}-iso-surface. (c) shows a 10^9 J.m^{-3}-iso-volume of the out-of-path contribution σd_k with $\pi = 0$, whereas (d) illustrates the energy profile onto two planes passing by variants V_1 and V_3 (upper plane) and variants V_5 and V_6 (lower plane). (e) and (f) are similar to (d) and (e) for the total inelastic energy ψ_t landscape, respectively.

the total inelastic energy ψ_t landscape, within which the volume in (c) is plotted with transparency as well, for comparison. In contrast with Figs. (2.4c) and (d), it is shown that the total energy has a "cone-shaped" profile, exhibiting the directional character of the transformations toward the pure hcp phases, as distinctly depicted onto both planes in Fig. (2.4f).

Transformational inelastic forces

The calculation of the inelastic driving forces for phase transformations in eq. (2.28) is deduced by computing the derivative of ψ_t with respect to $\mathbf{F}t$, which can be expressed as follows

$$\frac{\partial \psi_t}{\partial \mathbf{F}t} = 2\,\mathbf{F}t \cdot \frac{\partial \psi_t\,(\mathbf{C}t)}{\partial \mathbf{C}t}\,. \tag{2.52}$$

According to eq. (2.46), the derivative of the energy function in the right-hand side of eq. (2.52) yields

$$\frac{\partial \psi_{\mathrm{t}}\left(\mathbf{Ct}\right)}{\partial \mathbf{Ct}} = \sum_{k=1}^{18} \psi_{\mathrm{t}_k}\left(\mathbf{Ct}\right) \frac{\partial \omega_k\left(\mathbf{Ct}\right)}{\partial \mathbf{Ct}} + \omega_k\left(\mathbf{Ct}\right) \frac{\partial \psi_{\mathrm{t}_k}\left(\mathbf{Ct}\right)}{\partial \mathbf{Ct}}\,, \tag{2.53}$$

where the derivative of the weighting functions $\omega_k\left(\mathbf{A}\right)$ with respect to $\mathbf{A}$ is given, without loss of generality, by

$$\frac{\partial \omega_k\left(\mathbf{A}\right)}{\partial \mathbf{A}} = h \sum_{i=1}^{18} \frac{\omega_i\left(\mathbf{A}\right)}{d_i\left(\mathbf{A}\right)} \left(\omega_k\left(\mathbf{A}\right) - \delta_{ik}\right)\, {}^{i}\mathbf{N}\left(\mathbf{A}\right)\,, \tag{2.54}$$

with δ_{ik} the Kronecker delta, i.e., $\delta_{ik} = 1$ if $i = k$ and $= 0$, otherwise, and, ${}^{i}\mathbf{N}\left(\mathbf{A}\right)$ represents the normal tensor to the pathway i in the direction of $\mathbf{A}$, obtained in the following form:

$${}^{i}\mathbf{N}\left(\mathbf{A}\right) = \frac{\partial d_i\left(\mathbf{A}\right)}{\partial \mathbf{A}} = \frac{{}^{i}\mathbf{\Pi}\left(\mathbf{A}\right)}{d_i\left(\mathbf{A}\right)}\,, \tag{2.55}$$

such that $|{}^{i}\mathbf{N}\left(\mathbf{A}\right)| = 1$, and, ${}^{i}\mathbf{N}\left(\mathbf{A}\right) : {}^{i}\hat{\mathbf{D}} = 0$ when $\zeta_k^{\infty}\left(\mathbf{A}\right) \in [0,1]$. Moreover, the derivative of ψ_{t_k} with respect to $\mathbf{Ct}$ in eq. (2.53) leads to

$$\frac{\partial \psi_{\mathrm{t}_k}\left(\mathbf{Ct}\right)}{\partial \mathbf{Ct}} = \frac{\partial \hat{\psi}_{\mathrm{t}_k}\left(\zeta_k\left(\mathbf{Ct}\right)\right)}{\partial \zeta_k} {}^{k}\hat{\mathbf{D}} + \sigma\, {}^{k}\mathbf{N}\left(\mathbf{Ct}\right) + \pi\, \mathrm{sgn}\left(\mathrm{tr}\, {}^{k}\mathbf{\Pi}\left(\mathbf{Ct}\right)\right) \left(\mathbf{I} - {}^{k}\hat{\mathbf{D}}\, \mathrm{tr}\, {}^{k}\hat{\mathbf{D}}\right). \tag{2.56}$$

Substituting eqs. (2.54) and (2.56) into eq. (2.53), and, then into eq. (2.52), it is also shown that two directions are included in the transformational inelastic forces: one component is related to the longitudinal directions ${}^{k}\hat{\mathbf{D}}$ along the reaction pathways, while the second component is associated with the normal directions ${}^{k}\mathbf{N}\left(\mathbf{Ct}\right)$ towards $\mathbf{Ct}$.

Mechanical elastic forces

Since the phase-field model aims at modeling high-pressure phase transitions in iron, particular attention is paid to the configuration within which the nonlinear elastic stiffness tensor is expressed. The out-of-path elasticity tensor $\mathbb{D}\left(\mathbf{Cet}\right)$ in eq. (2.28), which depends on the elastic and transformational deformation states, is given in the whole strain space by

$$\mathbb{D}\left(\mathbf{Cet}\right) = \sum_{k=1}^{18} \omega_k\left(\mathbf{Cet}\right)\, {}^{k}\mathbb{D}\left(\zeta_k\left(\mathbf{Cet}\right)\right)\,, \tag{2.57}$$

where ${}^{k}\mathbb{D}$ are the elasticity tensors associated with the reaction pathways k, and, $\zeta_k\left(\mathbf{Cet}\right)$ are the reaction coordinates that minimize the Euclidean distance $d_k\left(\mathbf{Cet}\right)$ between $\mathbf{Cet}$ and the individual paths k. The weighting functions $\omega_k\left(\mathbf{Cet}\right)$ are also defined by eq. (2.47), where the partition of unity is written as a function of $\mathbf{Cet}$. The projected tensors ${}^{k}\hat{\mathbf{C}}\mathbf{et}$ are also mapped onto the reaction pathways (as well as ${}^{k}\hat{\mathbf{C}}\mathbf{t}$) and the corresponding reaction coordinates are consistently determined by solving $\partial_{\zeta_k} d_k\left(\mathbf{Cet}\right) = 0$. Imposing $\partial_{\mathbf{Cet}}\mathbb{D}\left(\mathbf{Cet}\right) = \mathbf{0}$ for all pure (meta)stable phases (i.e., at the ends of all reaction pathways k, when $\zeta_k = 0$ and $\zeta_k = 1$) with $\mathbf{Cet} = {}^{k}\hat{\mathbf{C}}\mathbf{et}$, the elasticity tensors ${}^{k}\mathbb{D}$ in eq. (2.57) may be represented by a cubic interpolation function to ensure numerical stability, i.e.,

$${}^{k}\mathbb{D}\left(\zeta_k\left(\mathbf{Cet}\right)\right) = \left(1 - 3{\zeta_k}^2 + 2{\zeta_k}^3\right) \mathbb{D}^{\alpha} + \left(3{\zeta_k}^2 - 2{\zeta_k}^3\right) \mathbb{D}^{\epsilon}\,, \tag{2.58}$$

with $\mathbb{D}^{\alpha}$ and $\mathbb{D}^{\epsilon}$ the elastic stiffness tensors of the pure bcc and hcp iron phases, respectively. In particular, if $\zeta_k^{\infty}\left(\mathbf{Cet}\right) < 0\ (> 1)$, also ${}^{k}\mathbb{D}\left(\zeta_k\left(\mathbf{Cet}\right)\right) = \mathbb{D}^{\alpha}\ (= \mathbb{D}^{\epsilon})$. For instance, for such pure hcp

ϵ-Fe phases, the finite hyperelasticity condition from eq. (2.18) leads therefore to

$$\mathbb{D}^{\epsilon} = \rho_0 \left. \frac{\partial^2 \psi_{\mathrm{e}}}{\partial \mathbf{Ee}\, \partial \mathbf{Ee}} \right|_{\epsilon} = \left. \frac{\partial \mathbf{Se}}{\partial \mathbf{Ee}} \right|_{\epsilon} , \tag{2.59}$$

where $\mathbb{D}^{\epsilon}$ is defined in the reference configuration Ω_0 and obeys the left and right minor symmetries. However, the elastic tensor differs from experimental or computed (e.g. using atomistic simulations) elasticity tensors $\mathbb{b}^{\epsilon}$, expressed in the current and deformed Ω by

$$\mathbb{b}^{\epsilon} = \left. \frac{\partial \boldsymbol{\sigma}}{\partial \boldsymbol{\varepsilon}} \right|_{\epsilon} , \tag{2.60}$$

with $\boldsymbol{\varepsilon}$ the Eulerian strain tensor [269, 232, 66]. In the present work, the relevant tensor $\mathbb{b}^{\epsilon}$ for a pure hydrostatic compression is obtained by considering the following two-step deformation state along the reaction pathways: first, a material is subjected to a volumetric deformation $\mathbf{F}_{\mathrm{vol}}$ from initial volume V_0 to the final volume $V = j\, V_0$ with $\mathbf{F}_{\mathrm{vol}} = j^{1/3}\mathbf{I}$, and then, to a small and symmetric shear isochoric deformation $\mathbf{F}_{\mathrm{iso}} = \mathbf{I} + \boldsymbol{\varepsilon}$ with $|\boldsymbol{\varepsilon}| \ll 1$, such as it is commonly performed using density functional theory calculations [163, 143]. Without plasticity, the total deformation gradient is also given by $\mathbf{F} = j^{1/3}\,(\mathbf{I} + \boldsymbol{\varepsilon})$. Using eq. (2.60) with the aid of eq. (2.30) and considering $\boldsymbol{\sigma} = p\,\mathbf{I}$ with the Cauchy pressure $p \leq 0$, the relation between the elasticity tensors $\mathbb{D}^{\epsilon}$ and the incremental tangent modulus $\mathbb{b}^{\epsilon}$ is reduced to

$$\mathbb{D}^{\epsilon}_{ijkl} = j^{-1/3}\big(\mathbb{b}^{\epsilon}_{ijkl} + p^{\epsilon}\big(\delta_{ij}\delta_{kl} - \delta_{ik}\delta_{jl} - \delta_{il}\delta_{jk}\big)\big)\,, \tag{2.61}$$

exhibiting the same symmetries as in eq. (2.59). Thus, the elasticity tensors $\mathbb{D}^{\epsilon}$ is obtained by identifying the values of $\mathbb{b}^{\epsilon}$ as well as the corresponding equilibrium pressures p^{ϵ} from experiments or atomistic calculations. Inserting eq. (2.61) into eq. (2.58) with $\mathbb{D}^{\alpha} = \mathbb{b}^{\alpha}$ (here, the bcc α-Fe phase is thermodynamically stable at zero pressure and zero temperature), and, then into eq. (2.57), the mechanical elastic driving forces in eq. (2.25) may therefore be determined in a computational Lagrangian framework.

2.2.6 Computational framework

The present model is implemented in a three-dimensional Lagrangian code using an element-free Galerkin least-squares formulation [25] with explicit time integration that handles acoustic wave propagation and rapid phase changes. The objective is to obtain solutions of the 12 unknown primary solution variables (i.e., degrees of freedom (DoFs) at integration nodes) namely, the displacement field $\boldsymbol{u}$ (3 DoFs) and the non-symmetric transformational distortion $\mathbf{Ft}$ (9 DoFs) at each reference point $\boldsymbol{X}$ in Ω_0, by solving the system of partial differential equations, as follows

$$\left\{\begin{aligned}
\rho_0\,\ddot{\boldsymbol{u}} &= \sum_{k=1}^{18} \boldsymbol{\nabla}\cdot\Big\{\omega_k\,(\mathbf{Cet})\;\; \mathbf{Fe}\cdot\big({}^{k}\mathbb{D}\,(\zeta_k\,(\mathbf{Cet})) : \mathbf{Ee}\big)\cdot\mathbf{Ft}^{-\mathrm{t}}\cdot\mathbf{Fp}^{-\mathrm{t}} \\
&\quad + \omega_k\,(\mathbf{Cet})\,\big(\mathbf{Ee} : {}^{k}\mathbb{D}'\,(\zeta_k\,(\mathbf{Cet})) : \mathbf{Ee}\big)\;\mathbf{Fet}\cdot{}^{k}\hat{\mathbf{D}}\cdot\mathbf{Fp}^{-\mathrm{t}} + \big(\mathbf{Ee} : {}^{k}\mathbb{D}\,(\zeta_k\,(\mathbf{Cet})) : \mathbf{Ee}\big)\;\mathbf{Fet}\cdot\frac{\partial\omega_k\,(\mathbf{Cet})}{\partial\mathbf{Cet}}\cdot\mathbf{Fp}^{-\mathrm{t}}\Big\} \\
v\dot{\mathbf{Ft}} &= \sum_{k=1}^{18} \omega_k\,(\mathbf{Cet})\;\; \mathbf{Ce}\cdot\big({}^{k}\mathbb{D}\,(\zeta_k\,(\mathbf{Cet})) : \mathbf{Ee}\big)\cdot\mathbf{Ft}^{-\mathrm{t}} + \lambda\,\boldsymbol{\nabla}^2\mathbf{Ft} \\
&\quad - 2\rho_0\big(\hat{\psi}_{\mathrm{t}_k}\,(\zeta_k\,(\mathbf{Ct})) + \sigma\, d_k(\mathbf{Ct}) + \pi\,|\,\mathrm{tr}\;{}^{k}\boldsymbol{\Pi}\,(\mathbf{Ct})|\big)\;\mathbf{Ft}\cdot\frac{\partial\omega_k\,(\mathbf{Ct})}{\partial\mathbf{Ct}} \\
&\quad - 2\rho_0\,\omega_k\,(\mathbf{Ct})\,\Big(\hat{\psi}'_{\mathrm{t}_k}\,(\zeta_k\,(\mathbf{Ct}))\;\; \mathbf{Ft}\cdot{}^{k}\hat{\mathbf{D}} + \sigma\;\mathbf{Ft}\cdot{}^{k}\mathbf{N}\,(\mathbf{Ct}) + \pi\,\mathrm{sgn}\big(\mathrm{tr}\;{}^{k}\boldsymbol{\Pi}\,(\mathbf{Ct})\big)\,\big(\mathbf{Ft} - \mathbf{Ft}\cdot{}^{k}\hat{\mathbf{D}}\;\mathrm{tr}\;{}^{k}\hat{\mathbf{D}}\big)\Big)\,,
\end{aligned}\right. \tag{2.62}$$

where $'$ denotes the derivative with respect to the reaction coordinates ζ_k, while the derivatives of the weighting functions ω_k with respect to $\mathbf{C}$t and $\mathbf{C}$et are determined by using eq. (2.54). The calculation of the first Piola-Kirchhoff stress tensor in the linear momentum balance in eqs. (2.62) is given in Appendix B from Ref. [252].

2.3 Pure hydrostatic compression

The phase-field formalism coupled with finite elastoplastic deformations is applied to analyze the α-Fe into ϵ-Fe phase transitions under high hydrostatic compression. The simulations exhibit the major role played by the plastic deformation in the morphological and microstructure evolution processes.

2.3.1 Material and model inputs

Tables (2) and (3) in Ref. [252] list the values for the material and model parameters for iron under high pressure compression, respectively, which have been collected from a variety of sources.

In the present phase-field model, the elastic pressure-dependent properties of iron are defined by four pressures: $\{p^\alpha, p^\epsilon\}$, for which the crystalline phases are fully bcc, and, fully converted to hcp, respectively; and: $\{p^{\alpha\to\epsilon}, p^{\epsilon\to\alpha}\}$, which characterize the transition states where the forward and reverse transformations start, respectively. Here, the equilibrium pressures $\{p^\alpha = 0\,, p^\epsilon = -20\}$ GPa, with the corresponding atomic volumes $\{v^\alpha = 11.75\,, v^\epsilon = 10.20\}$ Å^3/at, are selected from Ref. [78]. In accordance with these experimental measures, the associated elastic components $\mathbb{b}^\alpha$ and $\mathbb{b}^\epsilon$ for both pure bcc and hcp phases are given in Ref. [163], while the stiffness tensor $\mathbb{D}^\epsilon$ is expressed in the current configuration by using eq. (2.61), and, $\mathbb{D}^\alpha = \mathbb{b}^\alpha$ at zero pressure.

The ratio $c/a = 1.603$ of the hcp close-packed structure has been experimentally determined in Ref. [179], so that $\det \mathbf{U} = 9c/a\,/16 = 0.902$. However, $\mathbf{U}$ corresponds to the complete phase transformation into the hcp iron sample at $p^\epsilon = -20$ GPa, for which the experimental measurements contain indistinctly elastic and transformational distortions. According to eq. (2.38) and following the procedure in Appendix C from Ref. [252], the transformational part $\mathbf{U}$t is related to $\mathbf{U}$ as follows

$$\mathbf{U}\mathrm{t} = \kappa\mathbf{U} = \sqrt{2}\left(1 + \sqrt{1 + \frac{8}{3}\frac{j_{\exp}\, p^\epsilon}{D^\epsilon}}\right)^{-1/2}\mathbf{U}\,, \tag{2.63}$$

where D^ϵ is the hcp bulk modulus, and, $j_{\exp} = v^\epsilon/v^\alpha$ is the experimental volume change from the initial pure bcc sample, at $p^\alpha = 0$ GPa, to the final pure polycrystalline hcp iron, at $p^\epsilon = -20$ GPa.

In the present perfect plasticity theory, a constant yield stress is chosen to analyze the crucial role of plasticity on nucleation and selection of variants during phase transformations, i.e., $\sigma_0 = 0.25$ GPa, which is fairly of the same order of magnitude with Hugoniot elastic limits in Ref. [214].

The positive parameter h of the weighting functions controls the energetic part of the phase transition during a possible jump from one reaction pathway to the neighboring branches. The energy variation for such transition may be determined using molecular dynamics simulations [77], for which the exponent can be tuned to reproduce the atomistic results. However, without relevant information about the bcc-bcc and hcp-hcp phase transitions in iron, it is therefore assumed that all reaction pathways are mainly controlled by their immediate surroundings. This consideration may be achieved by imposing large magnitudes for h, e.g. $h = 10$, as well as large values for the energy barrier parameters σ and π. The relation $\pi = 10\,\sigma$ (in GPa) is used in the energy penalty part of eq. (2.51) to consider higher pull-back forces onto the pathways for the volumetric than the isochoric phase transformations, which are conveniently applied to non-zero strain states that are out of the transition pathways, i.e., for any $\mathbf{C}$t with ${}^k\mathbf{\Pi}\,(\mathbf{C}\mathrm{t}) \neq \mathbf{0}$.

The onset of a new crystalline phase can be viewed as the product of a morphological instability involving elastic energy, interfacial energy, inelastic energy, transformational dissipation,

plastic dissipation, additional energies due to the long-range elastic interactions between variants, etc. Because of the complexity in modeling such phase instability, a phenomenological form is adopted to define the minimum energy density $\hat{\psi}_{\mathrm{t}_k}$ as a function of the reaction coordinate ζ_k along each individual pathway k, i.e.,

$$\rho_0 \hat{\psi}_{\mathrm{t}_k}\left(\zeta_k\left(\mathbf{Ct}\right)\right) = \tfrac{1}{2} c_1\, \zeta_k^2 + c_2\, \zeta_k\,, \tag{2.64}$$

with c_1 and c_2 (in J.m^{-3}) two parameters that may be calibrated to experimental data. As described in Appendix D from Ref. [252], these parameters are given by

$$c_2 = \tfrac{1}{2} j^{\alpha\to\epsilon} p^{\alpha\to\epsilon}\, \mathrm{tr}\, {}^k\hat{\mathbf{D}}\,, \;\; \text{and,} \;\; c_1 \;\; = \tfrac{1}{2} j^{\epsilon\to\alpha} p^{\epsilon\to\alpha}\, ({}^k\mathbf{Ut}^{-2} : {}^k\hat{\mathbf{D}}) - c_2\,, \tag{2.65}$$

with $j^{\alpha\to\epsilon} = v^{\alpha\to\epsilon}/v^{\alpha}$ and $j^{\epsilon\to\alpha} = v^{\epsilon\to\alpha}/v^{\alpha}$ the experimental volume changes from the initial pure bcc sample to the Hugoniot states where the forward and reverse transitions occur, at $p^{\alpha\to\epsilon}$ and $p^{\epsilon\to\alpha}$, respectively. According to the recent experimental results from Ref. [78], the forward transition starts at $p^{\alpha\to\epsilon} = -14.9$ GPa, with the corresponding volume $v^{\alpha\to\epsilon} = 11.0$ Å^3/at, and, the reverse at $p^{\epsilon\to\alpha} = -12.0$ GPa, with $v^{\epsilon\to\alpha} = 10.6$ Å^3/at. The minimum energy density profile along the individual reaction pathways from eq. (2.64) with eq. (2.65), for which the values of c_1 and c_2 are provided in Tab. 3 from Ref. [252], is depicted in Fig. (2.4a).

The parameter v in the relaxation eq. (2.23) is akin to viscosity in classical viscoplastic approaches. For the face-centered cubic (fcc) to bcc phase transitions in Fe_3Ni, an attempt to fit the magnitude $v = 14$ mPa.s, comparable to the viscosity of liquid metals, has been investigated by using molecular dynamics simulations [77]. Such quantitative data analysis is not available for the bcc-hcp transformations in iron, but it is assumed that the amount of stress state due to the viscosity is lower than the yield stress, i.e., $v\dot{\varepsilon}_{\mathrm{t}} < \sigma_0$, where $\dot{\varepsilon}_{\mathrm{t}}$ is a measure of the transformational strain rate. This measure can be estimated by $\dot{\varepsilon}_{\mathrm{t}} = \varepsilon_{\mathrm{t}}/\Delta t = \frac{1}{2}|\mathbf{Ct} - \mathbf{I}|/\Delta t$ during a time interval Δt awaited for the transformation, with ε_{t} the norm of the transformational Green-Lagrange deformation tensor. Thus, it follows that $v < \sigma_0 t_f/\varepsilon_{\mathrm{t}}$, with t_f the final simulation time. According to the mentioned material inputs and time characteristics discussed in the following section, it is also considered that $v \approx \sigma_0 t_f/\varepsilon_{\mathrm{t}} \approx 2.6$ kPa.s.

Finally, the Laplacian operator in eq. (2.28) can be approximated using the mesh discretization in the finite element framework, such that $\lambda = \lambda^*/\ell^2$, where $\lambda^* = 0.5$ GPa is a mesh-size parameter and ℓ is an average element size of the simulation grid.

2.3.2 Analysis of the pressure-volume responses

The simulated material is a cube containing 1 million finite elements with full periodic boundary conditions, within which each element volume is $V_e = \ell^3 = 1\ \mu$m^3. In the present dynamic continuum mechanics framework, the final simulation time t_f is related to the physical time t_c, needed for acoustic waves to travel through the samples. Assuming that $t_f = 100\, t_c$, the latter relation also means that the acoustic waves run over 100 times during the entire simulations for each sample, which ensures the quasi-static loading conditions. Thus, $t_c = L/c_L$, with $L = 100\ell = 0.1$ mm, the initial box length, and c_L, the longitudinal wave celerity in iron, i.e., $c_L = \sqrt{b_{11}^{\alpha}/\rho_0}$. It therefore follows that: $c_L = 5850$ m.s^{-1}, and, $t_f \approx 1.7\ \mu$s, corresponding to the duration of the all performed calculations. Here and in the following, the subscript $_f$ will denote the final state.

The initial single-crystal bcc iron is subjected to a three-step loading, as follows. First, all edges are continuously and proportionally decreased to a global volume reduction imposed by $j = V/V_0 = 0.86$, for which the volume change is achieved within a time step from t_0 to $t = 0.4\, t_f$. Then, a constant volume is maintained from $t = 0.4\, t_f$ to $0.6\, t_f$, and, finally the volume is released back to the initial volume, so that $j_f = V_f/V_0 = 1$, at $t = t_f$.

Figure (2.5) illustrates the volume change j as a function of the pressure p in GPa. Although different in shape and magnitude, both hysteresis loops characterize martensitic transitions over

a wide range of pressure, involving an important stored elastic strain energy caused by the coexistence of numerous solid-state phases. The difference in both phase transformation hysteresis is due to plastic deformation in samples, which exhibits a larger width for the case with plasticity than without. When increased pressure, the appearance of the high pressure hcp phase is reached at -25.6 GPa, followed by a sudden drop to -23.1 GPa (without) and -19.7 GPa (with plasticity), due to dissipative effects during the forward $\alpha \rightarrow \epsilon$ transitions. However, the reverse $\epsilon \rightarrow \alpha$ transition without plasticity is characterized by a slow martensitic transformation, compared to an instantaneous volume change that occurs between -7.4 and -2.1 GPa with plasticity. Significantly, the forward transformation pressures predicted by the present model are higher than the experimental values for bcc samples that have been fully converted to hcp phases, within the range of -18.4 GPa [78] and -23.0 GPa [239] at room temperature. The experimental measurements from Refs. [100, 78] have been plotted in Fig. (2.5) with symbols, where the more recent data in Ref. [78] for high-purity Fe single crystals in helium pressure medium (shown by the oriented blue arrows) can be compared to the simulated hysteresis widths. Within the pressure range of coexistence of both phases, the experimental bcc (open symbols) and hcp (solid symbols) atomic volumes are separately deduced from X-ray diffraction measurements of lattice parameters at each applied pressure step. On the other hand, the computed results (solid lines) are obtained using the average pressure and volume states over the simulation samples. In addition, the pressure discrepancies are possibly due to the approximations/presumptions in the present coupled formalism and, more precisely, to the absence of free boundaries in the prescribed simulation setups. For instance, simulations in a helium pressure media, which is a fluid with a very low viscosity, together with a dislocation density-based crystal plasticity model, should give rise to a better description of the nonhydrostatic effects and anisotropic stresses in the transition pressures, and also of the hysteresis widths of iron. In accordance with the present calculations with periodic boundary conditions, classical molecular dynamics simulations using an embedded atom method potential have shown that the simulated transition pressure of the hcp and face-centered cubic (fcc) phases is significantly higher for uniform ($31 - 33$ GPa) than uniaxial (14 GPa) compression [270]. Although the simulated coexistence domain is larger than the experimental domain under quasi-hydrostatic conditions, the present P-V equation-of-state curves behave in good agreement with experimental responses when increasing (from 0 to -18 GPa) and decreasing (from -23 to -7 GPa) pressures [100, 78].

Figure (2.6) illustrates the partitioning of the total energy ψ in terms of elastic ψ_e/ψ (in blue) and inelastic $(\psi_t + \psi_\nabla)/\psi$ (green) energy ratios as a function of the dimensionless simulation time $t^* = t/t_f$, for calculations without and with plasticity. It is also shown that the total energy is mainly composed by the elastic strain energy until the nucleation of the first hcp phases in iron occurs at $t^* \approx 0.28$, as depicted by the two vertical arrows. When the volume is maintained constant, Fig. (2.6a) shows that the dissipative transformational process leads to 38% decrease in the amount of elastic energy, while the latter represents 54% of the total energy. During the early stages of the pressure release (as shown by a double-headed arrow), the stress state decreases, but the pressure remains sufficiently high to maintain the newly formed phases, as depicted by $*$ in Fig. (2.6a) when the internal elastic stored energy increases then to $t^* = 0.90$, before completely releasing back to zero. However, plastic deformation allows for a considerably higher stress relaxation between variants when phase transformations occur at large volume change states, as shown in Fig. (2.6b), where the upper thin curve for the elastic energy ratio without plasticity has been included for comparison. It also emphasizes the reduction of the stored elastic energy due to the plastic dissipation, for which the elastic strain energy falls down to 42% (compared to 54% without plasticity) of the total energy and remains constant during the second loading step. When the volume increases back to the initial volume, the elastic energy is then dramatically reduced to zero, significantly dissipated by plastic deformation.

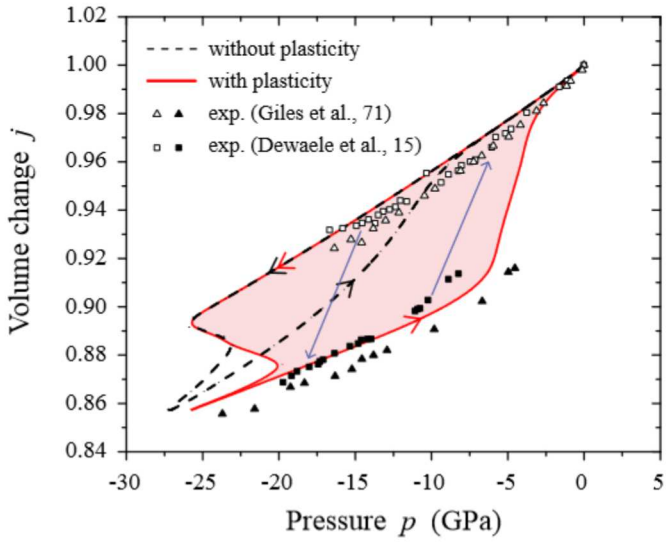

FIGURE 2.5: Volume change j as a function of the pressure p in GPa, for calculations without (black dotted line) and with (red full line) plasticity, with $\sigma_0 = 0.25$ GPa. The experimental bcc (open symbols) and hcp (solid symbols) atomic volumes are separately deduced from X-ray diffraction measurements of lattice parameters at each applied pressure step, while the computed results (solid lines) are obtained using the average pressure and volume states over the simulation samples.

2.3.3 Microstructure and variant selection

Figure (2.7a) illustrates the microstructure texture variation of transition-induced volume change j versus the dimensionless time t^* in the form of histograms. These histograms are obtained by splitting the simulation volume change (ranging from $j = 0.80$ to 1) into 100 bins of constant width, within which the phase fraction of materials is computed for all time steps. Coexistence of α-Fe and ϵ-Fe phases with different equilibrium volumes therefore leads to a multimodal histogram in the large range of pressure, where the grayscale represents the volume fractions of phases. For both simulations, the single-crystal volume is homogeneously decreased with respect to the prescribed hydrostatic conditions, as depicted by the points A. Without plasticity, Fig. (2.7a) shows a single-mode histogram: the volume change is slightly spread out over a large time interval, starting from the first forward phase transitions at $t^* = 0.28$ (point B). This spreading regime is spatially correlated to the strong elastic interactions between numerous variants that have partially been reversed into hcp phases only, from point B to D. However, continued pressure release results in a decrease in the proportion of the hcp phase compensated by an increase of the bcc phase between C and D. When the simulated iron is transformed back to the initial single-crystal material (point D), the volume exhibits no spatial variation, corresponding to a sharp single-mode histogram. With plasticity, the volume spreading is dramatically reduced after a brief fluctuation (point B) and remains a single mode until the first reverse phase transitions occur. Between $t^* \approx 0.75$ and 0.90, a mixed-mode regime can be pointed out, which exhibits the structural texture formation of heterogeneous microstructure. The higher volume (point C′) is greater in magnitude than the average prescribed volume, until all reversions are achieved (point D′). The second mode (point C) corresponds to a volume that remains constant and slightly increases during the reversions (point D). According to these different modes, a particular microstructure texture evolution in iron associated with preferential variant selection during the phase transitions is also expected.

Figure (2.7b) shows the volume fractions of each variant V_k as a function of the simulation time t^*. Without plasticity, Fig. (2.7b) illustrates that the initial phase is partially transformed into the 6 possible hcp variants with comparable phase fractions, within which a residual amount of bcc phase persists in the microstructure, even for a large pressure range up to -25 GPa. When the compression is released to the original volume, all hcp variants are transformed back to the initial

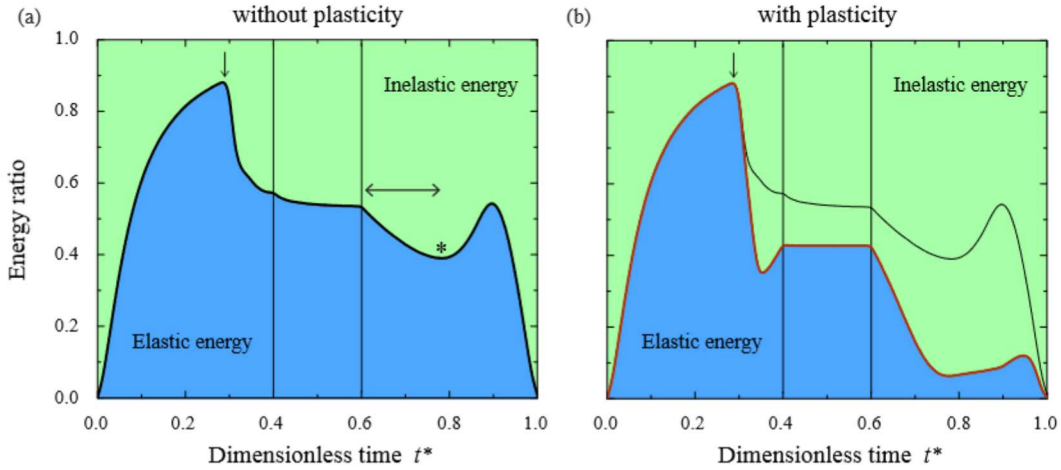

FIGURE 2.6: Partitioning of the total energy into the elastic and inelastic components as a function of the dimensionless simulation time t^*, for calculations (a) without and (b) with plasticity.

single-crystal bcc iron, behaving partially as a shape-memory alloy. For this case, most of transformations to ϵ-Fe phases are partial only. These pseudo-hcp structures break the symmetries of fully formed hcp lattice, and, cannot lead to the formation of reversed α'-Fe phases. Because the mismatch between bcc and hcp phases is not taken into account in the present formalism, the elastic strain state due to the interaction between variants is mainly responsible for the incomplete polymorphic phase transformations without plasticity. Therefore, when numerous hcp nucleus are considered, the long-range elastic interactions between variants dramatically increase the overall elastic energy, which in turn hinder the forward $\alpha \rightarrow \epsilon$ phase transitions. Because plasticity dissipates considerably the stored elastic strain energy, the onset of plasticity screens the elastic interactions between variants and thus decreases the energy cost to form the hcp variants. It also appears as an essential mechanism to enhance phase transformations by relaxing stresses due to elastic interactions, so that the complete formation of a polycrystalline iron formed by the 6 hcp variants is energetically favorable, as shown in Fig. (2.7b). In addition, a sudden burst of reversed α'-Fe nucleation of variants occurs at $t^* \approx 0.90$, with $\sim$2% volume fraction for each $\{V_{12}, V_{13}, V_{15}\}$, $\sim$1% for each $\{V_{11}, V_{14}, V_{16}\}$, and, $\sim$0.5% for each of the 6 other bcc variants. Thus, both initial α-Fe and reversed α'-Fe phases coexist at $t^* = 1.0$, without any retained hcp phases. However, the initial α-Fe phase orientation largely dominates the forward and reverse transitions, while the volume fraction of α' inclusions is $\sim$ 12.3% in the final microstructure.

To summarize, Fig. (2.8) illustrates the microstructure evolution under hydrostatic pressure at $t^* = 0.6$ and $t^* = 1.0$, defined in both strain and current mesh spaces. As shown in Fig. (2.8a), the non-flat sample surfaces capture the signature of the local unconstrained deviatoric stress component of the externally applied hydrostatic conditions. For the simulation without plasticity, the initial bcc α-Fe phase (in gray) is not completely converted into hcp ϵ-Fe phases, with a retained $\sim$26.6% volume fraction of bcc phase at $t^* = 0.6$. However, the calculation with plasticity exhibits a polycrystalline iron that has been entirely transformed into 6 hcp ϵ-Fe grain variants (red gradient). Such close-packed grains have been observed by performing large-scale molecular dynamics simulations under shock loading [137]. It is worth mentioning that various morphologies of hcp phases have been observed for structural phase transformations in iron, e.g. needle-like ϵ-Fe phases [276], lath-like ϵ-Fe regions [55], and, ellipsoidal ϵ-Fe particles [202], for which the $\alpha \leftrightarrow \omega$ martensitic transitions exhibit similar discrepancies in zirconium [18]. On the release of hydrostatic pressure, the calculation without plasticity transforms back to the initial single-crystal bcc iron at $t^* = 1.0$, while the calculation with plasticity leads to 12 reversed bcc α'-Fe, heterogeneously nucleated in pairs (e.g. $\{V_{11}, V_{12}\}$, in light and dark green) from one single ϵ-Fe variant.

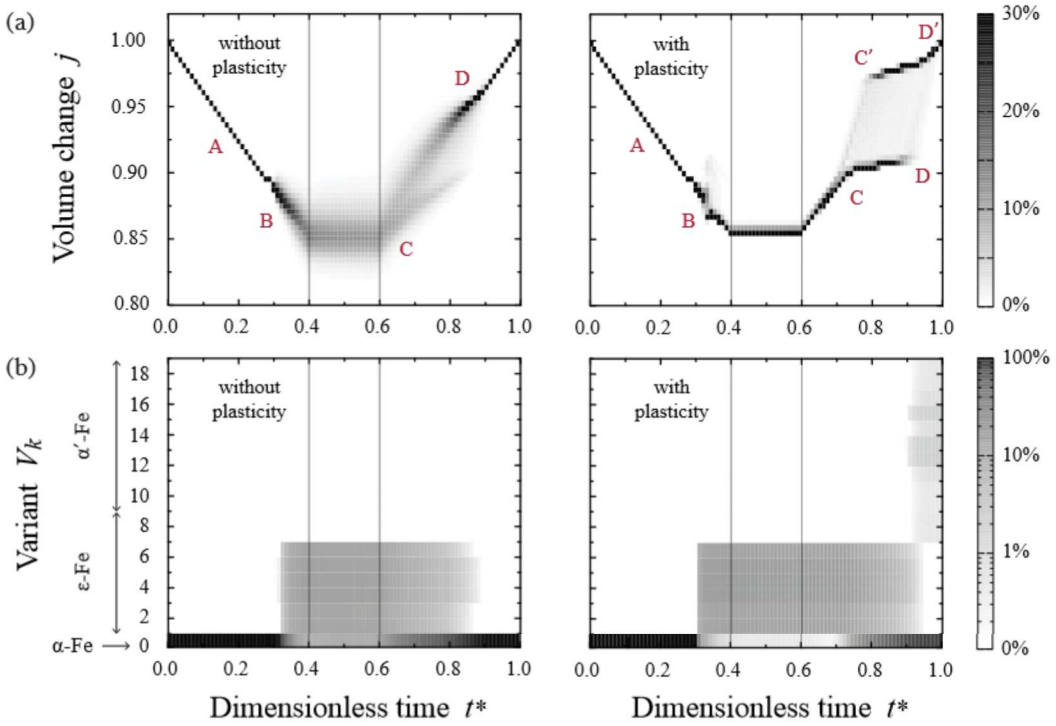

FIGURE 2.7: Evolution of (a) the volume change j and (b) the phase fractions of variants V_k as a function of the dimensionless simulation time t^*, for calculations without and with plasticity.

2.4 Shock wave propagation

The numerical shock wave calculations accurately describe some important features reported by the experimental literature, and strongly complement our understanding of the phase-change dynamics in iron at larger time and length scales than hitherto explored by molecular dynamics simulations in the last two decades. The numerical model is able to reproduce unstable shock waves (which break up into elastic, plastic and phase-transition waves), providing new stress-informed insights into the coupling between the high strain-rate plasticity and microstructure evolution during the displacive phase transitions.

2.4.1 The internal structure of shock waves

In the following dynamical analyses, the three-dimensional iron samples are oriented along the [100] directions, and the shock waves are generated along the $\boldsymbol{z} \parallel [001]_{\text{bcc}}$ direction, using $80 \times 80 \times 1280$ element-free Galerkin nodes (~ 8.2 millions), with periodic boundary conditions transverse to the direction of shock front propagation, i.e., to $\boldsymbol{x} \parallel [100]_{\text{bcc}}$ and $\boldsymbol{y} \parallel [010]_{\text{bcc}}$. The initial shock compression is induced by imposing a velocity of 850 m.s^{-1} on the rear face along $\boldsymbol{z} \parallel [001]_{\text{bcc}}$, while the free surface is located at the extremity of the rectangular parallelepiped-shaped samples, as depicted in Fig. (2.9a). The unshocked material is at rest at $t = t_0 = 0$, while the final simulation time t_f is related to the physical time t_c for acoustic waves to travel through the sample. The dynamical loading conditions are controlled by assuming that $t_f = 2.5\, t_c$, such that the acoustic waves run over 2.5 times the samples during the entire simulations. Thus, $t_c = L_z/c_L$, where L_z is the initial box length in the $[001]_{\text{bcc}}$ shock direction, with $L_z = 16\, L_x = 16\, L_y = 1.28$ mm, and c_L is the longitudinal wave celerity in iron, defined by $c_L = \sqrt{b^{\alpha}_{11}/\rho_0}$, with $b^{\alpha}_{11} = 271$ GPa the corresponding low-pressure elastic component of the pure bcc iron [163]. It therefore follows that: $c_L = 5850$ m.s^{-1}, so that $t_f \approx 0.55\ \mu$s, which corresponds to the duration of all calculations. For convenience, a dimensionless time t^* is defined as $t^* = t/t_f$, while the dimensionless length

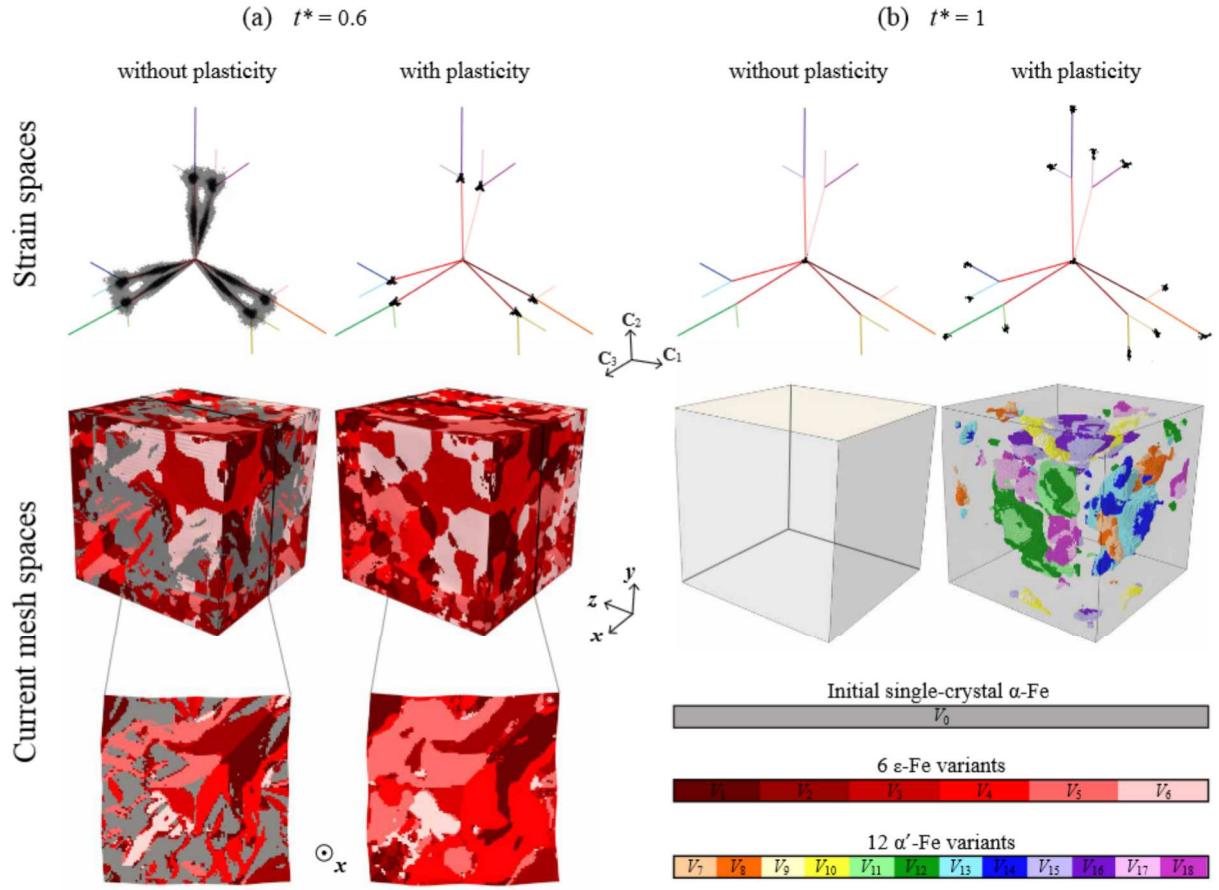

FIGURE 2.8: Transformational states defined in both strain and current mesh spaces at (a) $t^* = 0.6$ and (b) $t^* = 1.0$, for calculations without and with plasticity. Each black dot in the strain space represents the current transformational strain **C**t for all mesh elements, while the colors along the pathways are associated with the corresponding phases and variants in the 3D simulated microstructures. Without plasticity, the initial bcc α-Fe phase remains in a large fraction ($\sim$26.6%, in gray) at $t^* = 0.6$, whereas the calculation with plasticity exhibits a polycrystalline iron formed by the 6 hcp ϵ-Fe variants only (red gradient). On the release of hydrostatic pressure, the former is transformed back to the initial single-crystal bcc iron at $t^* = 1.0$, while the latter shows the presence of 12 reversed bcc α'-Fe with $\sim$12.3% volume fraction.

L^* along $\boldsymbol{z}$ is given by $L^* = z/L_z$, so that both quantities t^* and L^* are ranged between 0 and 1. Moreover, the classical sign convention in continuum mechanics is used, so that compressive (extensive) volumetric stresses have negative (positive) signs.

The capability of the continuum element-free Galerkin model to reproduce the experimental multiple split-wave structure is illustrated in Fig. (2.9) by displaying the spatial heterogeneous distribution of the pressure behind the incident compressive wave. Figures (2.9c) and (2.9d) show the corresponding two- and three-wave structures for representative simulations without and with plasticity at $t^* = 0.35$, respectively. Different regions, namely, the initial unshocked, the elastically compressed bcc iron, and the transformed regions with high-pressure hcp Fe multivariants are also depicted. Furthermore, the plastically deformed bcc iron can be displayed for the calculation with plasticity in Fig. (2.9d). A sharp PT wave front is exhibited without plasticity, while a more complex rough PT front (see inset in Fig. (2.9d)) is shown to generate multiple planar pulses (as depicted by the vertical double-headed arrows) that propagate toward the leading plastic front. These localized traveling-wave fronts are suddenly produced by the dynamical phase transitions with high velocity in the compressed bcc region with high-pressure elastic properties. The consequences of the complex three-wave structure and competing wave interactions in the evolving

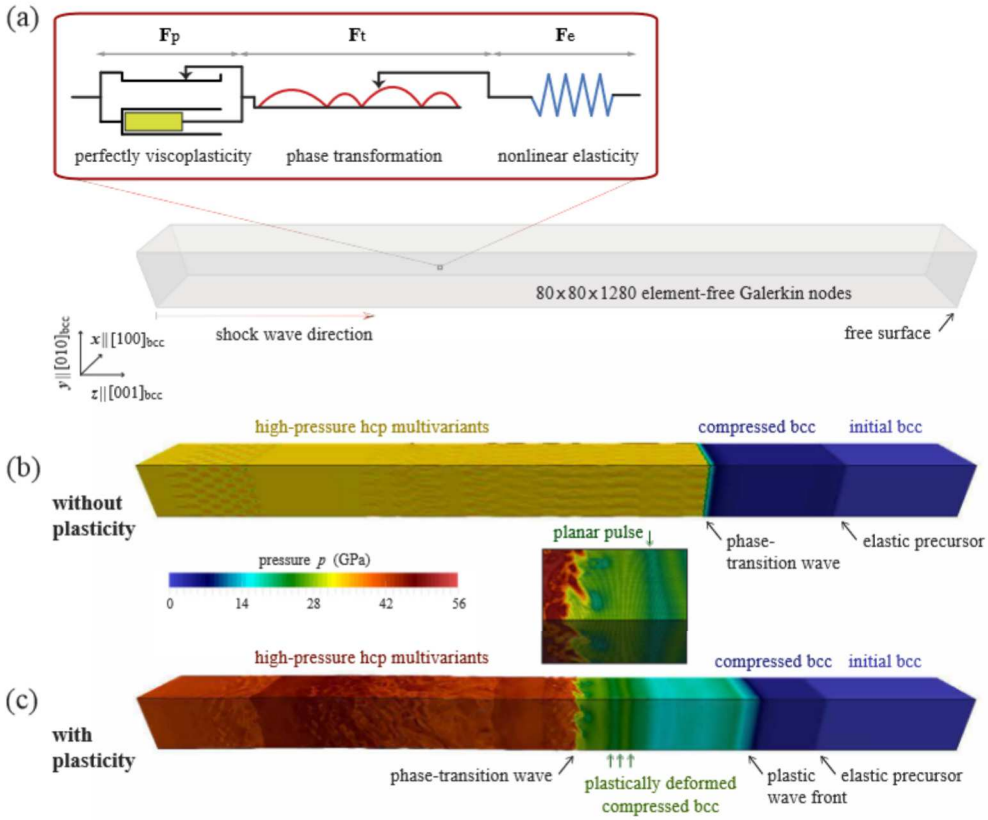

FIGURE 2.9: (a) Schematics of the finite deformation framework that combines nonlinear elasto-viscoplasticity and multivariant phase-field theory to model the shock-induced response of single-crystal iron along the $[001]_{bcc}$ direction. (b) Distribution of the pressure resulting from three-dimensional simulation without plasticity. The unstable shock wave breaks up into the elastic precursor and the phase-transition wave, which leads to different internal deformation states at material points. (c) Similar calculation with plasticity, within which an intermediate plastic wave front propagates between the elastic and phase-transition wave fronts. The inset shows a rough phase-transition front, leaving behind a complex high-pressure microstructure with preferred selection and evolution of hcp variants.

deformation microstructure are elucidated in the following sections.

The shocked-induced microstructure during the martensitic phase transitions (also, the PT front) is analyzed in the six-dimensional Cauchy-Green strain space, as illustrated in Fig. (2.10). Thus, the deformation states that are mapped and visualized by colored points correspond to the local transformational distortions experienced by the iron samples. Each color is associated with the index of the nearest first-rank variant V_k. Figures (2.10a) and (2.10b) depict the corresponding states that are captured when the elastic fronts reach the free surfaces for calculations without plasticity and with plasticity, respectively. The former shows that two hcp variants are nucleated without plasticity, denoted by V_1 and V_2. These two preferential ϵ-Fe variants are formed with different volume fractions, i.e., 62% for V_1 and 35% for V_2, and are thoroughly promoted by the $[001]_{bcc}$ direction of the shock. On the other hand, although the calculations with plasticity initiate the early formation of the same two variants, the four companion hcp variants are rapidly nucleated behind the PT wave front with comparable volume fractions. This microstructural fingerprint exhibits a crucial role played by the plastic deformation in nucleating and selecting all six energetically equivalent hcp variants in Fig. (2.10b). According to the previous simulations under high-pressure hydrostatic compression, the single-crystal iron has been transformed at high pressure into a polycrystalline microstructure that consists of the same six hcp variants, without any retained initial bcc phase. It is therefore suggested that the present high strain-rate plastic

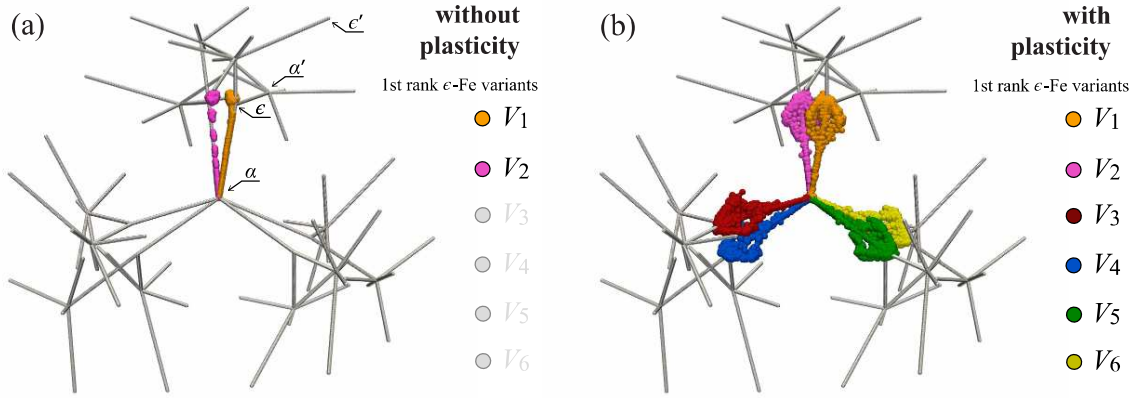

FIGURE 2.10: (a) The three-rank network of reaction pathways is projected in a $\{\mathbf{C}_1, \mathbf{C}_2, \mathbf{C}_3\}$ strain space, within which the local transformational Cauchy-Green **C**t strain states at all material points are displayed with different colors (each color is associated with a specific hcp variant from the first-rank group symmetry operation). The results are related to the simulation without plasticity, captured at the instant when the elastic front reaches the free surface, revealing the nucleation of two (from amongst six possible variants) preferred hcp variants. (b) Similar simulation with plasticity at the same time instant as in (a), where the other four energetically equivalent hcp variants are activated in the transformed polymorphic microstructure. Such structural features indicate that the high strain-rate plastic deformation is locally capable of producing a nearly relaxed hydrostatic state from the uniaxial strain state produced by the shock-wave compression.

deformation can locally achieve a similar nearly relaxed three-dimensional hydrostatic state from the uniaxial strain state produced by the shock-wave compression. The nucleation of all (also, six) high-pressure hcp variants have never been described by atomistic calculations of shock-loaded iron, certainly because of the small dimensions that hinder plastic relaxation needed to nucleate these four companion hcp variants. For instance, two twinned hcp variants, separated by noncoherent grain boundaries (GBs), are observed in Refs. [137, 138].

2.4.2 Effect of plasticity in shock-loaded iron

Because the deformation processes act as distinctive signatures in shock-compressed samples, reflecting the history the solid experienced (in terms of velocity, shock pressure, etc.), three averaged quantities over the computational samples are plotted in Fig. (2.11). Slice-averaged quantities within spatial planar bins (of one element width) are also used to quantify the role of plasticity in tailoring the complex microstructure from the uniaxial strain deformation, namely the free-surface velocity v_z in Fig. (2.11a), the pressure $p = -(\sigma_{xx} + \sigma_{yy} + \sigma_{zz})/3$ in Fig. (2.11b), and the von Mises stress σ_{vM} in Fig. (2.11c) with respect to t^*, obtained without (gray curves) and with (black curves) plasticity. Both averaged quantities p and σ_{vM} are displayed with respect to L^* along the $z \parallel [001]_{\text{bcc}}$ loading direction of the samples.

Figure (2.11a) shows the presence of two distinct plateaus for the free-surface velocity profile without plasticity (gray curve), supporting by the split two-wave structure into the noticeable fastest elastic and the phase-transition (denoted by PT, see arrow) waves. The elastic wave is characterized by the elastic precursor Ep with $v_z = 255$ m.s^{-1}, while the phase-transition front produces a considerable increase of the velocity at free surface, up to $v_z = 1660$ m.s^{-1}. On the other hand, the simulation with plasticity shows a much more complex velocity profile, where the multiple-wave structure consists inter alia of the elastic precursor Ep with the same velocity as the case without plasticity, the plastic (P wave) front, and the elastic wave reverberation with the on-going PT wave, i.e., the rEp wave. This wave profile is comparable to those reported in experimental works with distinct three-wave structures [19, 130]. The instants when both P and

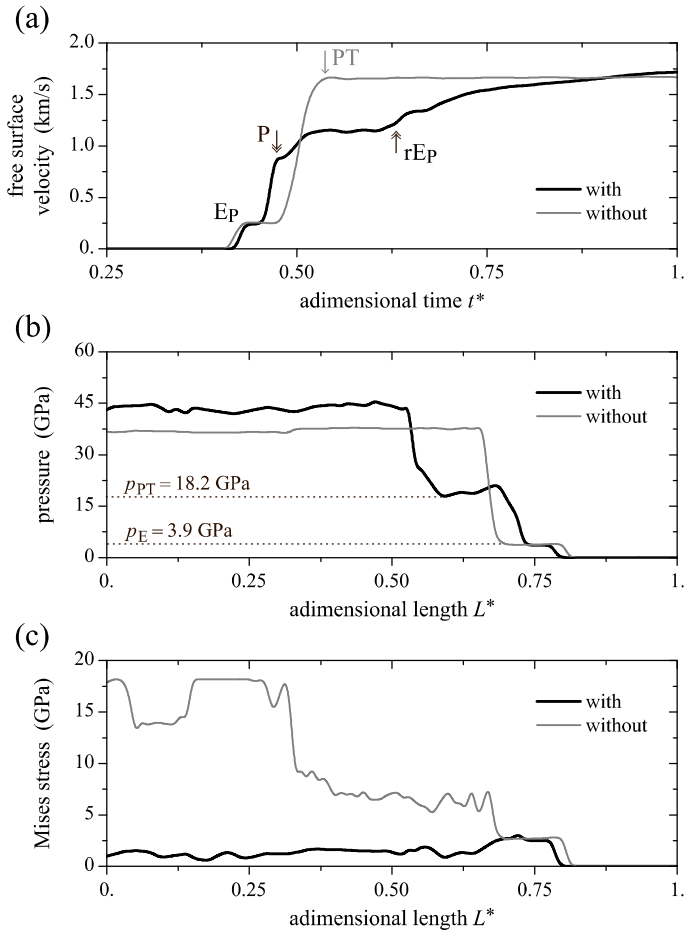

FIGURE 2.11: (a) Free surface velocity histories from shock-loaded iron samples without (gray curve) and with (black curve) plasticity. The former is caused by the arrival of the elastic precursor (denoted by Ep) and of the phase-transition (PT) wave. The latter is decomposed by Ep, the plastic (P) wave front, and rEp that results from the interaction between the reflected Ep front at the free surface and the on-coming PT wave. (b) The representative profiles of pressure in GPa along the $[001]_{\text{bcc}}$ direction for both calculations without and with plasticity. The slice-averaged values within spatial planar bins of one finite element width correspond to the three-dimensional microstructures in Figs. (2.9c) and (2.9d). (c) The von Mises stress in GPa for both calculations without and with plasticity.

rEp waves reach the free surface are displayed by the double-headed arrows in Fig. (2.11a), corresponding to $v_z = 880$ m.s^{-1} and $v_z = 1170$ m.s^{-1}, respectively. It is worth noting that both reflected Ep and P waves that propagate back in the elastically compressed and plastically deformed bcc iron (thus, along the $[00\bar{1}]_{\text{bcc}}$ direction) produce a residual stress state that does not favor the mandatory forward $\alpha \rightarrow \epsilon$ phase transitions. The interaction in releasing the stresses between the reflected Ep and P waves with the PT wave encourages therefore the reverse $\epsilon \rightarrow \alpha$ phase transitions, without retaining any ϵ-Fe hcp phase nor without forming any α'-Fe bcc variants. Interestingly, this feature differs from the pure hydrostatic compression loading, for which a significant residual volume fraction ($\sim$ 12%) of α' bcc inclusions has been obtained in the microstructure after the reverse phase transformations. Consequently, the incident PT wave cannot reach the free surface for calculations with plasticity, in contrast to the simulation case without plasticity. Additionally, it is worth mentioning that the amplitude of the steady-state free-surface velocity with plasticity is close to the one without plasticity, i.e., $v_z = 1707$ m.s^{-1}, which is roughly twice the particle velocity of 850 m.s^{-1} imposed on the rear face behind the incident shock as a loading condition, consistently with the traction-free conditions at free surfaces.

Both calculations without and with plasticity in Fig. (2.11b) exhibit a similar elastic state where

compression remains uniaxial in the $[001]_{bcc}$ direction, characterized by a pressure $p_E = 3.9$ GPa in the elastically compressed bcc phase. By considering this threshold pressure as the Hugoniot elastic limit for the plasticity-free case, the value of 3.9 GPa is defined between two reference experimental data in polycrystalline iron samples, i.e., $\sim$ 2.1 GPa [292] and $\sim$ 5.5 GPa [230]. It is worth mentioning that the similar computed values for both uniaxial elastic limits without and with plasticity are fortuitous since the former corresponds to the transformational front (accompanied by both hydrostatic and deviatoric stresses), while the latter is related to the plastic front (mainly controlled by deviatoric stresses). In practice, once the phase transformation operated by one specific variant is initiated, the excess free energy between both bcc and hcp iron phase promotes a partially-to-complete shock-induced transition that behaves differently than pure pressure, as quantified by eq. (2.37). The corresponding released stress state after this phase transformation is much more complex than the stress state behind the deviatoric stress-driven plastic front. The changes from the uniaxial shock compression to a complex stress state after phase transitions in the plastically deformed iron cannot therefore be captured by a usual pressure-shock velocity (e.g. represented by a Rayleigh line), yielding an important distinction between the shock physics described at the macroscopic scale and ones described at the grain scale. Behind the traveling Ep wave front, the pressure profile depicts the presence of one (two) plateaus for calculations without (with) plasticity. The former exhibits the presence of the PT wave front as the pressure dramatically increases up to $p_{PT} = 37.7$ GPa. The latter profile shows an intermediate pressure plateau that characterizes the plastically deformed bcc region, within which the forward $\alpha \rightarrow \epsilon$ phase transitions start roughly at the onset pressure $p_{PT} = 18.2$ GPa, as indicated by the dotted line in Fig. (2.11b). This value is on the range of experimental values for single-crystal iron under hydrostatic pressure [78], and in excellent agreement with large-scale molecular dynamics simulations in single-crystal iron as well, i.e., 18 GPa along the same $[001]_{bcc}$ shock direction [274]. Here, the value deviates from the conventional macroscopic threshold from experiments on polycrystalline Fe samples (occurring at 13 GPa [17, 19]), for which the GBs with pre-existing intrinsic defects reduce the amplitude of the forward transition pressure [105, 275, 297]. Achieved after the complete phase transformation of the bcc into hcp variants, the upper plateau is governed by the load intensity and is reached at $p = 44.1$ GPa, slightly higher than the pressure without plasticity. This value is in very good agreement with recent results from molecular dynamics simulations in shocked iron [4], where a maximum mean pressure of $\sim$ 40 GPa has been measured by applying a comparable piston velocity of 800 m.s^{-1}.

Figure (2.11c) shows the corresponding values for the von Mises stress, with $\sigma_{vM} = 2.7$ GPa for both simulations in the elastically compressed bcc iron. Then, the large von Mises stress profile increases inhomogeneously in the sample without plasticity, which is due to a heterogeneous distribution of both hcp variants V_1 and V_2 in the microstructure with lamellar arrangements along the shock direction (not shown here). The maximum value is $\sigma_{vM} = 18.1$ GPa. With plasticity, however, the volume-preserving plastic deformation relaxes significantly the internal von Mises stress to reach an averaged von Mises stress of $\sigma_{vM} = 1.1$ GPa (< 3.9 GPa, at the peak Hugoniot elastic state) in the shocked-induced hcp multivariant region. This difference asserts the role played by plasticity to release the shear stress state produced by the uniaxial strain compression to obtain a roughly hydrostatic state with 6 high-pressure hcp variants (instead of 2 variants without plasticity) in the transformed heterogeneous microstructure.

Figures (2.12a) and (2.12b) capture the evolution of the longitudinal stress component in the shock direction σ_{zz} in the Lagrangian adimensional position-time (L^*, t^*) diagrams, without and with plasticity, respectively. The non-steady-state regimes of the present elastic precursor (Ep, solid lines), plastic (P, dashed), and phase-transition (PT, dotted) waves −moving with different average speed so that net distances between the respective fronts increase with time− exhibit a more complicated picture for the three-wave structure with the high strain-rate plasticity than the corresponding diagram without plasticity. The reflection of the incident fronts from the free surfaces are depicted as well.

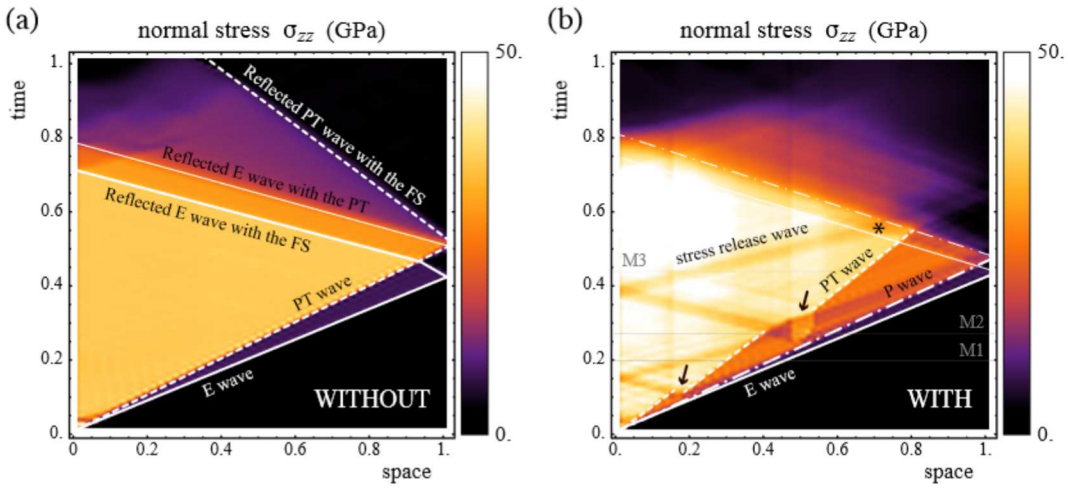

FIGURE 2.12: (a) Slice-averaged maps of the longitudinal stress component σ_{zz} in the Lagrangian adimensional position-time (L^*, t^*) diagram from simulation without plasticity. The two-wave (composed of the elastic Ep and phase-transition PT waves) structure with the reflection of both waves at the free surface are shown using different line types. (b) The three-wave structure with the presence of the intermediate plastic wave (P wave) front illustrates a considerably more complicated scenario of nonlinear wave interaction. As depicted by the arrows, this calculation with plasticity reveals two nucleation events at $t^* = 0.10$ and $t^* = 0.27$, which result in the inhomogeneous propagation of the the trailing PT wave and in the presence of a stress-release envelope. The latter travels faster than the leading shock and is characterized by a lower longitudinal stress in magnitude.

The leading E wave front, traveling at 5412 m.s^{-1} (5541 m.s^{-1}) for calculation with (without) plasticity, leaves the iron system in an elastically compressed state with high-pressure properties. The former value is in excellent agreement with the computed shock velocity of 5409 m.s^{-1} using atomistics simulations in single-crystal iron without pre-existing defects [137], which is consistent with the present calculations. Without plasticity, the trailing PT front travels homogeneously in the sample at 4655 m.s^{-1}. For the three-wave structure, the nearly over-driven P front (but not over-run, i.e., characterized by a finite separation between the E and P waves) propagates at 5059 m.s^{-1}, while the slower heterogeneous PT front travels with intermittent regimes at 3002 ± 99 m.s^{-1}, which is much lower than the homogeneous PT front without plasticity. In contrast to the case without plasticity, the intermittent propagation of the PT front with plasticity reveals the presence of i) sudden nucleation events of hcp variants (as depicted by the arrows in Fig. (2.12b)), and consequently of ii) a so-called traveling release-stress envelope. This envelope propagates by reflection between the rear surface on the left-hand side of the sample and the PT wave before interacting the (unloading) reflected Ep wave with the free surface, as displayed by the asterisk $*$ in Fig. (2.12b). It precedes always the slower wave, i.e., the PT wave, but travels faster than the elastic wave at 8312 m.s^{-1} in the transformed high-pressure regions of iron (i.e., with high pressure-induced stiffness and density). These distinct nucleation sites of hcp variants are not experienced for calculations without plasticity, exhibiting again the specific role played by the plastic deformation in governing such microstructural features. Analogous distinct nucleation events in position-time diagrams have been observed in shocked crystalline 1,3,5-triamino-2,4,6-trinitrobenzene using large values for the input parameter σ in molecular dynamics simulations [152].

2.4.3 Residual stresses in the plastically-deformed microstructure

Figures (2.13a) display three shock-induced microstructures M_1, M_2, and M_3 in Fig. (2.12b) that are associated with $t^* = 0.21$, $t^* = 0.27$, and $t^* = 0.44$, respectively, for the calculation with plasticity only. For these microstructures, various stress-related quantities, i.e., the longitudinal Cauchy

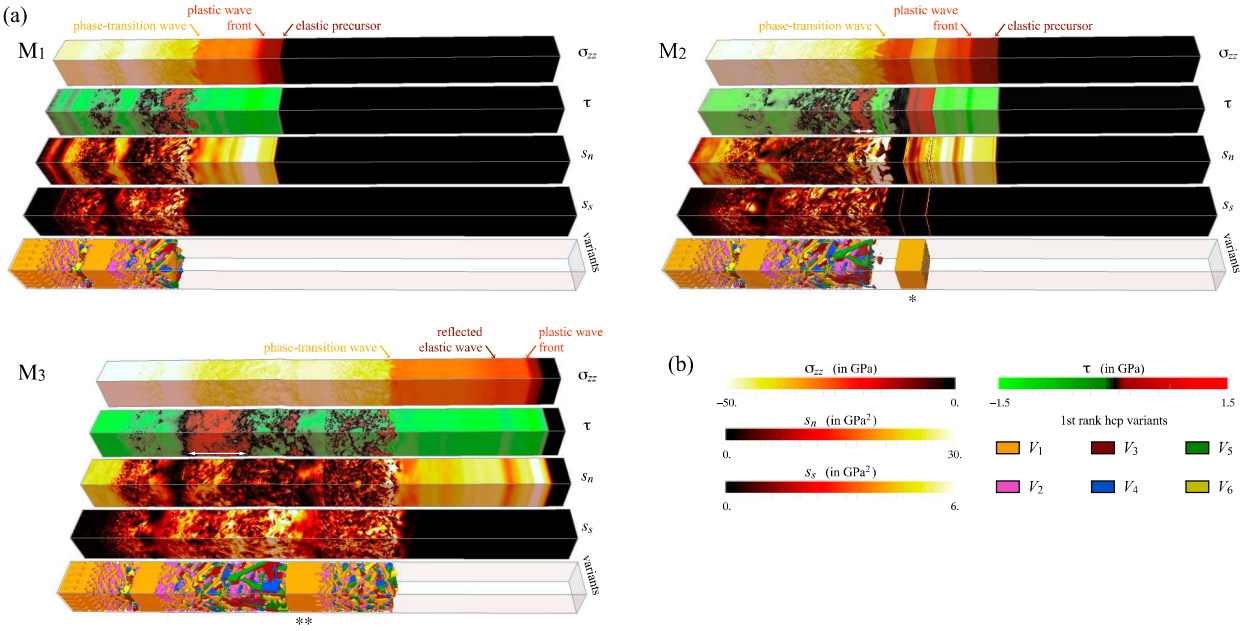

FIGURE 2.13: (a) Three-dimensional time snapshots of shock-induced microstructures, designated M_1 at $t^* = 0.21$, (b) M_2 at $t^* = 0.27$, and (c) M_3 at $t^* = 0.44$, from the position-time diagram in Fig. (2.12b) for simulation with plasticity. From top to the bottom, each panel captures the heterogeneous distribution of various stress quantities, namely, the longitudinal Cauchy stress σ_{zz}, the shear stress τ, the stress-related quantities s_n and s_s to the second invariant J_2 using eq. (2.66), as well as the polycrystalline high-pressure domains composed of six hcp variants. These variants are colored using the same code as in Fig. (2.10b), while the transparent zones are associated with the initial unshocked bcc iron. As displayed by $*$, a dynamic instability in the polymorphic phase transitions is observed in M_2, leading to the nucleation of a large monovariant with columnar growth in the microstructure that is still visible ($**$) after the propagation of the incident phase-transition wave front. (b) The color legends associated with the stress-related quantities.

stress tensor component in the shock direction σ_{zz}, the shear stress $\tau = \left(\sigma_{zz} - \left(\sigma_{xx} + \sigma_{yy}\right)/2\right)/2$, s_n, and s_s, as well as the corresponding hcp variant selection, are displayed. Both stress quantities s_n and s_s are related to the second invariant of the stress deviator J_2 and the von Mises stress σ_{vM} by

$$3J_2 = \sigma_{\text{vM}}^2 = \tfrac{3}{2}\,\text{dev}\,\boldsymbol{\sigma} : \text{dev}\,\boldsymbol{\sigma} = \tfrac{1}{2}s_n + 6s_s\,, \tag{2.66}$$

where $\text{dev}\,\boldsymbol{\sigma}$ is the deviatoric part of $\boldsymbol{\sigma}$, so that s_n and s_s are defined by

$$\begin{aligned} s_n &= (\sigma_{xx} - \sigma_{yy})^2 + (\sigma_{yy} - \sigma_{zz})^2 + (\sigma_{xx} - \sigma_{zz})^2 \\ s_s &= \sigma_{xy}^2 + \sigma_{yz}^2 + \sigma_{xz}^2\,, \end{aligned} \tag{2.67}$$

with σ_{xy}, σ_{xz}, and σ_{yz} being the orthogonal shear stresses. As a signed quantity, the shear stress τ, which equals to the von Mises stress if the off-diagonal terms are neglected, can also have positive (in red) or negative (green) values depending on the magnitude of σ_{zz} with respect to $\left(\sigma_{xx} + \sigma_{yy}\right)/2$. All color legends for the stress-related quantities are displayed in Fig. (2.13b).

At instant $t^* = 0.21$, the split three-wave structure into the Ep, P, and PT wave fronts is clearly distinguishable by the change in magnitude of σ_{zz} in Fig. (2.13a). Close to the phase-transition front, the transformed region with 6 high-pressure hcp variants is characterized by positive values of the shear stress τ (values in red). Between the PT and P wave fronts, the shear stress τ is negative (green), the stress field s_s is zero, while the quantity s_n exhibits the presence planar surfaces as pulses generated by the PT front that dynamically nucleates the hcp variants. These six variants are pictured with the same colors as in Fig. (2.10b). Behind the complex rough PT front, some hcp grains grow preferentially into flaky morphology with $(110)_{\text{bcc}}$ and $(1\bar{1}0)_{\text{bcc}}$ habit

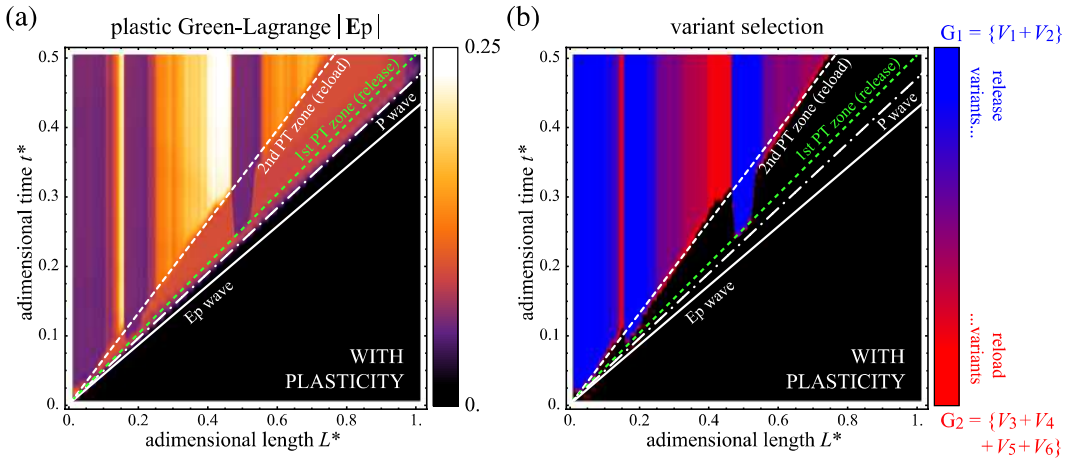

FIGURE 2.14: (a) Slice-averaged magnitude of the plastic Green-Lagrange strain tensor **Ep** in the Lagrangian adimensional position-time (L^*, t^*) diagram from simulation with plasticity. The elastic and plastic wave fronts with constant velocities are shown using different line types as well as two (primary and secondary) phase-transition zones that are associated with specific nucleation of release and reload variants (see text for details). (b) The corresponding selection of hcp variants, categorized into two groups, so-called $\mathrm{G}_1 = \{V_1 + V_2\}$ (in blue) and $\mathrm{G}_2 = \{V_3 + V_4 + V_5 + V_6\}$ (red).

planes of the bcc iron, which are transformed into the $(0001)_{\mathrm{hcp}}$ close-packed planes after the phase transition.

At $t^* = 0.27$, the presence of a dynamical instability in the compressed and plastically deformed microstructure is shown. This occurs under a complex stress state that is responsible to an extremely rapid nucleation of a large single-crystal hcp variant V_1 (in orange, as depicted by $*$ in M_2 in Fig. (2.13a)) with columnar growth in the direction of the shock loading. This spontaneous nucleation is characterized by a notable change in sign of the shear stress τ from negative (green) to positive (red) values. The ideal volume-reducing transition path of the strain-free monovariant V_1 requires a compression of $\sim 12.5\%$ along the $z \parallel [001]_{\mathrm{bcc}}$ direction, as defined by the zz component in eq. (2.37). This sudden nucleation event gives rise to the aforementioned traveling release-stress envelop in Fig. (2.12b), which is also characterized by a finite domain with positive shear stress values, as depicted by white double-sided arrows in M_2 and M_3. Surrounded by the initial bcc phase, the variant V_1 is able to grow in the shock direction, whereas the confined region between the PT front and V_1 in M_2 becomes an unstable zone for nucleation of high-pressure variants. Similar shock-driven regions of instabilities, within which local nucleation of hcp embryos occur, have been observed by Wang et co-workers using atomistic simulations [273].

Although V_1 is still visible at instant $t^* = 0.44$, the phase-transition wave front continues to propagate in the shock direction, exhibiting the coalescence of the hcp variants and also a specific morphological fingerprint of shock-induced hcp variants with large transformed bands (due to the periodic boundary conditions) at high pressure. A thickness of ~ 77 μm for V_1 is found in the $z \parallel [001]_{\mathrm{bcc}}$ direction, which also depends on the shock velocity (results not shown here). Overall, s_n exhibits large values in the elastically compressed zones, which significantly decrease as soon as the nucleation of growth of hcp variants take place during the polymorphic phase transitions. In turn, because both quantities s_n and s_s quantities play a complementary role in the present J_2 plasticity theory, s_s gives rise to large values in the phase-transformed hcp regions. The aforementioned transformed bands are therefore considered here as an important mechanism of stress relaxation under shock compression at high strain rate, thus providing novel guidelines for future experimental diagnostics of shock wave propagation in iron.

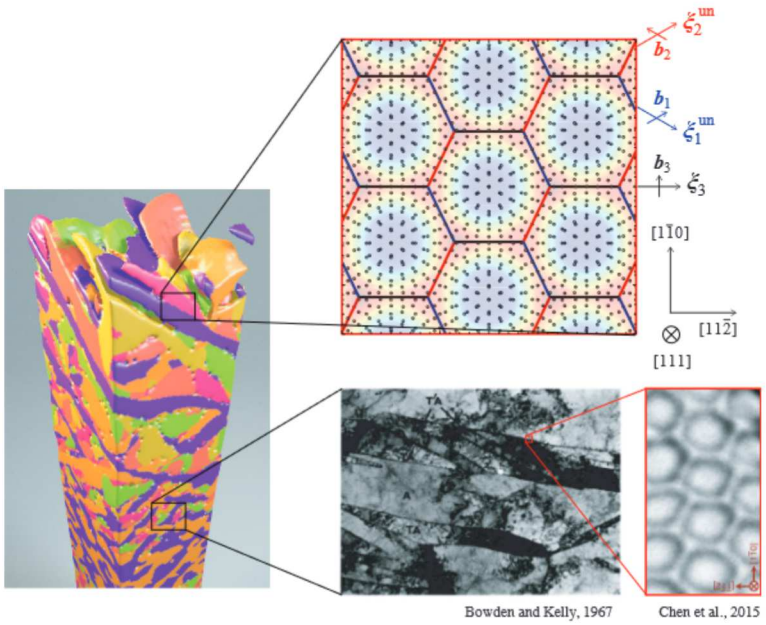

FIGURE 2.15: Schematics of the presence of internal dislocation structures at solid-solid interfaces.

2.4.4 Dynamical instability in structural phase transitions

Figure (2.14a) illustrates the shock-induced instability in the structural phase transitions by means of the magnitude of the plastic Green-Lagrange deformation $\mathbf{Ep}$, defined by $|\mathbf{Ep}| = |\mathbf{Fp}^t \cdot \mathbf{Fp} - \mathbf{I}|/2$. This quantity is plotted in the Lagrangian adimensional position-time (L^*, t^*) diagram, where t^* is restricted between 0 and 0.5 for clarity, so that the multiple reflections of incident waves from the free surface are conveniently omitted in the following discussion. It is shown that the propagation of the PT front gives rise to a spatially (not temporally) heterogeneous distribution of $|\mathbf{Ep}|$ with local values up to 0.25. This localization of plastic deformation is therefore strongly correlated with the specific selection of shock-induced hcp variants, which can be separated into two pertinent groups, so-called $G_1 = \{V_1 + V_2\}$ and $G_2 = \{V_3 + V_4 + V_5 + V_6\}$, each set involving different features of the microstructural fingerprints in shock-loaded iron. Thus, Fig. (2.14b) displays the variant selection during the shock wave propagation using a linear interpolation of color to distinguish the presence of both groups G_1 (blue) and G_2 (red) in the microstructure. As already mentioned, both V_1 and V_2 variants (from amongst six available variants) of G_1 are promoted by the shock direction in the first instants of the shock wave propagation. Since the two-phase mixture induces a large contraction along the loading $\boldsymbol{z} \parallel [001]_{bcc}$ direction, the corresponding group G_1 is composed of variants designated by "release variants". However, the second group G_2, which consists of a mixture of the complementary four variants with identical volume fractions, experiences an expansive reaction in the shock direction. In contrast to G_1, these newly-formed variants of G_2 are also expected to generate an expansion (or reloading) wave, which are therefore not promoted by the initial compressive (or loading) wave. In the following, the four variants of G_2 are denoted by "reload variants", for which the nucleation is accompanied by severe plastic deformation with large values of $|\mathbf{Ep}|$, as indicated by Fig. (2.14a).

2.5 Limitations

While the present phase-field approach is capable of considering the elastic mismatch between low- and high-pressure variants during the pure pressure- and shock-induced phase transformations in iron, the coexistence of both solid-state phases with different crystal structures (e.g. lattice parameters) yields to the loss of lattice coherence at the interfaces. This also means that the

perfect lattice correspondence across the bcc/hcp interfaces as well as the misoriented hcp/hcp grain boundaries obtained in Fig. (2.8) becomes an implausible model assumption, and that the current description of the crystalline interfaces during solid-solid phase transitions remains obviously incomplete. In fact, experimental observations of such interfaces show that coherent interfaces break down through the formations of misfit dislocation structures, as sketched in Fig. (2.15) with internal hexagonal dislocation patterns. The resulting "semicoherent interfaces" consist of coherent regions separated by these interfacial dislocation structures. Since the earliest observations of dislocation arrangements into periodic patterns along solid-state interfaces in a variety of conditions [6, 54, 5, 65], the advantages/inconveniences introduced by the presence of such crystal defects in high-technology applications have been addressed in interdisciplinary materials science and engineering [237, 95], involving chemistry, physics, electronics, metallurgy, mechanics, etc. Extensive investigations have indicated that the interfacial dislocation patterns at grain and interphase boundaries may, however, be designed to increase the unprecedented levels of high strength [7], ductility [300], and radiation-induced damage tolerances [26] in nanocrystalline polycrystals, nanolayered laminated composites, precipitation-strengthened alloys, and epitaxial free-standing thin films. In part, the fundamental problem of characterizing the dislocation structures and energetics at heterophase interfaces is treated in the following chapter 3.

Chapter 3

Dislocation structures and energetics at heterophase interfaces

Selected peer-reviewed articles

[P28] **A. Vattré**, E. Pan. *Dislocation singularities in layered magneto-electro-elastic plates*. International Journal of Engineering Science, 181, 103765, 2022.

[P21] **A. Vattré**, E. Pan. *Semicoherent heterophase interfaces with core-spreading dislocation structures in magneto-electro-elastic multilayers under external surface loads*. Journal of the Mechanics and Physics of Solids, 124, 929-956, 2019.

[P20] **A. Vattré**, N. Abdolrahim, S. Navale, M. Demkowicz. *The relaxed structure of intrinsic dislocation networks in semicoherent interfaces: predictions from anisotropic elasticity theory and comparison with atomistic simulations*. Extreme Mechanics Letters, 28, 50-57, 2019.

[P19] T. Jourdan, **A. Vattré**. *A continuous model including elastodiffusion for sink strength calculation of interfaces*. Computational Materials Science, 153, 473-478, 2018.

[P18] **A. Vattré**, E. Pan. *Three-dimensional interaction and movements of various dislocations in anisotropic bicrystals with semicoherent interfaces*. Journal of the Mechanics and Physics of Solids, 116, 185-216, 2018.

[P17] **A. Vattré**, E. Pan. *Interaction between semicoherent interfaces and Volterra-type dislocations in dissimilar anisotropic materials*. Journal of Materials Research, 32, 3947-3957, 2017.

[P16] **A. Vattré**. *Elastic strain relaxation in interfacial dislocation patterns: II. From long- and short-range interactions to local reactions*. Journal of the Mechanics and Physics of Solids, 105, 283-305, 2017.

[P15] **A. Vattré**. *Elastic strain relaxation in interfacial dislocation patterns: I. A parametric energy-based framework*. Journal of the Mechanics and Physics of Solids, 105, 254-282, 2017.

[P14] **A. Vattré**, T. Jourdan, H. Ding, C. Marinica, M. Demkowicz. *Non-random walk diffusion enhances the sink strength of semicoherent interfaces*. Nature communications, 7, 1-10, 2016.

[P13] **A. Vattré**. *Elastic interactions between interface dislocations and internal stresses in finite-thickness nanolayered materials*. Acta Materialia, 114, 184-197, 2016.

[P10] **A. Vattré**. *Mechanical interactions between semicoherent heterophase interfaces and free surfaces in crystalline bilayers*. Acta Materialia, 93, 46-59, 2015.

[P9] **A. Vattré**, M. Demkowicz. *Partitioning of elastic distortions at a semicoherent heterophase interface between anisotropic crystals*. Acta Materialia, 82, 234-243, 2015.

[P8] **A. Vattré**, N. Abdolrahim, K. Kolluri, M. Demkowicz. *Computational design of patterned interfaces using reduced order models*. Scientific report, Nature, 4, 2014.

[P7] **A. Vattré**, M. Demkowicz. *Effect of interface dislocation Burgers vectors on elastic fields in anisotropic bicrystals*. Computational Materials Science, 88, 110-115, 2014.

[P5] **A. Vattré**, M. Demkowicz. *Determining the Burgers vectors and elastic strain energies of interface dislocation arrays using anisotropic elasticity theory*. Acta Materialia, 61, 5172-5187, 2013.

3.1 Motivation

Far from being featureless dividing surfaces between neighboring crystals, interfaces in homo- and hetero-phase solids have internal structures of their own. These structures depend on interface crystallographic character (misorientation and interface plane orientation) and affect the physical properties of interfaces, such as interface energy [73], resistivity [42], permeability [125], mechanical properties [141], morphology and variant selection of precipitates [210], point defect sink efficiencies [225], and mobilities [147]. To better understand and control the properties of interfaces, it is desirable to be able to predict their internal structures. The first part of this chapter 3 presents a method for predicting a specific interface structural feature: the Burgers vectors of intrinsic dislocations in semicoherent homophase and heterophase interfaces. This information is then used to compute the interface elastic strain energies in standard tilt and twist GBs as well as the partition of elastic distortions at complex heterophase interfaces. An application to the sink strength of semicoherent interfaces is described in section 3.5, for which the non-random walk diffusion of radiation-induced defects is highly sensitive to the detailed character of interfacial stresses. The follow-up extensions to the elastic strain relaxation in interfacial dislocation patterns and to the elastic interaction with extrinsic dislocation arrays and loops are investigated in sections 3.6 and 3.7, respectively.

One way of studying interface structure is through atomistic simulations, which explicitly account for all the atoms that make up an interface. However, this approach is not always practical or efficient: it can be very resource-intensive because it requires a separate simulation for each individual interface. Thus, it does not lend itself to rapidly scanning over many different interfaces, for example if one were searching for trends in interface structures or for tailored interfaces with a specific structure. Low-cost, analytical techniques for predicting interface structure would be preferable in such situations.

One widely used analytical approach applies to semicoherent interfaces and describes interface structures in terms of intrinsic dislocations using the closely related Frank-Bilby [93, 30] and O-lattice [32, 296, 237] techniques. Both procedures require the selection of a reference state, within which the Burgers vectors of individual interface dislocations are defined. Because this choice does not affect the calculated spacing and line directions of interface dislocations, it has sometimes been viewed as if it were arbitrary. In practice, one of the adjacent crystals [145, 110, 289] or a "median lattice" [91] have often been used as the reference state.

However, the choice of reference state does influence the values of far-field stresses, strains, and rotations associated with interface dislocations. These, in turn, are usually subject to constraints, namely that the far-field stresses be zero and that the far-field rotations be consistent with a prescribed misorientation. Thus, the choice of reference state is in fact not arbitrary. As discussed by Hirth and co-workers [119, 122, 123], the importance of selecting proper reference states has often been overlooked in part because the best-known applications of interface dislocation models are to interfaces of relatively high symmetry, such as symmetric tilt or twist GBs, for which correct reference states are easy to guess. Furthermore, many analyses assume uniform isotropic elasticity, which leads to equal partitioning of interface dislocation elastic fields between the neighboring crystals. In general, however, interfaces need not have high symmetry and the

neighboring crystals may have unlike, anisotropic elastic constants. By use of heterogeneous and anisotropic elasticity theory, the correct selection of reference states in such general cases is far more challenging.

Elasticity theory for analyzing semicoherent interfaces and determining the field solutions produced by interface dislocations has been initiated by van der Merwe [244]. The concept of misfit dislocations, which act as stress annihilators to free the total stress fields far from the interfaces, has been introduced using the Peierls-Nabarro model to formulate a misfit dislocation theory for critical thicknesses of strained and layer systems during epitaxial growth of structures with two isotropic semi-infinite solids [245, 243]. The problem of single straight screw and edge dislocations and dislocation arrays situated at the interface between two anisotropic elastic half-spaces has received special attention in the literature [282, 60, 21, 34, 283, 277, 260, 146], for which the dislocation-based calculations and also mechanisms may be significantly altered when isotropic elastic approximation is considered.

By means of the Stroh sextic formalism [234, 235] with a Fourier series-based technique, the geometry of interface dislocation patterns as well as the corresponding Burgers vectors have been solved using anisotropic elasticity theory in bicrystals with two sets of dislocations [260, 258, 261]. This computational method for structural and energetic properties of individual heterophase interfaces has been extended by taking into account the presence of free surfaces in bi- and tri-layered materials [247, 248] and the local reactions between planar and crossing dislocation arrays to form new dislocation arrangements [249, 250]. Application examples have revealed the significant influence played by elastic anisotropy in the interactions between the semicoherent interfaces and radiation-induced point defects [255] as well as extrinsinc dislocation loops [256].

3.2 Determining the Burgers vectors of interface dislocation arrays

The notion of introducing Volterra dislocations into a reference state for constrained interfaces is consistently defined with the Frank-Bilby equation that are free of far-field stresses.

3.2.1 Planar interfaces in linear elastic bicrystals

In the present analysis, planar interfaces are considered formed by joining two semi-infinite linear elastic crystals, for which the crystallography of the interfaces has been specified completely. For a GB, this requires five parameters: three to describe the relative misorientation between neighboring crystals and two to describe the orientation of the GB plane [237]. For a heterophase interface, the number of crystallographic DoFs may be higher. For example, an interface between two fcc crystals such as Al and Ni would require the lattice parameters of the two neighboring metals to be given in addition to the five parameters needed for a GB. Interfaces between materials with differing crystal structures may require further parameters.

To describe completely the crystallography of a heterophase interface between elements A and B, the notion of a "reference" state for the interface is adopted: in the reference state, the interface is coherent, i.e. the two separate crystals that meet at the interface are rotated and strained [131, 237] such that they are in perfect registry with each other across the interface plane after bonding. Thus, the reference state has the interface structure of a single perfect crystal.

Starting from the reference state, materials A and B are mapped separately into new configurations that yield an interface with the required crystallographic character and zero far-field stresses, as shown in Fig. (3.1). Following Hirth, Pond, and co-workers [123], the state of the interface after this mapping is referred as the "natural" state. For a GB, the maps applied to materials A and B are proper rotations while for a pure misfit interface they are pure strains. To account for both cases as well as for heterophase interfaces between misoriented crystals, the maps are described as uniform displacement gradients ${}_{\mathrm{A}}\mathbf{F}$ and ${}_{\mathrm{B}}\mathbf{F}$. In the reference state, the neighboring crystals might not

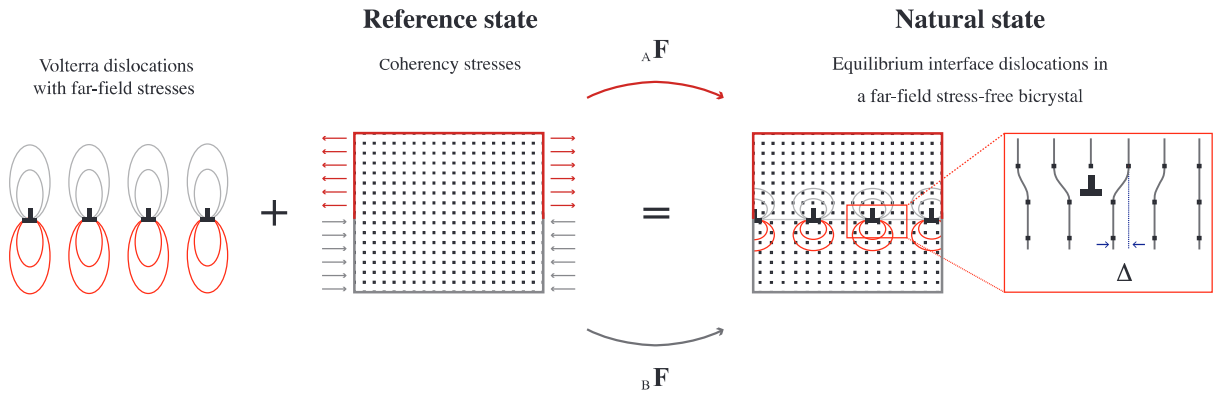

FIGURE 3.1: Mapping from a coherent reference state to the natural state using displacement gradients $_A\mathbf{F}$ and $_B\mathbf{F}$. Volterra dislocations introduced into the reference state remove coherency stresses and may change the misorientation of the neighboring crystals.

be stress free, but the interface is coherent. In the natural state, the interface is not coherent, but the neighboring crystals are both free of far-field stresses.

This framework is sufficiently general to describe the crystallography of many commonly studied heterophase interfaces, e.g. ones formed by fcc and bcc metals [73, 75], but not all. For example, mapping from a common reference state to an interface between a cubic and hcp crystal cannot directly be accomplished by a displacement gradient alone and requires an internal shuffle rearrangement, as mentioned in section 2.2.5. The present chapter 3 is also focused on materials that may be mapped to a common reference state using displacement gradients alone.

The crystallographic considerations described above do not require a single, unique reference state. On the contrary, an infinite number of new reference states may be generated from an original one by applying to it any uniform displacement gradient $_R\mathbf{F}$. If the original reference state may be mapped to the natural state with $_A\mathbf{F}$ and $_B\mathbf{F}$, then the new reference state may be mapped to the same natural state using $_A\mathbf{F}\,_R\mathbf{F}^{-1}$ and $_B\mathbf{F}\,_R\mathbf{F}^{-1}$. However, a consistent description of the elastic fields of a discrete dislocation network in an interface of specified crystallography and free of far-field stresses does require a single specific reference state.

3.2.2 Volterra dislocations in the reference state

The atomic structures of real interfaces are not like those generated by the linear mappings from a reference state. Instead, for any given interface crystallography, the atomic structure may undergo a variety of local relaxations or reconstructions that lower its energy. In many low-misorientation GBs and low-misfit heterophase interfaces, these changes lead to formation of regions of coherency (which generally have low energies) separated by networks of intrinsic dislocations. Many such interface dislocation networks have been imaged using transmission electron microscopy [5].

There are two common ways of describing interface dislocations. In one, they are viewed not as conventional Volterra dislocations, but rather as special kinds of interface defects with short-range elastic fields that are formed when the interface atomic structure in the natural state relaxes [120, 37]. The superimposed elastic fields of all such defects residing within an interface decay away to zero at long range and therefore do not alter the far-field stress state or the crystallography of the natural interface state.

Another description—the one adopted here—views interface dislocations as genuine Volterra dislocations with resultant elastic stress fields that need not decay to zero at long range. For example, the structure of some pure misfit heterophase interfaces may be described as an array of equally spaced edge dislocations residing on the same glide plane [181]. Such an array of Volterra

dislocations has a non-zero far-field stress [7]. Certain symmetric tilt GBs may be described as arrays of edge dislocations lying directly one above the other on separate glide planes. These Volterra dislocation arrays have zero far-field strains (hence, also zero stresses [7]), but possess non-zero rotations at long range [213, 164]. In general, arrays of Volterra dislocations may have non-zero far-field strains, rotations, or both.

In the work described here, interface dislocations are viewed as Volterra dislocations that have been introduced into the reference state, as shown in Fig. (3.1). Therefore, the far-field stresses due to these dislocations ${}_{\mathrm{A}}\boldsymbol{\sigma}^{\infty}_{\mathrm{dis}}$ and ${}_{\mathrm{B}}\boldsymbol{\sigma}^{\infty}_{\mathrm{dis}}$ are equal and opposite to the coherency stresses ${}_{\mathrm{A}}\boldsymbol{\sigma}_{\mathrm{c}}$ and ${}_{\mathrm{B}}\boldsymbol{\sigma}_{\mathrm{c}}$ in the reference state respectively, leading to the removal of all far-field stresses in the natural state:

$$ {}_{\mathrm{A}}\boldsymbol{\sigma}_{\mathrm{c}} + {}_{\mathrm{A}}\boldsymbol{\sigma}^{\infty}_{\mathrm{dis}} = \mathbf{0}\,, \quad \text{and,} \quad {}_{\mathrm{B}}\boldsymbol{\sigma}_{\mathrm{c}} + {}_{\mathrm{B}}\boldsymbol{\sigma}^{\infty}_{\mathrm{dis}} = \mathbf{0}\,. \tag{3.1} $$

Although free of long-range stresses, interface dislocation networks in the natural state have non-zero short-range elastic fields as a result of the superposition of the non-uniform stress fields of the Volterra dislocation networks and the uniform coherency stresses in the reference state. Additionally, the far-field rotations due to the Volterra dislocations are required to conform to the given interface crystallographic character. These requirements restrict the choice of reference states to a single specific one.

The notion of introducing Volterra dislocations into the reference state primarily is treated as a hypothetical operation. However, this operation may be a physically meaningful analog of processes occurring at some real interfaces. For example, the transformation of certain coherent heterophase interfaces into ones that are not coherent, but free of far-field stresses, occurs by the deposition on the interface of Volterra dislocations that glide through the neighboring crystalline layers [181, 182]. Similarly, subgrain boundaries are thought to assemble from glide dislocations formed during plastic deformation of polycrystals [8].

3.2.3 Crystallographic constraints on interface dislocations

A variety of shapes of interface dislocation networks have been observed [5], such that the ones that may be represented by $j \leq 2$ arrays of parallel dislocations with Burgers vectors $\boldsymbol{b}_j$, line directions $\boldsymbol{\xi}_j$, and inter-dislocation spacings d_j. Following previous investigators [93, 30, 237], these quantities are related to the density of admissible Volterra dislocations in the reference state and interface crystallography as

$$ \boldsymbol{B} = \sum_{i=1}^{j} \left(\frac{\boldsymbol{n} \times \boldsymbol{\xi}_i}{d_i} \cdot \boldsymbol{p} \right) \boldsymbol{b}_i = \left({}_{\mathrm{A}}\mathbf{F}^{-1} - {}_{\mathrm{B}}\mathbf{F}^{-1} \right) \boldsymbol{p} = \mathbf{T}\,\boldsymbol{p}\,, \tag{3.2} $$

where $\boldsymbol{n}$ is a unit vector normal to the interface and the so-called probe vector $\boldsymbol{p}$ is any vector contained within the interface plane. Equation (3.2) is known as the quantized Frank-Bilby equation [237, 289], where $\mathbf{T}$ corresponds to an average operation that maps $\boldsymbol{p}$ to the resultant Burgers vector $\boldsymbol{B}$ of interface dislocations intersected by $\boldsymbol{p}$.

The individual Burgers vectors $\boldsymbol{b}_i$ of interface dislocations are assumed to be related to the crystal structure of the reference state. For example, if the reference state is an fcc crystal of lattice parameter a, values of $\boldsymbol{b}_i$ may be drawn from a set of $\frac{a}{2}\langle 110\rangle$-type glide or $\frac{a}{6}\langle 112\rangle$-type Shockley partial dislocation Burgers vectors. Once the set of admissible Burgers vectors is known, well-studied methods stemming from Bollmann's O-lattice theory [32] may be used to compute $\boldsymbol{n}$, $\boldsymbol{\xi}_i$, and d_i [145, 289] from the O-lattice vectors $\boldsymbol{p}^{\mathrm{o}}_i$, defined by

$$ \boldsymbol{b}_i = \mathbf{T}\,\boldsymbol{p}^{\mathrm{o}}_i\,. \tag{3.3} $$

The O-lattice vectors $\boldsymbol{p}^{\mathrm{o}}_i$—and therefore both $\boldsymbol{\xi}_i$ and d_i—do not depend on the choice of reference state. If an original reference state is mapped to a new one using displacement gradient ${}_{\mathrm{R}}\mathbf{F}$, then $\boldsymbol{b}_i$

is mapped to $\check{\boldsymbol{b}}_i = {}_{\mathrm{R}}\mathbf{F}\,\boldsymbol{b}_i$. Here and in the following, the superimposed inverse caret will be used to indicate trial values of variables. The new reference state may also be mapped to the natural state using ${}_{\mathrm{A}}\check{\mathbf{F}} = {}_{\mathrm{A}}\mathbf{F}\,{}_{\mathrm{R}}\mathbf{F}^{-1}$ and ${}_{\mathrm{B}}\check{\mathbf{F}} = {}_{\mathrm{B}}\mathbf{F}\,{}_{\mathrm{R}}\mathbf{F}^{-1}$, as discussed in section 3.2.1. Assuming that rank $\mathbf{T} = 3$, the O-lattice vectors computed from the original and new reference states are identical:

$$\boldsymbol{p}_i^{\mathrm{o}} = \mathbf{T}^{-1}\boldsymbol{b}_i = \left({}_{\mathrm{A}}\check{\mathbf{F}}^{-1} - {}_{\mathrm{B}}\check{\mathbf{F}}^{-1}\right)^{-1}\check{\boldsymbol{b}}_i = \check{\boldsymbol{p}}_i^{\mathrm{o}}\,. \tag{3.4}$$

This conclusion may also be shown for matrix $\mathbf{T}$ of rank 2 or 1. Thus, for a given set of Burgers vectors $\boldsymbol{b}_i$, interface crystallography uniquely determines interface dislocation line directions $\boldsymbol{\xi}_i$ and spacings d_i, but not the reference state. Based on this result, some authors have argued that the choice of reference state is truly arbitrary [32]. However, in different reference states, $\boldsymbol{b}_i$ will clearly have different magnitudes and directions, both of which influence the magnitudes of the elastic fields generated by interface dislocations (the latter by altering their characters).

3.2.4 Solution strategy

Determining the elastic fields of semicoherent interfaces requires finding the correct interface dislocation Burgers vectors, which are defined in the coherent reference state. The following five-step strategy is applied to determine the specific reference state that meets the constraints of interface crystallographic character and zero far-field stresses.

Step 1: Solving for geometry of dislocation networks

As shown in section 3.2.3, the geometry of interface dislocations (their line directions and spacings) is independent of the choice of reference state. Thus, a reference state is chosen identical to one of the crystals adjacent to the interface in its natural state. This choice provides an initial guess of the interface dislocation Burgers vectors. Then, the interface dislocation geometry is determined by using standard methods [31, 145, 110]. Multiple dislocation geometries are possible in some interfaces, but attention is restricted in this section to interfaces with unique geometries.

Step 2: Solving for interface dislocation elastic fields

The complete elastic fields, produced by the arrays of dislocations found in step 1, are determined using anisotropic linear elasticity theory in bicrystals. The elastic fields are assumed to follow the periodicity of the two-dimensional dislocation structures predicted in step 1 and must also satisfy specific boundary conditions at the interfaces.

Step 3: Solving for far-field distortions

The far-field distortions associated with each set of parallel dislocations are computed separately and then superimposed to obtain the resultant far-field distortions of the interface dislocation network as a whole. These elastic distortions are key for determining the correct reference state for the interfaces of interest. Far-field strains, stresses, and rotations may also be deduced.

Step 4: Solving for the reference state

The correct reference state is the one in which the superposition of the strains produced by interface dislocation arrays eliminate the coherency strains, giving a bicrystal that is free of far-field stresses and has far-field rotations that agree with the given interface crystallographic character. This condition is met by continuously adjusting the reference state along a specified transformation pathway, starting with the initial guess selected in step 1.

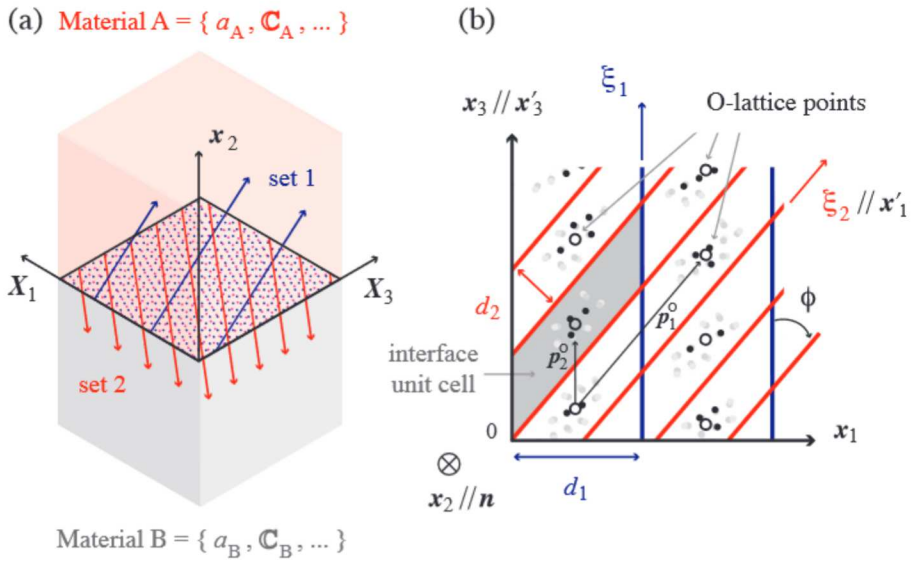

FIGURE 3.2: (a) Schematic illustration of a planar interface dislocation network formed by bonding materials A and B. (b) The geometry of an interface containing two sets of dislocations described by O-lattice vectors p_1^o and p_2^o. Open circles represent O-lattice points and filled circles illustrate atoms with nearly matching positions in materials A and B.

Step 5: Solving for the interface elastic strain energy

Incomplete cancellation of the coherency and Volterra fields near the interface gives rise to short-range stresses and strains. These stresses and strains are used to compute the elastic energies of semicoherent interfaces.

3.2.5 Elastic fields of interface dislocation arrays

This section is focused on interfaces containing up to two arrays of infinitely long straight, and uniformly spaced parallel dislocations at equilibrium, as illustrated in Fig. (3.2a). The Stroh formalism of anisotropic linear elasticity [234, 235, 59] and a Fourier series-based solution technique are used to compute the elastic fields outside the cores of interface dislocations [22, 68, 34]. For clarity in this section, the pre-subscripts A and B in the field expressions will be omitted if no distinction between materials is required.

Problem formulation

The geometry of a dislocation network consisting of two arrays of straight parallel dislocations may be described by two O-lattice vectors $p_1^o \neq p_2^o$ in the interface of interest using a Cartesian coordinate system with basis vectors (x_1, x_2, x_3), as shown in Fig. (3.2b). An interface containing only one array of straight parallel dislocations is a special case of this more general geometrical description. The unit vector normal to the interface is $n \parallel x_2$, with the interface located at $x_2 = 0$: $x_2 > 0$ for material A, and $x_2 < 0$ for material B. The dislocation line direction ξ_1 is parallel to p_2^o and $\xi_2 \parallel p_1^o$, as illustrated in previous studies [110, 237, 289].

A representative interface unit cell of the dislocation pattern is illustrated in Fig. (3.2b). Translations of the unit cell by the basis vectors p_1^o and p_2^o tessellate the interface plane. It is also convenient to identify a non-orthogonal (oblique) frame with basis vectors (x'_1, x_2, x'_3), where $x'_1 \parallel p_1^o \parallel \xi_2$ and $x'_3 \parallel x_3 \parallel p_2^o \parallel \xi_1$. The oriented angle between ξ_2 and ξ_1 is denoted by ϕ, so that $x'_1 = x_1 \csc\phi$ and $x'_3 = x_3 - x_1 \operatorname{ctg}\phi$. Thus, any position vector in this non-orthogonal frame may be expressed as $r = x'_1 p_1^o + x'_3 p_2^o$.

Due to the periodicity of the interface dislocation structure, it is useful to seek a complete set of wavevectors $\boldsymbol{k}$ such that the elastic fields in the interface may be analyzed using plane waves $\mathrm{e}^{i2\pi\boldsymbol{k}\cdot\boldsymbol{r}}$. The set of all $\boldsymbol{k}$ is conveniently written as $\boldsymbol{k} = n\,\boldsymbol{p}_1^{\times} + m\,\boldsymbol{p}_2^{\times}$ with respect to the reciprocal vectors $\boldsymbol{p}_1^{\times}$ and $\boldsymbol{p}_2^{\times}$, defined by the orthogonality conditions $\boldsymbol{p}_\alpha^{\times}\cdot\boldsymbol{p}_\beta^{\mathrm{o}} = \delta_{\alpha\beta}$, where n, m are integers.

The complete elastic distortion field $\mathbf{D}$ is the superposition of the uniform coherency and the Volterra dislocation distortions, $\mathbf{D}_{\mathrm{c}}$ and $\mathbf{D}_{\mathrm{dis}}$, as discussed in section 3.2.2. Following the seminal work of Bonnet [34, 35, 36], outside of dislocation cores, $\mathbf{D}$ may be expressed as the biperiodic Fourier series, i.e.

$$\mathbf{D}\left(\boldsymbol{x}\right) = \mathbf{D}_{\mathrm{c}} + \mathbf{D}_{\mathrm{dis}}\left(\boldsymbol{x}\right) = \mathbf{D}_{\mathrm{c}} + \mathrm{Re}\sum_{\boldsymbol{k}\neq\boldsymbol{0}} \mathrm{e}^{i2\pi\boldsymbol{k}\cdot\boldsymbol{r}}\,\mathbf{D}^{\boldsymbol{k}}\left(x_2\right)\,, \tag{3.5}$$

with $i = \sqrt{-1}$, while Re stands for the real part of a complex quantity and the sum spans over all non-zero wavevectors $\boldsymbol{k}$. The Fourier amplitudes of the complete distortion waves $\mathbf{D}^{\boldsymbol{k}}\left(x_2\right)$ are required to converge (not necessary to zero) in the far-field, i.e. $x_2 \to \pm\infty$. The components k_1 and k_3 of the wavevector $\boldsymbol{k}$ satisfy

$$\boldsymbol{k}\cdot\boldsymbol{r} = k_1\,x_1 + k_3\,x_3 = \left(\frac{n\,\mathrm{csc}\,\phi}{|\boldsymbol{p}_1^{\mathrm{o}}|} - \frac{m\,\mathrm{ctg}\,\phi}{|\boldsymbol{p}_2^{\mathrm{o}}|}\right)x_1 + \frac{m}{|\boldsymbol{p}_2^{\mathrm{o}}|}\,x_3\,. \tag{3.6}$$

The complete displacement field $\boldsymbol{u}$ may be found by integrating eq. (3.5) as

$$\boldsymbol{u}\left(\boldsymbol{x}\right) = \underbrace{\boldsymbol{u}_0 + \mathbf{D}_{\mathrm{c}}\,\boldsymbol{x}}_{\text{affine part}} + \mathrm{Re}\sum_{\boldsymbol{k}\neq\boldsymbol{0}} \mathrm{e}^{i2\pi\boldsymbol{k}\cdot\boldsymbol{r}}\,\boldsymbol{u}^{\boldsymbol{k}}\left(x_2\right) = \boldsymbol{u}_{\mathrm{aff}}\left(\boldsymbol{x}\right) + \boldsymbol{u}_{\mathrm{dis}}\left(\boldsymbol{x}\right)\,, \tag{3.7}$$

where $\boldsymbol{u}_0$ is an arbitrary constant displacement. The complete displacement field $\boldsymbol{u}$ may be decomposed into an affine part $\boldsymbol{u}_{\mathrm{aff}}$ corresponding to $\mathbf{D}_{\mathrm{c}}$ and a biperiodic Fourier series representation of displacement fields $\boldsymbol{u}_{\mathrm{dis}}$ generated by the Volterra dislocations.

The Fourier amplitudes in eqs. (3.5) and (3.7) are determined from linear elasticity in the absence of body forces and subject to boundary conditions associated with interface dislocations. The complete displacement gradients $\mathbf{D}\left(\boldsymbol{x}\right) = \mathrm{grad}\;\boldsymbol{u}\left(\boldsymbol{x}\right)$ in crystals A and B must fulfill the partial differential equations of mechanical equilibrium

$$\mathrm{div}\left(\mathbb{C} : \mathrm{grad}\;\boldsymbol{u}\left(\boldsymbol{x}\right)\right) = \boldsymbol{0}\,, \tag{3.8}$$

where : denotes the double inner product and $\mathbb{C}$ is a fourth-order anisotropic elasticity tensor.

Complete field solutions

Substituting the displacement field eq. (3.7) into eq. (3.8), the second-order differential equation applied to both half-spaces is obtained as follows

$$w_1\mathbf{W}_1\,\boldsymbol{u}^{\boldsymbol{k}}\left(x_2\right) + w_2\left(\mathbf{W}_2 + \mathbf{W}_2^{\mathrm{t}}\right)\frac{\partial\,\boldsymbol{u}^{\boldsymbol{k}}\left(x_2\right)}{\partial\,x_2} + \mathbf{W}_3\,\frac{\partial^2\,\boldsymbol{u}^{\boldsymbol{k}}\left(x_2\right)}{\partial\,x_2^2} = \boldsymbol{0}\,. \tag{3.9}$$

with $w_1 = -4\pi^2$ and $w_2 = i2\pi$. Here, $^{\mathrm{t}}$ denotes the matrix transpose and $\mathbf{W}_1$, $\mathbf{W}_2$, and $\mathbf{W}_3$ are 3×3 real matrices related to the wavevectors (i.e. interface geometry) and the stiffness constants

(i.e. elasticity) indexed in Voigt notation:

$$\begin{aligned}
\mathbf{W}_1 = \mathbf{W}_1^{\mathrm{t}} &= \begin{bmatrix} k_1^2c_{11}+2k_1k_3c_{15}+k_3^2c_{55} & k_1^2c_{16}+k_1k_3(c_{14}+c_{56})+k_3^2c_{45} & k_1^2c_{15}+k_1k_3(c_{13}+c_{55})+k_3^2c_{35} \\ & k_1^2c_{56}+k_1k_3(c_{36}+c_{45})+k_3^2c_{34} & k_1^2c_{66}+2k_1k_3c_{46}+k_3^2c_{44} \\ \text{sym} & & k_1^2c_{55}+2k_1k_3c_{35}+k_3^2c_{33} \end{bmatrix} \\
\mathbf{W}_2 &= \begin{bmatrix} k_1c_{16}+k_3c_{56} & k_1c_{12}+k_3c_{25} & k_1c_{14}+k_3c_{45} \\ k_1c_{66}+k_3c_{46} & k_1c_{26}+k_3c_{24} & k_1c_{46}+k_3c_{44} \\ k_1c_{56}+k_3c_{36} & k_1c_{25}+k_3c_{23} & k_1c_{45}+k_3c_{34} \end{bmatrix} \\
\mathbf{W}_3 = \mathbf{W}_3^{\mathrm{t}} &= \begin{bmatrix} c_{66} & c_{26} & c_{46} \\ & c_{22} & c_{24} \\ \text{sym} & & c_{44} \end{bmatrix} .
\end{aligned} \tag{3.10}$$

As demonstrated in Appendix A from Ref. [260], the complete displacement field (3.7) is written as follows

$$\boldsymbol{u}(\boldsymbol{x}) = \boldsymbol{u}_0 + \mathbf{D}_{\mathrm{c}}\,\boldsymbol{x} + \mathrm{Re}\,\frac{1}{i2\pi}\sum_{\boldsymbol{k}\neq\mathbf{0}} \mathrm{e}^{i2\pi\boldsymbol{k}\cdot\boldsymbol{r}} \sum_{\alpha=1}^{3} \lambda^{\alpha}\mathrm{e}^{i2\pi p^{\alpha}x_2}\,\boldsymbol{a}^{\alpha} + \zeta^{\alpha}\mathrm{e}^{i2\pi p_*^{\alpha}x_2}\,\boldsymbol{a}_*^{\alpha}\,, \tag{3.11}$$

where the eigenvalues p^{α} and eigenvectors $\boldsymbol{a}^{\alpha}$ are calculated by solving the sextic algebraic equation of the Stroh formalism [234, 235] for each material A and B. The asterisk indicates complex conjugates of solutions with positive imaginary parts, i.e. $p^{\alpha+3} = p_*^{\alpha}$ and $\boldsymbol{a}^{\alpha+3} = \boldsymbol{a}_*^{\alpha}$, indexed by $\alpha = 1, 2, 3$. The complete elastic strains and stresses are also deduced from eq. (3.11) by

$$\begin{aligned}
\mathbf{E}(\boldsymbol{x}) &= \{\mathbf{D}(\boldsymbol{x})\} = \tfrac{1}{2}\left(\mathrm{grad}\,\boldsymbol{u}(\boldsymbol{x}) + \mathrm{grad}\,\boldsymbol{u}^{\mathrm{t}}(\boldsymbol{x})\right) \\
\boldsymbol{\sigma}(\boldsymbol{x}) &= \mathbb{C} : \mathbf{E}(\boldsymbol{x})\,,
\end{aligned} \tag{3.12}$$

respectively. Equation (3.12a) gives the strain-displacement relationship, where $\{\mathbf{D}(\boldsymbol{x})\}$ denotes the symmetric component of the distortion field, while eq. (3.12b) is the Hooke's law for small strains that determines the stress field. The general solutions of elastic fields of eqs. (3.11−3.12) are expressed as linear combinations of the eigenfunctions given by eq. (3.76), and include λ^{α} and ζ^{α} as complex unknown quantities that are to be determined by the boundary conditions, as follows.

Boundary condition 1: Convergence of far-field solutions

In accordance with Saint Venant's principle, the convergence of the Fourier amplitudes $\boldsymbol{u}^{\boldsymbol{k}}(x_2)$ when $x_2 \to \pm\infty$ leads to the requirement that ${}_{\mathrm{A}}\zeta^{\alpha} = 0$ and ${}_{\mathrm{B}}\lambda^{\alpha} = 0$. This condition applies to infinite bicrystals and would not be appropriate for bicrystals terminated with free-surfaces.

Boundary condition 2: Absence of far-field strains

The elimination of the coherency strains $\mathbf{E}_{\mathrm{c}}$ by the far-field strains of the interface Volterra dislocations $\mathbf{E}_{\mathrm{dis}}^{\infty}$ is taken into account by requiring the total elastic strain field $\mathbf{E}$ to decay to zero when $x_2 \to \pm\infty$, i.e.

$$\lim_{x_2\to\pm\infty} \mathbf{E}(\boldsymbol{x}) = \mathbf{E}^{\infty} = \mathbf{E}_{\mathrm{c}} + \mathbf{E}_{\mathrm{dis}}^{\infty} = \mathbf{0}\,, \tag{3.13}$$

where $\mathbf{E}_{\mathrm{c}} = \{\mathbf{D}_{\mathrm{c}}\}$ and $\mathbf{E}_{\mathrm{dis}}^{\infty} = \{\mathbf{D}_{\mathrm{dis}}^{\infty}\}$ is the far-field strain produced by the interface dislocations. Equation (3.13) is equivalent to eqs. (3.1) expressed using strains rather than stresses. As detailed in Appendix B from Ref. [260], the far-field distortions, calculated individually for each set of dislocations, $i = 1$ and 2, and then superposed, are given as follows

$$\mathbf{D}_{\mathrm{dis}}^{\infty} = -\mathrm{sgn}(x_2)\ \mathrm{Re}\sum_{i=1}^{2} d_i^{-1}\sum_{\alpha=1}^{3} \bar{\lambda}_i^{\alpha}\mathbf{G}_i^{\alpha} + \bar{\zeta}_i^{\alpha}\mathbf{G}_{i*}^{\alpha}\,. \tag{3.14}$$

Here, ${}_{\mathrm{A}}\bar{\zeta}_1^{\alpha} = {}_{\mathrm{A}}\bar{\zeta}_2^{\alpha} = 0$ and ${}_{\mathrm{B}}\bar{\lambda}_1^{\alpha} = {}_{\mathrm{B}}\bar{\lambda}_2^{\alpha} = 0$ for the reasons described in boundary condition 1. Superimposed bars are used to indicate quantities related to the far-field boundary conditions, while the complex constants ${}_{\mathrm{A}}\bar{\lambda}_i^{\alpha}$ and ${}_{\mathrm{B}}\bar{\zeta}_i^{\alpha}$ are determined by solving a specific system of equations, as described in Ref. [260].

Boundary condition 3: Disregistry due to interface Volterra dislocations

Disregistry is the discontinuity of displacements across an interface [7], expressed in terms of the relative displacements between neighboring atomic planes. Each dislocation produces a stepwise change in disregistry at its core with magnitude equals its Burgers vector. The disregistry at $x_2 = 0$ of a network of two sets of dislocations may be represented by the staircase functions

$$\Delta\boldsymbol{u}\left(x_1, x_3\right) = {}_{\mathrm{A}}\boldsymbol{u}\left(x_1, x_3\right) - {}_{\mathrm{B}}\boldsymbol{u}\left(x_1, x_3\right) = -\boldsymbol{b}_1\left\lceil\frac{\csc\phi\, x_1}{|\boldsymbol{p}_1^{\mathrm{o}}|}\right\rceil - \boldsymbol{b}_2\left\lceil\frac{x_3 - \operatorname{ctg}\phi\, x_1}{|\boldsymbol{p}_2^{\mathrm{o}}|}\right\rceil, \tag{3.15}$$

as illustrated in Fig. (3.3), where only one set has been displayed for clarity, for which the complete displacement discontinuity at the interface can therefore be expressed as

$$\Delta\boldsymbol{u}\left(x_1, x_3\right) = \Delta\boldsymbol{u}_{\mathrm{aff}}\left(x_1, x_3\right) + \Delta\boldsymbol{u}_{\mathrm{dis}}\left(x_1, x_3\right). \tag{3.16}$$

The left-hand side of eq. (3.16) gives the relative displacement field $\Delta\boldsymbol{u}_{\mathrm{aff}}$ at the interface generated by the uniform macroscopic distortions ${}_{\mathrm{A}}\mathbf{D}_{\mathrm{c}}$ and ${}_{\mathrm{B}}\mathbf{D}_{\mathrm{c}}$ in the affine form

$$\Delta\boldsymbol{u}_{\mathrm{aff}}\left(x_1, x_3\right) = \Delta\boldsymbol{u}_0 + [\![\left({}_{\mathrm{A}}\mathbf{D}_{\mathrm{c}} - {}_{\mathrm{B}}\mathbf{D}_{\mathrm{c}}\right)\boldsymbol{x}]\!]_{x_2=0}, \tag{3.17}$$

where $\Delta\boldsymbol{u}_0 = -\frac{1}{2}\left(\boldsymbol{b}_1 + \boldsymbol{b}_2\right)$ is chosen, without loss of generality. As shown in Fig. (3.3), eq. (3.17) may be interpreted as a continuous distribution of (fictitious) Volterra dislocations with infinitesimal Burgers vectors and spacing [30, 195].

The right-hand side of eq. (3.16) is the displacement discontinuity $\Delta\boldsymbol{u}_{\mathrm{dis}}$ produced by equilibrium interface dislocations in the natural state, shown as Δ in Fig. (3.1). According to eqs. (3.7) and (3.11), the quantity $\Delta\boldsymbol{u}_{\mathrm{dis}}$ is given in Ref. [260]

$$\Delta\boldsymbol{u}_{\mathrm{dis}}\left(x_1, x_3\right) = \frac{1}{i2\pi}\sum_{\boldsymbol{k}\neq\boldsymbol{0}} \mathrm{e}^{i2\pi\boldsymbol{k}\cdot\boldsymbol{r}} \sum_{\alpha=1}^{3} {}_{\mathrm{A}}\lambda^{\alpha}\,{}_{\mathrm{A}}\boldsymbol{a}^{\alpha} - {}_{\mathrm{B}}\zeta^{\alpha}\,{}_{\mathrm{B}}\boldsymbol{a}_{*}^{\alpha}, \tag{3.18}$$

which may be represented by sawtooth functions [87, 34, 90], as illustrated in Fig. (3.3). Using the Fourier sine series analysis and superposing the sawtooth-shaped functions associated with the two sets of dislocations, eq. (3.18) can be expressed as

$$\Delta\boldsymbol{u}_{\mathrm{dis}}\left(x_1, x_3\right) = \underbrace{\sum_{n=1}^{\infty} -\frac{\boldsymbol{b}_1}{n\pi}\sin 2\pi n\frac{\csc\phi\, x_1}{|\boldsymbol{p}_1^{\mathrm{o}}|}}_{\text{set 1}} + \underbrace{\sum_{m=1}^{\infty} -\frac{\boldsymbol{b}_2}{m\pi}\sin 2\pi m\frac{x_3 - \operatorname{ctg}\phi\, x_1}{|\boldsymbol{p}_2^{\mathrm{o}}|}}_{\text{set 2}}. \tag{3.19}$$

Thus, the boundary condition in eq. (3.19) for equilibrium interface dislocations, combined with eq. (3.18), leads a set of 6 linear equations:

$$\Sigma_1 : \begin{cases} \mathrm{Re}\displaystyle\sum_{\alpha=1}^{3} {}_{\mathrm{A}}\lambda^{\alpha}\,{}_{\mathrm{A}}\boldsymbol{a}^{\alpha} - {}_{\mathrm{B}}\zeta^{\alpha}\,{}_{\mathrm{B}}\boldsymbol{a}_{*}^{\alpha} = \boldsymbol{\vartheta} \\ \mathrm{Im}\displaystyle\sum_{\alpha=1}^{3} {}_{\mathrm{A}}\lambda^{\alpha}\,{}_{\mathrm{A}}\boldsymbol{a}^{\alpha} - {}_{\mathrm{B}}\zeta^{\alpha}\,{}_{\mathrm{B}}\boldsymbol{a}_{*}^{\alpha} = \boldsymbol{0}, \end{cases} \tag{3.20}$$

where Im stands for the imaginary part of a complex quantity and $\boldsymbol{\vartheta}$ is given by

$$\boldsymbol{\vartheta} = \begin{cases} -\dfrac{\boldsymbol{b}_1}{n} & \text{if } m = 0 \qquad (n \geq 1) \\ -\dfrac{\boldsymbol{b}_2}{m} & \text{if } n = 0 \qquad (m \geq 1) \\ \mathbf{0} & \text{if } nm \neq 0 \quad (n, m \geq 1)\,. \end{cases} \tag{3.21}$$

Boundary condition 4: No net tractions along the interfaces

The solution must satisfy the traction-free boundary condition along the interfaces:

$$_{\mathrm{A}}\boldsymbol{\sigma}\,(x_1,\, 0,\, x_3)\,\boldsymbol{n} = {}_{\mathrm{B}}\boldsymbol{\sigma}\,(x_1,\, 0,\, x_3)\,\boldsymbol{n}\,, \tag{3.22}$$

where $\boldsymbol{\sigma}\,(x_1,\, 0,\, x_3)$ is reduced to the short-range stress field produced by the interface equilibrium dislocations when eqs. (3.1) are satisfied. In that case, the tractions at the interface read

$$\boldsymbol{\sigma}\,(x_1,\, 0,\, x_3)\,\boldsymbol{n} = \mathrm{sgn}\,(x_2) \sum_{\boldsymbol{k} \neq \mathbf{0}} \mathrm{e}^{i2\pi \boldsymbol{k}\cdot\boldsymbol{r}} \sum_{\alpha=1}^{3} \lambda^{\alpha} \boldsymbol{h}^{\alpha} + \zeta^{\alpha} \boldsymbol{h}^{\alpha}_{*}\,, \tag{3.23}$$

where the subsidiary complex vectors $\boldsymbol{h}^{\alpha}$ are related to the vectors $\boldsymbol{a}^{\alpha}$ by

$$\boldsymbol{h}^{\alpha} = \left(\mathbf{W}_2^{\mathsf{t}} + p^{\alpha}\,\mathbf{W}_3\right)\boldsymbol{a}^{\alpha} = -{p^{\alpha}}^{-1}\left(\mathbf{W}_1 + p^{\alpha}\,\mathbf{W}_2\right)\boldsymbol{a}^{\alpha}\,, \tag{3.24}$$

with $h^{\alpha}_{k} = H^{\alpha}_{k2}$. Boundary condition in eq. (3.22) together with eq. (3.23) leads the additional system of 6 linear equations:

$$\Sigma_2 : \begin{cases} \mathrm{Re} \sum_{\alpha=1}^{3} {}_{\mathrm{A}}\lambda^{\alpha}\,{}_{\mathrm{A}}\boldsymbol{h}^{\alpha} - {}_{\mathrm{B}}\zeta^{\alpha}\,{}_{\mathrm{B}}\boldsymbol{h}^{\alpha}_{*} = \mathbf{0} \\ \mathrm{Im} \sum_{\alpha=1}^{3} {}_{\mathrm{A}}\lambda^{\alpha}\,{}_{\mathrm{A}}\boldsymbol{h}^{\alpha} - {}_{\mathrm{B}}\zeta^{\alpha}\,{}_{\mathrm{B}}\boldsymbol{h}^{\alpha}_{*} = \mathbf{0}\,. \end{cases} \tag{3.25}$$

The two latter conditions 3. and 4. may be rewritten in a eigenvalue problem for equilibrium interface dislocation arrays. Indeed, the elastic fields of these dislocations in an anisotropic bicrystal free of far-field strains are given in terms of the 12 eigenvalues Eval and 12 corresponding eigenvectors Evec with $\alpha = 1, 2, 3$, i.e.

$$\begin{aligned} \mathrm{Eval} &= \{\, \mathrm{Re}\,{}_{\mathrm{A}}p^{\alpha},\, \mathrm{Im}\,{}_{\mathrm{A}}p^{\alpha},\, \mathrm{Re}\,{}_{\mathrm{B}}p^{\alpha},\, \mathrm{Im}\,{}_{\mathrm{B}}p^{\alpha} \,\} \\ \mathrm{Evec} &= \{\, {}_{\mathrm{A}}\boldsymbol{a}^{\alpha},\, {}_{\mathrm{B}}\boldsymbol{a}^{\alpha},\, {}_{\mathrm{A}}\boldsymbol{h}^{\alpha},\, {}_{\mathrm{B}}\boldsymbol{h}^{\alpha} \,\}\,. \end{aligned} \tag{3.26}$$

All these quantities are determined by solving a 6-dimensional eigenvalue problem that may be recast with the aid of eqs. (3.24) into the form

$$\mathbb{N} \begin{bmatrix} \boldsymbol{a}^{\alpha} \\ \boldsymbol{h}^{\alpha} \end{bmatrix} = p^{\alpha} \begin{bmatrix} \boldsymbol{a}^{\alpha} \\ \boldsymbol{h}^{\alpha} \end{bmatrix} \tag{3.27}$$

where the real nonsymmetric 6×6 matrices $\mathbb{N}$ depend on the wavevectors and the stiffness constants for crystals A and B through the $\mathbf{W}$ matrices given by eqs. (3.10), i.e.

$$\mathbb{N} = \begin{bmatrix} -\mathbf{W}_3^{-1}\,\mathbf{W}_2^{\mathsf{t}} & \mathbf{W}_3^{-1} \\ -\mathbf{W}_1 + \mathbf{W}_2\,\mathbf{W}_3^{-1}\,\mathbf{W}_2^{\mathsf{t}} & -\mathbf{W}_2\,\mathbf{W}_3^{-1} \end{bmatrix}. \tag{3.28}$$

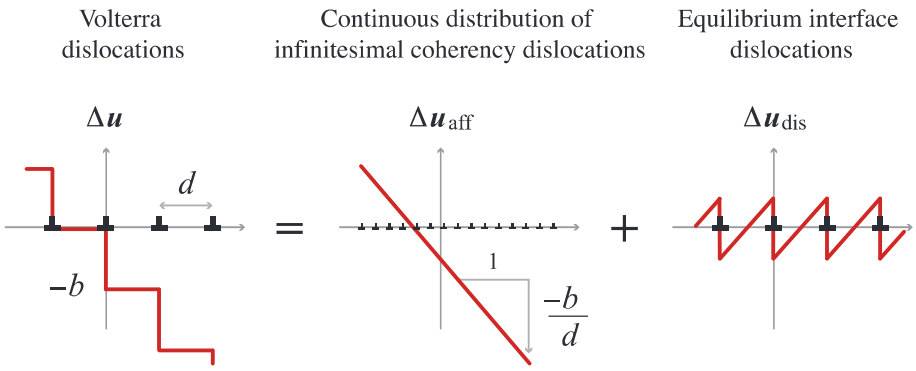

FIGURE 3.3: The disregistry $\Delta \boldsymbol{u}$ due to interface Volterra dislocations is a staircase function. It may be decomposed into an affine part $\Delta \boldsymbol{u}_{\text{aff}}$ generated by a uniform distortion (represented by a continuous distribution of fictitious infinitesimal dislocations) and a sawtooth function $\Delta \boldsymbol{u}_{\text{dis}}$ associated with the equilibrium interface dislocations in the natural state.

Properties		Materials				
Symbol	Unit	Cu	Nb	Fe	Al	Ni
a	Å	3.615	3.301	2.866	4.050	3.524
c_{11}	GPa	168.4	246.0	242.0	108.2	246.5
c_{12}	GPa	121.4	134.0	146.5	61.3	147.3
c_{44}	GPa	75.4	28.7	112.0	28.5	124.7

TABLE 3.1: Material properties for copper, niobium, iron, aluminium, and nickel. The values of lattice parameters a for all materials are those listed by Gray [104] and elastic components c_{11}, c_{12}, and c_{44} by Hirth and Lothe [7].

Finally, the linear systems Σ_1 and Σ_2 are solved numerically to determine the 12 real constants Ecst, i.e.

$$\text{Ecst} = \{ \operatorname{Re}_{\text{A}}\lambda^{\alpha}, \operatorname{Im}_{\text{A}}\lambda^{\alpha}, \operatorname{Re}_{\text{B}}\zeta^{\alpha}, \operatorname{Im}_{\text{B}}\zeta^{\alpha} \} \,, \tag{3.29}$$

completing the solutions of the elastic fields.

3.2.6 Interface elastic strain energy

Using the divergence theorem, the elastic strain energy γ_{e} of equilibrium interface dislocation arrays may be expressed as a surface integral over a unit cell A of the interface dislocation network, i.e.

$$\gamma_{\text{e}}(r_0) = \frac{1}{2A} \iint_{A(r_0)} \boldsymbol{\sigma}(x_1, 0, x_3)\, \boldsymbol{n} \cdot \Delta \boldsymbol{u}_{\text{dis}}(x_1, x_3)\; dS \,, \tag{3.30}$$

where $\boldsymbol{\sigma}(x_1, 0, x_3)\, \boldsymbol{n}$ is the total traction vector produced at the interface of interest. Stress fields at dislocation cores diverge, so regions near the cores must be excluded from the integral in eq. (3.30). Following standard practice [7], the domain of integration is limited to parts of the interface unit cell that are not within a pre-determined cutoff distance r_0 of the dislocation cores.

3.3 Symmetric example applications

The model described in the forgoing sections is applied to simple example interfaces: symmetric tilt and twist GBs as well as a pure misfit heterophase interface. The materials properties used in these examples are listed in Table 3.1.

3.3.1 Pure tilt grain boundary

Tilt boundaries that contain one set of interfacial dislocations have been discussed extensively [237]. To illustrate and validate the present method, a symmetrical tilt boundary with [001] tilt axis and tilt angle $\theta = 2^\circ$ is analyzed in detail. The calculations are carried out for Cu, which has a moderately high anisotropy ratio, $A_{\text{Cu}} = 2c_{44}/(c_{11} - c_{12}) = 3.21$. The boundary consists of one set of straight parallel dislocations with Burgers vector content $\boldsymbol{B}$, expressed as

$$\boldsymbol{B} = \left(\frac{\boldsymbol{n}\times\boldsymbol{\xi}}{d}\cdot\boldsymbol{p}\right)\boldsymbol{b} = \underbrace{\left(\mathbf{R}_+^{-1} - \mathbf{R}_-^{-1}\right)}_{\mathbf{T}}\boldsymbol{p} = 2\sin\theta/2\ \boldsymbol{p}\times\boldsymbol{\omega}\,. \tag{3.31}$$

Here, the "median lattice" is used as the obvious reference state: the mapping matrices $\mathbf{F}$ have been replaced by rotation matrices $\mathbf{R}$, with $\mathbf{R}_+$ representing a rotation of the upper crystal by angle $\theta_+ = \theta/2$ about the tilt axis and $\mathbf{R}_-$ the rotation $\theta_- = -\theta/2$ of the adjacent lower crystal. Equation (3.31) is known as Frank's formula [91, 48], which gives the density of interface dislocations needed to create the tilt boundary. Selecting $\boldsymbol{b} = a_{\text{Cu}}\,[010] \parallel \boldsymbol{n}$, eq. (3.31) shows that $\boldsymbol{\xi} = [001]$ and $d = 10.3567$ nm.

As expected, the far-field stresses vanish for this choice of reference lattice, and only non-zero stresses are short-ranged. Figure (3.4) plots interface stresses as a function of x_1 and x_2 (the stresses are invariant along the dislocation line direction, $\boldsymbol{x}_3$). The red contour illustrates where the stresses fall to zero when $|x_2| \geq 7 - 10$ nm (depending on the stress components), showing that their range is comparable to the dislocation spacing. The far-field rotations may be calculated from the antisymmetric part of the far-field distortions, i.e. $\boldsymbol{\Omega}^\infty = \}\mathbf{D}^\infty_{\text{dis}}\{$. They satisfy $\boldsymbol{\Omega}^\infty_+ - \boldsymbol{\Omega}^\infty_- = \mathbf{T}$ and yield a net non-vanishing rotation about the tilt axis, as excepted [180, 121]:

$$\boldsymbol{\omega} = \boldsymbol{\omega}^\infty_+ - \boldsymbol{\omega}^\infty_- = -\begin{pmatrix}0\\0\\0.03490\end{pmatrix} = -\frac{\boldsymbol{x}_1\times\boldsymbol{b}}{d}\,. \tag{3.32}$$

The disregistry Δu_2 and the displacement discontinuity $\Delta u_{2\,\text{dis}}$ associated with the Volterra and equilibrium tilt boundary dislocations are plotted in Fig. (3.5a). They are in good quantitative agreement with the applied boundary conditions, represented by staircase and sawtooth curves.

The average elastic energy per unit interface area γ_{e} is determined for several values of the core cutoff parameter r_0. Following eq. (3.30), γ_{e} may be written as

$$\gamma_{\text{e}}\,(r_0) = \frac{1}{2\,d}\int_{r_0}^{d-r_0} \underbrace{\sigma_{22}\,(x_1,\,0,\,0)\ \Delta u_{2\,\text{dis}}\,(x_1,\,0)}_{W}\ dx_1\,. \tag{3.33}$$

The variation of stress component σ_{22} at $x_2 = 0$ with x_1 is plotted as a black line in Fig. (3.5b). The core region is shaded in grey. Local contributions to the interface elastic energy W (values of the integrand in eq. (3.33)) are plotted in red. The average elastic energy per unit interface area will depend on the choice of r_0. For example, $\gamma_{\text{e}} = 142.8$ mJ.m^{-2} with $r_0 = b/2$ and $\gamma_{\text{e}} = 167.8$ mJ.m^{-2} with $r_0 = b/3$, where b is the magnitude of $\boldsymbol{b}$. An appropriate r_0 value is selected by comparing the interface elastic energies computed with the present dislocation-based method to experimentally measured energies of small angle [001] tilt boundaries [102], plotted as solid triangles in Fig. (3.6). The calculations using $r_0 = b/2$ are in good agreement with the experiments up to $\sim 5^\circ$ while $r_0 = b/3$ fits better in the range of $\sim 5 - 12^\circ$. The classical energy per unit area given by Read and Shockley [213], $E_{\text{RS}}\,(\theta) = 1450\ \theta\,(-3 - \ln\theta)$ mJ.m^{-2}, is also shown in Fig. (3.6). It compares well with the calculations for $r_0 = b/3$.

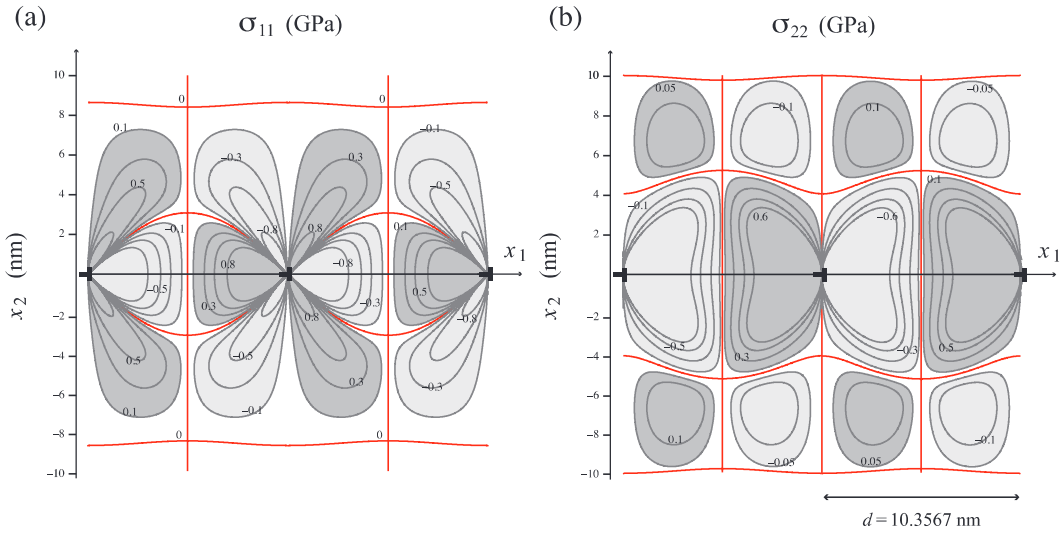

FIGURE 3.4: Contour plots of stress components (a) σ_{11} and (b) σ_{22}, for the 2° symmetric tilt boundary described in the text. The negative values (compression) are plotted in light grey, and the positive values (extension) in dark grey. The stresses decay away over distances comparable to the interface dislocation spacing. In red, the stress field values are equal to zero.

3.3.2 Twist grain boundary

As shown in Fig. (3.7a), small-angle (010) twist GBs contain two sets of dislocations, so their dislocation content $\boldsymbol{B}$ is expressed as

$$\boldsymbol{B} = \left(\frac{\boldsymbol{n}\times\boldsymbol{\xi}_1}{d_1}\cdot\boldsymbol{p}\right)\boldsymbol{b}_1 + \left(\frac{\boldsymbol{n}\times\boldsymbol{\xi}_2}{d_2}\cdot\boldsymbol{p}\right)\boldsymbol{b}_2 = \left(\mathbf{R}_+^{-1} - \mathbf{R}_-^{-1}\right)\boldsymbol{p}\,. \tag{3.34}$$

The twist boundaries of angle $\theta = 2°$ is considered in Cu, where the rotation axis is perpendicular to the boundary, $\boldsymbol{\omega} = \boldsymbol{x}_2 = [010]$. As in the case of the tilt boundary, the obvious reference state for twist boundaries is the "median lattice" suggested by Frank [92]. In this state, the total rotation across the boundary is equally partitioned between the two grains. However, to illustrate the importance of selecting the correct reference state, other possible reference states are considered. A common choice is to use of the adjacent crystal grains as the reference state. There is a continuum of other possible reference states between these two extremes, and the angle $\theta_c = -\kappa\,\theta$ is introduced to define the rotation of the reference state from the case where the upper crystal above the boundary has been chosen as the reference lattice. Here, κ is a dimensionless parameter that varies from 0 to 1. Equipartitioning of rotations between the adjacent crystals (i.e. the "median lattice") occurs when $\kappa = 1/2$.

Section 3.2.3 demonstrated that interface dislocation geometry is independent of reference state. In this example, the twist boundary contains an orthogonal grid of dislocations with line directions $\boldsymbol{\xi}_1 = 1/\sqrt{2}\,[\bar{1}01]$ and $\boldsymbol{\xi}_2 = 1/\sqrt{2}\,[101]$. The spacings between successive parallel dislocations are $d_1 = d_2 = d = 7.3233$ nm. Because of the pure twist misorientations, the coherency stress fields are zero for all possible reference states. Figure (3.7b) plots the dependence of non-vanishing far-field stress components on κ. If a reference state with $\kappa = 0$ is chosen, then the interface dislocations deviate by 1° from pure screw character and possess non-zero far-field stress components $\sigma^{\infty}_{11+} = \sigma^{\infty}_{33+}$ and $\sigma^{\infty}_{11-} = \sigma^{\infty}_{33-}$. This demonstrates that $\kappa = 0$ does not represent the correct reference state since eqs. (3.1) (and eqs. (3.13) via eq. (3.12b)) are not satisfied. Furthermore, the far-field rotation with $\kappa = 0$ does not equal 2°, but discrepancies on the order of 0.001° between the rotation vector component and the prescribed misorientation are found. As κ increases, the

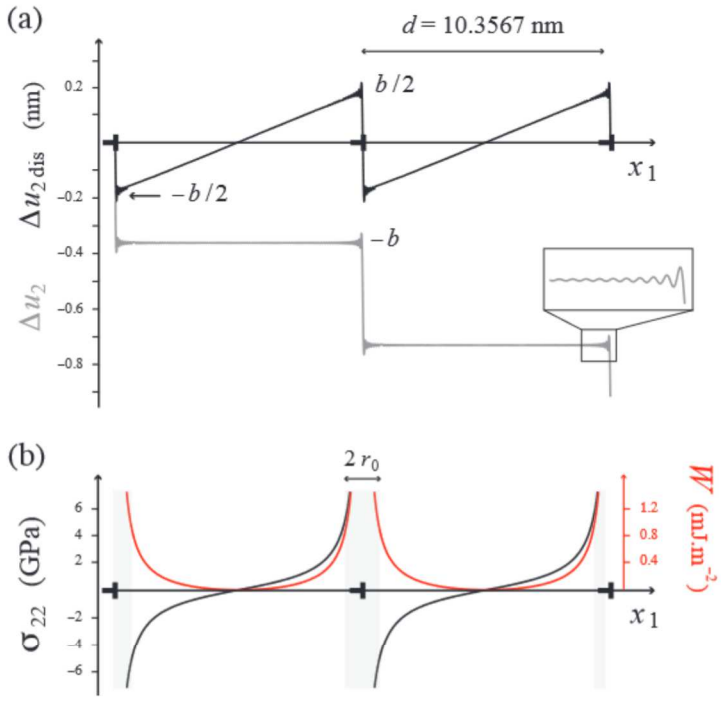

FIGURE 3.5: (a) Disregistries Δu_2 (staircase function) and $\Delta u_{2\,\mathrm{dis}}$ (sawtooth function) computed using 100 harmonics for the 2° symmetric tilt boundary described in the text. (b) Stress distribution σ_{22} and local elastic energy density γ_e at the GB.

far-field stresses decrease and eventually reach zero at $\kappa = 1/2$, as expected. The interface dislocations have perfect screw characters for this reference state, where non-zero far-field stresses are again obtained when κ is increased beyond $\kappa = 1/2$.

Taking $\kappa = 1/2$, the elastic strain energy per unit area γ_e is calculated for the twist GB using the expression:

$$\gamma_\mathrm{e}\,(r_0) = \frac{1}{2\,A} \iint_{r_0}^{d-r_0} \left(W_{(1)} + W_{(2)} + W_{(1-2)}\right)\, dx_1\, dx_3\,, \tag{3.35}$$

with $A = |\boldsymbol{p}_1^\mathrm{o} \times \boldsymbol{p}_2^\mathrm{o}|$ the area of the interface unit cell. Equation (3.35) is decomposed into self-energy densities $W_{(1)}$ and $W_{(2)}$ for each set of parallel dislocations and the interaction energy density $W_{(1-2)}$ between the two sets. These energies are obtained from the separate elasticity solutions for each set of dislocations:

$$\begin{aligned} W_{(1)} + W_{(2)} &= \sigma_{23\,(1)}(x_1,\,0,\,0)\;\Delta u_{3\,\mathrm{dis}\,(1)}(x_1,\,0) + \sigma_{12\,(2)}(0,\,0,\,x_3)\;\Delta u_{1\,\mathrm{dis}\,(2)}(0,\,x_3) \\ W_{(1-2)} &= \sigma_{23\,(1)}(x_1,\,0,\,0)\;\Delta u_{1\,\mathrm{dis}\,(2)}(0,\,x_3) + \sigma_{12\,(2)}(0,\,0,\,x_3)\;\Delta u_{3\,\mathrm{dis}\,(1)}(x_1,\,0)\,. \end{aligned} \tag{3.36}$$

The local self- and interaction energies are shown in Figs. (3.8a) and (b), respectively. The integral of the interaction energy $W_{(1-2)}$ over area A is zero for any value r_0, in agreement with the classical dislocation theory result that orthogonal screw dislocations do not exert any forces on each other [7]. The total elastic energy is plotted in Fig. (3.9) as a function of the twist angle up to 12° for three core cutoff parameters: $r_0 = b_1/2$, $r_0 = b_1/3$, and $r_0 = b_1/4$.

3.3.3 Pure misfit interface

Lastly, the model is illustrated on an Al/Ni heterophase interface. The terminal planes of both adjacent crystals are fcc (010) planes. The [100] and [001] directions of both crystals are parallel in the interface plane. Thus, the interface is in the cube-on-cube orientation and contains two sets of

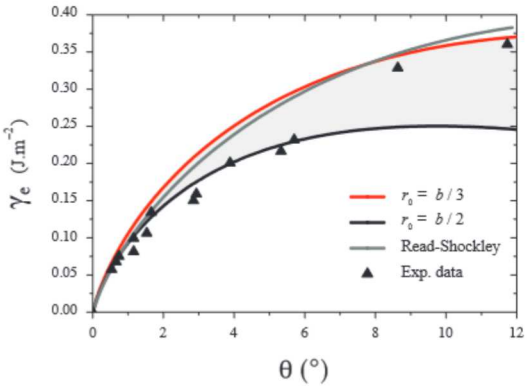

FIGURE 3.6: Interface elastic energies γ_e computed using two different core cutoff parameters r_0 for a [001] tilt GB in Cu as a function of the tilt angle θ. The gray line shows the Read-Shockley solution. Experimental values are shown with solid triangles [102].

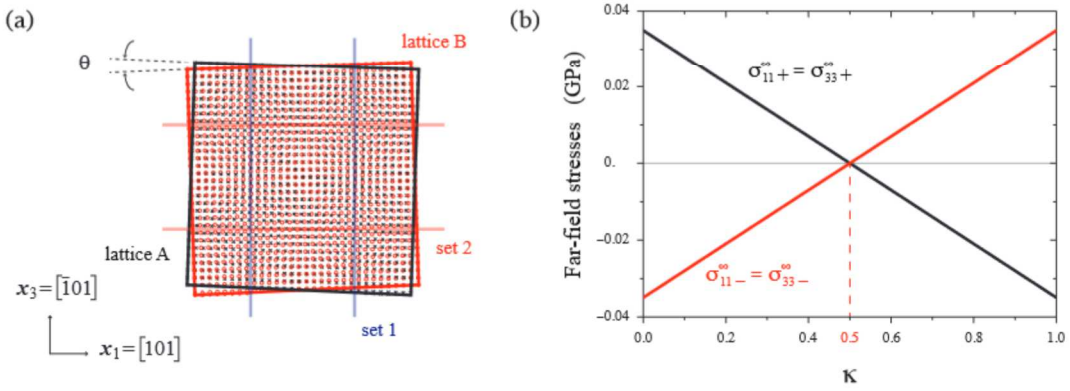

FIGURE 3.7: (a) Small-angle twist GB on a (010) plane containing two sets of orthogonal dislocations. (b) Dependence of far-field stresses on κ for the 2° twist boundary described in the text.

parallel dislocations. Following eq. (3.2), the Burgers vector content $\boldsymbol{B}$ is written as

$$\boldsymbol{B} = \left(\frac{\boldsymbol{n}\times\boldsymbol{\xi}_1}{d_1}\cdot\boldsymbol{p}\right)\boldsymbol{b}_1 + \left(\frac{\boldsymbol{n}\times\boldsymbol{\xi}_2}{d_2}\cdot\boldsymbol{p}\right)\boldsymbol{b}_2 = \underbrace{\left({}_{\mathrm{Al}}\mathbf{S}^{-1}(r_{\mathrm{Al}}) - {}_{\mathrm{Ni}}\mathbf{S}^{-1}(r_{\mathrm{Ni}})\right)}_{\mathbf{T}}\boldsymbol{p}\,. \tag{3.37}$$

The reference state for this interface is a crystal oriented identically to the Al and Ni in their natural state, but strained such that its lattice constant in the interface plane is a_c, with $a_{\mathrm{Ni}} \leq a_c \leq a_{\mathrm{Al}}$. Only strains within the interface are necessary to ensure coherency: normal strains are not required. Thus, the matrix $\mathbf{T}$ in eq. (3.37) is composed of two equibiaxial stretch matrices (no rotations), ${}_{\mathrm{Al}}\mathbf{S}^{-1} = {}_{\mathrm{Al}}\mathbf{E}_c + \mathbf{I}$ and ${}_{\mathrm{Ni}}\mathbf{S}^{-1} = {}_{\mathrm{Ni}}\mathbf{E}_c + \mathbf{I}$, where $\mathbf{I}$ represents the identity matrix. These mapping matrices depend on the ratios of lattice parameters between Al and Ni in their natural and reference states, $r_{\mathrm{Al}} = a_{\mathrm{Al}}/a_c \geq 1$ and $r_{\mathrm{Ni}} = a_{\mathrm{Ni}}/a_c \leq 1$. The matrix $\mathbf{T}$ in eq. (3.37) may also be rewritten as the difference between the coherency strains prescribed in Al and Ni:

$${}_{\mathrm{Al}}\mathbf{E}_c - {}_{\mathrm{Ni}}\mathbf{E}_c = \mathbf{T}\,. \tag{3.38}$$

Following the procedure described in section 3.2.4, Ni is initially chosen as the reference lattice, so that $r_{\mathrm{Al}} = a_{\mathrm{Al}}/a_{\mathrm{Ni}}$ and $r_{\mathrm{Ni}} = 1$, and identify $\breve{\boldsymbol{b}}_1 = a_{\mathrm{Ni}}/\sqrt{2}\,[101]$ and $\breve{\boldsymbol{b}}_2 = a_{\mathrm{Ni}}/\sqrt{2}\,[10\bar{1}]$. Then, using eq. (3.3), an interface that consists of an orthogonal grid of edge dislocations with $\boldsymbol{\xi}_1 = 1/\sqrt{2}\,[\bar{1}01]$

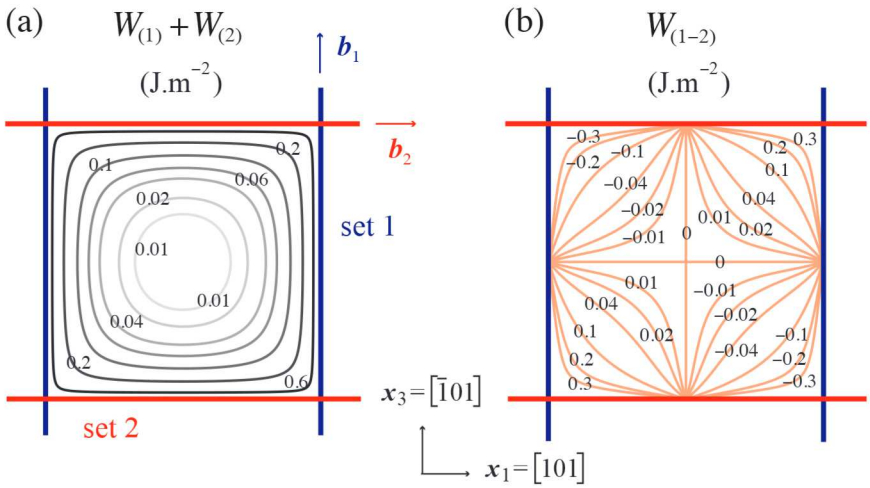

FIGURE 3.8: Local (a) self- $\{W_{(1)}+W_{(2)}\}$ and (b) interaction $W_{(1-2)}$ elastic energies arising from two sets of orthogonal screw dislocations in a 2° twist boundary on a (010) plane in Cu.

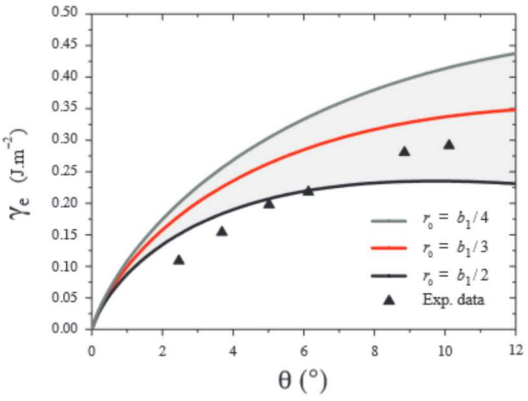

FIGURE 3.9: Elastic energies per unit area γ_e as a function of the rotation angle θ of twist GBs along (010) planes in Cu for three core cutoff parameters r_0.

and $\boldsymbol{\xi}_2 = 1/\sqrt{2}\,[101]$ is found, and the corresponding dislocation spacings $d_1 = d_2 = 1.902$ nm. Using this choice of reference state, the far-field strains produced by the interface dislocations are:

$$ {}_{\text{Al}}\mathbf{E}^{\infty}_{\text{dis}} = \begin{bmatrix} 0.10133 & 0 & 0 \\ 0 & 0 & 0 \\ 0 & 0 & 0.10133 \end{bmatrix}, \text{ and, } {}_{\text{Ni}}\mathbf{E}^{\infty}_{\text{dis}} = \begin{bmatrix} -0.03243 & 0 & 0 \\ 0 & 0 & 0 \\ 0 & 0 & -0.03243 \end{bmatrix}, \tag{3.39} $$

such that the matrices in eqs. (3.39) satisfy

$$ -\left({}_{\text{Al}}\mathbf{E}^{\infty}_{\text{dis}} - {}_{\text{Ni}}\mathbf{E}^{\infty}_{\text{dis}}\right) = \mathbf{T}\,. \tag{3.40} $$

Combining eqs. (3.38) and (3.40), it follows

$$ {}_{\text{Al}}\mathbf{E}_{\text{c}} + {}_{\text{Al}}\mathbf{E}^{\infty}_{\text{dis}} = \underbrace{{}_{\text{Ni}}\mathbf{E}_{\text{c}}}_{=\mathbf{0}} + {}_{\text{Ni}}\mathbf{E}^{\infty}_{\text{dis}} = \begin{bmatrix} -0.03243 & 0 & 0 \\ 0 & 0 & 0 \\ 0 & 0 & -0.03243 \end{bmatrix} \neq \mathbf{0} \quad \left(\Leftrightarrow \; {}_{\text{Al}}\mathbf{E}^{\infty} = {}_{\text{Ni}}\mathbf{E}^{\infty}\right), \tag{3.41} $$

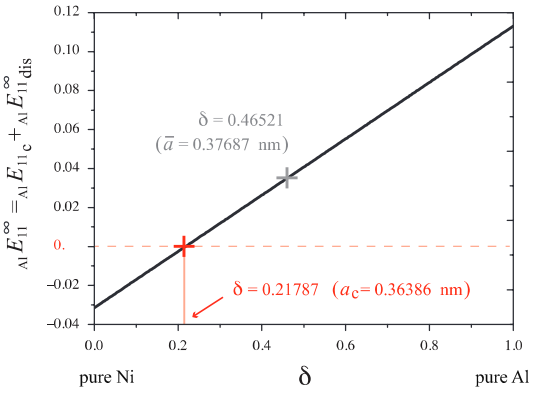

FIGURE 3.10: Dependence of the total far-field strain component ${}_{Al}\mathbf{E}_{11}^{\infty}$ in Al on δ for a Al/Ni heterophase interface. The red dotted line gives the unique reference state, for which the far-field decay to zero and the coherent parameter a_c is defined. The lattice parameter $\bar{a} = 2a_{Al}\,a_{Ni} / (a_{Al} + a_{Ni})$, which is a good approximation for an interface between crystals of different lattice parameters but identical elastic constants [93, 131], is marked by a grey cross symbol.

with ${}_{Ni}\mathbf{E}_c = \mathbf{0}$ here, because Ni has been chosen as the reference lattice. However, according to eq. (3.41b), condition 2. given by eq. (3.13) is not satisfied since the total far-field strains in each individual material do not decay to zero when $x_2 \to \pm\infty$. This demonstrates that the initial choice of reference state is not correct.

To find the correct reference state, a variable δ, with $0 \leq \delta \leq 1$ that interpolates a_c between a_{Al} and a_{Ni} is introduced as follows

$$a_c = \delta a_{Al} + (1 - \delta)\, a_{Ni}\,. \tag{3.42}$$

It is shown that the far-field strains in Al and Ni are equal for all δ, so that eq. (3.41a) is always satisfied, i.e. ${}_{Al}\mathbf{E}^{\infty} = {}_{Ni}\mathbf{E}^{\infty}$ with ${}_{Ni}\mathbf{E}_c = \mathbf{0}$ if $\delta = 0$, and ${}_{Al}\mathbf{E}_c = \mathbf{0}$ if $\delta = 1$. However, only one unique reference state (corresponding to an unique value of δ) gives vanishing far-field strains in the bicrystal in its natural state by satisfying eq. (3.13) as well. The pure misfit interface example serves to show that eq. (3.41a) is a necessary, but not sufficient condition for determining the reference state.

The total far-field strain component ${}_{Al}\mathbf{E}_{11}^{\infty}$ in Al is plotted in Fig. (3.10) as a function of δ and is identical to the component ${}_{Al}\mathbf{E}_{33}^{\infty}$, according to the interface symmetry (all other strain components are zero). Because eq. (3.41a) is verified for all δ, the same components in Ni give the same plot as in Fig. (3.10). The far-field strains vary linearly with δ and become zero when $\delta = 0.21787$, so that $a_c = 0.36386$ nm. This value of a_c is the unique coherent reference state for which the pure misfit Al/Ni interface of interest is consistent with the Frank-Bilby equation. It is closer to a_{Ni} than to a_{Al} because Ni is the stiffer of these two materials and so carries a lower coherency strain in the reference state. The far-field rotations are zero for all values of δ, as excepted.

To demonstrate the errors that come about from ignoring the unequal partitioning of elastic fields and to validate the current calculation, a_c is recomputed under the assumption that both sides of the interface have the same stiffness (equal to that of Al or Ni), but different natural lattice parameters (a_{Al} and a_{Ni}, as the original calculation). For this case, the calculated value for a_c is in very good agreement with the well-known approximate result $\bar{a} = 2a_{Al}\,a_{Ni} / (a_{Al} + a_{Ni}) = 0.37687$ nm [93, 131], corresponding to $\delta = 0.46521$. This value, however, is far from the correct lattice parameter of the reference state when the differing stiffnesses of Al and Ni are taken into account, as illustrated by cross symbols in Fig. (3.10). It is also shown that $\bar{a}$ deviates from the prediction and is not consistent with the Frank-Bilby equation when the heterogeneous distortions of bicrystals are explicitly described at equilibrium.

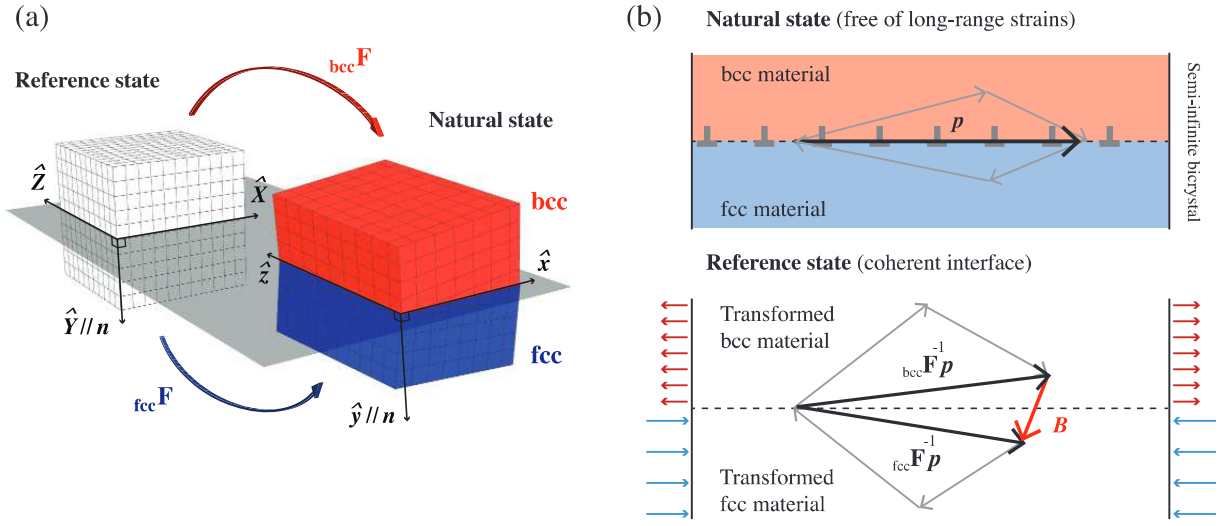

FIGURE 3.11: (a) The reference and natural states of an interface are related by transformation matrices $_{fcc}\mathbf{F}$ and $_{bcc}\mathbf{F}$. (b) The correspondence between a closed right-handed circuit enclosing the probe vector $\boldsymbol{p}$ in the natural state and its corresponding path with closure failure $\boldsymbol{B}$ in the reference state.

3.4 Partitioning of elastic distortions at fcc/bcc interfaces

In this section, the study is focused on semicoherent heterophase interfaces comprised of two sets of dislocations and formed along closest-packed planes in fcc/bcc bimetals, especially for fcc{111}/bcc{110} (Cu/Nb, Ag/V, and Cu/Mo) interfaces in the Nishiyama-Wassermann (NW) orientation relations (OR) [279, 192] as well as in ORs that differ from the NW by an in-plane twist rotation. It is showed that elastic distortions, i.e. strains as well as tilt and twist rotations, are in general unequally partitioned at such interfaces. The correct partitioning of these fields determines the coherent reference state for which the bicrystal of interest is free of far-field strains. Using these results, the stress fields generated by misfit dislocation patterns are computed and analyzed for the Cu/Nb system in the NW and Kurdjumov-Sachs (KS) [154] ORs. The dislocation structure (i.e. the Burgers vectors, spacings, and line directions) is also determined in lowest strain energy solutions of the Frank-Bilby equation along a specific transformation pathway between the NW and KS ORs.

Similarly to Fig. (3.1), the concept of reference and natural states of an interface is depicted in Fig. (3.11). The natural state contains an interface formed by joining two crystals with prescribed misorientation and interface planes as well as vanishing far-field strains. This state is also related to a single crystal, coherent reference state by uniform displacement gradients $_{A}\mathbf{F} = {}_{fcc}\mathbf{F}$ and $_{B}\mathbf{F} = {}_{bcc}\mathbf{F}$, which map the reference state to the natural state, as shown in Fig. (3.11a). In the reference state, the two adjacent materials that meet at the interface are rotated and strained such that they are in perfect registry with each other across the $\hat{\boldsymbol{X}} - \hat{\boldsymbol{Z}}$ interface plane after bonding. In general, these displacement gradients entail interface misorientations that have both tilt and twist components [7, 237, 123]. Again, the interface along the $\hat{x} - \hat{z}$ plane is not coherent in the natural state, but rather semicoherent due to the presence of misfit dislocations.

The atomically sharp fcc{111}/bcc{110} interfaces in NW and in-plane twisted-NW ORs contain two periodic arrays of infinitely long, straight, and uniformly spaced dislocations. In the NW OR, one of the ⟨110⟩ directions in a fcc {111} plane lies parallel to the ⟨100⟩ direction in a bcc {110} plane [279, 192]. The in-plane twisted-NW ORs considered here differ from the NW OR only by a twist rotation of one crystal (here, the bcc material) with respect to the adjacent (fcc) crystal about the axis normal to the interface. The procedure described in section 3.2.4 is adopted

Systems	$\hat{c}_{11}$ (GPa)	$\hat{c}_{12}$ (GPa)	$\hat{c}_{44}$ (GPa)	a (Å)
Cu	178.8	122.6	81.03	3.615
Nb	245.6	133.7	28.8	3.3008
Ag	124.2	93.9	46.1	4.090
V	220.15	130.7	42.8	3.039
Cu	187.8	125.7	70.6	3.615
Mo	545.9	219.3	108.8	3.147

TABLE 3.2: Material properties for copper (Cu), niobium (Nb), silver (Ag), vanadium (V), and molybdenum (Mo). The values of stiffness constants $\hat{c}_{11}$, $\hat{c}_{12}$, $\hat{c}_{44}$, and lattice parameters a for all materials are those listed in Ref. [258].

to determine the unique reference states that meet the condition of vanishing far-field strains and prescribed misorientation for such interfaces. Thus, the dislocation content $\boldsymbol{B}$ of an interface, intersected by a probe vector $\boldsymbol{p}$ contained within the interface plane as illustrated in Fig. (3.11b), is described by the Frank-Bilby equation in eq. (3.2). For interfaces in the NW OR, a transformation pathway is defined by continuously adjusting the reference state from the strain-free state of the fcc crystal present at the interface to that of the adjacent bcc crystal. For all reference states along this path, the method described in section 3.2 is used to compute the superposition of the uniform coherency strains, $\mathbf{E}_c$, needed to maintain perfect registry and the far-field strain fields produced by the Volterra dislocation arrays, $\mathbf{E}^{\infty}_{\text{dis}}$. In the correct reference state, these quantities cancel and the total far-field strain field $\mathbf{E}$ vanishes in both upper fcc ($\hat{y} > 0$) and lower bcc ($\hat{y} < 0$) materials, as defined by eqs. (3.13), as

$$\lim_{\hat{y}\to\pm\infty} \mathbf{E}\,(\hat{x},\hat{y},\hat{z}) = \mathbf{0} \quad \Leftrightarrow \quad \begin{cases} {}_{\text{fcc}}\mathbf{E}^{\infty} = {}_{\text{fcc}}\mathbf{E}_c + {}_{\text{fcc}}\mathbf{E}^{\infty}_{\text{dis}} = \mathbf{0} \\ {}_{\text{bcc}}\mathbf{E}^{\infty} = {}_{\text{bcc}}\mathbf{E}_c + {}_{\text{bcc}}\mathbf{E}^{\infty}_{\text{dis}} = \mathbf{0}\,, \end{cases} \tag{3.43}$$

for which the far-field rotation state in the NW OR is consistent with the given crystallographic character (interface plane and misorientation).

To find the reference state for interfaces differing from those in the NW ORs by an in-plane twist angle θ, a second pathway is defined by rotating the previously determined reference state in the NW OR from 0 to θ. Along this second path, the rotated reference state, for which eqs. (3.43) are satisfied, also yields far-field rotations that must be consistent with the in-plane prescribed twist misorientations. Using the correct reference states for all ORs, the short-range interface strains and stresses that arise from the incomplete cancellation of the coherency and Volterra dislocation fields near the interfaces are also computed as well as the interface elastic energy γ_e from eq. (3.30) as a surface integral over a unit cell. The domain of integration is related to a pre-determined cutoff distance r_0 of the dislocation cores to determine the likeliest interface misfit dislocation configurations whenever the Frank-Bilby equation (eq. (3.2)) admits multiple solutions.

In this section, a detailed discussion of partitioning of distortions at Cu/Nb interfaces is presented, while analogous results for Ag/V and Cu/Mo interfaces are shown, albeit without going into detail. The material properties (elastic constants and lattice parameters) used in all calculations for these three interface types are listed in Table 3.2.

3.4.1 Mapping between states in the Nishiyama-Wassermann orientations

Without loss of generality, the following specific relation is used among 12 possible equivalent variants of the NW OR [106] to construct the mapping from the fcc to the bcc crystal:

$$\text{NW}: \quad \begin{array}{rcccc} & \hat{\boldsymbol{x}} & \parallel \boldsymbol{x}_{\text{fcc}} = [11\bar{2}]_{\text{fcc}} & \parallel & \boldsymbol{x}_{\text{bcc}} = [01\bar{1}]_{\text{bcc}} \\ \boldsymbol{n} \parallel & \hat{\boldsymbol{y}} & \parallel \boldsymbol{y}_{\text{fcc}} = [111]_{\text{fcc}} & \parallel & \boldsymbol{y}_{\text{bcc}} = [011]_{\text{bcc}} \\ & \hat{\boldsymbol{z}} & \parallel \boldsymbol{z}_{\text{fcc}} = [1\bar{1}0]_{\text{fcc}} & \parallel & \boldsymbol{z}_{\text{bcc}} = [100]_{\text{bcc}}\,. \end{array} \tag{3.44}$$

Dislocation structures in NW Cu/Nb					
$*$ solutions by selecting the fcc Burgers vectors					
Cases	d_1 (nm)	d_2 (nm)	ϕ °	ϕ_1 °	ϕ_2 °
$c1 : \{\boldsymbol{b}_1^{\text{fcc}}, \boldsymbol{b}_2^{\text{fcc}}\}$	1.1234	1.1234	15.03	37.51	37.51
$c2 : \{\boldsymbol{b}_1^{\text{fcc}}, \boldsymbol{b}_3^{\text{fcc}}\}$	4.2953	1.1234	82.49	60.00	82.49
$c3 : \{\boldsymbol{b}_2^{\text{fcc}}, \boldsymbol{b}_3^{\text{fcc}}\}$	4.2953	1.1234	82.49	60.00	82.49
$*$ solutions by selecting the proper reference Burgers vectors					
Cases	d_1 (nm)	d_2 (nm)	ϕ °	ϕ_1 °	ϕ_2 °
$c1 : \{\hat{\boldsymbol{b}}_1^{\text{ref}}, \hat{\boldsymbol{b}}_2^{\text{ref}}\}$	1.1234	1.1234	15.03	39.62	39.62
$c2 : \{\hat{\boldsymbol{b}}_1^{\text{ref}}, \hat{\boldsymbol{b}}_3^{\text{ref}}\}$	4.2953	1.1234	82.49	57.89	82.49
$c3 : \{\hat{\boldsymbol{b}}_2^{\text{ref}}, \hat{\boldsymbol{b}}_3^{\text{ref}}\}$	4.2953	1.1234	82.49	57.89	82.49

TABLE 3.3: Dislocation spacings d_i, angle between the two sets of dislocations ϕ, and characters ϕ_i for three solutions, namely $c1$, $c2$, and $c3$, for which the fcc (here, Cu) and the proper Burgers vectors have been selected as the reference state in NW Cu/Nb interface.

Here and in the following, the superimposed hat will indicate quantities expressed in a frame with basis vectors, $\hat{\boldsymbol{x}} = [100]$, $\hat{\boldsymbol{y}} = [010]$, and $\hat{\boldsymbol{z}} = [001]$. A schematic representation of a Cu/Nb interface in the NW OR is shown in Fig. (3.12a). Labeling of Burgers vectors for the other fcc/bcc systems of interest here follows the same pattern as shown for NW Cu/Nb in Figs. (3.12a) and (b).

If the fcc Cu material is used as the reference state, then three trial Burgers vectors may be selected in the interface plane:

$$\boldsymbol{b}_1^{\text{fcc}} = \frac{a_{\text{Cu}}}{2}\,[\bar{1}01]\ ,\quad \boldsymbol{b}_2^{\text{fcc}} = \frac{a_{\text{Cu}}}{2}\,[0\bar{1}1]\ ,\quad \text{and,}\quad \boldsymbol{b}_3^{\text{fcc}} = \frac{a_{\text{Cu}}}{2}\,[\bar{1}10]\ . \tag{3.45}$$

The transformation matrix $\mathbf{T}_{\text{Nb}\to\text{Cu}}$ that represents the transformation of the bcc Nb material to the fcc Cu material may be written as

$$\mathbf{T}_{\text{Nb}\to\text{Cu}} = \mathbf{I} - \mathbf{F}_{\text{Cu}\to\text{Nb}}^{-1}\,, \tag{3.46}$$

where $\mathbf{I}$ is the identity matrix and $\mathbf{F}_{\text{Cu}\to\text{Nb}}$—the mapping that transforms the fcc Cu to the bcc Nb crystal—is written in the fcc reference system $(\boldsymbol{x}_{\text{fcc}}, \boldsymbol{y}_{\text{fcc}}, \boldsymbol{z}_{\text{fcc}})$ as:

$$\mathbf{F}_{\text{Cu}\to\text{Nb}} = \begin{bmatrix} 1.281998 & -0.009298 & 0.109180 \\ -0.009298 & 1.281998 & 0.109180 \\ -0.154404 & -0.154404 & 0.899935 \end{bmatrix}\ . \tag{3.47}$$

For this interface, the Frank-Bilby equation has three different solutions, namely $c1$, which uses the pair $\{\boldsymbol{b}_1^{\text{fcc}}, \boldsymbol{b}_2^{\text{fcc}}\}$, $c2$ with $\{\boldsymbol{b}_1^{\text{fcc}}, \boldsymbol{b}_3^{\text{fcc}}\}$, and $c3$ with $\{\boldsymbol{b}_2^{\text{fcc}}, \boldsymbol{b}_3^{\text{fcc}}\}$. Due to the crystal symmetry along $\hat{\boldsymbol{z}}$ in the NW OR, which exhibits the $p2/m11$ layer space group, two of the three solutions ($c2$ and $c3$) are mirror images. Analysis of dislocation structures for all three cases are given in Table 3.3, with ϕ the angle between the two sets of dislocations and ϕ_i their individual characters. The dislocation line directions and spacings are schematically depicted in Fig. (3.12c), where the filled circles represent the O-lattice points [32, 237].

If the bcc Nb lattice is used as the reference state, then corresponding expressions for $\mathbf{F}_{\text{Nb}\to\text{Cu}}$ and $\mathbf{T}_{\text{Cu}\to\text{Nb}}$ may also be obtained. In this case, Burgers vectors are equivalently expressed in the bcc crystal structure and the same dislocation geometries are found. Neither the fcc nor the bcc reference states satisfy the condition of vanishing far-field strains and stresses [123, 260] because neither accounts for the required partitioning of strains and rotations between the adjacent crystals [119].

There is a continuum of other possible reference states between these two extreme cases. To find the correct reference state, a dimensionless variable δ that interpolates linearly between the

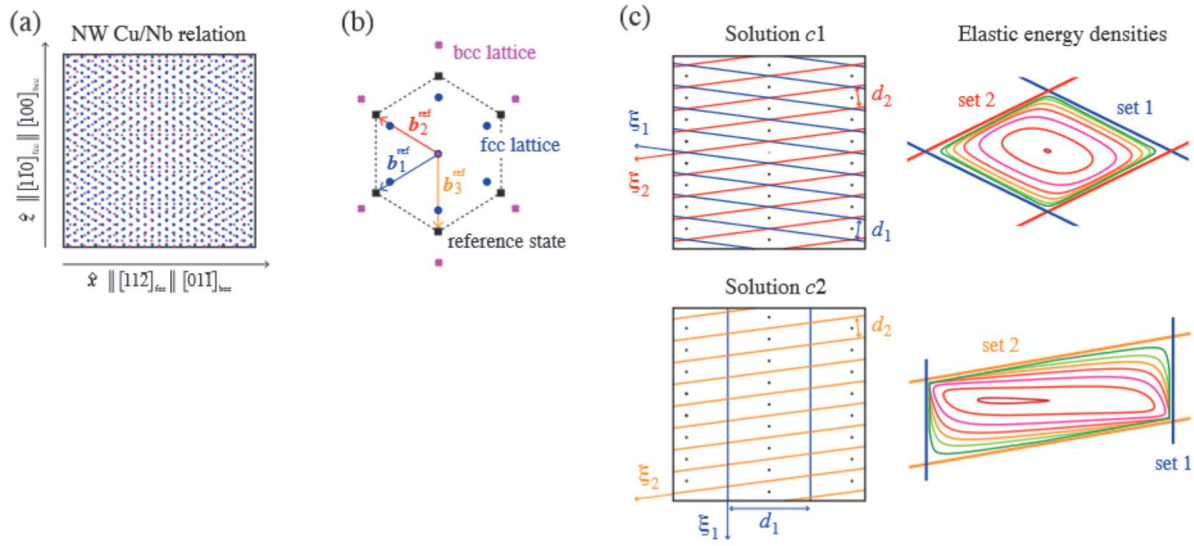

FIGURE 3.12: (a) Representation of the NW OR between fcc {111} (blue atoms) and bcc {110} (red atoms) close packed planes in Cu/Nb interfaces. (b) The reference state is depicted by the dashed black polyhedron, within which the Burgers vectors (corresponding to the sides of each polyhedron) are defined. The difference between the positions of the fcc and bcc atoms have been exaggerated for clarity. (c) Schematic illustrations of two admissible dislocation structures (solutions $c1$ and $c2$) with O-lattice points (black circles) and the local elastic energy densities stored in a representative unit cell of the dislocation patterns. The colors of the dislocations are associated with the Burgers vectors that are colored in (b). Contour values (from the center of the patterns to the dislocation lines): $\{0, 0.2, 0.6, 1.2, 2.0, 3.2, 5.2\}$ J.m^{-2}.

pure Cu and Nb materials is introduced as follows

$$\begin{cases} {}_{\text{Cu}}\mathbf{F} = (1-\delta)\,\mathbf{I} + \delta\,\mathbf{F}_{\text{Nb}\to\text{Cu}} \\ {}_{\text{Nb}}\mathbf{F} = \delta\,\mathbf{I} + (1-\delta)\,\mathbf{F}_{\text{Cu}\to\text{Nb}}\,. \end{cases} \tag{3.48}$$

For $\delta = 0$, $\mathbf{T} = \mathbf{T}_{\text{Nb}\to\text{Cu}}$ and for $\delta = 1$, $\mathbf{T} = \mathbf{T}_{\text{Cu}\to\text{Nb}}$. Along the transformation pathway characterized by δ, the elastic distortions (strain and rotation fields) in the NW ORs can also be computed.

3.4.2 Far-field strains and rotations

As shown in Refs. [126, 123, 260], and illustrated in Fig. (3.11b) the natural state of semi-infinite bicrystals is homogeneously transformed into a reference state by biaxial distortions parallel to the plane with normal $\boldsymbol{n} \parallel \hat{\boldsymbol{y}}$, so that the removal of the strains $\hat{e}_{2j\,\text{tot}} = *$, with $j = 1, 2, 3$ [126, 123]. Thus, only six components (three for strains and three for rotations) of the distortion matrices are needed to meet the condition of vanishing total far-field strains and prescribed misorientations.

In the linear-elastic approximation, the distortion matrices $\hat{\mathbf{D}}$ may also be separated into symmetric $\hat{\mathbf{E}}$ and antisymmetric $\hat{\boldsymbol{\Omega}}$ parts:

$$\hat{\mathbf{D}} = \underbrace{\begin{bmatrix} \hat{\epsilon}_{11} & * & \hat{\epsilon}_{13} \\ * & * & * \\ \hat{\epsilon}_{13} & * & \hat{\epsilon}_{33} \end{bmatrix}}_{\hat{\mathbf{E}}} + \underbrace{\begin{bmatrix} 0 & -\hat{\omega}_{12} & \hat{\omega}_{13} \\ \hat{\omega}_{12} & 0 & -\hat{\omega}_{23} \\ -\hat{\omega}_{13} & \hat{\omega}_{23} & 0 \end{bmatrix}}_{\hat{\boldsymbol{\Omega}}}. \tag{3.49}$$

The coherency strain fields $\hat{\mathbf{E}}_{\text{c}}$ on both sides of the interface are given by

$${}_{\text{Cu}}\hat{\mathbf{E}}_{\text{c}} = \text{sym}\ {}_{\text{Cu}}\hat{\mathbf{F}}^{-1} - \mathbf{I}\,, \quad \text{and,} \quad {}_{\text{Nb}}\hat{\mathbf{E}}_{\text{c}} = \text{sym}\ {}_{\text{Nb}}\hat{\mathbf{F}}^{-1} - \mathbf{I}\,, \tag{3.50}$$

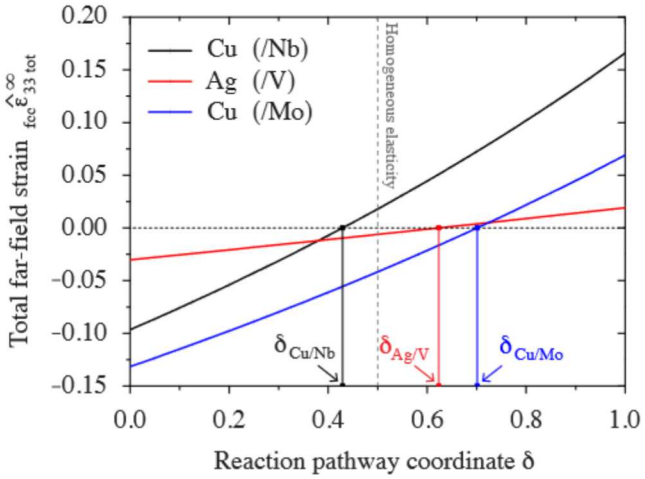

FIGURE 3.13: Dependence of the total far-field strain component ${}_{\text{fcc}}\hat{\epsilon}^{\infty}_{33}$ on δ in the fcc material for the Cu/Nb, Ag/V and Cu/Mo heterophase interfaces. The vertical dotted line shows the δ under the assumption that both materials at the interface have the same stiffness.

where ${}_{\text{Cu}}\hat{\mathbf{F}}^{-1}$ and ${}_{\text{Nb}}\hat{\mathbf{F}}^{-1}$ are obtained from eqs. (3.48). Superposing the elastic strains produced by the interface dislocations in Cu and Nb, i.e. ${}_{\text{Cu}}\mathbf{E}^{\infty}_{\text{dis}}$ and ${}_{\text{Nb}}\mathbf{E}^{\infty}_{\text{dis}}$, the total far-field strain state in the entire bicrystal may be calculated [260].

Figure (3.13) shows the total strain component ${}_{\text{Cu}}\hat{\epsilon}^{\infty}_{33}$ in Cu as a function of δ (black line). This strain vanishes, i.e. ${}_{\text{Cu}}\hat{\epsilon}^{\infty}_{33} = 0$, for $\delta_{\text{Cu/Nb}} = 0.429103$. All other elastic components are consistent with the absence of strains in the far-field and the total far-field strain in Nb vanishes at the same δ as in Cu. Thus, the reference state is closer to Cu than to Nb, i.e. $\delta_{\text{Cu/Nb}} < 0.5$. This result cannot be easily predicted from inspection of the stiffness constants alone (see Table 3.2). Figure (3.13) also shows that $\delta_{\text{Ag/V}} = 0.623359$ and $\delta_{\text{Cu/Mo}} = 0.701109$, i.e. the reference state is closer to the bcc material (V and Mo) in both cases.

Knowing the δ value at which far-field stresses vanish, the crystal structure of the reference state is given by the uniform displacement gradients, obtained using eqs. (3.48) and (3.50):

$$
\begin{aligned}
{}_{\text{Cu}}\hat{\mathbf{E}}_{\text{c}} = -{}_{\text{Cu}}\hat{\mathbf{E}}^{\infty}_{\text{dis}} &= \begin{bmatrix} 0.022615 & 0.072664 & 0 \\ 0.072664 & 0.047550 & 0 \\ 0 & 0 & 0.107173 \end{bmatrix} \\
-{}_{\text{Nb}}\hat{\mathbf{E}}_{\text{c}} = {}_{\text{Nb}}\hat{\mathbf{E}}^{\infty}_{\text{dis}} &= \begin{bmatrix} 0.030089 & 0.096675 & 0 \\ 0.096675 & 0.063262 & 0 \\ 0 & 0.154414 & 0.142588 \end{bmatrix} .
\end{aligned}
\tag{3.51}
$$

The Burgers vectors of the interfacial misfit dislocations are to be drawn from this reference state. The correct reference state of the NW OR is depicted by the dashed polyhedron in Fig. (3.12b), within which the Burgers vectors are defined by:

$$
\Sigma_{\text{NW}} \begin{cases} \hat{\boldsymbol{b}}^{\text{ref}}_1 = -0.226379\,\hat{\boldsymbol{x}} - 0.141507\,\hat{\boldsymbol{z}}\ \ (\text{nm}) \\ \hat{\boldsymbol{b}}^{\text{ref}}_2 = -0.226379\,\hat{\boldsymbol{x}} + 0.141507\,\hat{\boldsymbol{z}}\ \ (\text{nm}) \\ \hat{\boldsymbol{b}}^{\text{ref}}_3 = \hat{\boldsymbol{b}}^{\text{ref}}_1 - \hat{\boldsymbol{b}}^{\text{ref}}_2 = -0.283015\,\hat{\boldsymbol{z}}\ \ (\text{nm})\,. \end{cases}
\tag{3.52}
$$

Systems	strains			tilt rotations °	
	δ	${}_{\text{fcc}}\hat{\epsilon}_{33\,\text{c}}$	${}_{\text{bcc}}\hat{\epsilon}_{33\,\text{c}}$	ϑ_{fcc}	ϑ_{bcc}
Cu/Nb	0.429103	0.107173	−0.142588	−4.17	5.55
Ag/V	0.623359	0.031076	−0.018777	−6.03	3.68
Cu/Mo	0.701109	0.152295	−0.064925	−6.91	2.88

TABLE 3.4: Partitioning of strains and rotations for various fcc/bcc bicrystals.

In addition to completely accommodating the coherency strains, interface dislocations also give rise to unequally partitioned rotation fields, given in the case of Cu/Nb in the NW OR by

$$\begin{aligned} {}_{\text{Cu}}\hat{\mathbf{\Omega}}^{\infty}_{\text{dis}} &= -0.072664\,(-\hat{\boldsymbol{x}}\otimes\hat{\boldsymbol{y}}+\hat{\boldsymbol{y}}\otimes\hat{\boldsymbol{x}}) \\ {}_{\text{Nb}}\hat{\mathbf{\Omega}}^{\infty}_{\text{dis}} &= -0.096675\,(\hat{\boldsymbol{x}}\otimes\hat{\boldsymbol{y}}-\hat{\boldsymbol{y}}\otimes\hat{\boldsymbol{x}})\ , \end{aligned} \tag{3.53}$$

yielding a net non-vanishing rotation vector, i.e.

$$\hat{\boldsymbol{\omega}} = {}_{\text{Cu}}\hat{\boldsymbol{\omega}}^{\infty} - {}_{\text{Nb}}\hat{\boldsymbol{\omega}}^{\infty} = (-0.072664 - 0.096675)\ \hat{\boldsymbol{z}} = -0.169339\,\hat{\boldsymbol{z}}\,, \tag{3.54}$$

about the $\hat{\boldsymbol{z}}$ tilt axis. The unequal partition of far-field rotations given by eqs. (3.53) shows that, to achieve the NW OR, the upper material in the reference state must be rotated by a rigid-body rotation through a tilt angle $\vartheta_{\text{Cu}} \sim -4.17^{\circ}$ about the tilt axis $\hat{\boldsymbol{z}} \parallel \boldsymbol{z}_{\text{fcc}} = [1\bar{1}0]_{\text{fcc}}$ to the Cu material in the natural state. In addition, the lower material must be rotated through a tilt angle $\vartheta_{\text{Nb}} \sim 5.55^{\circ}$ about the tilt axis $\hat{\boldsymbol{z}} \parallel \boldsymbol{z}_{\text{bcc}} = [100]_{\text{bcc}}$ to form the Nb material. Thus, the net rotation angle is $\sim 9.72^{\circ}$ about $\hat{\boldsymbol{z}}$, as discussed in Ref. [106]. This result can be shown by computing the polar decomposition of eq. (3.47) such that $\mathbf{F}_{\text{Cu}\to\text{Nb}} = \mathbf{R}(\sim 9.72^{\circ}, [1\bar{1}0]_{\text{fcc}}) \cdot \mathbf{B}$, i.e.

$$\mathbf{R} = \begin{bmatrix} 0.992799 & -0.007201 & 0.119573 \\ -0.007201 & 0.992799 & 0.119573 \\ -0.119573 & -0.119573 & 0.985599 \end{bmatrix}\ ,\ \text{and,}\ \ \mathbf{B} = \begin{bmatrix} 1.291296 & 0 & 0 \\ 0 & 1.291296 & 0 \\ 0 & 0 & 0.913084 \end{bmatrix}\ , \tag{3.55}$$

with $B_{11} = B_{22} = \sqrt{2}/\lambda$, $B_{33} = 1/\lambda$ and the lattice parameter ratio $\lambda = a_{\text{Cu}}/a_{\text{Nb}}$. In eqs. (3.55), the matrix $\mathbf{R}$ corresponds to a rigid-body rotation matrix of angle $\sim 9.72^{\circ}$ about $[1\bar{1}0]_{\text{fcc}}$ and $\mathbf{B}$ is the Bain strain matrix [16, 295]. The compression axis for the Bain strain is $[1\bar{1}0]_{\text{fcc}} \parallel \hat{\boldsymbol{z}}$, because $B_{33} < 1$.

Table 3.4 summarizes the main results of unequal partitioning of elastic strains and tilt rotations between the adjacent materials of Cu/Nb, Ag/V and Cu/Mo systems in the NW OR.

3.4.3 Spurious fields from incorrect reference states

As indicated in Table 3.3, the correct dislocation Burgers vectors for the Cu/Nb interface in the NW OR differ from what they would have been had the fcc crystal (Cu) been selected as the coherent reference state. Their directions differ by $\sim 2.11^{\circ}$, which affect the character of the interface dislocations. The magnitudes of the Burgers vectors in the fcc crystal and the correct reference state also differ, with $|\boldsymbol{b}_j^{\text{fcc}}| : |\boldsymbol{b}_j^{\text{ref}}| = 0.90$. The consequences of these deviations in character and magnitude may be seen in Fig. (3.14): a residual stress state in Cu persists with ${}_{\text{Cu}}\hat{\sigma}^{\infty}_{33} = -20.01$ GPa, corresponding to a residual strain state ${}_{\text{Cu}}\hat{\epsilon}^{\infty}_{33} = -0.10$, as shown in Fig. (3.13). A residual stress field exists in Nb as well, with ${}_{\text{Nb}}\hat{\sigma}^{\infty}_{33} = 16.67$ GPa. Figure (3.14) illustrates the variations of the spurious stress field component $\hat{\sigma}^{\infty}_{33}$ in the neighboring materials as a function of δ. This elastic field arises when an incorrect reference state is selected.

To emphasize the need for accounting for the unequal partitioning of elastic distortions, the coherency strain matrices is recomputed under the assumption that both sides of the interface have the same stiffness (i.e. homogeneous elasticity problem), equal to that of Cu, but with their

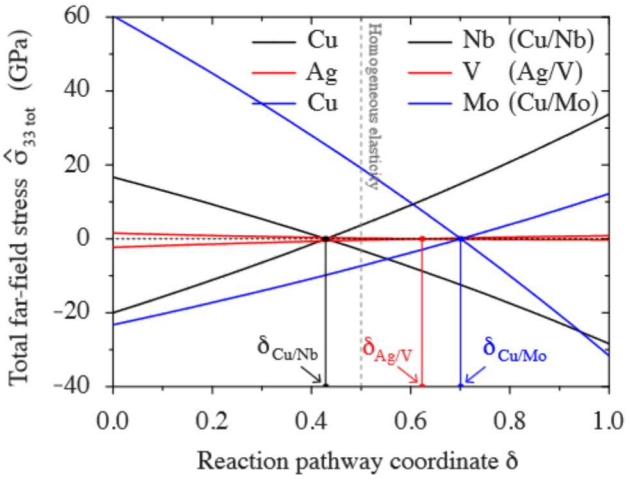

FIGURE 3.14: Dependence of the total far-field stress component $\hat{\sigma}_{33}^{\infty}$ on δ in the fcc and bcc materials for the Cu/Nb, Ag/V and Cu/Mo interfaces.

natural (unequal) lattice parameters, as in the original calculation for the Cu/Nb interface. The results are in agreement with the well-known approximate calculation for equally partitioned strains due to simple geometrical considerations [123], i.e.

$$ {}_{\mathrm{Cu}}\hat{\mathbf{E}}_{\mathrm{c}}^{\mathrm{iso}} = -{}_{\mathrm{Nb}}\hat{\mathbf{E}}_{\mathrm{c}}^{\mathrm{iso}} = \begin{bmatrix} 0.026451 & 0.085660 & 0 \\ 0.085660 & 0.055845 & 0 \\ 0 & 0 & 0.127132 \end{bmatrix}, \tag{3.56} $$

with ${}_{\mathrm{Cu}}\hat{\epsilon}_{33\,\mathrm{c}}^{\mathrm{iso}} = {}_{\mathrm{Nb}}\hat{\epsilon}_{33\,\mathrm{c}}^{\mathrm{iso}} = (a_{\mathrm{Nb}} - a_{\mathrm{Cu}}/\sqrt{2})/(a_{\mathrm{Nb}} + a_{\mathrm{Cu}}/\sqrt{2})$ and a net rotation vector $\hat{\boldsymbol{\omega}}^{\mathrm{iso}} = -2 \times 0.085660\ \hat{\mathbf{z}}$, corresponding to equipartitioning of rotations with tilt angles $-\vartheta_{\mathrm{Cu}} = \vartheta_{\mathrm{Nb}} \sim 4.91°$.

In the nomenclature given by eqs. (3.48), the homogeneous anisotropic (or isotropic) case is associated with $\delta = 0.5$, as depicted by the vertical dotted lines in Figs. (3.13) and (3.14). The vertical dotted line in Fig. (3.14) shows a (non-zero) excess far-field stress state with ${}_{\mathrm{Cu}}\hat{\sigma}_{33}^{\infty} = 3.69$ GPa in Cu and ${}_{\mathrm{Nb}}\hat{\sigma}_{33}^{\infty} = -3.09$ GPa in Nb in the NW Cu/Nb interface or ${}_{\mathrm{Cu}}\hat{\sigma}_{33}^{\infty} = -7.36$ GPa and ${}_{\mathrm{Mo}}\hat{\sigma}_{33}^{\infty} = 19.08$ GPa in the NW Cu/Mo interface. Thus, even if the choice of equipartitioning of strains and (tilt) rotations is better than selecting the fcc material as the reference state, a spurious far-field stress field still remains. As a consequence, the associated dislocation structures for the homogeneous anisotropic (or isotropic) elasticity case of the Cu/Nb bicrystal are designated as non-equilibrium structures.

3.4.4 Orientations differing from the Nishiyama-Wassermann relations

Another commonly studied misorientation of interfaces between close-packed planes of neighboring {111} fcc and {110} bcc solids is the KS OR [154]. In the KS OR, one of the ⟨110⟩ directions in a fcc {111} plane lies parallel to one of the ⟨111⟩ directions in a bcc {110} plane. A schematic representation of a Cu/Nb interface in the KS OR is shown in Fig. (3.15a), where the bcc atoms have been rotated by 5.26° from their positions in the NW OR. The geometrical characteristics (line directions and spacings) of dislocation structures in the KS OR for the three cases are given in Table 3.5 and depicted in Fig. (3.15c).

To treat the KS OR and other ORs related to the NW by an in-plane twist, the rigid-body rotation matrix $\mathbf{R}(\theta)$ that rotates all bcc atoms in the natural state is introduced with respect to the fixed fcc atoms by angle θ about the interface normal $\boldsymbol{n}$. The NW OR corresponds to $\theta = 0°$. The

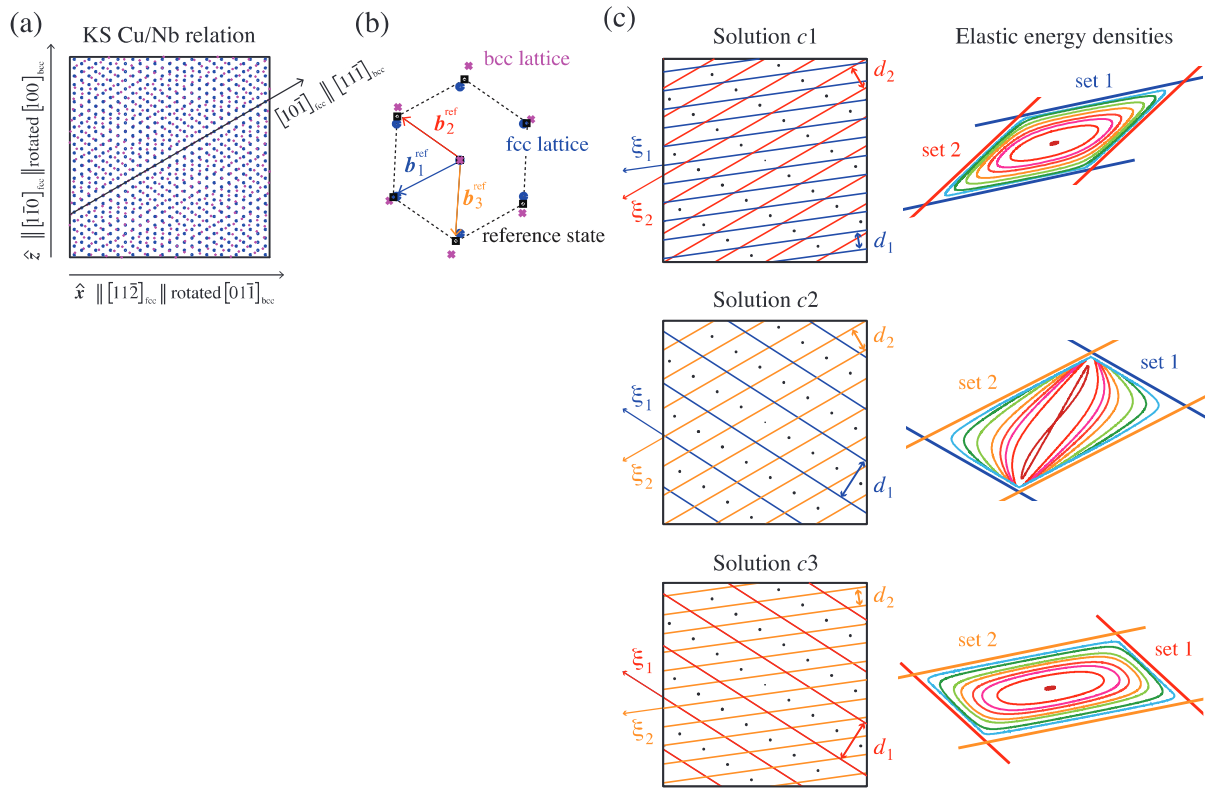

FIGURE 3.15: Similar illustration as in Fig. (3.12), but for a Cu/Nb interface in the KS OR. Contour values (from the center of the patterns to the dislocation lines): $\{0, 0.2, 0.4, 0.6, 1.0, 1.4, 2.8, 4.8\}$ J.m^{-2}.

KS OR differs from the original NW OR by a twist rotation of angle $\theta \sim 5.26°$ about the interface normal axis $\boldsymbol{n}$.

To describe the relation between the natural and reference states for fcc/bcc in the in-plane twisted ORs, ${}_{\text{fcc}}\mathbf{F}^{-1}$ and ${}_{\text{bcc}}\mathbf{F}^{-1}$ in eq. (3.2) are replaced by ${}_{\text{fcc}}\mathbf{R}\,(\kappa\,\theta)\,{}_{\text{fcc}}\mathbf{F}^{-1}_{\text{NW}}$ and ${}_{\text{bcc}}\mathbf{R}\,(\kappa\,\theta)\,{}_{\text{bcc}}\mathbf{F}^{-1}_{\text{NW}}$, where κ is a dimensionless parameter that varies from 0 to 1, such that $\mathbf{R}\,(\kappa\,\theta)$ is the rotation matrix that continuously adjusts the reference state in the KS OR from the one determined in the NW OR. This rotation matrix is expressed in the fcc $(\boldsymbol{x}_{\text{fcc}}, \boldsymbol{y}_{\text{fcc}}, \boldsymbol{z}_{\text{fcc}})$ and bcc $(\boldsymbol{x}_{\text{bcc}}, \boldsymbol{y}_{\text{bcc}}, \boldsymbol{z}_{\text{bcc}})$ systems by ${}_{\text{Cu}}\mathbf{R}\,(\kappa\,\theta)$ and ${}_{\text{Nb}}\mathbf{R}\,(\kappa\,\theta)$ in the Cu/Nb bicrystal, respectively. Equipartitioning of twist between the adjacent crystals occurs when $\kappa = 0.5$ [193, 123].

The condition that determines κ is that the far-field rotations produced by the interface dislocations must be in accordance with the prescribed twist misorientation. The κ value that satisfies this condition for Cu/Nb in the KS OR is $\kappa = 0.570897$, yielding unequal partitioning of the twist rotations $\theta_{\text{Cu}} \sim 3.20°$ and $\theta_{\text{Nb}} \sim -2.06°$. The correct Burgers vectors associated with this reference state are illustrated in Fig. (3.15b). If the approximation of equipartitioning of distortions is considered, i.e. $\kappa = 0.5$, the partitioning of rotations gives rise to $\theta_{\text{Cu}} = \theta_{\text{Nb}} = 2.63°$, such that the dislocation characters differ by $\sim 0.57°$ from the results obtained with the unequally partitioned distortions. This difference is not large because $\theta \sim 5.26°$ is small, but the elastic (short- and long-range) fields may be significantly affected by deviations associated with larger twist rotations [123].

3.4.5 Short-range elastic fields

Although the far-field strains vanish when the correct reference state for ORs differing from the NW by an in-plane twist is used, the dislocation structures depicted in Figs. (3.12b) and (3.15b) nevertheless generate non-zero short-range strains and stresses. For instance, Fig. (3.16) plots

Dislocation structures in KS Cu/Nb $*$ solutions by selecting the proper reference Burgers vectors					
Cases	d_1 (nm)	d_2 (nm)	ϕ °	ϕ_1 °	ϕ_2 °
$c1 : \{\hat{\boldsymbol{b}}_1^{\text{ref}}, \hat{\boldsymbol{b}}_2^{\text{ref}}\}$	0.9073	1.2394	22.04	21.06	65.00
$c2 : \{\hat{\boldsymbol{b}}_1^{\text{ref}}, \hat{\boldsymbol{b}}_3^{\text{ref}}\}$	2.1457	1.2394	62.54	61.57	57.02
$c3 : \{\hat{\boldsymbol{b}}_2^{\text{ref}}, \hat{\boldsymbol{b}}_3^{\text{ref}}\}$	2.1457	0.9073	40.51	2.45	79.05

TABLE 3.5: Dislocation structures associated with Cu/Nb in the KS OR. See the caption of Table 3.3 for definitions of notation.

stress components σ_{21} and σ_{22} for set 1 only and for both sets of dislocations of $c1$ for the Cu/Nb interface in the NW OR, as a function of x' ($\boldsymbol{x}' \perp \boldsymbol{\xi}_1$) and y ($\hat{\boldsymbol{y}} \parallel \boldsymbol{n}$), with $z = 0$. Negative values (compression) are plotted in light grey and the positive values (extension) in dark grey. The thick black lines show the locations where the stresses are equal to zero. The fields are asymmetric due to the material elastic anisotropy and the characters of the dislocation arrays.

Using these short-range fields at the interface, i.e. $y = 0$, the local self- and interaction energy densities are computed as a function of x and z, as shown in Figs. (3.12c) and (3.15c) for all potential solutions predicted by the Frank-Bilby equation in the Cu/Nb NW and KS ORs, respectively. The unique solution of the Frank-Bilby equation is predicted by integrating the strain energy densities over each candidate solution and choosing the dislocation pattern with lowest elastic energy [258]. It is illustrated in the next section 3.4.6 that the present formalism predicts that $c3$ is in near perfect quantitative agreement with atomistic simulations for $\theta > 1°$. For instance, both approaches predict that Cu/Nb interface energy is minimized at $\theta = 2°$. The insets of Fig. (3.17) illustrates a qualitative comparison between the elasticity and atomistic calculations.

Using the minimum strain energy criterion for finding the likeliest dislocation structures, Fig. (3.17) plots the geometrical characteristics in terms of dislocation spacings, d_i (in black), and characters, ϕ_i (light grey), for both sets of dislocations as a function of θ (between the NW and KS ORs). The geometry (i.e. dislocation spacing and character) of set 2 does not vary significantly as a function of θ. In particular, the low spacing between misfit dislocations of set 2 is $d_2 \sim 1$ nm and is almost perfectly edge for $\theta = 2°$. On the other hand, the dislocation spacing and character of set 1 change markedly with θ, e.g. from mixed dislocation character to almost perfectly screw character, and the dislocation spacing decreases almost by a factor 2. Set 1 is almost perfectly screw for $\theta = 4.75°$. The vertical line in Fig. (3.17) shows the lowest interface energy reported in Ref. [258] with the corresponding geometrical characteristics, i.e. dislocation spacings and characters. Surprisingly, this interface does not correspond to the interface with the largest dislocation spacings or nearly perfectly screw dislocation characters, contrary to what may be expected based on the theory of dislocations in uniform isotropic solids [7]. However, the approach predicts a dislocation structure with $d_1 = 3.5856$ nm, $\phi_1 = 24.37°$, $d_2 = 1.0426$ nm, $\phi_2 = 89.61°$, which is in agreement with the atomistic calculations [258] .

3.4.6 Comparison with atomistic simulations

The present approach to interface design is to construct a mesoscale (as opposed to atomic-level) model that predicts misfit dislocation patterns with accuracy comparable to atomistic simulations, but at a fraction of the cost. The model is a reduced order model because it replaces the millions of variables associated with atomic positions with ≤ 15 variables needed to describe misfit dislocations. The misfit dislocations are viewed as Volterra dislocations that have been inserted into the coherent reference state, suggesting that the total interface energies γ be expressed as

$$\gamma = \gamma_{\text{e}}(r_0) + \gamma_{\text{core}} + \gamma_{\text{relax}} + \dots . \tag{3.57}$$

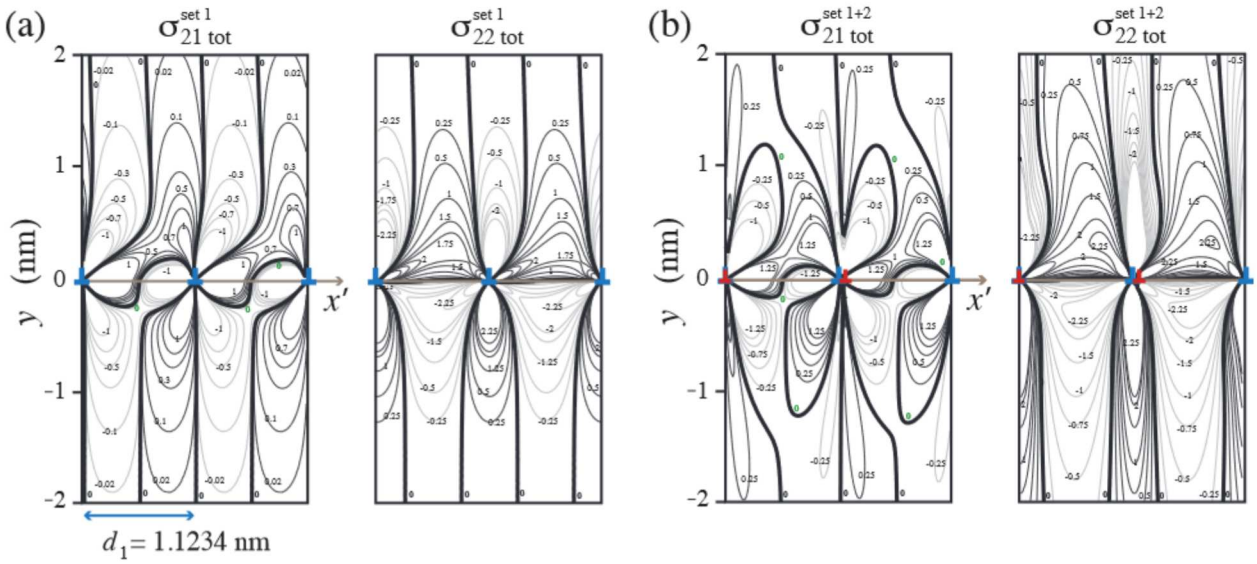

FIGURE 3.16: Contour plots of short-range stress component σ_{21} and σ_{22} for the Cu/Nb interface in the NW OR of $c1$, related to (a) the set 1, $\perp_1$ only and (b) both sets, $\perp_1$ and $\perp_2$ of interface dislocations. Contours with negative values (compression) are plotted in light gray while positive values (extension) are shown in dark gray. The thick black lines show the locations where stresses are zero.

with γ_e the elastic strain energy due to misfit dislocations from eq. (3.30), γ_{core} the core energy, γ_{relax} the energy part due to relaxations of the misfit dislocation network, and perhaps additional terms that have not yet been recognized. For the present purposes, it is not necessary to calculate the absolute value of γ, but rather only differences in γ between the candidate solutions of the Frank-Bilby equation.

The outputs of the elasticity-based model are compared with atomistic calculations, which provide an opportunity for rigorous validation of the elasticity theory of dislocations. They are also convenient for atomistic simulations because embedded atom method potentials are available for several fcc/bcc binaries. The elasticity-based model is validated against the interface compositions: Cu/Nb [72], Ag/V [281], Cu/Fe [174], and Cu/Mo [103]. These choices fix the elastic constants, crystal structures, and lattice parameters of the adjoining constituents. Because attention is restricted to interfaces along fcc $\langle 111 \rangle$ and bcc $\langle 110 \rangle$ planes, only one crystallographic DoF remains to be specified: the twist angle θ describing the relative rotation of the crystals parallel to the interface plane. The θ is measured with respect to the NW OR, where a bcc $\langle 100 \rangle$ direction is parallel to a fcc $\langle 110 \rangle$ direction, such that $\theta = \pi/3 - \cos^{-1}(1/\sqrt{3}) \sim 5.26°$ yields the KS OR. Due to the symmetry of the interface planes, all crystallographically distinct interfaces fall within $0° \leq \theta \leq 15°$. However, the analysis limited to $0° \leq \theta \leq 10°$ because for greater twists, misfit dislocations are too closely spaced to characterize reliably in atomic models.

For any composition and θ, the Frank-Bilby equation has three distinct candidate solutions, as illustrated in Fig. (3.15b), which corresponds to one of three combinations of interfacial Burgers vectors, as described in the previous sections . The first candidate, termed "case 1" ($\equiv c1$), uses Burgers vectors $\boldsymbol{b}_1$ and $\boldsymbol{b}_2$. "Case 2" ($\equiv c2$) and "case 3" ($\equiv c3$) use Burgers vectors $\boldsymbol{b}_1$, $\boldsymbol{b}_3$, and $\boldsymbol{b}_2$, $\boldsymbol{b}_3$, respectively. Using the elasticity-based model, γ_e of all three cases is computed for each composition and θ of interest. For all interfaces, the atomic-scale models are also constructed by joining cylindrical fcc and bcc blocks following the required interface crystallography. The models are large enough to contain a representative area of the misfit dislocation pattern and to avoid elastic images from free surfaces.

Figure (3.18a) compares γ_e from the elasticity-based model with γ from atomistic simulations for Cu/Nb interfaces. Because the relative energies of the three cases are the key quantities for

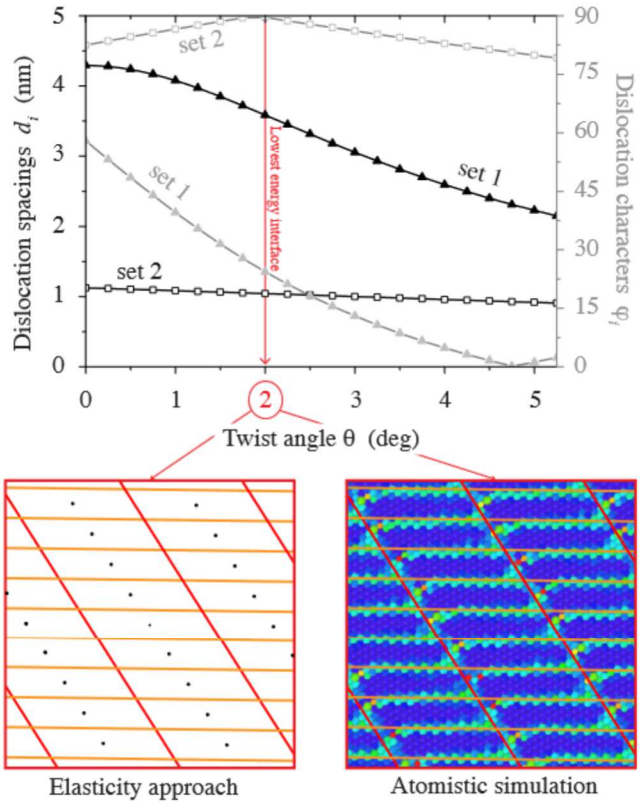

FIGURE 3.17: Dislocation spacings and characters predicted by the Frank-Bilby equation for both sets of dislocations in the Cu/Nb interface as a function of θ (from the NW, i.e. $\theta = 0°$ to the KS, i.e. $\theta \sim 5.26°$, ORs). The red line corresponds to the lowest energy interface for $\theta = 2°$, reported in Ref. [258]. In insets: comparison of the dislocation geometries in the minimum energy state computed by the elasticity and atomistic approaches.

comparison, both the elasticity-based model and atomistic data are shifted so that their energy minima occur at 0 J/m^2. The elasticity-based model predicts that case 3 has lowest γ_e for all θ. Furthermore, γ_e for case 3 is in near perfect quantitative agreement with γ for $\theta > 1°$. Figure (3.18b) shows a similar comparison for Ag/V interfaces. Here, the elasticity-based model predicts that case 1 has lowest γ_e for all θ outside $4.25° < \theta < 5.25°$, where γ_e is lowest for case 2. γ_e and γ are in qualitative agreement over the entire twist angle range and in quantitative agreement for $\theta > 5°$. As described in the Supplementary Note from Ref. [258], it is found comparable agreement between the elasticity-based model and atomistic interface energies for the remaining two compositions. Agreement between γ_e and γ is not sufficient to validate the present formalism. For that, it must be determined whether the lowest energy cases predicted by the elasticity-based model match the misfit dislocation patterns in atomistic simulations. Each of the three Frank-Bilby solutions predicts a different misfit dislocation pattern and therefore also a different disregistry. The present goal is to compare the disregistries of all three cases with that found in atomistic simulations. The model is validated if the case with lowest γ_e has the best match with the atomistic disregistry. As shown in Figs. (3.18a) and (b), and detailed in Ref. [258], the disregistry analysis is in agreement with the elastic predictions for all Cu/Nb and Ag/V interfaces (circle filled with light grey) except Cu/Nb at $\theta = 0°$. The disagreement is attributed to the reconstruction of the misfit dislocation network that is known to occur at that interface [272], which can be treated by further extensions from section 3.6. One further case of disagreement where dislocation network reconstruction occurs is found for Cu/Mo at $\theta = 0°$ (see Supplementary Note). However, the agreement between the elasticity-based model and the atomistic models is excellent, overall.

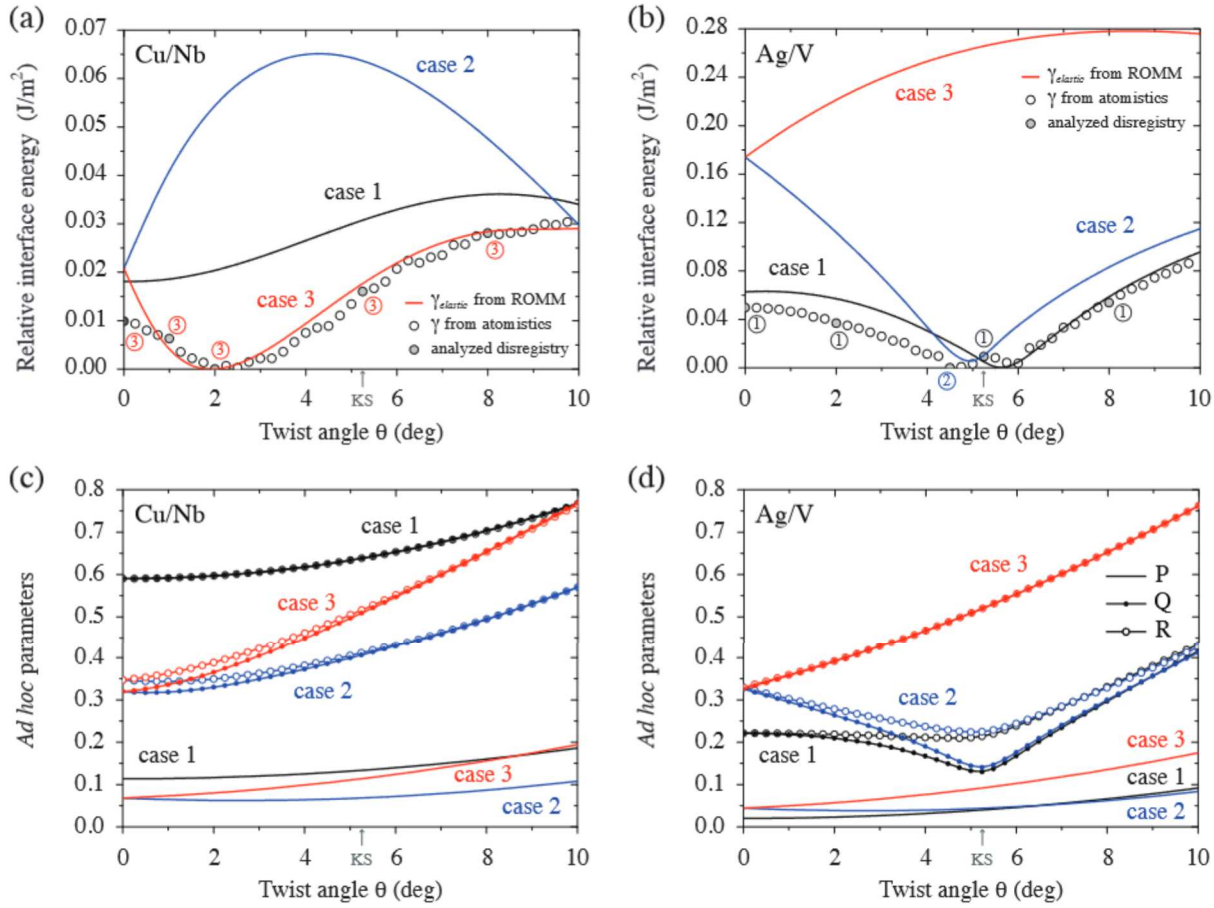

FIGURE 3.18: Interface energies computed as a function of θ using the elasticity-based model (designated by ROMM as "Reduced Order Mesoscale Model") and atomistic modeling for (a) Cu/Nb and (b) Ag/V. Filled circles indicate atomic models whose disregistry was analyzed. The ringed numbers next to them state the case that best matches the atomic disregistry. Ad hoc parameters P, Q, and R for (c) Cu/Nb and (d) Ag/V.

The general approach may be compared with several ad hoc parameters proposed previously to determine which of the cases predicted by the Frank-Bilby equation is likeliest. Bollmann suggested that the likeliest case minimizes [32]

$$P = \sum_i \frac{b_i^2}{d_i^2}\,, \tag{3.58}$$

which is analogous to the Frank rule for predicting dislocation reactions [7]. Similarly, Ecob and Ralph propose two parameters [82] to distinguish between cases, defined by Q and R, as follows

$$Q = \sum_i \sum_j \frac{b_i b_j}{d_i d_j}\,, \quad \text{and,} \quad R = \sum_i \sum_j \sqrt{\frac{b_i b_j}{d_i d_j}}\,, \tag{3.59}$$

using geometrical arguments for the energy of semicoherent interfaces. Figures (3.18c) and (d) plot these parameters for Cu/Nb and Ag/V interfaces. Comparing with Figs. (3.18a) and (b), none of them predicts the misfit dislocation patterns seen in atomistic models. For example, for Cu/Nb, all three parameters favor case 2, while the true interface structure is case 3. The elasticity-based model is therefore viewed as superior to these parameters and as validated for the purpose of

computational design of patterned interfaces.

3.5 Application to the sink strength of semicoherent interfaces

Clean, safe, and economical nuclear energy requires new materials capable of withstanding severe radiation damage. One way of removing radiation-induced defects is to provide a high density of sinks, such as GBs or heterophase interfaces [227] that continually absorb defects as they are created. This motivation underlies ongoing exploration of the radiation response of nanocomposite materials [74, 57], due to the large total interface area per unit volume they contain. These investigations have demonstrated wide variations in sink behavior of different interfaces. Some easily absorb defects, preventing damage in neighbouring material, but become damaged themselves [111]. Others are poor sinks for isolated defects, but excellent sinks for defect clusters [75]. The sink behavior of yet others changes with radiation dose [15, 14]. This wide variety of radiation responses prompts the physicists to ask:

* Are some specific interfaces best suited to mitigate radiation damage?
* Is it possible to identify them without resorting to resource-intensive irradiation experiments?

Here it is demonstrated that elastic interactions between point defects and semicoherent interfaces lead to a marked enhancement in interface sink strength. The conclusions stem from simulations that integrate first principles, object kinetic Monte Carlo, and anisotropic elasticity calculations. Surprisingly, the enhancement in sink strength is not due primarily to increased thermodynamic driving forces [144, 133], but rather to reduced defect migration barriers, which induce a preferential drift of defects towards interfaces. The sink strength enhancement is highly sensitive to the detailed character of interfacial stresses, suggesting that "super-sink" interfaces may be designed by optimizing interface stress fields. These findings motivate a computational search for "super-sink" interfaces: ones that optimally attract, absorb, and annihilate radiation-induced defects.

3.5.1 Computational multi-model strategy

To answer the aforementioned questions, an improved computational method for rapidly assessing the vacancy and interstitial sink strength of semicoherent interfaces is proposed. This method builds on the interfacial dislocation-based model for elastic fields of heterophase bicrystals, previously described. Such interfaces are of particular interest because many of them contain a high density of defect trapping sites [73, 220]. Moreover, semicoherent interfaces generate elastic fields that interact directly with radiation-induced defects [255]. These elastic fields have an unexpectedly large influence on interface sink strength, as quantified by the following computational multi-model approach.

Elastic dipole tensor calculation

Defect **P**-tensors are calculated using VASP [149], a plane wave-based, first principles density functional theory code. A fcc supercell containing 256 ± 1 atoms ($+1$ and -1 for interstitial and vacancy, respectively) is used. Calculations are also performed LAMMPS [207] classical potential simulations using embedded atom method potentials for Ag [88] and Cu [187] to study the convergence of the elastic dipole tensors up to supercell sizes of 2048 atoms. The discrepancy in the elastic **P**-tensor components between the 256-atom supercell and that of 2048-atom supercell is found lower than 4%. This supercell size ensures the convergence of defect formation energies to within few meV, as detailed in the Supplementary Note from Ref. [255]. The 256-atom density functional

theory simulations is therefore viewed as well converged with respect to model size. A $3 \times 3 \times 3$ shifted Monkhorst-Pack K-point grid mesh, a Hermite-Gaussian broadening of 0.25 eV [184], and a plane wave cutoff energy of 400 eV are used. The change of the elastic dipole tensors is less than 0.5% compared to tighter settings. The Perdew-Burke-Ernzerhof [205] exchange-correlation functional is conveniently used within the projector-augmented-wave approach [150]. The structures are internally relaxed with a force convergence criterion of 10^{-3} eV/Å. The climbing image nudged elastic band method [117] is employed to find the saddle points for defect migration.

Object kinetic Monte Carlo algorithm

The defect diffusion is investigated by using an object kinetic Monte Carlo code with a residence time algorithm to advance the simulation clock [38, 101]. At time t, the time step is chosen according to $\Delta t = -(\ln r_1)/w_{\text{tot}}$, where r_1 is a random number with $r_1 \in]0,1]$ and w_{tot} is the sum of frequencies of all events that may occur at t, i.e. $w_{\text{tot}} = \sum_i^N w_i$. The chosen event j is such that $\sum_i^{j-1} w_i < r_2 w_{\text{tot}} \leq \sum_i^j w_i$, where r_2 is another random number with $r_2 \in]0,1]$.

Three kinds of events are considered in the simulations: the jump of a point defect from one stable point to a neighbouring one, the absorption of a defect by an interface, and the creation of a new point defect through irradiation. Jump frequencies are given by $w_i = \nu \exp(-\Delta E_i/(kT))$, where ν is an attempt frequency and $\Delta E_i = E_i^{\text{sad}} - E_i^{\text{sta}}$ is the energy difference between the saddle position and the initial stable position of the jump considered. The stable point energy is

$$E_i^{\text{sta}} = -\sum_{k,l} P_{kl,i}^{\text{sta}} \, \varepsilon_{kl}^{\text{int}}(\boldsymbol{r}_i^{\text{sta}}) \,, \tag{3.60}$$

while the saddle point energy is

$$E_i^{\text{sad}} = E^{\text{m}} - \sum_{k,l} P_{kl,i}^{\text{sad}} \, \varepsilon_{kl}^{\text{int}}(\boldsymbol{r}_i^{\text{sad}}) \,, \tag{3.61}$$

with E^{m} the migration energy in the absence of elastic interactions. Here, $\mathbf{P}^{\text{sta}}$ and $\mathbf{P}^{\text{sad}}$ are the defect $\mathbf{P}$-tensors in the ground state and saddle point configurations, respectively. For simplicity, the position of the saddle point $\boldsymbol{r}_i^{\text{sad}}$ is taken mid-way between the two stable points explored by the jump [236].

The defect is considered to have been absorbed by an interface if it reaches the nearest atomic row to the interface. It is then simply removed from the simulation. This absorption condition is used to obtain a first estimate of sink strength, without taking into account the diffusion of point defects along interfaces or their possible reemission. The irradiation rate is fixed at the beginning of each simulation to keep the average number of point defects equal to 200 in the material where the measurements are performed, if no elastic interactions are considered. The actual number of point defects in the system, averaged over the simulation time when steady state is reached, constitutes the basis for the sink strength calculation.

The concentration of defects is recorded every 10^4 iterations, after the concentration has become stationary. At the end of the simulation, an estimate of the average defect concentration $\overline{C}$ is computed by averaging over the values C_j, with $j = 1, \ldots, n$, as follows

$$\overline{C}_n = \frac{1}{n} \sum_{j=1}^{n} C_j \,. \tag{3.62}$$

The final time is adjusted to obtain sufficient accuracy on $\overline{C}$ and thus on the associated sink strength k^2 in accordance with the mean field rate theory formalism [301]. For this purpose, the

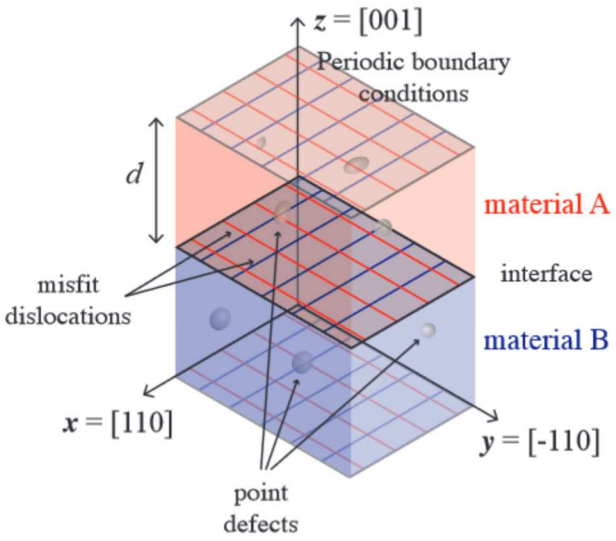

FIGURE 3.19: Schematic illustration of the diffusion of radiation-induced point defects (illustrated by ovals) to interfaces under the influence of interface elastic fields. In general, materials A and B may be any two crystalline solids. In the present work, they are chosen to be either Cu or Ag.

estimation of the error on the concentration is given by the standard error of the mean value, i.e.

$$\delta\overline{C}_n = \frac{\sigma_n}{\sqrt{n}}, \tag{3.63}$$

where

$$\sigma_n^2 = \frac{1}{n-1}\sum_{j=1}^{n}\left(C_j - \overline{C}_n\right)^2 . \tag{3.64}$$

The final time for each system is chosen so that the relative error on $\overline{C}$ and k^2 is less than 0.5%.

3.5.2 Kinetic Monte Carlo simulations with elastic interactions

Modelling the removal of radiation-induced point defects at sinks is a challenging task: on one hand, the variety and complexity of defect behaviors call for the flexibility of atomistic modelling. On the other, the relatively slow, thermally activated mechanisms of defect motion require longer simulation times than may be reached using conventional atomistic techniques, such as molecular dynamics. The object kinetic Monte Carlo (OKMC) method [38, 101, 56, 135] is employed, which is well suited to modeling long-time, thermally activated processes yet is also able to account for nuances of defect behavior uncovered through atomistic modeling.

Figure (3.19) illustrates the setup of the simulations containing two crystalline layers—A and B—separated by semicoherent interfaces. Periodic boundary conditions are applied in all directions, so each model contains two A-B interfaces. Due to their inherent internal structure, the interfaces create characteristic stress fields in the neighbouring crystalline layers. These stress fields interact with radiation-induced point defects, modifying their diffusion.

The interface stress fields is computed by the approach discussed in section 3.2. For illustration, two specific interfaces are treated in the present work: a low-angle twist GB on a (001) plane in Ag and a pure misfit (zero misorientation) heterophase interface between (001) planes of Ag and Cu. Figure (3.20a) shows a plan view of the Ag twist GB, where the adjacent GB planes have been rotated by $\pm\theta/2$ (θ: twist angle). The boundary plane contains two sets of parallel, pure screw dislocations: one aligned with the $x = [110]$ direction and the other with the $y = [\bar{1}10]$ direction. For a relative twist angle of $\theta = 7.5°$, the spacing between dislocations within each set is ~ 2.2 nm.

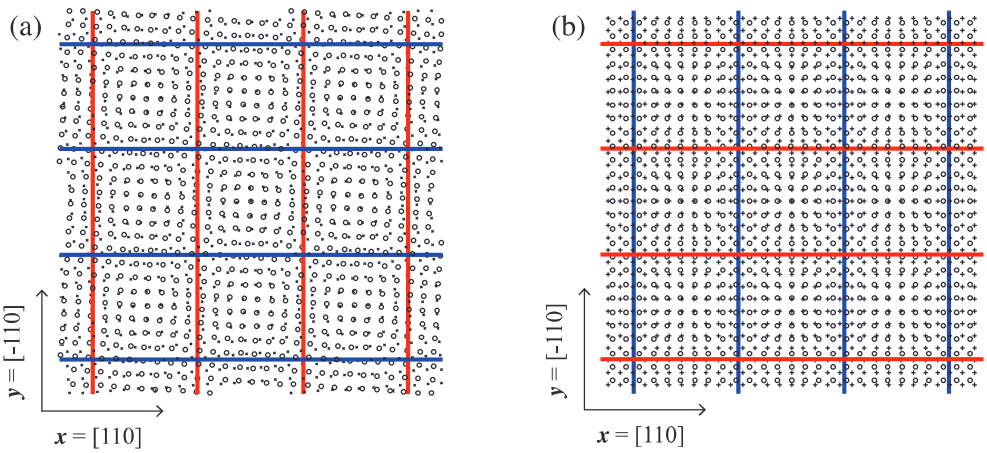

FIGURE 3.20: Planar semicoherent interfaces with identical misfit dislocation arrangements in (a) Ag twist GB with pure screw dislocations and (b) a Ag/Cu misfit interface with pure edge dislocations.

Figure (3.20b) shows the interface plane of the Ag/Cu pure misfit interface. Similar to the twist boundary in Fig. (3.20a), this interface also contains two sets of parallel dislocations aligned with the $\boldsymbol{x} = [110]$ and $\boldsymbol{y} = [\bar{1}10]$ directions. Furthermore, the spacing between dislocations in the Ag/Cu interface is the same as in the twist boundary of Fig. (3.20a): ~ 2.2 nm. However, unlike in the twist boundary, both sets of dislocations in the misfit interface are of pure edge type.

The two interfaces in Fig. (3.20) have identical dislocation arrangements, but different dislocation characters. Thus, they contain identical dislocation densities, but have differing stress fields. For instance, all normal stress components for the twist GB are zero throughout the entire bicrystal. This stress field is therefore purely deviatoric. By contrast, due to symmetry, the shear stress σ_{12} is everywhere zero for the Ag/Cu interface, but all of its other stress components are in general non-zero. In particular, this interface generates significant hydrostatic stresses. These differences have important implications for interface-defect interactions and defect migration pathways.

The force dipole moment approximation is used to compute elastic interaction energies between point defects and interfaces, $E^{\mathrm{PD/int}}$ [140, 226, 71]:

$$E^{\mathrm{PD/int}} = -P_{ij}\,\varepsilon_{ij}^{\mathrm{int}}\,(x,y,z)\ . \tag{3.65}$$

Here, $\varepsilon_{ij}^{\mathrm{int}}\,(x,y,z) = E_{ij}\,(x,y,z)$ are the short-range components of the previously calculated interface strain field, given by eq. (3.12a). On the other hand, P_{ij} are the components of the elastic dipole tensor (the "**P**-tensor"), which describes the elastic fields generated by a point defect. $E^{\mathrm{PD/int}}$ values are used to compute stress-dependent energy barriers for defect migration at each location in the simulation cell. A similar approach has been adopted in previous OKMC studies to describe point defect interactions with dislocations [228, 236].

The density functional theory is used to calculate **P**-tensors for two types of point defects in Ag and Cu: vacancies and self-interstitials of lowest formation energy, namely $\langle 100\rangle$-split dumbbells [242]. The **P**-tensor values for these defects are obtained in their ground states as well as at their saddle point configurations during migration (found using the climbing image nudged elastic band method [117]). Starting from a simulation cell containing a perfect, stress-free crystal, the point defect of interest is inserted in the desired location and relax the atom positions while keeping the simulation cell shape fixed. The point defect induces stresses, σ_{ij}, in the simulation cell. They are related to the defect **P**-tensor through

$$P_{ij} = V\,\sigma_{ij} = P_{ij}^{\mathrm{d}} + p^{\mathrm{h}}\,\delta_{ij}\,, \tag{3.66}$$

Element	Interstitial		Vacancy	
	Ground state	Saddle point	Ground state	Saddle point
Ag	$\begin{bmatrix} 26.80 & 0 & 0 \\ 0 & 26.86 & 0 \\ 0 & 0 & 26.86 \end{bmatrix}$	$\begin{bmatrix} 26.69 & 2.59 & 0 \\ 2.59 & 26.69 & 0 \\ 0 & 0 & 27.74 \end{bmatrix}$	$\begin{bmatrix} -3.04 & 0 & 0 \\ 0 & -3.04 & 0 \\ 0 & 0 & -3.04 \end{bmatrix}$	$\begin{bmatrix} -2.64 & -0.39 & 0 \\ -0.39 & -2.64 & 0 \\ 0 & 0 & 2.15 \end{bmatrix}$
Cu	$\begin{bmatrix} 17.46 & 0 & 0 \\ 0 & 17.66 & 0 \\ 0 & 0 & 17.66 \end{bmatrix}$	$\begin{bmatrix} 18.01 & 1.78 & 0 \\ 1.78 & 18.01 & 0 \\ 0 & 0 & 18.46 \end{bmatrix}$	$\begin{bmatrix} -3.19 & 0 & 0 \\ 0 & -3.19 & 0 \\ 0 & 0 & -3.19 \end{bmatrix}$	$\begin{bmatrix} -3.61 & -0.37 & 0 \\ -0.37 & -3.61 & 0 \\ 0 & 0 & 2.12 \end{bmatrix}$

TABLE 3.6: Elastic dipole tensors **P**-tensors (in eV) of point defects from first principles for a ⟨100⟩-split dumbbell self-interstitial and a vacancy in Ag and Cu at both the ground state and saddle point configurations. The ground state interstitial is oriented in the [100] direction. Its saddle point configuration is for a [100]-to-[010] migration path. The vacancy saddle point is for migration along the [110] direction.

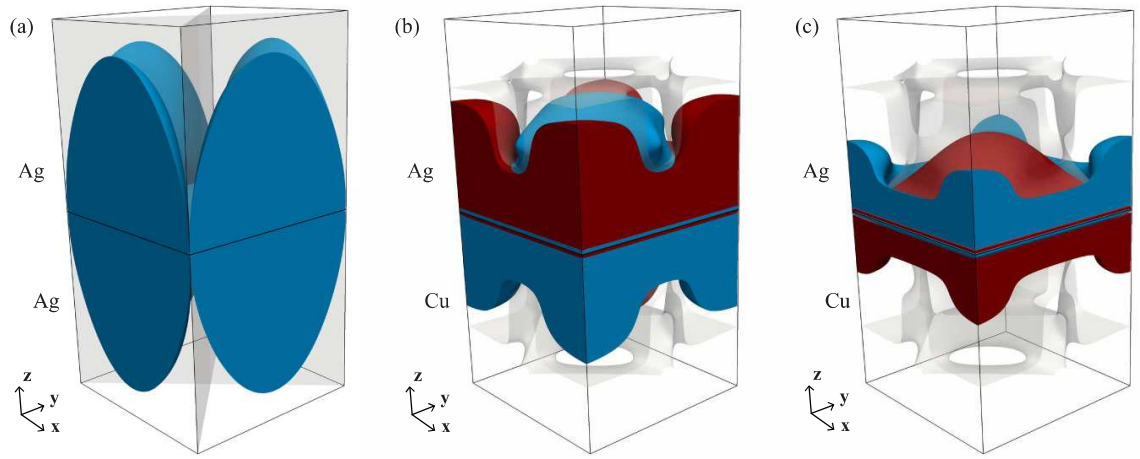

FIGURE 3.21: Elastic interaction energy between (a) an interstitial with the Ag twist GB ($E^{\mathrm{PD/int}} < -0.002$ eV in the blue isovolume), and between the Ag/Cu misfit interface with (b) an interstitial and (c) a vacancy ($E^{\mathrm{PD/int}} < -0.06$ eV in the blue isovolume; $E^{\mathrm{PD/int}} > 0.06$ eV in the red; gray contours are locations with zero interaction energy).

where V is the simulation cell volume. P^{d}_{ij} and p^{h} are the deviatoric and hydrostatic (isotropic) **P**-tensor components, respectively. The former is associated with a pure shear (no volume change) while the latter is related to isotropic tension (interstitials) or compression (vacancies), which leads to a volume change.

Table 3.6 lists the **P**-tensors used in the present study. All of them are expressed in the Nye frame, where the **X**-, ***Y***-, and ***Z***-axes are aligned with the [100], [010], and [001] Miller index directions, respectively. The form of the **P**-tensor reflects the symmetry of the corresponding defect. Thus, the **P**-tensor for a vacancy in its ground state is isotropic while that of an interstitial is tetragonal. **P**-tensors for defect orientations other than those given in Table 3.6 may be calculated using coordinate system rotations. The **P**-tensors for ⟨100⟩-split dumbbell self-interstitials and vacancies in Cu agree with experimental data [114, 242, 285]. Furthermore, the present calculations of relaxation volumes of a vacancy in Ag and Cu are in very good agreement with recent ab-initio predictions [191].

Figure (3.21) shows the distribution of ground state interstitial and vacancy interaction energies with the Ag twist GB and the Ag/Cu misfit interface. A ⟨100⟩-split dumbbell interstitial may take on three different orientations. Figure (3.21) uses the orientation with lowest $E^{\mathrm{PD/int}}$. For the Ag twist GB, interstitial interaction energies are negative at all locations, as shown in Fig. (3.21a). Thus, all interstitials in the vicinity of this GB experience a thermodynamic driving force to migrate towards the boundary. The interstitials, however, have nearly isotropic **P**-tensors (see Table 3.6), so their interaction energies with the Ag twist GB are very small. The interaction

energy of vacancies with the Ag twist GB is everywhere zero due to the absence of hydrostatic stresses near this interface. However, the anisotropy of the vacancy saddle point configuration leads to non-zero interaction energies of migrating vacancies with the GB.

Interstitial interaction energies near the Ag/Cu misfit interface, shown in Fig. (3.21b), may be attractive or repulsive, depending on the location of the defect. Thus, interstitials in Ag are expected to migrate towards the center of the dislocation pattern while those in Cu are expected to migrate to dislocation cores. Figure (3.21c) shows the interaction energy between vacancies and the Ag/Cu misfit interface. The spatial variation of this interaction energy is similar to that of the interstitials, but with opposite sign.

The OKMC simulations assume a constant, uniform defect creation rate, G. Defects diffuse until they are absorbed by an interface. Only individual interstitials or vacancies are tracked in the simulations: defect reactions, such as clustering or recombination, are not considered. After a certain simulation time, defect distributions reach a steady state, whereupon the defect concentration is computed as a function of position along the z-direction (normal to the interface plane) based on the time spent by each defect on a given atomic site.

3.5.3 Effect of elastic interactions on interface sink strength

Figure (3.22) shows steady-state vacancy and interstitial concentrations for the two types of interfaces described above for models with 10 nm-thick Ag and Cu layers. In the absence of elastic interactions between defects and interfaces, steady-state defect concentrations may be computed analytically, which are successfully compared with the simulation results.

Elastic interactions have a dramatic effect on defect concentration profiles. In all cases shown in Fig. (3.22) except vacancies near Ag/Cu interfaces, there are nearly no defects within ~ 2 nm-wide zones adjacent to the interfaces. By contrast, without elastic interactions, defect concentrations are zero only at the interfaces themselves. Moreover, even though defect-interface elastic interaction energies are negligible beyond ~ 2 nm, the zones depleted of defects near the interfaces have a pronounced effect on defect concentrations throughout the entire layer, markedly reducing the average defect concentration. For the simulations in Fig. (3.22), elastic interactions reduce defect concentrations by about a factor of two even in the middle of the layers. This effect is even more pronounced for thinner layers. For vacancies in Ag/Cu, local traps are responsible for the sharp increase in concentration near the interface.

The simulations account for numerous aspects of defect-interface elastic interactions, such as defect anisotropy or differences in defect ground state and saddle point properties. To discover which ones are primarily responsible for the defect concentrations shown in Fig. (3.22), some of these characteristics are artificially "switched off" and repeated the OKMC simulations to see whether doing so changes the steady-state defect concentrations. These calculations demonstrate that the anisotropy of the **P**-tensor in the saddle point configurations is primarily responsible for the reduced defect concentrations in Figs. (3.22a) and (3.22b).

The saddle point anisotropy is "switched off" by replacing the saddle point **P**-tensor with $\mathbf{P}^{\text{sad}} = p^{\text{h}}_{\text{sad}}\,\mathbf{I}$, where $\mathbf{I}$ is the identity matrix and $p^{\text{h}}_{\text{sad}}$ is one third of the trace of the true saddle point **P**-tensor. This assumption is tantamount to modelling defects at saddle points as misfitting spherical inclusions in isotropic media. Concentration profiles obtained with this approximation are markedly different from the anisotropic case, as shown in Fig. (3.22). In the case of the Ag twist GB (Figs. (3.22c) and (3.22d)), isotropic saddle points yield the same defect concentrations as when there are no defect-interface interactions at all. Indeed, since the twist interface generates no hydrostatic strain field, only the deviatoric components of defect **P**-tensors may interact with these interfaces. Ground state vacancies have zero deviatoric **P**-tensor components, so the interaction energy with the Ag twist GB vanishes, similar to ground state interstitials with nearly isotropic **P**-tensors (Table 3.6). The same conclusions hold at saddle positions if saddle point anisotropy

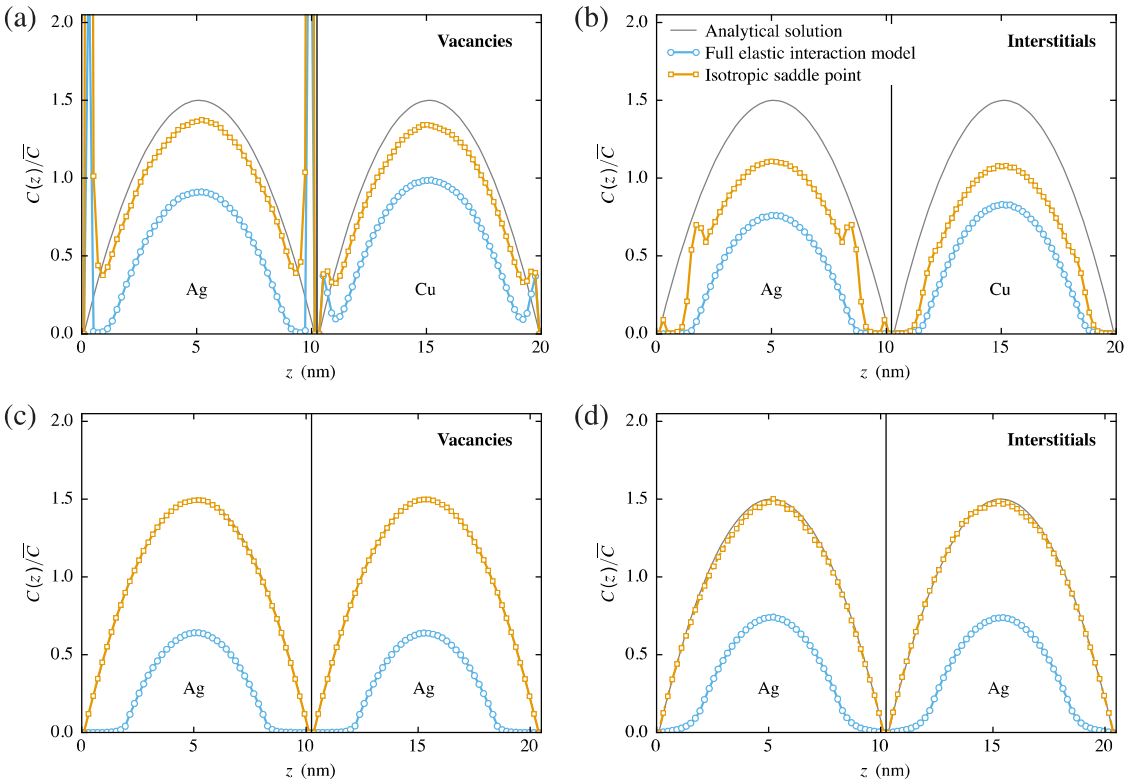

FIGURE 3.22: Steady-state point defect concentrations as a function of location normal to interface planes. The black vertical lines represent the interface planes, while the continuous gray lines denote the reference case with no elastic interactions, computed analytically. OKMC results for both isotropic (orange) and anisotropic (blue) saddle point configurations are shown. (a) Vacancy and (b) interstitial profiles near Ag/Cu pure misfit interfaces. (c) Vacancy and (d) interstitial profiles near Ag twist GBs. Concentrations are normalized by the average concentration $\overline{C}$ obtained when no elastic interactions are taken into account.

is "switched off", as describe above. Elastic interactions then do not affect migration energies, explaining why defect concentrations are identical to the case without elastic interactions.

For the Ag/Cu interface, concentration profiles computed without saddle point anisotropy lie between the non-interacting and fully anisotropic cases, as shown in Figs. (3.22a) and (3.22b). Vacancy concentrations are only marginally lower than the non-interacting case (Fig. (3.22a)), demonstrating the overriding importance of saddle point anisotropy in their behavior. Interstitial concentrations obtained without saddle anisotropy lie approximately mid-way between the fully anisotropic and non-interacting cases (Fig. (3.22b)), demonstrating that saddle point anisotropy is at least as important to their behavior as are $p\,\Delta V$ interactions, which are more commonly investigated.

Figure (3.23) gives a more detailed view of defect concentrations at different locations in the Ag layer of the Ag/Cu interface and in the Ag twist GB. Close to these interfaces, concentrations vary as a function of location parallel to the interface plane, following the strain field pattern created by the interfaces. Indeed, the strain field creates preferential paths for defect migration, as shown by the gray trajectories in Fig. (3.23). These paths are in general different for interstitials and vacancies. For both the Ag/Cu interface and Ag twist GB, vacancies preferentially migrate to the dislocation lines, while interstitials are mostly absorbed between dislocations. This preferential, non-random walk drift of point defects to specific locations is responsible for the enhanced interface sink strengths. Knowing the steady-state defect concentrations obtained by OKMC, sink strengths are derived for the two interfaces considered above. In the mean field rate theory formalism [41], "sink strengths" quantify the ability of sinks, such as interfaces, to absorb defects.

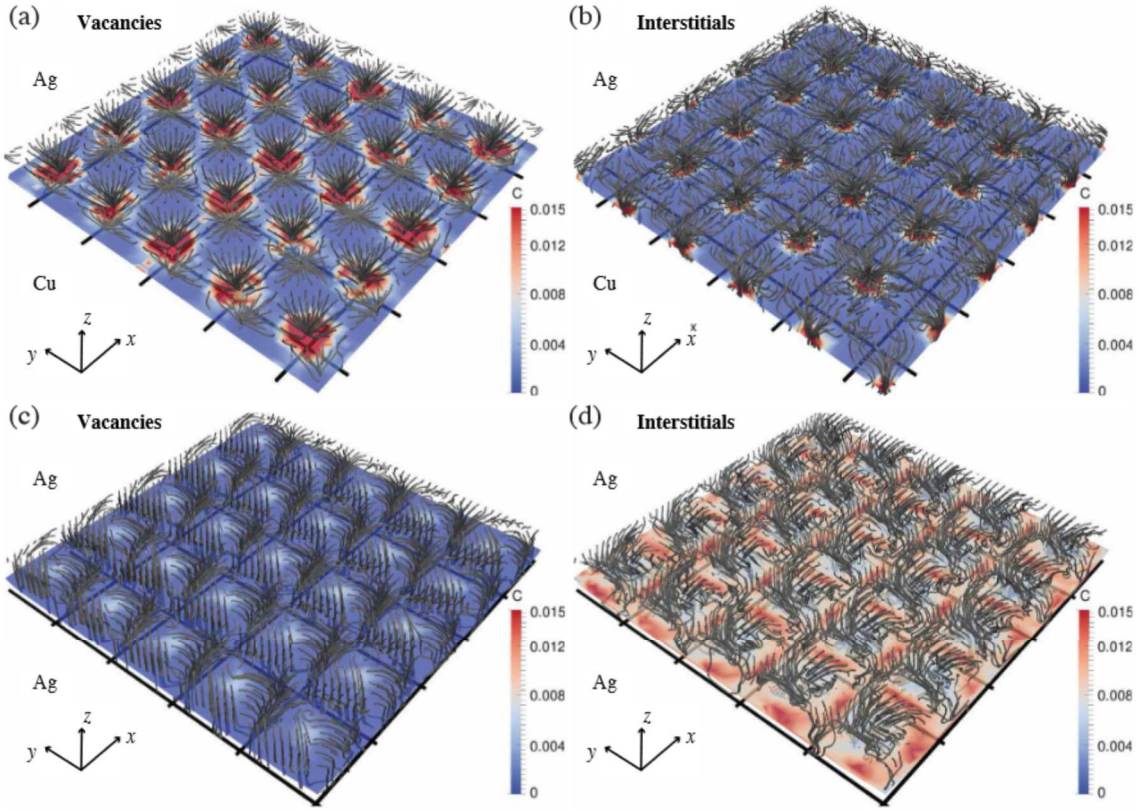

FIGURE 3.23: Preferential migration paths and local concentrations of (a) vacancies and (b) interstitials on the Ag side of the Ag/Cu interface and of (c) vacancies and (d) interstitials in the Ag twist GB. Migration paths are shown as gray lines originating from 1 nm away from the interface. The square grid of black lines represents interface dislocations. Concentrations are plotted in a plane located two atomic distances away from the interface. The concentrations are normalized by $\overline{C}$: the average concentration when no interactions are considered. Any normalized concentration values higher than 0.015 are shown as equal to 0.015.

Within this formalism, the evolution equation for the average defect concentration, $\overline{C}$, follows

$$\frac{d\overline{C}}{dt} = G - k^2 D\overline{C}\,, \tag{3.67}$$

where G is the defect creation rate and D is bulk defect diffusivity. The second term on the right hand side is related to the loss of defects at sinks with associated sink strength, k^2. At steady state, the sink strength may be computed from the average concentration:

$$k^2 = \frac{G}{D\overline{C}}\,. \tag{3.68}$$

Using the average of the concentration profile computed for defect removal at interfaces in the absence of elastic interactions, the interface sink strength is analytically found to be $k^2 = 12/d^2$ [46]. When interactions between interfaces and defects are present, the sink strength is numerically determined through eq. (3.68), by using the average steady-state concentration obtained by OKMC simulations and the diffusion coefficient without elastic interactions. The resulting vacancy and interstitial sink strengths for both interfaces are shown in Fig. (3.24a−f) as a function of layer thickness.

In all cases, the sink strength increases significantly when elastic interactions are taken into

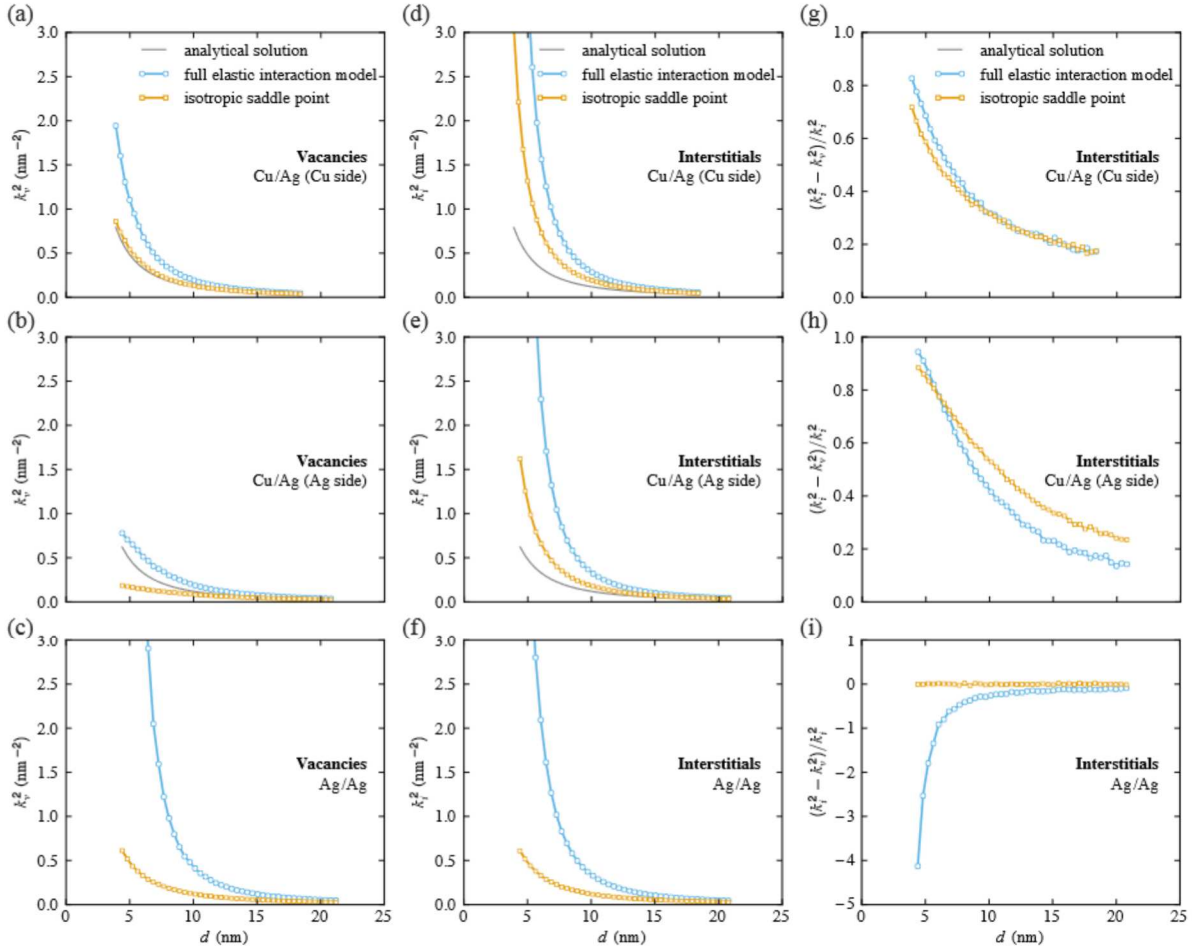

FIGURE 3.24: Enhancement in sink strength of Ag/Cu interfaces and Ag twist GBs for (a−c) vacancies (k_v^2) and (d−f) interstitials (k_i^2) in a given layer (Ag or Cu), as a function of layer thickness, d. (g−i) Bias factors of Ag/Cu interface and Ag twist GB. The gray line corresponds to the analytical solution when no interaction is present ($k^2 = 12/d^2$). Orange and blue lines correspond to OKMC calculations without saddle point anisotropy and with the fully anisotropic interaction model, respectively.

account. This effect is especially pronounced for thinner layers, as defects undergo elastic interactions with interfaces over a larger fraction of the layer. It is particularly strong for interstitials, whatever the interface type, and for vacancies for the twist interface. These results also confirm the importance of saddle point anisotropy: by comparing with OKMC simulations that use isotropic saddle-point **P**-tensors, it yields order-of-magnitude increases in sink strength, in some cases.

Another quantity of interest for radiation response is the bias factor, B, which expresses the propensity of a given sink to absorb more interstitials than vacancies. It is defined as

$$B = \frac{k_i^2 - k_v^2}{k_i^2}\,, \tag{3.69}$$

where k_v^2 and k_i^2 are the sink strengths for vacancies and interstitials, respectively. For example, small interstitial clusters and dislocations exhibit positive bias factors (typically between 0.01 and 0.3 [47, 116]) and thus absorb more interstitials than vacancies. The preferential absorption of interstitials by biased sinks leads to an excess of remaining vacancies, which cluster and eventually aggregate into voids [47, 178].

Bias factors for the semicoherent interfaces are shown in Fig. (3.24g−i). Values larger than 0.2

are obtained for the fully anisotropic interaction model in the case of the Ag/Cu interface. Such interfaces would compete for interstitials with dislocations. The presence of two sinks of differing bias magnitude has been given as a possible cause for void swelling suppression in ferritic steels [168]. Interestingly, for the Ag twist GB the bias factor is negative, meaning that these interfaces tend to absorb more vacancies than interstitials. Similar observations have been made in Ref. [229], where the bias factor for single screw dislocations is negative when using anisotropic elasticity theory and zero in the isotropic approximation. Such GBs may therefore deplete excess vacancy concentrations sufficiently to inhibit void nucleation.

3.6 Elastic strain relaxation in interfacial dislocation patterns

The interfacial dislocation-based model described in section 3.2 has been extended to investigate the equilibrium relaxed dislocation microstructures with specified constraints on semicoherent interfaces [249, 250]. The present parametric energy-based framework includes surface/interface stress and elasticity effects as additional constitutive relations, which are viewed as infinitely thin membranes in contact with each individual material, give rise to non-classical boundary conditions. The elastic field solutions are used to compute the corresponding strain energy landscapes for planar hexagonal-shaped configurations containing three sets of misfit dislocations with unextended three-fold nodes.

3.6.1 General considerations on hexagonal-shaped dislocation patterns

The mechanical dislocation-based problem for determining the elastic strain relaxation of interfacial patterns formed by joining two linear anisotropic elastic materials A and B is described by adopting specific notations and conventions in Fig. (3.25). In the global coordinate system $(O, \boldsymbol{x}_1^{or}, \boldsymbol{x}_2^{or}, \boldsymbol{x}_3^{or})$, corresponding to the orientation relations along fixed crystal directions of the system of interest, the semicoherent interface is located at the coordinate $x_2^{or} = 0$, with $x_2^{or} > 0$ for material A, and $x_2^{or} < 0$ for material B. Such directions are not necessary related to high symmetry directions, so that the anisotropic elastic constants may be displayed in the most general form. In the present work, the unit vector normal to the interface is $\boldsymbol{n} \parallel \boldsymbol{x}_2^{or}$, and a coplanar free surface to the semicoherent interface is potentially introduced at $x_2^{or} = h_A$, whereas B is always a semi-infinite linear elastic crystal.

The crystallography of all interfaces is completely specified between close-packed planes of neighboring materials, so that both orientation relations of crystals A and B with relative misorientations (tilt and twist) and differing lattice parameters (misfit) are described using the previous concept of reference/natural states, as defined in section 3.2. As an example, the 2.5° Ta (tantalum) twist boundary is illustrated in Fig. (3.25a). In the reference state, the interface is coherent, but the interface is not coherent in the natural state, and the atomic structures of interfaces lead to the formation of periodic networks of misfit dislocations that may undergo local relaxations or reconstructions [94].

The closely related quantized Frank-Bilby equation [93, 30, 29] and the O-lattice theory [32] are crystallographic approaches used to describe intrinsic dislocation structures at semicoherent interfaces, which provide the interfacial dislocation geometries in terms of line directions and spacings for one, two, or three independent, planar, and uniformly spaced parallel sets of infinitely long straight dislocations. As illustrated in the previous sections, however, such purely geometrical approaches are not able to characterize local reactions of crossing dislocations to form dislocation segments with different Burgers vectors in mesh networks that are energetically favorable.

The extended formalism for predicting the interface dislocations arrays linking the quantized Frank-Bilby equation and anisotropic elasticity theory under the condition of vanishing the far-field stresses is used to identify the periodicity of the structures with two sets of dislocations from

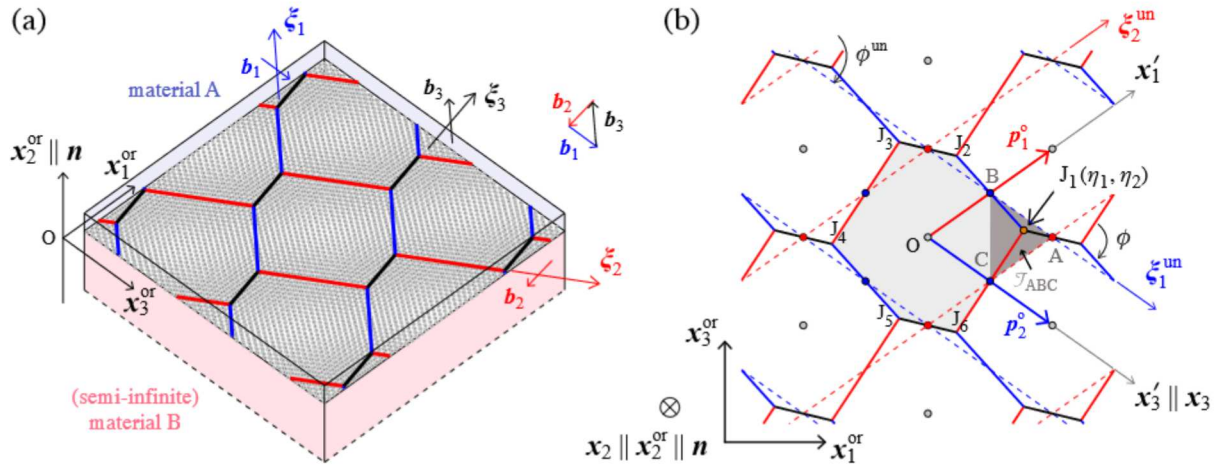

FIGURE 3.25: Geometry of a hexagonal-shaped dislocation pattern containing three sets of interface dislocations with the associated individual Burgers vectors. (a) The orientation relationships between the adjacent linear materials are defined with respect to the global coordinate system $(\mathrm{O}, \boldsymbol{x}_1^{\mathrm{or}}, \boldsymbol{x}_2^{\mathrm{or}}, \boldsymbol{x}_3^{\mathrm{or}})$, within which the semicoherent interface is located at $x_2^{\mathrm{or}} = 0$. For illustration, the current intrinsic dislocation structure is associated with a planar $\{011\} \parallel \boldsymbol{n}$ twist GB between two bcc crystals with a 2.5° rotation angle. (b) Anisotropic elasticity calculations are performed in the non-orthogonal $(\mathrm{O}, \boldsymbol{x}_1' \parallel \boldsymbol{p}_1^{\mathrm{o}}, \boldsymbol{x}_2 \parallel \boldsymbol{n}, \boldsymbol{x}_3' \parallel \boldsymbol{p}_2^{\mathrm{o}})$ frame with fixed basis vectors, where $\boldsymbol{p}_1^{\mathrm{o}}$ and $\boldsymbol{p}_2^{\mathrm{o}} \neq \boldsymbol{p}_1^{\mathrm{o}}$ are the O-lattice vectors that describe the periodicity of the dislocation structures. The fixed red and blue points characterize the initial lozenge-shaped unit cell and the pivot points for elastic strain relaxations, respectively. The grey points are related to the O-lattice points, separated by the networks of interfacial dislocations with three-fold dislocation junction nodes where the conservation law of Burgers vectors is satisfied, e.g. at the specific orange node J_1 that is parametrized by the dimensionless coordinates (η_1, η_2). For convex hexagonal-shaped dislocation configurations, J_1 may move within the shaded triangular domain $\mathcal{T}_{\mathrm{ABC}}$ in dark grey.

the pre-determined O-lattice vectors $\boldsymbol{p}_1^{\mathrm{o}}$ and $\boldsymbol{p}_2^{\mathrm{o}} \neq \boldsymbol{p}_1^{\mathrm{o}}$, as illustrated in Fig. (3.25b). These two vectors characterize the initial lozenge-shaped unit cell of crossing dislocation sets (red points), for which the translations of the unit cell by the basis vectors $\boldsymbol{p}_1^{\mathrm{o}}$ and $\boldsymbol{p}_2^{\mathrm{o}}$ tessellate the entire interface plane. In the following, the superscript $^{\mathrm{un}}$ will be used to indicate quantities related to the unrelaxed dislocation configurations, e.g. $\boldsymbol{\xi}_1^{\mathrm{un}} \parallel \boldsymbol{p}_2^{\mathrm{o}}$ and $\boldsymbol{\xi}_2^{\mathrm{un}} \parallel \boldsymbol{p}_1^{\mathrm{o}}$ correspond to the initial dislocation directions of the two sets that consist of the lozenge-shaped patterns, with Burgers vectors $\boldsymbol{b}_1$ and $\boldsymbol{b}_2$, respectively, as stated in section 3.2. Planar energetically favorable interactions may lead to the formation of dislocation junctions with coplanar Burgers vector $\boldsymbol{b}_3$, i.e.

$$\boldsymbol{b}_1 + \boldsymbol{b}_2 \rightarrow \boldsymbol{b}_3 \,, \tag{3.70}$$

such that the current semicoherent interfaces contain infinite, planar, and periodic dislocation structures with three sets of misfit dislocations. As illustrated in Fig. (3.25b), the third newly formed set (in black) is associated with the junction formation due to the local rearrangements between two initial crossing dislocation arrays, shown by the blue and red dashed lines. The current directions of the three sets of misfit dislocations are denoted by $\boldsymbol{\xi}_1$, $\boldsymbol{\xi}_2$, and $\boldsymbol{\xi}_3$ for which the latter is associated with the direction of the in-plane dislocation junctions.

The present reactions yield to hexagonal-shaped patterns with three-fold dislocation nodes, where the centers of the parent dislocation segments from the lozenge-shaped unit cells consist of pinning pivot points (blue points) for glissile planar dislocations. An useful triangular domain $\mathcal{T}_{\mathrm{ABC}}$ for performing parametric energy-based analyses, is represented by two blue pivot points (B and C) and the red intersection point A in which dislocation reactions occur, as shaded in dark grey in Fig. (3.25b). On the other hand, the newly formed representative hexagonal-shaped unit cell (light grey domain), which contains six vertices (dislocation nodes), indexed and ordered by

J_1, J_2, J_3, J_4, J_5, and J_6, is denoted by $\mathcal{H}_{J_1J_2J_3J_4J_5J_6}$. The determination of such infinitely repeated dislocation nodes with the type of rearrangement defined by eq. (3.70) produces neither orientation nor magnitude changes in the O-lattice vectors. Thus, the two-dimensional periodicity of the dislocation networks containing three families of straight parallel dislocation segments in the local Cartesian frame $(O, \boldsymbol{x}_1, \boldsymbol{x}_2, \boldsymbol{x}_3)$ with $\boldsymbol{x}_2 \parallel \boldsymbol{x}_2^{or} \parallel \boldsymbol{n}$, remains unchanged during the elastic strain relaxation processes.

In the previous non-orthogonal (oblique and fixed) frame with basis vectors $(O, \boldsymbol{x}_1', \boldsymbol{x}_2, \boldsymbol{x}_3')$, where $\boldsymbol{x}_1' \parallel \boldsymbol{p}_1^o \parallel \boldsymbol{\xi}_2^{un}$ and $\boldsymbol{x}_3' \parallel \boldsymbol{x}_3 \parallel \boldsymbol{p}_2^o \parallel \boldsymbol{\xi}_1^{un}$, the oriented angle between $\boldsymbol{\xi}_2^{un}$ and $\boldsymbol{\xi}_1^{un}$ is denoted by ϕ^{un}, so that $x_1' = x_1 \csc\phi^{un}$ and $x_3' = x_3 - x_1 \operatorname{ctg}\phi^{un}$. Thus, any position vector in this non-orthogonal frame may be expressed as: $\boldsymbol{r} = x_1' \boldsymbol{p}_1^o + x_3' \boldsymbol{p}_2^o = (x_1 \csc\phi^{un}) \boldsymbol{p}_1^o + (x_3 - x_1 \operatorname{ctg}\phi^{un}) \boldsymbol{p}_2^o$. In particular, the mobile dislocation three-fold node of interest J_1, which is parametrized by the dimensionless coordinates (η_1, η_2) in the first quadrant of the $(O, \boldsymbol{x}_1', \boldsymbol{x}_2, \boldsymbol{x}_3')$ frame, is also defined by: $\boldsymbol{j}_1 = \eta_1 \boldsymbol{p}_1^o + \eta_2 \boldsymbol{p}_2^o$, with $(\eta_1, \eta_2) \in]0, 1/2[^2$, excluding 0 and $1/2$ to describe convex hexagonal-shaped patterns with six distinct dislocation edges. For example, the limiting case of equilibrium arrays with two sets of orthogonal misfit dislocations is given by: $\phi^{eq} = \pi/2$, $\eta_1^{eq} \to 1/2$, and $\eta_2^{eq} \to 1/2$, so that $J_2 \simeq J_3$ and $J_5 \simeq J_6$, as the (010) twist GBs in fcc materials. On the other hand, the regular equilibrium hexagonal network corresponds to the particular case where: $\phi^{eq} = \pi/3$, and $\eta_1^{eq} = \eta_2^{eq} = 1/3$, as the (111) twist GBs in fcc crystals.

3.6.2 Solution methodology for strain-relaxed rearrangements

During the non-random elastic strain relaxations without externally applied stresses, misfit dislocations are rearranged into hexagonal-shaped networks due to local reactions that lower the elastic strain energy at semicoherent interfaces [94, 7]. Such strain-relaxed rearrangements of interfacial dislocation patterns also involve the mechanical problem of finding the minimum-energy paths from a given initial non-equilibrium lozenge-shaped microstructure with two sets of parent misfit dislocations to new unique or multiple (with the same strain energy) stable equilibrium hexagonal-shaped dislocation patterns of lowest energies with possible metastable configurations.

Without changing the interface crystallographic characters upon the relaxation processes, the prescribed displacement jumps for each periodic hexagonal unit cell are also assumed to vary linearly with the (algebraic) directed distance between the O-lattice points (displayed by the grey points in Fig. (3.25b)) and the nearest neighbor interfacial dislocation segments. At the positions of the dislocation segments, the relative displacements are completely described by the directions and constant magnitudes of the associated individual Burgers vectors. Furthermore, the non-classical boundary conditions due to the free surface excess stress and the semicoherent interface excess stress contributions are therefore applied at: $x_2^{or} = h_A$ and $x_2^{or} = 0$, respectively. Thus, the minimum-energy paths are entirely obtained by measuring the removal of the short-range elastic strain energy with respect to the coordinates (η_1, η_2) of J_1, along which the long-range elastic strain-free state is not altered by spurious non-zero far-field strains.

For a given crystallographic orientation relationship between materials A and B, the methodology for determining the equilibrium dislocation configurations for elastic strain relaxation processes along minimum-energy paths is described below. The two first items summarize the strategy procedure for computing the Burgers vectors of interface dislocations using anisotropic elasticity theory, which have been introduced in section 3.2.

1. The geometries in terms of dislocation spacings and line directions, i.e. $\boldsymbol{\xi}_1^{un}$ and $\boldsymbol{\xi}_2^{un}$, related to the initial lozenge-shaped patterns are found by using the quantized Frank-Bilby equation. For such networks containing two sets of straight, parallel, and infinite misfit dislocations, the periodicity of the dislocation structures is also obtained by mapping the O-lattice points at the interfaces. The corresponding computed O-lattice vectors $\boldsymbol{p}_1^o$ and $\boldsymbol{p}_2^o \neq \boldsymbol{p}_1^o$ are conveniently associated with the fixed and non-orthogonal basis vectors of the $(O, \boldsymbol{x}_1', \boldsymbol{x}_2, \boldsymbol{x}_3')$ frame for elasticity analyses, where $\boldsymbol{x}_1' \parallel \boldsymbol{p}_1^o \parallel \boldsymbol{\xi}_2^{un}$, $\boldsymbol{x}_2 \parallel \boldsymbol{n}$, and $\boldsymbol{x}_3' \parallel \boldsymbol{p}_2^o \parallel \boldsymbol{\xi}_1^{un}$.

2. The reference state, within which the individual Burgers vectors of both dislocation sets are defined, i.e. $\boldsymbol{b}_1$ and $\boldsymbol{b}_2$, is determined by combining the Frank-Bilby equation with anisotropic elasticity theory that meets the constraints of interface crystallographic character and zero long-range strains (or stresses) for infinite bicrystals. Because the latter far-field condition is still fulfilled during the elastic strain relaxation processes, the third Burgers vector $\boldsymbol{b}_3$ for the newly formed dislocation junctions is also obtained from the conservation eq. (3.70) of the Burgers vector content at the three-fold node J_1. In the limiting case where a coplanar free surface is located in material A, the reference state (and therefore also, the three Burgers vectors) is fully associated with material B, e.g. the case of a thin film on a semi-infinite substrate.

3. The specific triangular region $\mathcal{T}_{\mathrm{ABC}}$ in the representative lozenge-shaped unit cell, formed by the three fixed points A, B, and C in Fig. (3.25b), is discretized into four-node quadrilateral elements with respect to the i^{th} nodal points with coordinates (η_1^i, η_2^i), such that $\{\eta_1^i, \eta_2^i\} \in \,]0,\, 1/2[^2$. This discretization allows to represent any convex hexagonal-shaped dislocation patterns in the non-orthogonal $(\mathrm{O},\, \boldsymbol{x}_1',\, \boldsymbol{x}_2,\, \boldsymbol{x}_3')$ frame for mechanics-based calculations of elastic field solutions, e.g. displacements, stresses, traction forces, etc.

4. The elastic strain energy stored at semicoherent interfaces is computed at any mesh point (η_1^i, η_2^i), by using the persistent short-range stress and strain field solutions for convex and irregular hexagonal-shaped dislocation configurations. Furthermore, the complete elastic energy landscape $\gamma_{\mathrm{e}}(\eta_1, \eta_2)$ is interpolated for any $(\eta_1, \eta_2) \in \,]0,\, 1/2[^2$ with the aid of standard finite element bilinear shape functions for four-node elements.

5. For energetically favorable reactions, the minimum-energy dislocation configurations are numerically obtained by using the conjugate gradient algorithm on the pre-computed energy landscapes with a given prescribed tolerance. Then, the nudged elastic band method [117, 222] is used to provide access to the minimum-energy paths between the initial (non-equilibrium) lozenge-shaped structures and the determined elastically relaxed dislocation patterns with the aid of the elastic forces: $\boldsymbol{f}_{\mathrm{e}} = -\boldsymbol{\nabla}\gamma_{\mathrm{e}}(\eta_1, \eta_2)$. In practice, all elastic field solutions are recomputed along the curvilinear reaction coordinates of the minimum-energy paths.

3.6.3 Parametric energy-based framework

This section is concerned with the complete expressions of elastic fields for hexagonal-shaped dislocation patterns located at heterophase interfaces between two dissimilar anisotropic materials. The Stroh sextic formalism of anisotropic linear elasticity combined with the surface/interface treatment in Ref. [108] and a Fourier series-based solution technique is therefore used to compute the elastic fields outside the cores of dislocations. In the general case, all surfaces of interest (i.e. semicoherent interfaces and free surfaces) are distinctly considered as infinitely thin membranes with different, separate, and appropriate constitutive equations than the relations for both (bulk) materials A and B.

Again, the pre-subscripts A and B in the elastic properties and also the field expressions will be omitted for clarity in the following if no distinction between materials is required.

Elastic field equations and solutions in bulk materials

In the fixed Cartesian coordinate system $(\mathrm{O},\, \boldsymbol{x}_1,\, \boldsymbol{x}_2,\, \boldsymbol{x}_3)$, the three-dimensional stress field $\boldsymbol{\sigma}(\boldsymbol{x}) = \sigma_{ij}(x_1, x_2, x_3)$ and the displacement field $\boldsymbol{u}(\boldsymbol{x}) = u_i(x_1, x_2, x_3)$ in both crystals A and B are related by the Hooke's law in index form from Eq. (3.12b), as follows

$$\sigma_{ij}(x_1, x_2, x_3) = c_{ijkl}\; u_{k,l}(x_1, x_2, x_3)\,, \tag{3.71}$$

where a comma stands for differentiation, with repeated indices denoting summation convention ranging from 1 to 3, unless stipulated otherwise. The anisotropic elastic constants of the fourth-order stiffness tensor $\mathbb{C}$ are fully symmetric, i.e. $c_{ijkl} = c_{jikl} = c_{ijlk} = c_{klij}$, and the classical partial differential eq. (3.8) of mechanical equilibrium that is fulfilled in both crystals in terms of the displacement fields is given by

$$\sigma_{ij,j}(x_1, x_2, x_3) = c_{ijkl}\, u_{k,jl}(x_1, x_2, x_3) = 0\,. \tag{3.72}$$

According to eq. (3.7), the complete displacement field is expressed as the superposition of the linear displacement contribution from the proper selection of reference states for constrained interfaces and the total displacement fields produced by the arrays of interfacial Volterra dislocations. The latter dislocation displacement fields are also given as a biperiodic Fourier series, i.e.

$$u_k^{\text{dis}}(x_1, x_2, x_3) = \text{Re} \sum_{\boldsymbol{k} \neq \boldsymbol{0}} \text{e}^{i2\pi \boldsymbol{k}\cdot\boldsymbol{r}}\, u_k^{\boldsymbol{k}}(x_2) = 2\,\text{Re} \sum_{D} \text{e}^{i2\pi \boldsymbol{k}\cdot\boldsymbol{r}}\, u_k^{\boldsymbol{k}}(x_2)\,, \tag{3.73}$$

where the Fourier series expansion involves the harmonics $(n,\, m)$ that belong to the upper two-dimensional half-plane domain, defined by $D = \{\{n \in \mathbb{N}^*\} \cup \{m \in \mathbb{Z}^*,\, n = 0\}\}$. For clarity, the subscript $_{\text{dis}}$ in eq. (3.7) has been changed to superscript in eq. (3.73). The components $k_1(n, m)$ and $k_3(m)$ of the wavevectors $\boldsymbol{k}$ are given by eq. (3.6) as follows

$$\boldsymbol{k}\cdot\boldsymbol{r} = \frac{n}{p_1^{\text{o}}}\, x_1' + \frac{m}{p_2^{\text{o}}}\, x_3' = \left(\frac{n\,\csc\phi^{\text{un}}}{p_1^{\text{o}}} - \frac{m\,\text{ctg}\,\phi^{\text{un}}}{p_2^{\text{o}}}\right) x_1 + \frac{m}{p_2^{\text{o}}}\, x_3 = k_1(n, m)\, x_1 + k_3(m)\, x_3\,, \tag{3.74}$$

with $p_1^{\text{o}} = |\boldsymbol{p}_1^{\text{o}}|$ and $p_2^{\text{o}} = |\boldsymbol{p}_2^{\text{o}}|$. On the other hand, the far-field components are computed for two dislocation sets to determine the correct reference state [260], within which the Burgers vectors $\boldsymbol{b}_1$ and $\boldsymbol{b}_2$ (and also $\boldsymbol{b}_3$, by virtue of eq. (3.70)) are defined. Because the elastic (short-range) strain relaxations do not alter the long-range strain state during the junction formation of the third dislocation sets, the removal of the far-field strains (or stresses) in the natural state is fulfilled by solving the tensorial far-field eqs. (3.1), exhibiting non-zero and heterogeneous short-range elastic fields for interfacial dislocation patterns, only. Thus, substituting the displacement field eq. (3.73) into eq. (3.71), the second-order differential equation applied to both materials is obtained in index form as follows

$$-4\pi^2\, \text{W}_{1_{ik}}\, \tilde{u}_k^{\boldsymbol{k}}(x_2) + i2\pi\, (\text{W}_{2_{ik}} + \text{W}_{2_{ki}})\, \tilde{u}_{k,2}^{\boldsymbol{k}}(x_2) + \text{W}_{3_{ik}}\, \tilde{u}_{k,22}^{\boldsymbol{k}}(x_2) = 0\,, \tag{3.75}$$

where $\mathbf{W}_1$, $\mathbf{W}_2$, and $\mathbf{W}_3$ are 3×3 real matrices defined in eqs. (3.10). In eq. (3.75), the superimposed tilde to any quantities will be used to indicate that the corresponding field solutions are consistent with the Frank-Bilby equation under the condition of vanishing far-field strains (or stresses) for any dislocation patterns. For non-zero wavevectors $\boldsymbol{k}$, the standard solutions satisfying eq. (3.75) can be written in the following form [64]

$$\tilde{u}_k^{\boldsymbol{k}}(x_2) = \text{e}^{i2\pi p^{\boldsymbol{k}} x_2}\, a_k^{\boldsymbol{k}}\,, \tag{3.76}$$

where $p^{\boldsymbol{k}} = p$ and $\boldsymbol{a}^{\boldsymbol{k}} = a_k$ become the complex scalar and vectorial unknowns of the boundary value problems, respectively, for which the superscripts $\boldsymbol{k}$ are omitted, for clarity. Introducing eq. (3.76) into eq. (3.75), the vector $\boldsymbol{a}$ is found to satisfy the homogeneous linear system

$$\left[\text{W}_{1_{ik}} + p\, (\text{W}_{2_{ik}} + \text{W}_{2_{ki}}) + p^2\, \text{W}_{3_{ik}}\right] a_k = \Pi_{ik}\, a_k = 0\,, \tag{3.77}$$

which corresponds to the standard eigenvalue problem in anisotropic elasticity theory [234, 240]. A non-zero (non-trivial) solution can be found only if the determinant of $\boldsymbol{\Pi}$ is zero, i.e.

$$\det \Pi_{ik} = 0\,, \tag{3.78}$$

leading to a sextic equation for p. As mentioned in section 3.6.3, the solutions of eq. (3.78) have six imaginary roots, which are arranged such that the three first eigenvalue solutions p^α have positive imaginary parts, indexed by superscripts $\alpha = 1, 2, 3$. The remaining three solutions have negative imaginary parts, so that $p^{\alpha+3} = p^\alpha_*$. The corresponding eigenvectors $\boldsymbol{a}^\alpha = a^\alpha_k$ are also complex conjugates with $\boldsymbol{a}^{\alpha+3} = \boldsymbol{a}^\alpha_* = a^\alpha_{k_*}$, so that the general solution may be rewritten as a linear combination of the three eigenfunctions, i.e.

$$\tilde{u}^{\text{dis}}_k(x_1, x_2, x_3) = 2\,\text{Re}\sum_D \text{e}^{i2\pi \boldsymbol{k}\cdot\boldsymbol{r}} \sum_{\alpha=1}^{3} \lambda^\alpha \text{e}^{i2\pi p^\alpha x_2}\, a^\alpha_k + \zeta^\alpha \text{e}^{i2\pi p^\alpha_* x_2}\, a^\alpha_{k_*}\,, \tag{3.79}$$

which differs from eq. (3.11) by a multiplicative $i2\pi$ term, without loss of generality. It also follows from eq. (3.71) that

$$\tilde{\sigma}^{\text{dis}}_{ij}(x_1, x_2, x_3) = 4\pi\,\text{Re}\sum_D i\,\text{e}^{i2\pi \boldsymbol{k}\cdot\boldsymbol{r}} \sum_{\alpha=1}^{3} \lambda^\alpha \text{e}^{i2\pi p^\alpha x_2}\, \text{H}^\alpha_{ij} + \zeta^\alpha \text{e}^{i2\pi p^\alpha_* x_2}\, \text{H}^\alpha_{ij_*}\,, \tag{3.80}$$

where the 3×3 complex matrices $\mathbf{H}^\alpha$ are related to the eigenvectors $\boldsymbol{a}^\alpha$ by

$$\text{H}^\alpha_{ij} = \left(k_1\, c_{ijk1} + k_3\, c_{ijk3} + p^\alpha c_{ijk2}\right) a^\alpha_k\,, \tag{3.81}$$

from selected elastic constants of materials A and B. In particular, the surface tractions at the semicoherent interfaces, i.e. $x_2 = 0$, are reduced to

$$\tilde{t}^{\,\text{int}}_k(x_1, x_3) = \tilde{\sigma}^{\text{dis}}_{ki}(x_1, 0, x_3)\, n_i = 4\pi\,\text{Re}\sum_D i\,\text{e}^{i2\pi \boldsymbol{k}\cdot\boldsymbol{r}} \sum_{\alpha=1}^{3} \lambda^\alpha\, \text{H}^\alpha_{k2} + \zeta^\alpha\, \text{H}^\alpha_{k2_*}\,, \tag{3.82}$$

as well as the tractions at the free surface, i.e. $x_2 = h_\text{A}$, to

$$\tilde{t}^{\,\text{fs}}_k(x_1, x_3) = \tilde{\sigma}^{\text{dis}}_{ki}(x_1, h_\text{A}, x_3)\, n_i = 4\pi\,\text{Re}\sum_D i\,\text{e}^{i2\pi \boldsymbol{k}\cdot\boldsymbol{r}} \sum_{\alpha=1}^{3} \lambda^\alpha \text{e}^{i2\pi p^\alpha h_\text{A}}\, \text{H}^\alpha_{k2} + \zeta^\alpha \text{e}^{i2\pi p^\alpha_* h_\text{A}}\, \text{H}^\alpha_{k2_*}\,. \tag{3.83}$$

Free surface and semicoherent interface elasticity contributions

Combined with the surface tractions in eqs. (3.82) and (3.83), the additional surface/interface stress contributions, due to the work required by applying in-plane forces to elastically stretch the pre-existing free surfaces and interfaces neighboring both materials A and B into the correct reference states, are introduced as follows

$$\tau_{\chi\varphi}(x_1, x_3) = \gamma\,\delta_{\chi\varphi} + \frac{\partial\,\gamma}{\partial \epsilon^s_{\chi\varphi}(x_1, x_3)}\,, \tag{3.84}$$

where $\tau_{\chi\varphi}(x_1, x_3)$ and $\epsilon^s_{\chi\varphi}(x_1, x_3)$ are the 2×2 surface stress and strain tensors, and γ is the surface free energy [224, 53]. Because eq. (3.84) is derived for the plane stresses acting in the surface area, the stress and strain fields have only in-plane components, and Greek indices take values 1 and 3, only. In order to solve the elasticity problems with appropriate constitutive relations between the surface stress and strain components, a linear constitutive equation analogous to eq. (3.71) is used [221], i.e.

$$\tau_{\chi\varphi}(x_1, x_3) = \tau^0_{\chi\varphi} + d_{\chi\varphi\gamma\eta}\, \epsilon^s_{\gamma\eta}(x_1, x_3)\,, \tag{3.85}$$

where $\tau^0_{\chi\varphi}$ is the surface/interface residual stress tensor and $d_{\chi\varphi\gamma\eta}$ is the fourth-order stiffness tensor of surface/interface elastic constants. When the surface/interface entities are considered as elastic isotropic media, the elasticity tensor contains also two independent constants, known as surface/interface Lamé constants [53].

In the case of realistic semicoherent interfaces, the atomic structures are not exactly like those generated by the linear mappings from a reference state, as idealized and illustrated in Fig. (3.25a) with no atomic relaxations. Indeed, electron microscopy and atomistic calculations have revealed that such boundaries consist of coherent patches separated by networks of interfacial dislocations. The coherency and bounding conditions between such boundaries and the adjacent bulk materials yield therefore to the expression for the surface stresses in terms of the derivatives of the bulk displacement fields, i.e.

$$2\,\epsilon^{s}_{\gamma\eta}(x_1,x_3) = 2\,\tilde{\epsilon}^{\,\mathrm{dis}}_{\gamma\eta}(x_1,0,x_3) = \tilde{u}^{\mathrm{dis}}_{\gamma,\eta}(x_1,0,x_3) + \tilde{u}^{\mathrm{dis}}_{\eta,\gamma}(x_1,0,x_3)\,, \tag{3.86}$$

for all in-plane strain components, at $x_2 = 0$. Similarly to the model for interface stresses with application to misfit dislocations in Ref. [52], this interface/bulk conversion of strain fields in eq. (3.86) depends strongly on the presence of the misfit dislocations (and, therefore, on the non-arbitrary coherent reference states), which in the present case, gives rise to unequally partitioned distortion states, in terms of strains as well as tilt and twist rotations.

The elastic field solutions of the displacements, stresses and tractions of eqs. (3.79), (3.80), and (3.82−3.83) respectively, with respect to surface/interface effects defined by eqs. (3.85−3.86), are also written as linear combinations of the eigenfunctions, within which $\{\lambda^\alpha, \zeta^\alpha\}$ are complex unknown quantities that are to be determined by the boundary conditions. For hexagonal-shaped dislocation patterns, these specific required conditions are expressed in terms of the discontinuities of displacement and stress components across the semicoherent interfaces in bimaterials in presence (if any) of a free surface in the upper material.

3.6.4 Boundary conditions with surface/interface constitutive relations

In what follows in section 3.6.4, expressions of displacements, strains, and stresses, and also all related quantities that are needed to compute these field solutions (e.g., the elastic constants, Burgers vectors $\boldsymbol{b}_1$, $\boldsymbol{b}_2$, and $\boldsymbol{b}_3$, eigenvectors $\boldsymbol{a}^\alpha$, etc.), are expressed in the local oblique and fixed $(\mathrm{O}, \boldsymbol{x}'_1, \boldsymbol{x}_2, \boldsymbol{x}'_3)$ frame. In particular, the boundary conditions are written with respect to the geometry of the dislocation patterns, i.e. to the canonical coordinates (η_1, η_2) of the three-fold dislocation node J_1, as well as the magnitudes and directions of the individual Burgers vectors for three sets of dislocations.

Convergence of the elastic field solutions

For all constrained interfaces that are consistent with the Frank-Bilby equation, i.e. when eqs. (3.1) are fulfilled with respect to the correct reference state, the corresponding semi-infinite linear crystal (here, material B) is also necessary free of all far-field stress components. The elastic stress solution in eq. (3.80) is therefore required to converge to zero at long range, i.e. when $x_2 \to -\infty$. Hence, ${}_{\mathrm{B}}\lambda^\alpha = 0$, independently of interfacial boundary conditions. For infinite bicrystals of interest, the convergence conditions in both materials A and B yield to: ${}_{\mathrm{B}}\lambda^\alpha = {}_{\mathrm{A}}\zeta^\alpha = 0$, when $x_2 \to \pm\infty$, as already defined in section 3.2.5.

Relative displacement due to the interfacial dislocation patterns

In accordance with eq. (3.15), the prescribed relative displacement field $\boldsymbol{u}^p(x_1,x_3)$ for any (irregular) hexagonal-shaped dislocation patterns at the interface, i.e. $x_2 = 0$, is obtained by superposing the contributions of both Burgers vectors $\boldsymbol{b}_1$ and $\boldsymbol{b}_2$, i.e.

$$\boldsymbol{u}^p(x_1,x_3) = \frac{x_1 \csc\phi^{\mathrm{un}}}{p_1^{\mathrm{o}}}\,\boldsymbol{b}_1 + \frac{x_3 - x_1\,\mathrm{ctg}\,\phi^{\mathrm{un}}}{p_2^{\mathrm{o}}}\,\boldsymbol{b}_2 = z_1(x_1)\,\boldsymbol{b}_1 + z_2(x_1,x_3)\,\boldsymbol{b}_2\,, \tag{3.87}$$

where $z_1 = z_1(x_1)$ and $z_2 = z_2(x_1, x_3)$ are dimensionless linear functions. Assuming that the displacement jumps are zero at all positions of the O-lattice points, e.g. at O in the representative unit cell in Fig. (3.25b), the prescribed displacement field is also an odd function with respect to $\boldsymbol{r}$ in the oblique $(\mathrm{O}, \boldsymbol{x}_1', \boldsymbol{x}_2, \boldsymbol{x}_3')$ frame. According to the linear elasticity theory, these displacement jumps produced by each hexagonal-shaped dislocation cell can therefore be formally expressed as double Fourier series for any dislocation configurations with respect to (η_1, η_2), i.e.

$$\boldsymbol{u}^p(x_1, x_3) = \mathrm{Im} \sum_{\boldsymbol{k} \neq \boldsymbol{0}} \mathrm{e}^{i2\pi \boldsymbol{k}\cdot\boldsymbol{r}}\, \hat{\boldsymbol{u}}^p(\eta_1, \eta_2) = -\mathrm{Re}\, i \sum_{\boldsymbol{k} \neq \boldsymbol{0}} \mathrm{e}^{i2\pi \boldsymbol{k}\cdot\boldsymbol{r}} \left(\hat{\boldsymbol{u}}_1^p(\eta_1, \eta_2) + \hat{\boldsymbol{u}}_2^p(\eta_1, \eta_2)\right) , \tag{3.88}$$

where all real-valued expansion coefficients $\hat{\boldsymbol{u}}^p(\eta_1, \eta_2)$ in eq. (3.88) are additionally decomposed into the individual contributions $\hat{\boldsymbol{u}}_1^p(\eta_1, \eta_2)$ and $\hat{\boldsymbol{u}}_2^p(\eta_1, \eta_2)$, associated with $\boldsymbol{b}_1$ and $\boldsymbol{b}_2$, respectively. In particular, the vector quantity $\hat{\boldsymbol{u}}_1^p(\eta_1, \eta_2)$ for $\boldsymbol{b}_1$ is deduced by solving the double integral with respect to z_1 and z_2, as follows

$$\hat{\boldsymbol{u}}_1^p(\eta_1, \eta_2) = \mathrm{Re}\left[i \int_{\bar{z}_1(\eta_1)}^{\bar{\bar{z}}_1(\eta_1)} \left(z_1 \int_{\bar{z}_2(z_1,\eta_1,\eta_2)}^{\bar{\bar{z}}_2(z_1,\eta_1,\eta_2)} e^{-i2\pi(nz_1 + mz_2)}\, dz_2 \right) dz_1 \right] \boldsymbol{b}_1 , \tag{3.89}$$

for any $(\eta_1, \eta_2) \in \mathcal{H}_{\mathrm{J_1J_2J_3J_4J_5J_6}}$. Moreover, eq. (3.89) may be integrated over three separate unit domains, e.g. the parallelogram $\mathcal{P}_{\mathrm{J_1J_3J_4J_6}}$ and both triangles $\mathcal{T}_{\mathrm{J_1J_2J_3}}$ and $\mathcal{T}_{\mathrm{J_4J_5J_6}}$, i.e.

$$\hat{\boldsymbol{u}}_1^p(\eta_1, \eta_2) = \hat{\boldsymbol{u}}_1^p(\eta_1, \eta_2)|_{\mathcal{H}_{\mathrm{J_1J_2J_3J_4J_5J_6}}} = \hat{\boldsymbol{u}}_1^p(\eta_1, \eta_2)|_{\mathcal{P}_{\mathrm{J_1J_3J_4J_6}}} + \hat{\boldsymbol{u}}_1^p(\eta_1, \eta_2)|_{\mathcal{T}_{\mathrm{J_1J_2J_3}}} + \hat{\boldsymbol{u}}_1^p(\eta_1, \eta_2)|_{\mathcal{T}_{\mathrm{J_4J_5J_6}}} , \tag{3.90}$$

as illustrated by the different vertices in Fig. (3.25b). Because the boundaries of the hexagonal-shaped unit cells are composed of straight dislocation segments, the integral eq. (3.89) is necessarily bounded by affine functions with respect to the coordinates η_1 and η_2. The first quantity $\hat{\boldsymbol{u}}_1^p(\eta_1, \eta_2)|_{\mathcal{P}_{\mathrm{J_1J_3J_4J_6}}}$ in the right-hand side of eq. (3.90) is also computed by using the following bounds, i.e.

$$\forall\, \{\eta_1, \eta_2\} \in \mathcal{P}_{\mathrm{J_1J_3J_4J_6}} : \begin{cases} \bar{z}_1(\eta_1) = -\eta_1 \\ \bar{\bar{z}}_1(\eta_1) = \eta_1 \end{cases} , \quad \text{and} \quad \begin{cases} \bar{z}_2(z_1, \eta_1, \eta_2) = -\dfrac{1-2\eta_2}{2\eta_1} z_1 - \dfrac{1}{2} \\ \bar{\bar{z}}_2(z_1, \eta_1, \eta_2) = -\dfrac{1-2\eta_2}{2\eta_1} z_1 + \dfrac{1}{2} . \end{cases} \tag{3.91}$$

Similarly, the two quantities $\hat{\boldsymbol{u}}_1^p(\eta_1, \eta_2)|_{\mathcal{T}_{\mathrm{J_1J_2J_3}}}$ and $\hat{\boldsymbol{u}}_1^p(\eta_1, \eta_2)|_{\mathcal{T}_{\mathrm{J_4J_5J_6}}}$ in eq. (3.90) are determined by considering

$$\begin{aligned} &\forall\, \{\eta_1, \eta_2\} \in \mathcal{T}_{\mathrm{J_1J_2J_3}} : \begin{cases} \bar{z}_1(\eta_1) = \eta_1 \\ \bar{\bar{z}}_1(\eta_1) = 1 - \eta_1 \end{cases} , \quad \text{and} \quad \begin{cases} \bar{z}_2(z_1, \eta_1, \eta_2) = \dfrac{(1-2\eta_2)\, z_1 - 1 + \eta_2 + \eta_1}{1 - 2\eta_1} \\ \bar{\bar{z}}_2(z_1, \eta_1, \eta_2) = \dfrac{2\eta_2\, z_1 - \eta_2}{-1 + 2\eta_1} , \end{cases} \\ &\forall\, \{\eta_1, \eta_2\} \in \mathcal{T}_{\mathrm{J_4J_5J_6}} : \begin{cases} \bar{z}_1(\eta_1) = \eta_1 - 1 \\ \bar{\bar{z}}_1(\eta_1) = -\eta_1 \end{cases} , \quad \text{and} \quad \begin{cases} \bar{z}_2(z_1, \eta_1, \eta_2) = \dfrac{2\eta_2\, z_1 + \eta_2}{-1 + 2\eta_1} \\ \bar{\bar{z}}_2(z_1, \eta_1, \eta_2) = \dfrac{(1-2\eta_2)\, z_1 + 1 - \eta_2 - \eta_1}{1 - 2\eta_1} , \end{cases} \end{aligned} \tag{3.92}$$

respectively. Thus, after integrating eq. (3.90) analytically with respect to eqs. (3.91) and (3.92), it can also be found that

$$\hat{\boldsymbol{u}}_1^p(\eta_1, \eta_2) = \sin\left(2\pi\left(m\,\eta_2 + n\,\eta_1\right)\right) \frac{-1 + 2\eta_1}{2\pi^2\left(m + n - 2\left(m\,\eta_2 + n\,\eta_1\right)\right)\left(2m\,\eta_2 + n\left(-1 + 2\eta_1\right)\right)} \boldsymbol{b}_1 , \tag{3.93}$$

for any given (η_1, η_2). Analogously to eq. (3.89), the vector quantity $\hat{\boldsymbol{u}}_2^p(\eta_1, \eta_2)$ for $\boldsymbol{b}_2$ is written in the form

$$\hat{\boldsymbol{u}}_2^p(\eta_1, \eta_2) = \text{Re}\left[i \int_{\bar{z}_1(\eta_1)}^{\bar{\bar{z}}_1(\eta_1)} \left(\int_{\bar{z}_2(z_1,\eta_1,\eta_2)}^{\bar{\bar{z}}_2(z_1,\eta_1,\eta_2)} z_2\, e^{-i2\pi(nz_1+mz_2)}\, dz_2 \right) dz_1 \right] \boldsymbol{b}_2\,, \tag{3.94}$$

for which the same integral bounds defined by eqs. (3.91) and (3.92) are used to calculate eq. (3.94) over the hexagonal-shaped dislocation patterns. Hence, it follows

$$\hat{\boldsymbol{u}}_2^p(\eta_1, \eta_2) = \sin\left(2\pi\left(m\,\eta_2 + n\,\eta_1\right)\right) \frac{-1+2\eta_2}{2\pi^2\left(m+n-2\left(m\,\eta_2+n\,\eta_1\right)\right)\left(m\left(-1+2\eta_2\right)+2n\,\eta_1\right)}\, \boldsymbol{b}_2\,, \tag{3.95}$$

for any (η_1, η_2). Combining eq. (3.93) with eq. (3.95), the complete vectorial solution for $\hat{\boldsymbol{u}}^p(\eta_1, \eta_2)$ is given by

$$\hat{\boldsymbol{u}}^p(\eta_1, \eta_2) = \frac{\sin\left(2\pi\left(m\,\eta_2 + n\,\eta_1\right)\right)}{2\pi^2\left(m+n-2\left(m\,\eta_2+n\,\eta_1\right)\right)} \left[\frac{-1+2\eta_1}{2m\,\eta_2 + n\left(-1+2\eta_1\right)}\, \boldsymbol{b}_1 + \frac{-1+2\eta_2}{m\left(-1+2\eta_2\right)+2n\,\eta_1}\, \boldsymbol{b}_2 \right], \tag{3.96}$$

which closely corresponds to the same expression given in Ref. [39], after minor corrections. It is worth noting that three singular values for n and m give rise to null denominators in eq. (3.96), so that three cases must be distinguished, i.e. c1: $m+n-2(m\,\eta_2+n\,\eta_1) \neq 0$, c2: $n-2(m\,\eta_2+n\,\eta_1) \neq 0$, and c3: $m-2(m\,\eta_2+n\,\eta_1) \neq 0$. By defining the function $z(n,m) = n\,z_1 + m\,z_2$ in the exponential terms of both eqs. (3.89) and (3.94), all corresponding real-valued expansion coefficients are also obtained by replacing m with m^* in $z(n,m)$ for all different cases, i.e.

$$\text{c1:}\;\; m^* = -n\,\frac{1-2\eta_1}{1-2\eta_2}\,, \quad \text{c2:}\;\; m^* = n\,\frac{1-2\eta_1}{2\eta_2}\,, \text{ and } \quad \text{c3:}\;\; m^* = n\,\frac{2\eta_1}{1-2\eta_2}\,, \tag{3.97}$$

for which the expressions for these three cases are given in Appendix A from Ref. [249]. Finally, to exhibit the discontinuity condition in displacement, the prescribed jump in eq. (3.87) with the aid of the eqs. (3.96) may finally be related to the displacement fields generated by the interface dislocation patterns, i.e.

$$u_k^p(x_1, x_3) = \left[\!\left[\tilde{u}_k^{\text{dis}}(x_1, 0, x_3) \right]\!\right]_{\text{int}} = {}_{\text{A}}\tilde{u}_k^{\text{dis}}(x_1, 0, x_3) - {}_{\text{B}}\tilde{u}_k^{\text{dis}}(x_1, 0, x_3)\,, \tag{3.98}$$

where the complete elastic field solutions in both materials A and B are given by eq. (3.79). The symbol $\left[\!\left[y_k \right]\!\right]_{\text{int}} = \Delta\, y_k = {}_{\text{A}}y_k - {}_{\text{B}}y_k$ corresponds to the vectorial jump of the quantity $\boldsymbol{y}$ across the interface at $x_2 = 0$. Although all physical displacement fields in eq. (3.98) are defined as the real quantities of complex Fourier series-based expressions, the real part designation in eqs. (3.79) and (3.88) are conveniently omitted to express the complex equality, as follows

$$-i\,\hat{u}_k^p(\eta_1, \eta_2) = \sum_{\alpha=1}^{3} {}_{\text{A}}\lambda^{\alpha}\,{}_{\text{A}}a_k^{\alpha} + {}_{\text{A}}\zeta^{\alpha}\,{}_{\text{A}}a_{k_*}^{\alpha} - {}_{\text{B}}\zeta^{\alpha}\,{}_{\text{B}}a_{k_*}^{\alpha}\,, \tag{3.99}$$

so that both real and imaginary parts of eq. (3.99) lead to the equivalent homogeneous linear system Σ_1 of six real equations, i.e.

$$(\Sigma_1)\;\; \forall k \in \{1,2,3\} : \begin{cases} 0 = \text{Re} \displaystyle\sum_{\alpha=1}^{3} {}_{\text{A}}\lambda^{\alpha}\,{}_{\text{A}}a_k^{\alpha} + {}_{\text{A}}\zeta^{\alpha}\,{}_{\text{A}}a_{k_*}^{\alpha} - {}_{\text{B}}\zeta^{\alpha}\,{}_{\text{B}}a_{k_*}^{\alpha} \\ -\hat{u}_k^p(\eta_1, \eta_2) = \text{Im} \displaystyle\sum_{\alpha=1}^{3} {}_{\text{A}}\lambda^{\alpha}\,{}_{\text{A}}a_k^{\alpha} + {}_{\text{A}}\zeta^{\alpha}\,{}_{\text{A}}a_{k_*}^{\alpha} - {}_{\text{B}}\zeta^{\alpha}\,{}_{\text{B}}a_{k_*}^{\alpha}\,, \end{cases} \tag{3.100}$$

where $\hat{\boldsymbol{u}}^p(\eta_1, \eta_2)$ is defined in eq. (3.96), for any given $(\eta_1, \eta_2) \in \,]0,\, 1/2[^{\,2}$ and for all $\{n, m\} \in D$.

Stress conditions at the semicoherent interfaces

Due to the presence of the interfacial excess energy close to grain and interphase boundaries, the discontinuity of the tangential stress components is introduced using the generalized Young-Laplace equation [108, 209, 80], as an equilibrium boundary condition to solve the present boundary-value problem with interface stress effects, i.e.

$$[\![\tilde{\sigma}^{\mathrm{dis}}_{\varphi i}(x_1,0,x_3)\, n_i]\!]_{\mathrm{int}} + \tau_{\varphi\chi,\chi} = 0\,, \tag{3.101}$$

together with the stress discontinuity in normal direction of the boundaries, as follows

$$[\![\tilde{\sigma}^{\mathrm{dis}}_{ij}(x_1,0,x_3)\, n_j\, n_i]\!]_{\mathrm{int}} = \tau_{\chi\varphi}\,\kappa_{\chi\varphi}\,, \tag{3.102}$$

with $\kappa_{\chi\varphi}$ the curvature tensor of the solid-state interface of interest. Substituting the linear constitutive relation of eq. (3.85) into eqs. (3.101) and (3.102) respectively, the governing non-classical boundary equations lead to

$$\begin{cases} 0 = [\![\tilde{t}^{\,\mathrm{int}}_{\varphi}(x_1,x_3)]\!]_{\mathrm{int}} + d_{\varphi\chi\gamma\eta}\;\tilde{u}^{\mathrm{dis}}_{\gamma,\eta\chi}(x_1,0,x_3) \\ 0 = [\![\tilde{t}^{\,\mathrm{int}}_{2}(x_1,x_3)]\!]_{\mathrm{int}} - \left(\tau^0_{\chi\varphi} + d_{\chi\varphi\gamma\eta}\;\tilde{u}^{\mathrm{dis}}_{\gamma,\eta}(x_1,0,x_3)\right)\left(\kappa^0_{\chi\varphi} + \kappa^{\Delta}_{\chi\varphi}\right), \end{cases} \tag{3.103}$$

where $\kappa^0_{\chi\varphi}$ and $\kappa^{\Delta}_{\chi\varphi}$ are the deformation-independent curvature and curvature change tensors, respectively. In the classical theory of initially flat and infinitely thin membranes with small out-of-plane deflections [40], as the considered (and interpreted as surface stresses) elastically stretched membranes in Refs. [108, 109], the curvature change tensor may be approximated by

$$\kappa^{\Delta}_{\chi\varphi} = -\tilde{u}^{\mathrm{dis}}_{2,\chi\varphi}(x_1,0,x_3)\,, \tag{3.104}$$

without internal moments. Under the treatment of such specific boundary conditions normal to the initially flat (but, stretched) membranes, the distortion response caused by the presence of interface dislocations may elastically warp the semicoherent interfaces with radii defined by $r_{\chi\varphi} = 1/\kappa^{\Delta}_{\chi\varphi}$. Thus, the right-hand side of the second equation in eqs. (3.103) is deduced by subsequently imposing no initial curvature and neglecting the second-order effects compared with unity, as follows

$$\left(\tau^0_{\chi\varphi} + d_{\chi\varphi\gamma\eta}\;\tilde{u}^{\mathrm{dis}}_{\gamma,\eta}(x_1,0,x_3)\right)\left(\kappa^0_{\chi\varphi} + \kappa^{\Delta}_{\chi\varphi}\right) \simeq -\tau^0_{\chi\varphi}\;\tilde{u}^{\mathrm{dis}}_{2,\chi\varphi}(x_1,0,x_3)\,, \tag{3.105}$$

thus, imposing $\kappa^0_{\chi\varphi} = 0$ and $\tilde{u}^{\mathrm{dis}}_{\gamma,\eta}(x_1,0,x_3)\,\tilde{u}^{\mathrm{dis}}_{2,\chi\varphi}(x_1,0,x_3) \ll 1$. According to eq. (3.82), both discontinuous stress boundary conditions in eqs. (3.103) can also be recast in matrix form, i.e.

$$[\![\tilde{t}^{\,\mathrm{int}}_{k}(x_1,x_3)]\!]_{\mathrm{int}} - 4\pi^2\,\mathrm{V}_{ki}\;\tilde{u}^{\mathrm{int}}_{i}(x_1,0,x_3) = 0\,, \tag{3.106}$$

where the 3×3 real matrix $\mathbf{V}$ is expressed as

$$\mathrm{V}_{ki} = \mathrm{V}_{ik} = \begin{bmatrix} k_1^2 d_{11} + 2k_1k_3d_{15} + k_3^2 d_{55} & 0 & k_1^2 d_{15} + k_1k_3(d_{13}+d_{55}) + k_3^2 d_{35} \\ 0 & k_1^2\tau^0_{11} + 2k_1k_3\tau^0_{13} + k_3^2\tau^0_{33} & 0 \\ k_1^2 d_{15} + k_1k_3(d_{13}+d_{55}) + k_3^2 d_{35} & 0 & k_1^2 d_{55} + 2k_1k_3d_{35} + k_3^2 d_{33} \end{bmatrix}, \tag{3.107}$$

within which the surface/interface elastic constants are indexed using standard contracted notations. Mechanically balanced by the interface stress effects, eq. (3.106) shows that the infinitesimal in-plane strain fields in the membranes may influence the stresses in both bulk materials due to the elasticity contributions at the interphase boundaries. In contrast to the classical continuum elasticity, the tractions across the interface and the displacement fields are related to each other by the interface elasticity properties as well the interface geometries through the wavevector components.

Because the materials A and B are mapped separately from the reference state, the coherent regions at the interfaces (separated by the networks of interfacial dislocations) can also be viewed as infinitely thin membranes separately in contact with each individual bulk material. Furthermore, the determination of the reference states yielding (in general) to unequal partitioning of elastic distortions, the tractions that act on each individual upper and lower materials bonded by these coherent interfacial regions are consequently assumed to be different in both magnitude and direction. Using the concept of interface zone by in Ref. [146], the specific traction vector ${}_{\mathrm{coh}}\boldsymbol{t}^{\,\mathrm{int}}(x_1,x_3)$, acting on both neighboring crystals with fictitious infinitely thin inter-layered coherent patches at $x_2 = 0$, is introduced to transfer traction forces from the upper material to the adjacent lower material. The equilibrium condition between the interface coherent regions and material A also reads

$$ {}_{\mathrm{A}}\tilde{t}_k^{\,\mathrm{int}}(x_1,x_3) - {}_{\mathrm{coh}}t_k^{\,\mathrm{int}}(x_1,x_3) - 4\pi^2\,{}_{\mathrm{A}}\mathrm{V}_{ki}^{\mathrm{int}}\;{}_{\mathrm{A}}\tilde{u}_i^{\mathrm{dis}}(x_1,0,x_3) = 0\,, \tag{3.108} $$

by use of the boundary condition in eq. (3.106), while the equilibrium condition between the interface coherent regions and material B is given by

$$ {}_{\mathrm{coh}}t_k^{\,\mathrm{int}}(x_1,x_3) - {}_{\mathrm{B}}\,\tilde{t}_k^{\,\mathrm{int}}(x_1,x_3) - 4\pi^2\,{}_{\mathrm{B}}\mathrm{V}_{ki}^{\mathrm{int}}\;{}_{\mathrm{B}}\tilde{u}_i^{\mathrm{dis}}(x_1,0,x_3) = 0\,, \tag{3.109} $$

where ${}_{\mathrm{A}}\mathbf{V}^{\mathrm{int}}$ and ${}_{\mathrm{B}}\mathbf{V}^{\mathrm{int}}$ depend on the elastic properties of the interfaces with respect to each material A and B, respectively. Summing both eqs. (3.108) and (3.109), it also follows that

$$ {}_{\mathrm{A}}\tilde{t}_k^{\,\mathrm{int}}(x_1,x_3) - {}_{\mathrm{B}}\,\tilde{t}_k^{\,\mathrm{int}}(x_1,x_3) - 4\pi^2\left({}_{\mathrm{A}}\mathrm{V}_{ki}^{\mathrm{int}}\;{}_{\mathrm{A}}\tilde{u}_i^{\,\mathrm{int}}(x_1,0,x_3) + {}_{\mathrm{B}}\mathrm{V}_{ki}^{\mathrm{int}}\;{}_{\mathrm{B}}\tilde{u}_i^{\,\mathrm{int}}(x_1,0,x_3)\right) = 0\,, \tag{3.110} $$

which yields to the non-classical stress discontinuity conditions at the mismatched interfaces. Using eqs. (3.79) and (3.82), eq. (3.110) gives rise to the additional linear system Σ_2 of six equations, i.e.

$$ (\Sigma_2):\begin{cases} 0 = \mathrm{Re}\Big[\sum_{\alpha=1}^{3} {}_{\mathrm{A}}\lambda^{\alpha}\,{}_{\mathrm{A}}h_1^{\alpha} + {}_{\mathrm{A}}\zeta^{\alpha}\,{}_{\mathrm{A}}h_{1_*}^{\alpha} + i2\pi\big({}_{\mathrm{A}}\mathrm{V}_{11}^{\mathrm{int}}\big({}_{\mathrm{A}}\lambda^{\alpha}\,{}_{\mathrm{A}}a_1^{\alpha} + {}_{\mathrm{A}}\zeta^{\alpha}\,{}_{\mathrm{A}}a_{1_*}^{\alpha}\big) + {}_{\mathrm{A}}\mathrm{V}_{13}^{\mathrm{int}}\big({}_{\mathrm{A}}\lambda^{\alpha}\,{}_{\mathrm{A}}a_3^{\alpha} + {}_{\mathrm{A}}\zeta^{\alpha}\,{}_{\mathrm{A}}a_{3_*}^{\alpha}\big)\big) \\ \qquad - {}_{\mathrm{B}}\zeta^{\alpha}\big({}_{\mathrm{B}}h_{1_*}^{\alpha} - i2\pi\big({}_{\mathrm{B}}\mathrm{V}_{11}^{\mathrm{int}}\;{}_{\mathrm{B}}a_{1_*}^{\alpha} + {}_{\mathrm{B}}\mathrm{V}_{13}^{\mathrm{int}}\;{}_{\mathrm{B}}a_{3_*}^{\alpha}\big)\big)\Big] = \mathrm{Re}\sum_{\alpha=1}^{3} v_1^{\alpha} \\ 0 = \mathrm{Re}\Big[\sum_{\alpha=1}^{3} {}_{\mathrm{A}}\lambda^{\alpha}\,{}_{\mathrm{A}}h_2^{\alpha} + {}_{\mathrm{A}}\zeta^{\alpha}\,{}_{\mathrm{A}}h_{2_*}^{\alpha} + i2\pi\big({}_{\mathrm{A}}\mathrm{V}_{22}^{\mathrm{int}}\big({}_{\mathrm{A}}\lambda^{\alpha}\,{}_{\mathrm{A}}a_2^{\alpha} + {}_{\mathrm{A}}\zeta^{\alpha}\,{}_{\mathrm{B}}a_{2_*}^{\alpha}\big)\big) - {}_{\mathrm{B}}\zeta^{\alpha}\big({}_{\mathrm{B}}h_{2_*}^{\alpha} - i2\pi\;{}_{\mathrm{B}}\mathrm{V}_{22}^{\mathrm{int}}\,{}_{\mathrm{B}}a_{2_*}^{\alpha}\big)\Big] \\ \qquad = \mathrm{Re}\sum_{\alpha=1}^{3} v_2^{\alpha} \\ 0 = \mathrm{Re}\Big[\sum_{\alpha=1}^{3} {}_{\mathrm{A}}\lambda^{\alpha}\,{}_{\mathrm{A}}h_3^{\alpha} + {}_{\mathrm{A}}\zeta^{\alpha}\,{}_{\mathrm{A}}h_{3_*}^{\alpha} + i2\pi\big({}_{\mathrm{A}}\mathrm{V}_{13}^{\mathrm{int}}\big({}_{\mathrm{A}}\lambda^{\alpha}\,{}_{\mathrm{A}}a_1^{\alpha} + {}_{\mathrm{A}}\zeta^{\alpha}\,{}_{\mathrm{A}}a_{1_*}^{\alpha}\big) + {}_{\mathrm{A}}\mathrm{V}_{33}^{\mathrm{int}}\big({}_{\mathrm{A}}\lambda^{\alpha}\,{}_{\mathrm{A}}a_3^{\alpha} + {}_{\mathrm{A}}\zeta^{\alpha}\,{}_{\mathrm{A}}a_{3_*}^{\alpha}\big)\big) \\ \qquad - {}_{\mathrm{B}}\zeta^{\alpha}\big({}_{\mathrm{B}}h_{3_*}^{\alpha} - i2\pi\big({}_{\mathrm{B}}\mathrm{V}_{13}^{\mathrm{int}}\;{}_{\mathrm{B}}a_{1_*}^{\alpha} + {}_{\mathrm{B}}\mathrm{V}_{33}^{\mathrm{int}}\;{}_{\mathrm{B}}a_{3_*}^{\alpha}\big)\big)\Big] = \mathrm{Re}\sum_{\alpha=1}^{3} v_3^{\alpha} \\ 0 = \mathrm{Im}\Big[\sum_{\alpha=1}^{3} v_k^{\alpha}\Big]\,,\quad \forall k\in\{1,2,3\}\,, \end{cases} \tag{3.111} $$

with $h_k^{\alpha} = \mathrm{H}_{k2}^{\alpha}$, for any given $(\eta_1,\eta_2)\in\,]0,\,1/2[^{\,2}$ and for all $\{n,m\}\in D$.

Stress conditions at the free surfaces

Similarly to the semicoherent interface treatment, the free surfaces experience excess energy and excess energy due to different energy profiles close to such singular membrane-like boundaries. Thus, additional non-classical boundary conditions as eq. (3.110) are introduced on the outer free surface, at $x_2^{\mathrm{or}} = h_{\mathrm{A}}$, i.e.

$$ {}_{\mathrm{A}}\tilde{t}_k^{\,\mathrm{fs}}(x_1,x_3) + 4\pi^2\,{}_{\mathrm{A}}\mathrm{V}_{kl}^{\mathrm{fs}}\;{}_{\mathrm{A}}\tilde{u}_i^{\mathrm{dis}}(x_1,h_{\mathrm{A}},x_3) = 0\,, \tag{3.112} $$

where ${}_{\mathrm{A}}\mathbf{V}^{\mathrm{fs}}$ depends on the elastic constants of the free surfaces. It also yields to the following system Σ_3 of six other equations, i.e.

$$(\Sigma_3):\begin{cases} 0=\mathrm{Re}\Big[\sum\limits_{\alpha=1}^{3}{}_{\mathrm{A}}\lambda^{\alpha}\mathrm{e}^{i2\pi p^{\alpha}h_{\mathrm{A}}}\big({}_{\mathrm{A}}h_1^{\alpha}-i2\pi\big({}_{\mathrm{A}}\mathrm{V}^{\mathrm{fs}}_{11}\,{}_{\mathrm{A}}a_1^{\alpha}+{}_{\mathrm{A}}\mathrm{V}^{\mathrm{fs}}_{13}\,{}_{\mathrm{A}}a_3^{\alpha}\big)\big) \\ \qquad\qquad +{}_{\mathrm{A}}\zeta^{\alpha}\mathrm{e}^{i2\pi p_*^{\alpha}h_{\mathrm{A}}}\big({}_{\mathrm{A}}h_{1_*}^{\alpha}-i2\pi\big({}_{\mathrm{A}}\mathrm{V}^{\mathrm{fs}}_{11}\,{}_{\mathrm{A}}a_{1_*}^{\alpha}+{}_{\mathrm{A}}\mathrm{V}^{\mathrm{fs}}_{13}\,{}_{\mathrm{A}}a_{3_*}^{\alpha}\big)\big)\Big]=\mathrm{Re}\sum_{\alpha=1}^{3}w_1^{\alpha} \\ 0=\mathrm{Re}\Big[\sum\limits_{\alpha=1}^{3}{}_{\mathrm{A}}\lambda^{\alpha}\mathrm{e}^{i2\pi p^{\alpha}h_{\mathrm{A}}}\big({}_{\mathrm{A}}h_2^{\alpha}-i2\pi\,{}_{\mathrm{A}}\mathrm{V}^{\mathrm{fs}}_{22}\,{}_{\mathrm{A}}a_2^{\alpha}\big)+{}_{\mathrm{A}}\zeta^{\alpha}\mathrm{e}^{i2\pi p_*^{\alpha}h_{\mathrm{A}}}\big({}_{\mathrm{A}}h_{2_*}^{\alpha}-i2\pi\,{}_{\mathrm{A}}\mathrm{V}^{\mathrm{fs}}_{22}\,{}_{\mathrm{A}}a_{2_*}^{\alpha}\big)\Big] \\ \qquad\qquad =\mathrm{Re}\sum_{\alpha=1}^{3}w_2^{\alpha} \\ 0=\mathrm{Re}\Big[\sum\limits_{\alpha=1}^{3}{}_{\mathrm{A}}\lambda^{\alpha}\mathrm{e}^{i2\pi p^{\alpha}h_{\mathrm{A}}}\big({}_{\mathrm{A}}h_3^{\alpha}-i2\pi\big({}_{\mathrm{A}}\mathrm{V}^{\mathrm{fs}}_{13}\,{}_{\mathrm{A}}a_1^{\alpha}+{}_{\mathrm{A}}\mathrm{V}^{\mathrm{fs}}_{33}\,{}_{\mathrm{A}}a_3^{\alpha}\big)\big) \\ \qquad\qquad +{}_{\mathrm{A}}\zeta^{\alpha}\mathrm{e}^{i2\pi p_*^{\alpha}h_{\mathrm{A}}}\big({}_{\mathrm{A}}h_{3_*}^{\alpha}-i2\pi\big({}_{\mathrm{A}}\mathrm{V}^{\mathrm{fs}}_{13}\,{}_{\mathrm{A}}a_{1_*}^{\alpha}+{}_{\mathrm{A}}\mathrm{V}^{\mathrm{fs}}_{33}\,{}_{\mathrm{A}}a_{3_*}^{\alpha}\big)\big)\Big]=\mathrm{Re}\sum_{\alpha=1}^{3}w_3^{\alpha} \\ 0=\mathrm{Im}\Big[\sum\limits_{\alpha=1}^{3}w_k^{\alpha}\Big]\,,\quad\forall k\in\{1,2,3\}\,, \end{cases} \tag{3.113}$$

for any given $(\eta_1,\eta_2)\in\,]0,\,1/2[^{\,2}$ and for all $\{n,m\}\in D$.

Determination of the minimum-energy paths

When the linear systems in eqs. (3.100) with (3.111) and (3.113) are combined, the set Ecst of all eighteen real unknowns (twelve and six for A and B, respectively) are also solved with respect to the prescribed boundary conditions, i.e.

$$\mathrm{Ecst}=\sum_{\alpha=1}^{3}\{\,\mathrm{Re}\,{}_{\mathrm{A}}\lambda^{\alpha},\,\mathrm{Im}\,{}_{\mathrm{A}}\lambda^{\alpha},\,\mathrm{Re}\,{}_{\mathrm{A}}\zeta^{\alpha},\,\mathrm{Im}\,{}_{\mathrm{A}}\zeta^{\alpha},\,\mathrm{Re}\,{}_{\mathrm{B}}\zeta^{\alpha},\,\mathrm{Im}\,{}_{\mathrm{B}}\zeta^{\alpha}\,\}\,, \tag{3.114}$$

completing the solutions of the elastic displacement and stress fields, given by eqs. (3.79) and (3.80), respectively. Following the procedure described in section 3.6.2, the upper triangular domain $\mathcal{T}_{\mathrm{ABC}}$ in the representative unit dislocation cell, denoted by ABC in Fig. (3.25b), is discretized into four-node quadrilateral elements with respect to the i^{th} nodal point coordinates (η_1^i,η_2^i), such that $\{\eta_1^i,\eta_2^i\}\in\,]0,\,1/2[^{\,2}$ for convex hexagonal-shaped dislocation patterns. Thus, for any dislocation pattern that is geometrically characterized by the given coordinates (η_1^i,η_2^i), the corresponding elastic strain energy can be computed as a volume integral over the heterostructure of interest, i.e.

$$\gamma_{\mathrm{e}}^i(\eta_1^i,\eta_2^i)=\frac{1}{2\,A}\iiint_V\tilde{\sigma}_{ij}^{\mathrm{dis}}(x_1,x_2,x_3)\;\tilde{u}_{j,i}^{\mathrm{dis}}(x_1,x_2,x_3)\;\mathrm{d}V\,, \tag{3.115}$$

where all persistent short-range field solutions of the integrand depend specifically on (η_1^i,η_2^i) by the treatment of boundary conditions, described in section 3.6.4. For far-field stress-free bicrystals at equilibrium, the standard volume integral eq. (3.115) may be reduced to a surface integral by the use of integration by parts, together with the divergence theorem without any body forces [223, 260], as follows

$$\gamma_{\mathrm{e}}^i(\eta_1^i,\eta_2^i)=\frac{1}{2\,A}\iint_{A(r_0)}\tilde{t}_k^{\,\mathrm{int}}(x_1,x_3)\;\;[\![\tilde{u}_k^{\mathrm{dis}}(x_1,0,x_3)]\!]_{\mathrm{int}}\;\mathrm{d}S\,, \tag{3.116}$$

where $A(r_0)$ is the hexagonal-shaped unit cell. In eqs. (3.115) and (3.116), the expressions of elastic strain energy are conveniently expressed per unit area, for which $A=A(r_0=0)$, and account for several different contributions, i.e. interaction between Volterra-type dislocations against the

misfit strain state, self-energy induced by individual hexagonal-shaped dislocation configurations, as well as the interaction between the hexagonal-shaped unit cell with all infinitely repeated cells. Finally, the complete elastic strain energy landscape $\gamma_e(\eta_1, \eta_2)$ is interpolated for any $(\eta_1, \eta_2) \in]0, 1/2[^2$, as follows

$$\gamma_e(\eta_1, \eta_2) = \sum_{i=1}^{4} N_i(\eta_1, \eta_2)\, \gamma_e^i(\eta_1^i, \eta_2^i)\,, \tag{3.117}$$

where $N_i(\eta_1, \eta_2)$ are the standard finite element bilinear shape functions for four-node elements.

For elastic strain landscapes that favor the formation of dislocation junctions, the minimum-energy configurations are determined by computing the conjugate gradient algorithm, while the nudged elastic band method is used to find the corresponding minimum-energy paths. The nudged elastic band method is a chain-of-states method in which a string of images is used to describe the reaction pathways. These configurations are connected by spring forces to ensure equal spacing along the paths of interest. The ensemble of the configurations is then relax through a force projection scheme to converge to the most energetically favorable pathways [117, 222]. To identify the minimum-energy paths between the initial (non-equilibrium) lozenge-shaped pattern and the final elastically relaxed configurations (previously computed by the conjugate gradient algorithm), all images are simultaneously evolved to equilibrium under a nudged elastic band force (on image indexed by s_η) that contains two independent components on all images s_η, i.e.

$$\boldsymbol{f}_{s_\eta}^{\mathrm{NEB}} = \boldsymbol{f}_{s_\eta}^{\perp} + \boldsymbol{f}_{s_\eta}^{\parallel}\,, \tag{3.118}$$

where $\boldsymbol{f}_{s_\eta}^{\perp}$ is the component of the elastic force acting normal to the tangent of the elastic landscape, as follows

$$\boldsymbol{f}_{s_\eta}^{\perp} = -\boldsymbol{\nabla}\gamma_e(\eta_1, \eta_2) + \left(\boldsymbol{\nabla}\gamma_e(\eta_1, \eta_2) \cdot \hat{\boldsymbol{\tau}}_{s_\eta}\right) \hat{\boldsymbol{\tau}}_{s_\eta}\,, \tag{3.119}$$

with $\hat{\boldsymbol{\tau}}_{s_\eta}$ the unit tangent to the elastic energy landscape. In addition, the spring force $\boldsymbol{f}_{s_\eta}^{\parallel}$ in eq. (3.118), acting parallel to the energy landscape [117, 222] is defined by

$$\boldsymbol{f}_{s_\eta}^{\parallel} = k\left(|\boldsymbol{\eta}_{s_\eta+1} - \boldsymbol{\eta}_{s_\eta}| - |\boldsymbol{\eta}_{s_\eta} - \boldsymbol{\eta}_{s_\eta-1}|\right), \tag{3.120}$$

where $\boldsymbol{\eta}_{s_\eta} = \boldsymbol{\eta}_{s_\eta}(\eta_1, \eta_2)$ is the position of the ${s_\eta}^{\mathrm{th}}$ image and k the spring constant. The spring interaction between adjacent images is added to ensure continuity of the chain.

The present numerical procedure is identical to nudged elastic band calculations recently performed to analyze the calculation of attempt frequency for a dislocation bypassing an obstacle [231] using a nodal dislocation dynamics simulation with non-singular treatments for isotropic elastic fields [51].

3.6.5 Application to Au/Cu heterosystems

The section gives applications to two examples of the general parametric energy-based framework. The first simple and limiting case is concerned with two dislocation sets in pure misfit (010) Au/Cu interfaces, for which the strain energy landscape for formation of dislocation junctions is unfavorable. The subsequent investigation of the effects of surface/interface stress and elasticity properties with different boundary conditions in (010) Au/Cu interfaces can be found in Ref. [249]. On the other hand, the second case deals with the minimum-energy reaction pathway of the pre-computed (111) Au/Cu elastic energy landscape, where the initial and unrelaxed dislocation pattern solution is described by the Frank-Bilby equation. The materials properties used in these examples are listed in Table 3.7.

Symbols	Au (material A)	Cu (Material B)	Units	References
Lattice parameters				
a	0.4078	0.3615	nm	[104]
Elastic components (Voigt notation)				
c_{11}	187.0	168.4	GPa	[7]
c_{12}	157.0	121.4	GPa	[7]
c_{44}	43.6	75.4	GPa	[7]
Elasticity properties for the semicoherent interfaces (Voigt notation)				
$*$ Interface stress				
τ_{11}	-0.0465	0.645	N/m	[146]
τ_{13}	0	0	N/m	[146]
τ_{33}	-0.0465	0.645	N/m	[146]
$*$ Interface modulus				
d_{11}	-6.84	-5.99	N/m	[146]
d_{13}	-3.47	0.6540	N/m	[146]
d_{33}	-6.84	-5.99	N/m	[146]
d_{15}	0.0042	0.0032	N/m	[146]
d_{35}	0.0042	0.0032	N/m	[146]
d_{55}	-1.91	-3.67	N/m	[146]
Elasticity properties for the free surface (Voigt notation)				
$*$ Surface stress				
τ_{11}	1.49	–	N/m	[185]
τ_{13}	0	–	N/m	[185]
τ_{33}	1.49	–	N/m	[185]
$*$ Surface modulus				
d_{11}	-7.10	–	N/m	[185]
d_{13}	-5.67	–	N/m	[185]
d_{33}	-3.17	–	N/m	[185]

TABLE 3.7: Lattice parameters a of Au and Cu crystals, material properties c_{ij} of both bulk materials, surface stress $\tau_{\chi\varphi}$ and surface modulus $d_{\chi\varphi}$ of the semicoherent Au/Cu heterophase interface and the (010) free surface in Au.

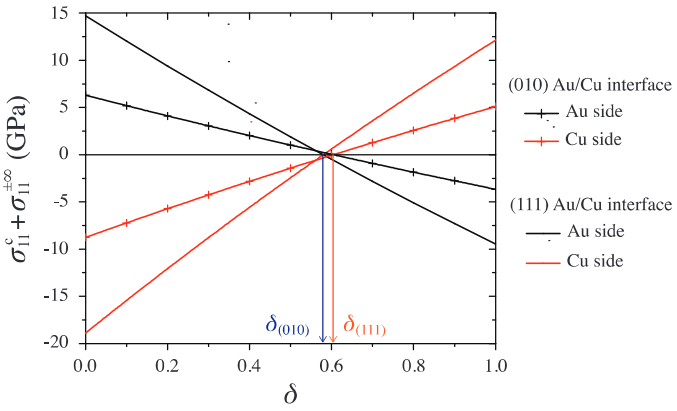

FIGURE 3.26: Dependence of the total far-field stress component $\sigma_{11}^{c}+\sigma_{11}^{\pm\infty}$ on δ in the Au and Cu materials for the (010) and (111) Au/Cu semicoherent interfaces.

Case 1: The (010) Au/Cu interface with two sets of dislocations

As a limiting case, the atomically sharp (010) Au/Cu misfit interface contains two sets of orthogonal dislocations in cube-cube orientation relationship, i.e. $\boldsymbol{x}_1^{\text{or}} = [10\bar{1}]$, $\boldsymbol{x}_2^{\text{or}} = \boldsymbol{n} = [010]$, and $\boldsymbol{x}_3^{\text{or}} = [101]$. Similar to eq. (3.37), the net Burgers vectors are expressed by using the quantized Frank-Bilby equation [93, 30, 29], as follows

$$\left(\frac{\boldsymbol{n}\times\boldsymbol{\xi}_1^{\text{un}}}{d_1^{\text{un}}}\cdot\boldsymbol{p}\right)\boldsymbol{b}_1+\left(\frac{\boldsymbol{n}\times\boldsymbol{\xi}_2^{\text{un}}}{d_2^{\text{un}}}\cdot\boldsymbol{p}\right)\boldsymbol{b}_2=n_1\,\boldsymbol{b}_1+n_2\,\boldsymbol{b}_2=\left(\mathbf{F}_{\text{Au}}^{-1}-\mathbf{F}_{\text{Cu}}^{-1}\right)\boldsymbol{p}\,, \tag{3.121}$$

where d_1^{un} and d_2^{un} are the regularly spaced inter-dislocation spacings, and the interface Burgers vectors $\boldsymbol{b}_1 \parallel [10\bar{1}]$ and $\boldsymbol{b}_2 \parallel [101]$ are both parallel to $\boldsymbol{x}_1$- and $\boldsymbol{x}_3$-axis, respectively. As a result of arbitrarily selecting the reference state identical to the Au (or Cu) natural state, for which the geometry of interface dislocations (line directions and spacings) is independent of the choice of reference state, the line directions are defined by $\boldsymbol{\xi}_1^{\text{un}} \parallel [101]$ and $\boldsymbol{\xi}_2^{\text{un}} \parallel [10\bar{1}]$, and the inter-dislocation spacings are given by $d_1^{\text{un}} = d_2^{\text{un}} = p_1^{\text{o}} = p_2^{\text{o}} = 2.25144$ nm. Thus, the Frank-Bilby equation predicts that an orthogonal network of straight parallel dislocations with pure edge characters is also needed to accommodate the pure misfit (010) Au/Cu interface.

The geometry of such orthogonal grid of dislocations can also be characterized by $\eta_1 \to 1/2$ and $\eta_2 \to 1/2$ in the general parametric framework, because $\phi^{\text{un}} = \pi/2$. According to the bilinear function $\boldsymbol{u}^p(\eta_1 \to 1/2, \eta_2 \to 1/2)$ for the prescribed displacement field in eq. (3.87), the corresponding real-valued expansion functions in eq. (3.88) for the individual set 1 can be computed by imposing $m = 0$, as follows

$$\begin{cases} \lim\limits_{\eta_1\to 1/2} {}_{\text{c2}}\hat{\boldsymbol{u}}_1^p(\eta_1,\eta_2) = \lim\limits_{\eta_2\to 1/2} {}_{\text{c2}}\hat{\boldsymbol{u}}_1^p(\eta_1,\eta_2) = \dfrac{(-1)^{n+1}}{2\pi n}\,\boldsymbol{b}_1 \\ \lim\limits_{\eta_2\to 1/2}\lim\limits_{\eta_1\to 1/2} {}_{\text{c2}}\hat{\boldsymbol{u}}_2^p(\eta_1,\eta_2) = \lim\limits_{\eta_2\to 1/2} \dfrac{(-1)^{n+1}\,(-1+2\eta_2)}{2\pi n}\,\boldsymbol{b}_2 = \boldsymbol{0}\,, \end{cases} \tag{3.122}$$

exhibiting that $\hat{\boldsymbol{u}}^p(\eta_1 \to 1/2, \eta_2 \to 1/2) = \hat{\boldsymbol{u}}_1^p(\eta_1 \to 1/2, \eta_2 \to 1/2)$ is evidently written as a function of $\boldsymbol{b}_1$, for set 1. By superposing the similar contribution of set 2 with $n = 0$, the final prescribed displacement field produced by an orthogonal network of dislocations in eq. (3.88) is therefore written in the form of two distinct one-dimensional sawtooth-shaped functions with

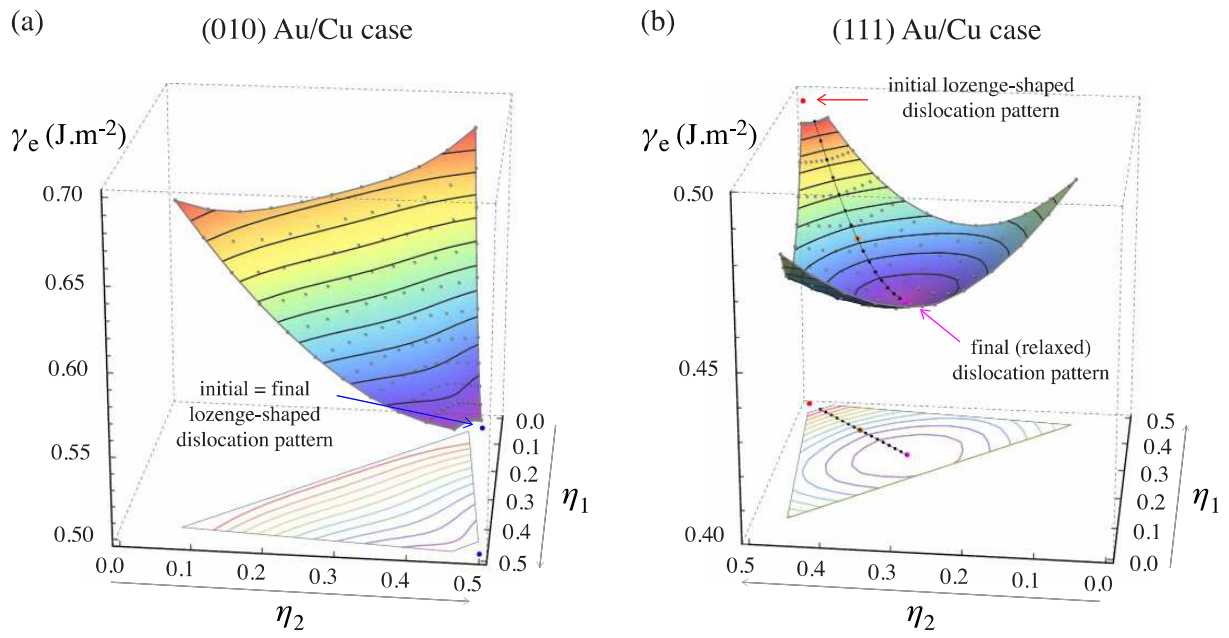

FIGURE 3.27: Elastic strain energy landscapes γ_e in J.m^{-2} of the hexagonal-shaped patterns with three-fold dislocation nodes as a function of η_1 and η_2, for the (a) (010) and (b) (111) Au/Cu heterophase interface cases. The large points at $\eta_1 = \eta_2 = 1/2$ correspond to the initial lozenge-shaped patterns, for which the two crossing dislocation sets are related to equilibrium and non-equilibrium dislocation configurations for the (010) and (111) interface planes, respectively. The latter case gives rise to the presence of a minimum-energy path (in black) between the initial pattern and the fully elastically strain-relaxed dislocation structure (magenta point) at stable equilibrium state. An intermediate state is displayed by the orange point.

Fourier sine series, as follows

$$\boldsymbol{u}^p(x_1,x_3) = -\sum_{\substack{n\geq 1\\ m=0}} \frac{(-1)^n}{\pi n}\sin\left(2\pi k_1(n,0)\; x_1\right)\; \boldsymbol{b}_1 - \sum_{\substack{n=0\\ m\geq 1}} \frac{(-1)^m}{\pi m}\sin\left(2\pi k_3(m)\; x_3\right)\; \boldsymbol{b}_2\,, \tag{3.123}$$

where $k_1(n,0)$ and $k_3(m)$ are defined in eq. (3.74), with $\phi^{\text{un}} = \pi/2$. Here, the sawtooth-shaped functions in eq. (3.123) differ from eq. (3.19) by individual translations of magnitude $d_i^{\text{un}}/2$. Similarly to Σ_1 and Σ_2 in eqs. (3.20) and (3.25), the simplest limiting case of bicrystals without any surface/interface elasticity effects leads to a set of twelve real and linear equations, i.e.

$$\begin{cases} \text{Re}\sum_{\alpha=1}^{3} {}_{\text{A}}\lambda^{\alpha}\,{}_{\text{A}}\boldsymbol{a}^{\alpha} - {}_{\text{B}}\zeta^{\alpha}\,{}_{\text{B}}\boldsymbol{a}^{\alpha}_{*} = \boldsymbol{0} \\ \text{Im}\sum_{\alpha=1}^{3} {}_{\text{A}}\lambda^{\alpha}\,{}_{\text{A}}\boldsymbol{a}^{\alpha} - {}_{\text{B}}\zeta^{\alpha}\,{}_{\text{B}}\boldsymbol{a}^{\alpha}_{*} = \boldsymbol{\vartheta}\,, \quad \text{with: } \boldsymbol{\vartheta} = \begin{cases} -\dfrac{(-1)^n}{\pi n}\,\boldsymbol{b}_1 & \text{if } m=0 \qquad n\in\mathbb{N}^* \\ -\dfrac{(-1)^m}{\pi m}\,\boldsymbol{b}_2 & \text{if } n=0 \qquad m\in\mathbb{N}^* \\ \boldsymbol{0} & \text{if } nm\neq 0 \qquad n\in\mathbb{N}^*, m\in\mathbb{N}^* \end{cases} \\ \text{Re}\sum_{\alpha=1}^{3} {}_{\text{A}}\lambda^{\alpha}\,{}_{\text{A}}\boldsymbol{h}^{\alpha} - {}_{\text{B}}\zeta^{\alpha}\,{}_{\text{B}}\boldsymbol{h}^{\alpha}_{*} = \boldsymbol{0} \\ \text{Im}\sum_{\alpha=1}^{3} {}_{\text{A}}\lambda^{\alpha}\,{}_{\text{A}}\boldsymbol{h}^{\alpha} - {}_{\text{B}}\zeta^{\alpha}\,{}_{\text{B}}\boldsymbol{h}^{\alpha}_{*} = \boldsymbol{0}\,, \end{cases} \tag{3.124}$$

with respect to the six associated complex unknown quantities, i.e. ${}_{\text{A}}\lambda^{\alpha}$ and ${}_{\text{B}}\zeta^{\alpha}$.

Following the procedure described in section 3.3.3, the two deformation gradients $\mathbf{F}_{\text{Au}}^{-1}$ and $\mathbf{F}_{\text{Cu}}^{-1}$ in eq. (3.121) (also, the magnitudes of both $\boldsymbol{b}_1$ and $\boldsymbol{b}_2$) are determined by ensuring the condition of vanishing far-field stresses along a transformation pathway between both materials Au and Cu. For cube-cube orientation relation, this condition is met by continuously adjusting the reference lattice parameter a_{ref} along a specified reaction pathway coordinate δ, starting with the pure lattice parameter of Au to Cu, i.e.

$$a_{\text{ref}} = (1-\delta)\ a_{\text{Au}} + \delta\, a_{\text{Cu}}\,, \tag{3.125}$$

where $0 \leq \delta \leq 1$ is a dimensionless variable that interpolates linearly between a_{Au} and a_{Cu}.

According to the far-field eq. (3.1), the dependence of the total large-range stress components $\sigma_{11}^{\text{c}} + \sigma_{11}^{\pm\infty}$ in Au (black line with symbols) and Cu (red line with symbols) on the transformation pathway coordinate δ is plotted in Fig. (3.26). For the (010) misfit case, both far-field stress components vanish for $\delta_{(010)} = 0.60392$, so that the corresponding reference state is closer to Cu than to Au, i.e. $\delta_{(010)} > 0.5$, where ${}_{\text{Cu}}c_{11} < {}_{\text{Au}}c_{11}$ and ${}_{\text{Cu}}c_{12} < {}_{\text{Au}}c_{12}$, but ${}_{\text{Cu}}c_{44} > {}_{\text{Au}}c_{44}$. All other elastic components are consistent with the absence of strains in the long range and no rotations are induced along the transformation path. Thus, it gives rise to the reference lattice parameter $a_{\text{ref}} = 0.37984$ nm, and also the magnitudes of correct Burgers vectors, i.e. $b_1 = b_2 = 0.26859$ nm, selected by the coherent reference state. When an incorrect reference state is arbitrary chosen, the corresponding Burgers vectors deviate in magnitude and non-zero spurious stress fields exist in the microstructure. For instance, a residual stress state in Au persists with ${}_{\text{Au}}\sigma_{11}^{\text{c}} + {}_{\text{Au}}\sigma_{11}^{+\infty} \simeq 6.29$ GPa and $\simeq -3.66$ GPa, for $\delta_{(010)} = 0$ and 1, respectively. A larger residual stress field exists in Cu as well, where ${}_{\text{Cu}}\sigma_{11}^{\text{c}} + {}_{\text{Cu}}\sigma_{11}^{-\infty} \simeq -8.77$ GPa, for $\delta_{(010)} = 0$, and $\simeq 5.09$ GPa, for $\delta_{(010)} = 1$.

For the following calculations in interfacial hexagonal-shaped dislocation patterns, the upper half-plane domain $D = \{\{0 \leq n \leq n_{\max}\} \cup \{|m| \leq n_{\max}\}\} \setminus \{m \leq 0,\ n = 0\}\}$ is defined by setting $n_{\max} = 50$, which is large enough to ensure accurate solutions in truncated elastic stress fields with three sets of dislocations.

Figure (3.27a) shows the elastic strain energy landscape for the (010) Au/Cu misfit interface with classical boundary conditions between both neighboring semi-infinite Au and Cu crystals, for simplicity. To determine such energy landscape, the triangular domain $\mathcal{T}_{\text{ABC}}$ is first discretized into 121 nodal points with coordinates (η_1^i, η_2^i), such that $\{\eta_1^i, \eta_2^i\} \in\ ]0,\ 1/2[^2$, as depicted by the gray dots in Fig. (3.27a). Using the persistent short-range elastic fields, the finite (guaranteed by the zero far-field stresses) stored elastic energy per unit area is computed for any (η_1^i, η_2^i) using eq. (3.116) with $r_0 = b_1/4$. Following the standard interpolation procedure of eq. (3.117), the elastic strain energy for any given $(\eta_1, \eta_2) \in\ ]0,\ 1/2[^2$ shows a smooth and symmetric landscape with respect to the median $(\eta_1 = \eta_2)$ of the triangular domain, within which the unique strain energy minima is obtained at $\eta_1 \to 1/2$ and $\eta_2 \to 1/2$, with $\gamma_{\text{e}}^{\min} = \gamma_{\text{e}}(\eta_1 \to 1/2, \eta_2 \to 1/2) \simeq 0.57344$ J.m^{-2}. Planar dislocation reactions and junctions for (010) misfit interfaces are also shown to be energetically unfavorable. It is therefore demonstrated that the initial orthogonal grid of uniformly spaced edge dislocations corresponds to the equilibrium structures for the (010)-type misfit interfaces, which satisfies the condition of vanishing far-field stresses as well as the minimum-energy criterion for predicting the most favorable dislocation structures.

Near the unreacted state of the (010) Au/Cu system, the present energy landscape shows concave slope profiles at $\eta_1 \simeq \eta_2 \simeq 1/2$. For calculations with other fcc/fcc heterosystems in the (010) cube-cube orientation relationship (not shown here), the corresponding unreacted state can exhibit convex energy profiles, which suggest different bound crossed states of dislocation reactions for the (010) twist GBs. Thus, the parent dislocations could also exhibit strong repulsive interactions or crossed states where local bend and twist of dislocations may locally occur at the short-range distances, as observed in non-coplanar dislocations [176].

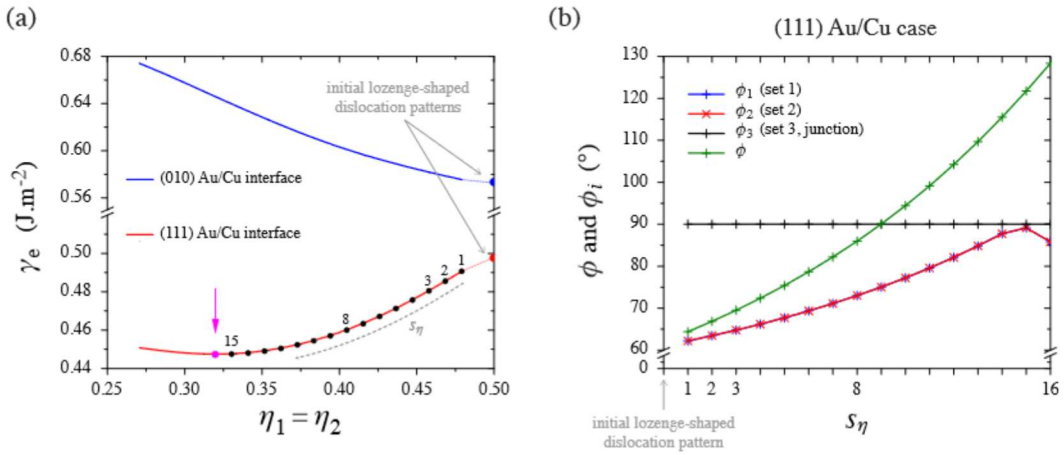

FIGURE 3.28: (a) Dependence on $\eta_1 = \eta_2$ of the elastic energy γ_e in J.m^{-2}, i.e. along the bisecting lines of the admissible triangular domains $\mathcal{T}_{ABC}$, as displayed in Figs. (3.27). The blue and the red curves correspond to the mismatched (010) and (111) Au/Cu interfaces, respectively. The latter exhibits black dots, indexed by $s_\eta = 1, \ldots, 16$, which represent the minimum-energy path from Fig. (3.27b). The large points at $\eta_1 = \eta_2 = 1/2$ are related to the initial lozenge-shaped patterns with two crossing sets of dislocations, whereas the vertical arrow shows the minimum-energy configuration associated with the (111) semicoherent interface. (b) Dependence on s_η of the dislocation characters ϕ_i for the three sets and the angle ϕ between the two parent dislocations for the corresponding (111) Au/Cu case. All these quantities are expressed in °.

Case 2: The (111) Au/Cu interface with three sets of dislocations

In contrast to the (010) Au/Cu case, the (111)-oriented habit interface planes exhibit different arrangements of atoms, which yield to more complex interface dislocation patterns and also to general elastic states where both constituent strains and rotations are unequally partitioned between the crystals [123].

The present orientation relations associated with the (111) Au/Cu misfit case are defined by $\boldsymbol{x}_1^{or} = [11\bar{2}]$, $\boldsymbol{x}_2^{or} = [111] \parallel \boldsymbol{n}$, and $\boldsymbol{x}_3^{or} = [1\bar{1}0]$, within which the fcc {111} close-packed planes contain $a_{ref}/2\langle 110\rangle$-type Burgers vectors. Similarly to the (010) case, such Burgers vectors must be defined in the proper reference state under the condition of vanishing far-field stresses in the (111) Au/Cu bicrystal. By arbitrarily choosing $\boldsymbol{b}_1 = a_{Au}/2[10\bar{1}]$ and $\boldsymbol{b}_2 = a_{Au}/2[0\bar{1}1]$ as the reference Burgers vectors, the quantized Frank-Bilby eq. (3.121) gives rise to the lozenge-shaped dislocation structure that is specifically comprised of two arrays of parallel dislocations (with no local reactions at nodes): the initial line directions are defined by $\boldsymbol{\xi}_1^{un} \parallel [01\bar{1}]$ and $\boldsymbol{\xi}_2^{un} \parallel [10\bar{1}]$, so that the individual characters are $\phi_1^{un} = \phi_2^{un} = 60°$, and the angle between these two unrelaxed sets of dislocations is $\phi^{un} = 60°$. In addition, $p_1^o = p_2^o = 2.25144$ nm, so that the inter-dislocation spacings are given here by $d_1^{un} = d_2^{un} = 1.94980$ nm.

As illustrated in Fig. (3.26), the dependence of the total far-field stress components in the (111) system, i.e. in both Au (black line) and Cu (red line) on δ, yields to a predicted reference state for $\delta_{(111)} = 0.57962$, so that $a_{ref} = 0.38096$ nm, and also to the magnitudes of correct Burgers vectors are defined by $b_1 = b_2 = 0.26938$ nm. Moreover, Fig. (3.26) shows stronger spurious stress values for the (111) than (010) system cases, by a factor of 2.33 (2.15) in Au (Cu) when $\delta = 0$, i.e. when Au is improperly selected as the reference state. The same qualitative conclusion regarding the spurious stress state can be drawn for $\delta = 1$.

Using the aforementioned Frank-Bilby solution as the initial dislocation structure for possible elastic strain relaxation, Fig. (3.27b) shows the pre-computed elastic landscape as function of η_1 and η_2, associated with the (111) misfit interface case. The symmetric landscape has been computed using the same number of nodal points than in Fig. (3.27a), for which the orientations of both plots are different for clarity. The elastic energy per unit interface area for the unrelaxed

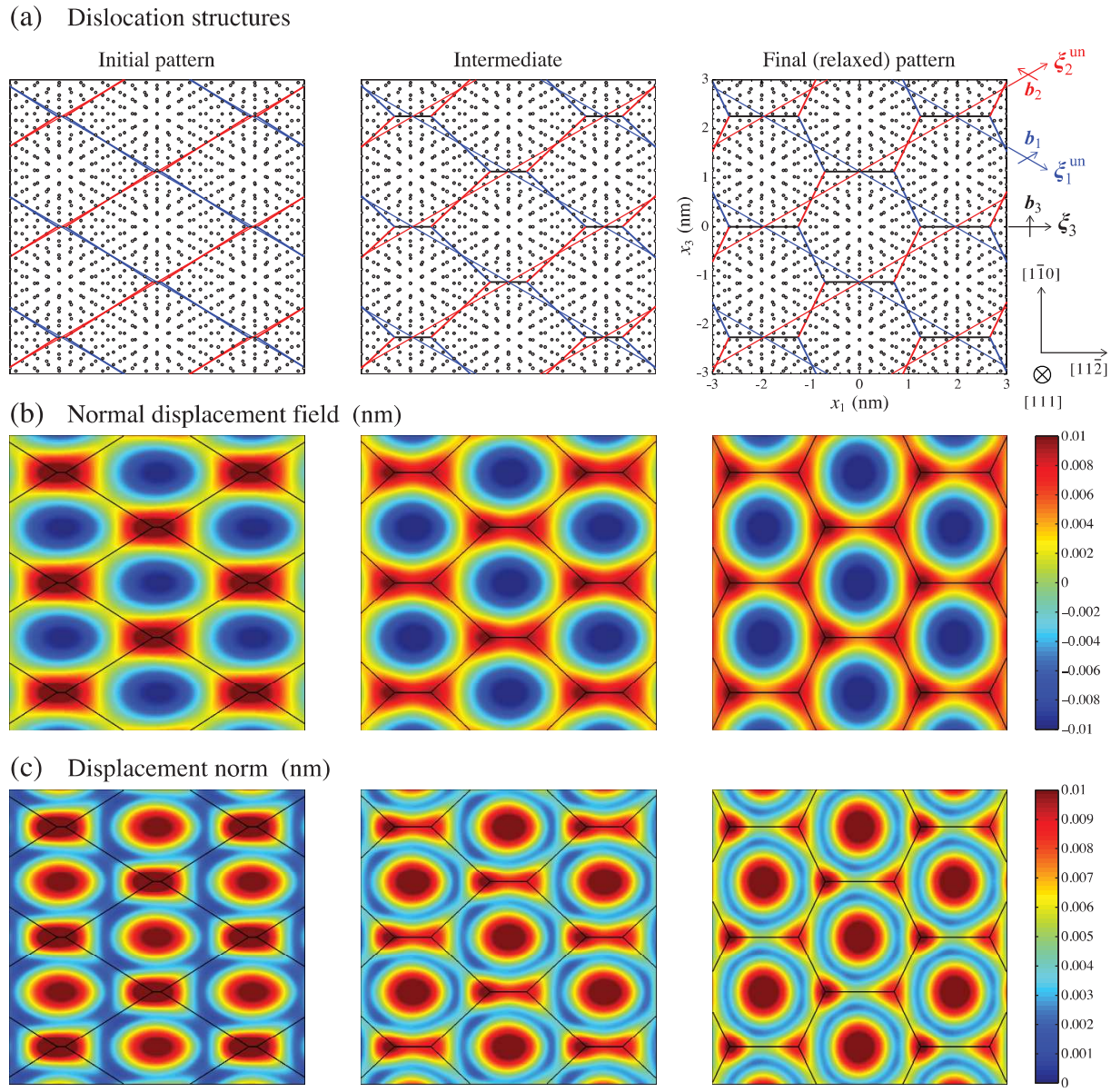

FIGURE 3.29: Plots of initial, intermediate, and final states along the computed minimum-energy path for the (111) Au/Cu heterophase interface. The initial periodic network of lozenge-shaped misfit dislocations undergoes local relaxations and also leads to a final elastically relaxed hexagonal-shaped dislocation pattern with lowest short-range strain energy. (a) Dislocation structures. Distribution of (b) the normal displacement component u_2 and (c) the displacement norm u. See text for the displacement field expressions.

lozenge-shaped dislocation pattern is given by $\gamma_e(\eta_1 \to 1/2, \eta_2 \to 1/2) \simeq 0.49568$ J.m^{-2}, with $r_0 = b_1/4$, which is slightly lower than the stored energy for the (111) Au/Cu system for $\eta_1 \to 1/2$ and $\eta_2 \to 1/2$. Here, the landscape for the (111) system is qualitatively and quantitatively different than the (010) case, since the former gives rise to the existence of a unique minimum-energy dislocation configuration with three sets of dislocations resulting from junction reactions.

The energy minimization procedure that involves the conjugate gradient algorithm is performed by using a prescribed convergence criterion in the pre-computed energy landscape. The interface dislocation structures with the lowest elastic energy are considered to be found when the difference between the values of the stored elastic energy for two subsequent iterations is less than 10^{-4} J.m^{-2}. The corresponding minimum-energy path is determined by using the nudged elastic band method between the initial non-equilibrium and the minimum-energy states, for which the spring constant k in eq. (3.120) has been varied over several orders of amplitude without noticeable effects on the computed path. The obtained minimum-energy path is displayed in Fig. (3.27b) by the black curved chain with equidistantly positioned images (i.e. intermediate states), where the final configuration state is designated as the final elastically strain-relaxed dislocation pattern. Here, the smooth path has no energy barrier (therefore also, no saddle point) and 15 intermediate states, which connect the initial and final states, are constructed. The minimum strain energy related to the relaxed dislocation pattern is given by $\gamma_e^{\min} = \gamma_e(\eta_1 \to 0.31981, \eta_2 \to 0.31981) = 0.44733$ J.m^{-2}, which corresponds to a significant decrease in strain energy of 9.75%.

The variations of strain energy along the median $(\eta_1 = \eta_2)$ of the two (010) and (111) Au/Cu landscapes, as displayed by the blue and red dotted lines in the insets of Fig. (3.28a), start from their initial corresponding lozenge-shaped dislocation structures at $\eta_1 = \eta_2 = 1/2$ with different stored energy values. The red (blue) line illustrates the (un)favorable elastic energy profile for junction formation that continuously decreases (increases) with decreasing both values of η_1 and η_2 from $1/2$ at the (111) ((010)) Au/Cu heterophase interface. The intermediate states between the lozenge-shaped and the relaxed hexagonal-shaped dislocation configurations for the (111) case are indexed by $s_\eta = 1, \ldots, 15$. Such considerable saving in strain energy along s_η is related to the change in dislocation structures, e.g. dislocation characters ϕ_i and the angle ϕ between $\boldsymbol{\xi}_2$ and $\boldsymbol{\xi}_1$, which can be examined along the determined minimum-energy path. Figure (3.28b) plots these geometrical characteristics in terms of ϕ (in green), ϕ_1 (blue), ϕ_2 (red), and ϕ_3 (black, for the newly formed set of dislocation junction) as a function of s_η. It is also found that the geometrical equilibrium configuration of the minimum-energy dislocation pattern is characterized by $\phi^{\text{eq}} \simeq 128.4^\circ$, $\phi_1^{\text{eq}} = \phi_2^{\text{eq}} \simeq 85.8^\circ$, and $\phi_3^{\text{eq}} = 90^\circ$. Both sets 1 and 2 deviate by 4.2° from pure edge characters, and the dislocation structure deviates by 8.4° from regular hexagonal-shaped configuration. Such dislocation arrangement is in agreement with atomistic analysis in iron, where deviations from pure screw dislocations in (110) bcc twist GBs with comparable order of dislocation spacings have been reported using molecular statics simulations [290].

Figures (3.29) illustrate the strain-relaxed rearrangements of the interfacial dislocations from the lozenge-shaped configurations on the (111) heterophase interface using different elastic quantities, which can, for example, be used to analyze the likely regions for nucleating interface dislocations or absorbing and annihilating point defects (interstitials and vacancies). All contour plots are displayed at $x_2 = 3\,a_{\text{Au}}$ with respect to the three dislocation configurations shown in Figs. (3.29a), i.e. the "initial"[1] at $s_\eta = 1$, intermediate ($s_\eta = 8$), and the final relaxed ($s_\eta = 16$) states, for which the specific intermediate case is located exactly halfway between both initial and final states, as depicted by the orange point along the computed minimum-energy path in Fig. (3.27b). A schematic representation of the atomically sharp (111) Au/Cu interface with current periodic dislocation lines is shown in Figs. (3.29a), where the Au (Cu) atoms are plotted by white (gray)

[1]Here, "initial" means the first admissible configuration with three sets of dislocations, where an initially small dislocation segment for the junction has been introduced (in the direction of the steepest descent between the two parent sets) to solve the corresponding solutions for hexagonal-shaped dislocation patterns.

dots. The three corresponding Burgers vectors on the (111) close-packed plane are represented as well.

Figures (3.29b) and (c) illustrate the normal displacement component $u_2 = \tilde{u}_2^{\mathrm{dis}}(x_1, 3\,a_{\mathrm{Au}}, x_3)$ and the displacement norm $u = |\tilde{\boldsymbol{u}}^{\mathrm{dis}}(x_1, 3\,a_{\mathrm{Au}}, x_3)|$, respectively. Figures (3.29b) show that the minimum values of $u_2 = -0.01$ nm are located in the centers of the dislocation patterns, while the maximum values yield close to the dislocation junctions for the initial unrelaxed pattern. In the final relaxed dislocation configuration, the maximum values are unequally distributed at the three-fold dislocation nodes, e.g. $\mathrm{J_I} = \{\mathrm{J_1}, \mathrm{J_3}, \mathrm{J_5}\}$ versus $\mathrm{J_{II}} = \{\mathrm{J_2}, \mathrm{J_4}, \mathrm{J_6}\}$, for which the set of junction nodes $\mathrm{J_I}$ gives rise to larger amplitudes of u_2 than $\mathrm{J_{II}}$. Figures (3.29c) display the complex relief of displacement norm u with the largest magnitudes at $\mathrm{J_I}$, for illustration.

3.6.6 Comparison with atomistic simulations

The model interfaces for the present comparisons with atomistic simulations are selected according to the following criteria:

1. The structure of the interface is describable as a dislocation network. The present study is concerned with dislocation-based models of interface structure. Thus, interfaces to which these models do not apply are not suitable.

2. This dislocation network undergoes a relaxation through the dissociation of four-fold junctions into three-fold junctions. Some interfacial dislocation networks are not suitable for the study because they contain stable four-fold junctions that do not undergo any relaxation.

3. The interface dislocation network is initially periodic and remains so as it relaxes. Moreover, the dislocations in the network do not dissociate into partials. These choices are necessitated by current limitations in modeling capabilities [249, 250]. The requirement of periodicity is met by selecting special interfaces that may be modeled by two overlapping sets of misfit dislocations, whereas general interfaces involve three overlapping dislocation sets [1]. The requirement of no dissociation excludes from consideration GBs in low stacking fault energy materials.

4. The final structure of the relaxed interface is not the outcome of any inherent symmetry that the interface possesses. For example, while twist boundaries on {111} planes in aluminum meet all the foregoing conditions, they are excluded from consideration because the relaxed dislocation structure in these interfaces has the same *p6m* symmetry as the underlying, unrelaxed dichromatic pattern [69, 70]. Such a symmetry-driven relaxation does not constitute a stringent test of the elasticity-based relaxation model.

5. Differences between the relaxed and unrelaxed dislocation network must be discernable in atomistic simulations. Thus, the dislocations should not be so closely spaced that they are difficult to distinguish yet not so far apart that they would require very large atomistic models. This criterion is met through judicious selection of the interface crystallographic character (misorientation, misfit, and plane orientation).

All of the foregoing criteria are met by the two classes of model interfaces selected for the present comparison: low-angle twist GBs on {110}-type planes in niobium (Nb t-GBs) as well as heterophase interfaces between {111}-type planes of silver and {110}-type planes of vanadium (Ag/V interfaces). For both interface types, a series of structures is considered by varying twist angle, θ, i.e. $0^\circ \leq \theta \leq 10^\circ$ for both interface types. When $\theta = 0^\circ$, the Nb t-GB reduces to a perfect single crystal while the Ag/V interface is in the NW OR [279, 192], where $\langle 110 \rangle_{\mathrm{fcc}}$ and $\langle 100 \rangle_{\mathrm{bcc}}$ are parallel within the interface plane.

Ag/V interfaces formed in magnetron sputtered multilayers have been characterized extensively [280]. They are observed in a variety of ORs and with a wide range of interface planes.

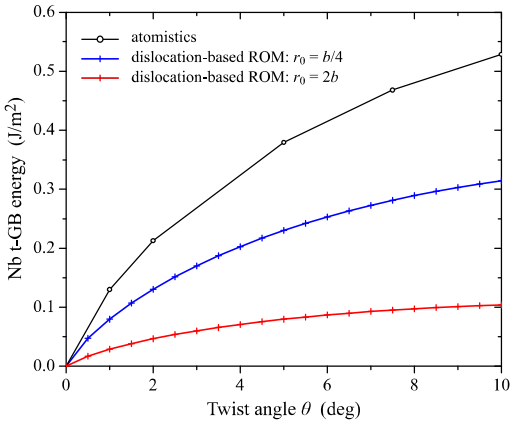

FIGURE 3.30: Nb-t GB energies computed as a function of θ using the dislocation-based model and atomistic modeling.

Among the structures reported are Ag/V interfaces in the KS and NW ORs, both along Ag $\{111\}$ and V $\{110\}$ planes. They have been previously modeled using elasticity theory, albeit without accounting for network relaxations, as well us using classical potential [172]. Comparisons with atomistic simulations revealed discrepancies that were hypothesized to arise from nodal reconstructions of the kind investigated here. The dislocation-based model is presented in details in section 3.6, while the embedded atom method potentials are used to model atomic interactions in both Nb [294] and Ag/V [281].

No experimental investigations of Nb $\{110\}$ t-GBs have been reported. Nevertheless, these interfaces were previously investigated by atomistic simulations [173], by anisotropic linear elasticity theory, and most recently using phase field models [211]. However, no quantitative comparison between structures predicted by the elasticity theory and atomistic modeling has been previously conducted.

Nb $\{110\}$ t-GBs

Figure (3.30) compares the energy of Nb t-GBs computed from atomistic models with values obtained using the dislocation-based model, the latter using two different core cutoff radii. Both atomistics and the elasticity theory reveal similar trends, with energies increasing monotonically as a function of θ within the range of twist angles investigated. Comparison of elastic results before and after relaxation of the dislocation network shows that this step in the calculation yields a relatively modest reduction in elastic energies. For example, for $\theta = 2^\circ$, the reduction is approximately 8% of the initial energy. Energies computed from atomistic models are higher than those obtained from the elasticity theory. This difference is due to dislocation core energies, which are inherently captured in the atomistic calculation, but are not accounted for in the dislocation approach. The larger the core cutoff, the lower the energy computed by the present calculations. Interestingly, regardless of the cutoff radius, the values are smaller than the atomistic ones by an apparently θ-independent factor, consistent with both the elastic and core energies scaling in proportion to the total length of dislocation segments in the network, to a first approximation.

Figure (3.31) compares the structure of Nb t-GB dislocation networks determined from atomistic modeling to ones found with the elasticity theory, using $\theta = 2^\circ$ as an example. Other twist angles give rise to qualitatively similar structures. The atomistic structure in Fig. (3.31a) consists of a 2-D tiling of hexagonal regions separated by a connected network of misfit dislocation segments of predominantly screw character. Two types of segments are present: ones with $\frac{1}{2}\langle 111\rangle$-type Burgers vectors as well as ones with $\langle 100\rangle$-type Burgers vectors. As shown in Fig. (3.31a), the former are approximately twice as long as the latter. Consistent with previous studies in bcc Nb [173]